THE NUMERICAL STUDY OF FLUID-SOLID INTERACTIONS FOR MODELLING BLOOD FLOW IN ARTERIES

by

Shunzhi ZHAO

A dissertation submitted to

City University

in fulfilment of the requirement

for the degree of

Doctor of Philosophy

OCTOBER 1999

Department of Mechanical Engineering & Aeronautics

City University

London

Contents

List of Figures

List of Tables

ACKNOWLEDGEMENTS

I wish to acknowledge and gratefully thank the UK Engineering and Physics Sciences Research Council for funding this project.

My special thanks go to my supervisor Dr. R.S. Neve for the guidance and advice generously provided during the course of the study.

Sincere thanks are due to my co-supervisor Dr. X.Y. Xu who provided me with the opportunity to carry out this project and furthermore for her guidance and support throughout.

I also wish to thank Prof. M.W. Collins who initiated me into haemodynamic studies.

I would like to thank my clinical collaborator: Drs. A.D. Hughes, S.A. Thom, A.V. Stanton and B. Ariff in St. Mary's hospital, Imperial College for helpful discussions and supplying the experiment data.

Finally, I would like to express my special thanks to my family for the encouragement and support affectionately given throughout the years of my study.

DECLARATION

I grant powers of discretion to the University Librarian to allow the thesis to be copied in whole or in part without further reference to the author. This permission covers only single copies made for study purposes, subject to normal conditions of acknowledgement.

Abstract

Atherosclerosis is a problem that affects millions of people worldwide. The causative factors that contribute to the formation of atherosclerotic lesions have been studied extensively. Haemodynamic factors are known to be important determinants. However, the precise role played by haemodynamics in the development and progression of vascular disease is incompletely understood and findings have sometimes been contradictory. At the same time much solid mechanics oriented work has been done with a specific focus on stress concentrations in the arterial wall in order to examine other possible factors. While great progress has been made in studies of both haemodynamics and vessel wall mechanics separately, it is apparent that the problem of blood flow in arteries is one of fluid-wall interaction, and this necessitates the incorporation of the wall mechanics into fluid dynamics. The combination of fluid/solid mechanics may lead to further insight into the mechanisms underlying the formation of atherosclerotic lesions by taking the dynamic interaction between the blood and vessel wall into account.

In this study, a novel numerical algorithm for coupled solid/fluid problems was developed and applied to arterial flows. The coupled model involves the use of two commercial codes, CFX and ABAQUS. The hybrid nature (finite volume method for the fluid and finite element method for the solid) makes itself a highly efficient tool for modelling fluid/solid interactions. The method is able to predict the full, time-dependent wall behaviour, as well as the details of the flow field. Computer programs, originally developed to process clinically obtained MRI images, have been modified in order to provide geometrical data of *in vivo* human carotid bifurcations and to generate computational grids. New program routines were developed for the incorporation of wall movement required by the computer simulation, and integration of the fluid and solid mechanics codes for the coupled model. A comprehensive range of code validation exercises have been carried out to determine the reliability of the computer codes.

Finally, the coupled model has been applied to the modelling of pulsatile flow in anatomically realistic compliant human carotid bifurcations. *In vivo* pressure and mass flow waveforms in the carotid arteries were obtained from the individual subjects using non-invasive techniques. The geometry of the computational models was reconstructed from magnetic resonance angiograms. Results have been validated against the *in vivo* MRI measurements obtained from the individuals scanned. High wall stress and low shear stress was found in those areas most prone to atherosclerosis. It is demonstrated that the presented coupled modelling scheme can be used as an efficient and reliable tool for detailed analysis of blood flow and vessel mechanics. In future, application of the coupled model in a large number of individual cases together with disease patterns may further elucidate the roles of haemodynamics and vessel wall mechanics in atherosclerosis.

Chapter 1

Introduction

Focal atherosclerosis is the major cause of death and morbidity in the world. Atherosclerosis is a complicated process involving intimal thickening, accumulation of lipids and calcium in the extracellular matrix, and smooth muscle cell proliferation. These changes often lead to intraluminal events causing narrowing and eventually total occlusion of the vessel. At an early stage of the disease atherosclerotic plaque formation may also induce thrombus formation, i.e. fragments of the thrombus break off and obstruct smaller arteries downstream.

Cardiovascular diseases such as atherosclerosis are known to be influenced by blood flow [1, 2, 3, 4]. In order to investigate the complex mechanisms involved in the development of atheroma, a thorough understanding of the haemodynamic phenomena is necessary. Modern techniques such as ultrasound and magnetic resonance imaging (MRI) enable *in vivo* measurements of pulsatile blood velocities to be undertaken. But they are subject to some uncertainties. The high level of computer technology and recent developments in computational fluid dynamics (CFD) now means that 3-dimensional flows in irregular geometries can be simulated as a matter of course by standard commercial codes. Also features such as flow unsteadiness and time-dependent boundaries can be accommodated. However, the real physiological system is far more complicated. The simulation of such an *in vivo* process cannot be completed satisfactorily by CFD alone.

On the other hand, biomechanical structural analysis is another research field which can

provide predictions of deformation and stresses in normal and diseased arteries. From engineering principles, it is known that the intensity of these stresses can be relatively large in regions where there are sudden changes in geometry, a phenomenon known as "stress concentration". It has been found that this type of stress concentration could occur in the arterial branching area and may play a role in atherogenesis [5]. Vascular structural analysis is useful to understand the interrelationship between arterial wall mechanics and transport properties and how this might relate to the arterial diseases. The structural response of a large artery is characteristically complex and includes the highly nonlinear, history-dependent response of a nonhomogeneous anisotropic segment undergoing finite deformations. Modern finite element techniques make it possible to treat such a complex material.

While great progress has been made in studies of both haemodynamics, mostly with rigid wall assumption, and arterial wall mechanics ignoring the flowing fluid, it soon became apparent that the general problem was one of fluid-wall interaction, and necessitated consideration of fluid dynamics and solid mechanics of the wall [6, 7, 8] together. Interactions between the flowing fluid and the surrounding structure are complex. A solution of the general coupled problem is difficult to obtain due to the non-linear nature of the whole system. Most researchers have used either self-developed packages or improved commercial packages. The various assumptions and approximations made in these studies preclude them from being extended to complex geometries such as bifurcations [7, 9, 10]. Alternative approaches which can solve the coupled system of equations governing the flow and wall motion in arbitrary geometries are needed.

1.1 Medical Background

1.1.1 Atherosclerosis

Atherosclerosis is not merely a disease in its own right, but a process that is the principal contributor to the pathogenesis of myocardial and cerebral infarction, gangrene and loss of function in the extremities. The process, in normal circumstances a pro-

tective response to insults to the endothelium and smooth muscle cells of the wall of the artery, consists of the formation of fibrofatty and fibrous lesions, preceded and accompanied by inflammation. The advanced lesions of atherosclerosis, which, when excessive, become the disease and which may occlude the artery concerned, result from an excessive inflammatory-fibroproliferative response to numerous different forms of insult. The earliest recognisable lesion of atherosclerosis is the so-called fatty streak, an aggregation of lipid-rich macrophages and T lymphocytes within the innermost layer of the artery wall, the intima. Animal observations have shown that fatty streaks precede the development of intermediate lesions [11], which are composed of layers of macrophages and smooth muscles and, in turn, develop into the more advanced, complex, occlusive lesions called fibrous plaques. The fibrous plaques increase in size and, by projecting into the arterial lumen, can impede the flow of blood. They are covered by a dense cap of connective tissue with embedded smooth muscle cells that usually overlays a core of lipid and necrotic debris. The fibrous plaques contain mononocyte-derived macrophages, smooth muscle cells and T lymphocytes. Recent data have shown that most of the sudden deaths from myocardial infarcts are due to ruptures or fissures, particularly in the margins of the fibrous cap where there are more macrophages, resulting in haemorrhage into the plaque, thrombosis and occlusion of the artery [12].

1.1.2 Mechanisms underlying the development of atherosclerosis

A variety of theories have been proposed regarding the cause of atherosclerosis. Among these are the role of haemodynamics and wall mechanics in terms of its genesis and progression [2, 13]. The blood vessels are permanently exposed to two types of mechanical stresses: tensile stress originating from the arterial pressure and shear stress resulting from the blood flow. These stresses operate not only to control vasomotor activity but also to regulate the growth and physiologic development of the blood vessels.

Haemodynamic factors

Previous studies have indicated that several global factors contribute to accelerated large

vessel atheroma, including: hypertension, aging, smoking, hypercholesterolemia, and diabetes mellitus [14]. Correction of some of these risk factors has been shown to reduce the rate of progression of plaque [15], and to reduce wall thickening [16]. However despite the importance of global risk factors, atheroma is essentially a focal disease. In this context, it is noteworthy that atheromatous lesions are seen at characteristic sites in blood vessels; occurring in regions of branching and marked curvature [17, 18]. These are regions where atypical flow patterns would be expected [1, 19, 20]. Reduced flow velocity and wall shear stress, flow separation, and departures from unidirectional laminar flow would all tend to increase the residence time of circulating atherogenic particles and increase endothelial transjunctional permeability. There are other wall shear stress indices that could be derived from the instantaneous wall shear stress, such as, wall shear stress temporal gradient, wall shear stress spatial gradient, oscillatory shear index (OSI) (defined by Ku et al. [18] to quantify cyclical variation in wall shear stress). Attempts were made to correlate them to the locations of atherosclerotic plaques without conclusive results.

Low shear on the outer walls of bifurcations and on the inner walls of curvatures may promote atherosclerosis through influences on leukocytes, platelets, and endothelial cell function [21]. Activated leukocytes show pseudopodium extensions and express surface adhesion molecules. These features facilitate adherence to, and migration through the endothelium. Although evidence shows that development of atherosclerotic lesion is associated with locations where the mean wall shear is relatively low, the role of oscillating wall shear in both direction and magnitude is not quite clear. At sites where shear stress is disorganised and fluctuated, it has been shown that endothelial cell mitosis rates are elevated, which suggests cell injury [22]. Shear is also known to affect endothelial morphology and function, and to enhance pinocytosis [23].

Mechanical wall factors

Although it is now recognised that specific patterns of local blood flow predispose the development of atheroma, the mechanisms underlying the important determinant of cardiovascular risk are less well understood. Many other possible factors are currently being

examined. One area that is gaining attention is the role of mechanical stress on the vessel itself in atherogenesis. However, compared to the haemodynamic related factors, the theory on mechanical wall factors is far from complete.

By mathematically analyzing the overall geometry of an idealized branch point, Niimi [24] calculated the stress concentration in an arterial bifurcation. Also, through the principles of engineering mechanics, areas of high wall stress were created due to the geometry of bifurcating arteries [25]. Most numerical research on vessel wall has been devoted to stress concentration analysis of the arterial wall, when it is loaded with a normal incremental pressure of, (usually) 40 mmHg [26, 5]. This corresponds to the pressure difference between peak systolic and diastolic pressure phases. These numerical studies also demonstrated that distinct areas of stress concentrations existed in artery bifurcations.

The elevated tensile stresses that occur at bifurcations and in regions of curvature may also promote atherosclerosis. High tensile stresses are associated with vessel wall thickening and alternations in composition [27]. These features affect transmural permeability and sieving [28], and would therefore be expected to play a role in determining particle efflux rates. Reduced particle efflux rates would favor intimal accumulation of atherogenic cholesterol and leukocytes.

Mechanical forces regulate cell growth and biosynthesis in many tissues. Numerous studies have demonstrated the existence of a direct relationship between circumferential stress to which the vessel wall is exposed and the structure of the wall itself. When the stress increases, there is hypertrophy of smooth muscle and an increase in the content of collagen and elastin. Conversely, when the stress falls, the wall undergoes atrophy. Several physiologic and experimental studies confirmed the relationship between stress and composition of the vessel wall. In a study by Bardy [29], it has been demonstrated that protein synthesis by smooth muscle cells was greatly increased when the vessels were subjected to elevated intraluminal pressures. Furthermore, pressure and angiotensin II were capable of inducing fibronectin expression in the arterial wall in a synergistic manner [30]. The effector mechanisms for the increased expression of fibronectin in response to pressure in-

volved local activation of the vascular renin–angiotensin system. Mechanical and humoral factors could therefore interact to promote vascular remodelling.

1.2 Numerical Modelling of Arterial Flows–Current Status

Cardiovascular haemodynamics forms an important current class of medical research. Accurate assessment of temporally and spatially varying wall shear stress and knowledge of wall mechanical behaviour, which are of considerable physiological interest, are quite difficult to obtain by current non-invasive techniques. An alternative approach to measurement of detailed arterial flow characteristics employs computer simulations, making it possible to determine temporally and spatially varying shear stresses. Over the last ten years, as the current generation of Computational Fluid Dynamics codes have been developed, they have been applied to arterial problems and have been demonstrated to be a valuable and reliable tool in this area.

The mathematical description of local blood flow uses the time-dependent, three-dimensional, incompressible Navier-Stokes equations for Newtonian or non-Newtonian fluids. Normally, these equations cannot be solved analytically because of the complexity of the problem. CFD techniques, therefore, were developed to solve complex problems numerically. In general, currently available techniques in CFD to solve the above equations fall into four categories. They are the finite difference, finite volume, finite element and boundary element approaches. The finite difference and the finite volume method were historically the first to be developed and have been available for many years. It has been established that these methods give stable results with relatively less computation time than is required by other methods. Although the finite element method allows greater flexibility to build the computational domain, much more time and memory space are necessary for computation. The boundary element method is mainly used for a class of flow problems (potential flow) which is not relevant to blood flow.

It is well known that CFD is a powerful tool for investigating the complex nature of blood flows [31, 32]. Computational modelling of blood flow has the potential of providing

complete haemodynamic data for flow related phenomena and any derived parameters of mechanics. This is particularly important in studies of the role of blood flow in atherogenesis because a combination of these parameters seems to play an influential role in the process. Although there are many difficult problems in applying CFD to blood flows, (for example, the nature of its pulsatility, and the non-Newtonian viscosity of blood) it now has become a matter of computing power to overcome them [33, 34]. In fact, there are a variety of CFD codes available to cover these issues. The combination of computational fluid dynamics and magnetic resonance imaging techniques has been increasingly used to provide subject-specific haemodynamic data in "real" arterial geometries, which becomes a new application field for both CFD and MRI. These include the comprehensive work contributed by Long [35, 36] and Milner et al. [37].

In contrast to the extensive haemodynamic studies, very little work has been done to address the fluid/wall interactions. The early study of fluid/solid coupling was the theoretical work by Womersley [38] based on linearisation of the basic governing equations. Although the effects of wall elasticity, fluid viscosity and flow pulsatility were all taken into account, these are linearised solutions for flow in elastic tubes. The nonlinear effects resulting from the convective acceleration have been considered in the solution developed by Wang and Tarbell [39] using a perturbation theory. However, theoretical analysis of the coupled fluid-solid interactions is only possible for the simplest cases (axisymmetric geometry, linear stress-strain relationship and small deformation). Several numerical studies have been carried out on the simulation of simplified compliant arterial models with purpose-built codes [40, 41, 42] and on the decoupled wall model [5]. It is recognised that the fluid-wall interaction type problem can not be properly dealt with by finite difference or finite volume method alone. In most efforts so far reported to solve the coupled equations for the wall motion and the fluid motion, a finite element method has been utilised. This is partly because the solid mechanics problems have been mostly solved by finite element method.

1.3 Earlier Work in the Group

In the first numerical simulations at the City University group, the ASTEC code [43] was used with its combination of unstructured gridding and finite-volume-type algorithms. ASTEC is now an option within CFDS-CFX4. When the *multi-block* version of the (then) FLOW3D code was released, it was found to be particularly effective for bifurcation studies [44]. However, the finite-element solver FEAT [45] was also used in early studies. The flow equation solver employed in the group over the last 10 years has been the well validated CFD code– now termed CFDS-CFX–a finite volume based code using a structured, patched multi-block, non-orthogonal, curvilinear coordinate grid with a collocated variable arrangement. The basic solution algorithm is the SIMPLEC pressure correction scheme [46], a variation of the original SIMPLE scheme. The SIMPLE algorithm was essentially a guess-and-correct procedure for the calculation of pressure. The difference lies that the momentum equations are manipulated so that the SIMPLEC velocity correction equations omit terms that are less significant than those omitted in SIMPLE.

Our group has been involved in blood flow simulation for over ten years and we have investigated flow in arteries, bifurcations, grafts, skeletal muscle ventricles and stents [47, 48, 49, 50]. Initially the haemodynamics of arterial bifurcations were studied, and after a comprehensive range of code validations involving in vitro (laboratory) data for 2- and 3-dimensional T-junction, simulations for *in vivo* clinical cases of femoral bifurcations and end-to-side anastomoses [51, 52] were carried out. As the moving boundary capability of CFD became available, the work was extended to study the blood flow in skeletal muscle ventricles (SMV) which is a wall-driven unsteady flow with a large volume change and time-dependent gridding [53]. In general velocity predictions compared well with measurements. Nevertheless, all these models either assumed a rigid wall or at most prescribed wall movement from experimental data. To obtain a much clearer understanding of physiological flows and wall behaviour, it is recognised that the blood-wall interaction cannot be neglected in such cases as the cardiovascular system. In the subsequent projects, emphases were placed on the fluid-wall coupled situation.

The stress-strain rate equations for fluids and stress-strain equations for solids are similar,

and considerable effort was spent on incorporating simple wall models into two (finite volume and finite element) CFD codes. This was not without success, both attempts resulting in satisfactory simulations (among others) of the Womersley problem for oscillating flow in a linearly elastic tube. Numerically, the initial efforts in the City group were based on the similarity of the equations of motion for both a fluid and a deformable wall. The Navier-Stokes equations for an incompressible fluid are:

$$\mu_f g^{jk} u_{i;jk} - \frac{\partial p}{\partial x^i} = \rho_f (a_i - b_i) \tag{1.1}$$

where μ_f is the viscosity, g^{jk} a metric coefficient, u_i the velocity vector, p the pressure, ρ_f the density of the fluid, a_i the acceleration vector, and b_i the body force vector per unit mass. Similarly the equations of motion for a linearly elastic, homogeneous, incompressible, isotropic material are:

$$\mu g^{jk} \xi_{i;jk} - \frac{\partial p}{\partial x^i} = \rho (a_i - b_i) \tag{1.2}$$

where, for an incompressible material, μ =2E/3, E the Young's modulus, ξ_i the displacement vector, and ρ is the density of the wall.

Considerable efforts were made by Drs. Frank Henry and Yun Xu to insert simple wall models into the finite volume CFDS-CFX and the finite element FEAT codes respectively. A number of code validation exercises were undertaken, notably the Womersley solution for pulsatile flow in an elastic tube. However, the wall model of Dr. Henry (based on finite volume method) was limited to axisymmetric, infinitesimal strain cases, while Dr. Xu's model with FEAT was based on the finite element method. Although the latter was not restricted to simple geometry, it was very time consuming and was limited to linear elastic, infinitesimal strain on which the coupling calculation was based. To overcome those limitations, the development of a generic advanced coupled fluid/solid mechanics model for use in realistic arterial flows is undertaken.

1.4 Objectives and the Strategy Employed

The ultimate goal of this research was to develop a reliable and robust fluid/solid interaction model for the simulation of blood flow in realistic arterial structures. This was achieved through accomplishment of the following tasks:

(1) to establish an advanced fluid and solid model separately for the simulation of blood flow in arterial structures.

(2) to develop an interface program for the coupling of fluid dynamics and solid mechanics codes.

(3) to construct the geometrical model required by the computer simulation from *in vivo* data obtained with ultrasound and MRI.

(4) to carry out a wide range of code validation tests for flow in simple structures.

(5) Finally, to perform numerical predictions for physiological flow in human carotid artery bifurcations and to validate the predictions against *in vivo* measurement data.

The strategy of the study followed a logical progression. The first stage involved the development of advanced fluid and solid coupled models for blood flow in arterial structures. After both the fluid and solid models were established, an interface program was developed for the coupling between the fluid dynamics and solid mechanics codes. Certain difficulties need to be resolved such as the convergence problem. In order to be able to rely on the numerically predicted results, validation exercises against experimental data were necessary. In addition, analytical solutions of simplified problems could be employed to test the numerical solutions. A wide range of benchmark tests were carried out by studying flow and structural behaviour of simple configurations.

The human carotid artery bifurcation was employed as the subject of the study. Software has been developed to perform 3D geometry reconstruction and grid generation from clin-

ically obtained data with ultrasound and MRI.

Having done these, detailed numerical analysis of blood flow and vessel mechanics in realistic human carotid artery bifurcations was performed and detailed information on both flow and arterial wall were obtained. Finally, predicted wall movement and velocity profiles were validated against *in vivo* obtained experimental data.

1.5 Outline of the Thesis

During the last decades numerical methods have been applied to study blood flow phenomena in great detail. Numerical methods are advantageous in two aspects: (1) to simulate accurately physiological conditions which are difficult to consider by experimental techniques, and (2) to isolate different factors in an investigation. The combination of CFD and SM is of high promise in seeking to provide information both inside the flow domain and on the surrounding structures; the inclusion of wall compliance is a natural extension of our previous work, in the direction of greater fidelity. A detailed description of the way in which the combination of state-of-the-art CFD and SM can give reliable numerical simulations of haemodynamics in compliant human arteries is presented in this thesis. The strategy is illustrated with typical results from the attempts to incorporate solid mechanics into haemodynamics in the vascular system.

Chapter 1 introduces the basic methodology and aspects of fluid-solid coupled problems in vascular system.

In chapter 2, a comprehensive literature survey is given. Firstly, the models for arterial wall behaviour are critically reviewed. Secondly, the overall problem of fluid-solid interactions in arterial flows is discussed.

In chapter 3, a novel numerical method combining two commercial codes for coupled solid/fluid problems is presented. A brief description is given of numerical techniques employed in the finite volume code CFX and finite element code ABAQUS. Automatic grid

generation from clinical data is described. The chapter finishes with discussion about the convergence technique.

In chapter 4, a comprehensive range of code validations are covered. Starting from decoupled problems of fluid flow and wall movement, it proceeds to pulsatile flow in an elastic tube.

Chapter 5 is concerned with the application of the coupled algorithm to more advanced problems such as blood flow in real arterial bifurcation structures. Physiologically realistic modelling of blood flow and vessel mechanics in the human carotid artery bifurcations has been carried out. Results of two subject-specific individual studies are presented. Maps of wall shear stress, contours of velocity in the flow field and wall movement and tensile stress on the arterial wall are all presented. To examine the influence of wall distensibility, comparison of the results for the distensible and rigid models are made. The comparisons of computed and measured wall movement and velocity field show generally good agreement.

Finally, in chapter 6 conclusions are made and topics for future research are addressed.

Chapter 2

Literature Survey

2.1 Introduction

Traditional interest in elastic vessels has focused on their effect on pressure wave propagation. The disorders and diseases of the arterial system represent some of the most actively investigated current clinical and research problems. Hence more attention has been paid to the arterial wall modelling and influence of wall motion on the local flow field at a particular position in an artery because of the recent interest in the possible role of haemodynamic factors in the localisation of vascular disease.

Cardiovascular diseases such as atherosclerosis are known to be influenced by blood flows in terms of their genesis and progression [2, 1]. Numerous *in vivo* and model studies on haemodynamics have been carried out over the last years both experimentally and numerically [13]. Special attention has been concentrated on the analysis of flow at arterial bifurcations.

In parallel, one area that is gaining attention is the role of wall mechanical stress in atherosclerosis. By mathematically analysing the overall geometry of an idealized branch point, Niimi [24] calculated the stress concentrations that would be likely to exist in an arterial bifurcation. Also, through the principles of engineering mechanics, it has been shown that, due to the geometry of bifurcating arteries, area of high pressure-induced wall stress are created [25]. Through experimental observations, lesions have been shown to

lie in locations where there is a variation in physical properties [54, 55]. Using these data in relation to arterial branch points, it has been suggested that high stress concentrations may be a risk factor in atherosclerosis [56, 57].

Up to the present, fluid dynamics and vessel mechanics have been studied separately, and in parallel, both with the aim to obtain knowledge of determinants underlying atheroma formation. The rapid advance in computational techniques and the advent of supercomputers now permit the treatment of complex wall behaviour and blood flow in realistic arterial models. Perhaps the combination of flow dynamics and wall mechanics, together with the study of disease patterns, will lead to a further understanding of the arterial disease processes.

In this review, both engineering and medical aspects concerning blood/wall modelling are surveyed. First, the structure and general characteristics of the arterial wall are discussed. This is followed by a comprehensive review of the constitutive laws. Structural analyses of the arterial wall by mathematical and numerical methods are then discussed. The effects of elasticity of blood vessels on wave propagation and local flow patterns in large arteries are also discussed. Blood flow in large or medium-sized arteries especially bifurcations are reviewed. Then the studies of wall mechanics and fluid dynamics were extended to the overall problem of fluid-solid interactions in arterial flows, which has become a specific topic in computational methods and applied mechanics. Finally, numerical techniques are reviewed together with the alternative coupled methods available in fluid-wall models.

2.2 Basic Characteristics of Arterial Walls

2.2.1 The structure and composition of the arterial wall

Classification of arteries is usually done by their size. Another classification that is very frequently used however is by structure which varies with species and location along the vascular tree [58]. In general, arteries are categorised according to two broad types: elastic and muscular [59]. The larger arteries leading from the heart and the first few branches

are known as the elastic arteries, because of the large amount of elastin in them. These include the aorta, main pulmonary artery, common carotids, and common iliacs. As the distance from the heart increases, the amount of muscle cells, that lie in rings around the lumen of the artery increases, and the arterial structure transforms to what is known as muscular arteries. These include the femorals, renals, coronaries, and cerebrals. Obviously, there are transitional arteries as, for example, the internal carotids, which exhibit some characteristics of both the elastic and muscular type. This classification is very simple, since the two kinds do not differ only by the relative amount of muscle cells or elastin.

The vessel wall comprises five components: endothelial lining, collagen fibres, elastin fibres, smooth muscle cells and ground substances. The ratio between them varies according to the vessel size and the task of each specific segment in the arterial tree, but mainly with age. These components are arranged in three layers: the tunica intima, tunica media, and tunica adventitia (Figure 2.1). The tunica intima typically consists of a one-cell-thick layer of axially oriented endothelial cells with a thin layer of elastin and collagen fibres. An exception is, however, the aorta, in which the intima also includes a subendothelial layer that contains some smooth muscle cells (often oriented axially) and connective tissue [59]. The intima is similar in most elastic and muscular arteries. The internal elastic lamina separates the intima and media, but it is often considered to be part of the latter. A little thicker in muscular arteries, this elastic lamina is primarily a fenestrated "sheet" which allows transport of, for example, H_2O and electrolytes across the wall. The tunica media, which forms the large part of the wall of the vessel, consists primarily of smooth muscle cells that are embedded in a plexus of collagen and elastin and a ground substance gel matrix. The orientation and distribution of each of these fibrous constituents vary with species and location along the vascular tree. The outermost sheet of elastin is called the external elastic lamina; it separates the media and adventitia although it is often considered to belong to the former.

The adventitia, or outermost layer, consists primarily of collagen fibres with admixed elastin, nerves, fibroblasts, and the vasa vasorum. The latter is a vascular network that serves the outer portion of the wall in arteries that are too thick for diffusion of O_2 from

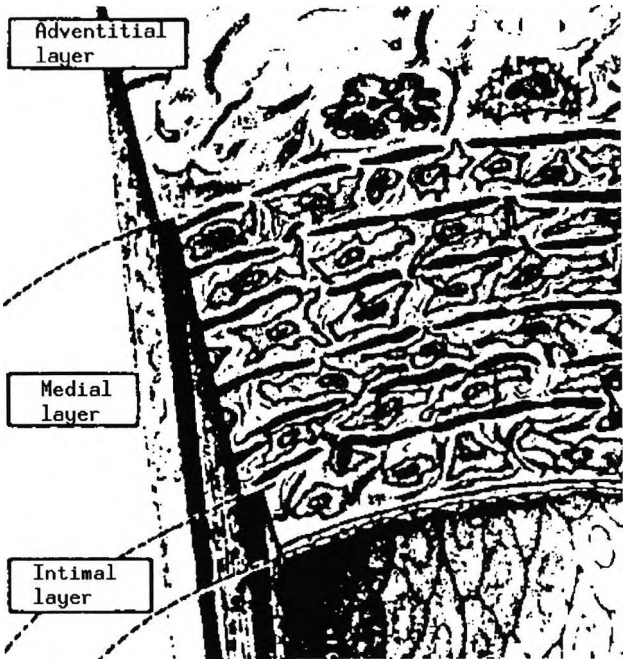

Figure 2.1: Schematic cross-section of typical arteries showing three layers.

the intimal surface to suffice. The adventitia comprises $\sim$ 10% and 50% of the arterial wall in elastic and muscular arteries, respectively.

2.2.2 Mechanical properties of arterial wall components

It is obvious that analytical evaluation of the performance of vessel walls must consider the vessel as a composite material. This requires a description of the interaction between wall components when load-bearing. However, it is well known that elastin, collagen, and smooth muscle play roles in the mechanical performance of the vessel wall only at certain stages of load-bearing and only in specific ways. Hence, before discussing the *overall* properties of the vessel wall as a lumped material it is necessary to consider the mechanical properties of each of the components.

The endothelial layer plays no significant role in determining the mechanical properties of the wall, since its task is to provide a relatively smooth surface at the blood wall interface and to offer selective and controlled permeability. Hence, the mechanical properties of this

monocell layer can be omitted from the discussion on overall elastic performance.

The elastin fibres are a rubbery material which is very extensible. In stretching up to about 60% their original length the fibres follow Hooke's law. However, extensions beyond this value become highly nonlinear. Because of this they are referred to as a non-Hookean material. The range of Young's modulus of the elastin fibres is $3X10^5$ to $6X10^5$Pa [58], with a maximum extension from 100% to 300% and with very little incremental rise in elastic modulus. The elastin fibres form the sole elastic mechanism of the arterial wall at *low pressures* (approximately below 60mmHg), resulting in only a small increase in diameter. At *higher pressures* there is a larger circumferential extension of the material of the wall and there is a recruitment of collagen that results in an increase in wall stiffness which limits further extension. It can be concluded that elastin plays a major role in the small displacement of the arterial wall associated with pulsatile behaviour. When such displacement becomes large the collagen fibres dominate the performance of the wall.

Collagen is regarded as a structural component in various kinds of living tissues. Its geometry usually defines its mechanical properties. In tendons, for example, collagen is found in straight parallel bundles, resulting in very strong and inelastic performance. This contrasts to the heart leaflet where the collagen is arranged in very thin sheets that result in highly flexible properties. In the arterial wall the role of collagen is to maintain the vessel walls in steady tension, which requires a higher resistance to stretch. However, it is essential that at small displacements of the vessel wall the collagen fibres will not interfere. This is achieved by the serpentine shape of the fibres, which permit a certain amount of radial extension and very small longitudinal extension. Although the fibres are built to withstand stretching they have a maximum extension of 50%, beyond which irreversible damage can be caused. The behaviour of collagen is non-Hookean, and exhibits some plastic deformation. The most commonly used value for its Young's modulus is $3.10X10^5$Pa for 100% elongation.

Smooth muscles have more effect on the geometrical cross section of the arterial walls that on its mechanical properties. In the passive state they act more like a viscous fluid and

less like a viscoelastic solid, and thus contribute very little to the total elastic tension in the wall. However, under sympathetic stimulation they can change the vessel diameter by between 10 and 20% in the elastic vessels and can constrict the smaller muscular vessels, even up to a total closure of the lumen. Tension in the smooth muscles causing this vasomotor action is stimulated by many mechanisms. The Young's modulus of smooth muscles varies from $6X10^3$Pa in the passive state to $5X10^7$Pa. In both passive and active state the maximum extension of smooth muscle is about 300%.

2.2.3 The elastic properties of the arterial wall as a composite material

Mechanical characterisation of the blood vessels is an important prerequisite for quantitative descriptions of wave propagation phenomena of the vessels, flow-wall interactions and modelling of arterial structures. A variety of efforts has been devoted to the characterisation of the mechanical properties of blood vessels over the last two decades.

Two different types of experiments can be employed to study these properties. One is the classical stress-strain test on an isolated segment of vessel wall. The other is the pressure-diameter test which treats the vessel as a cylinder with variable internal pressure.

Consistent with histology, the behaviour exhibited by an artery depends on its location along the vascular tree. This observation is illustrated well by in vitro pressure-diameter data, using an *in vivo* length, collected by Cox [60] from various canine arteries. The behaviour is both nonlinear and viscoelastic. However, Patel et al. [61], Vaishnav et al. [62], and Young et al. [63] have shown that elasticity dominates the nonlinear mechanical properties of arterial tissues, whereas the viscosity can be considered as a second-order effect. Detailed stress-strain and pressure-diameter relationships will be discussed in section 2.3.

2.2.4 Incompressibility

Many rubberlike materials are relatively incompressible in the sense that their resistance to volume changes is orders of magnitude greater than their resistance to shape changes. The incompressibility assumption has been used by most of the investigators for arterial

mechanics. Carew et al. [64] confirmed this assumption by measuring the change in the total volume of arterial tissue during deformation. Chuong and Fung [65] reported radial compression tests on regular slabs of rabbit aorta, the edges of the specimens being open to air to allow measurement of load-induced fluid extrusion. They found the fluid extrusion to be 0.5-1.26% of the undeformed tissue volume per 10kPa compressive stress. Based on these results, they concluded that the arterial tissue is only slightly compressible or nearly incompressible. In an incompressible body, the incompressibility condition should be taken into account and incorporated in the formation of an arbitrary amount of hydrostatic stress that cannot be determined from the knowledge of deformation alone, but should be deduced from the knowledge of stress somewhere at the boundary. In an incompressible material like the arterial tissue, the same approach must be used.

2.2.5 Anisotropy

Because of the anisotropic architecture of arterial tissue, it is reasonable to regard the elastic properties of the arterial wall as anisotropic. Many investigators [66, 67] showed that the arterial wall is stiffer in the circumferential direction than axially, but others reported opposite results [68, 69]. Tanaka and Fung [70] showed that the canine thoracic aorta is stiffer in the longitudinal direction than circumferentially, and vice versa in the iliac and femoral arteries. The reported discrepancies are attributable to differences in such factors as methodology, elasticity parameter, animal species and arterial sites. The high deformability, non-linearity, and anisotropy of arterial walls are closely interconnected. Experimental results [66, 71] showed that arteries are cylindrically orthotropic, that is the elastic properties are symmetric with respect to planes perpendicular to the axes of a cylindrical system. Arteries are usually subjected to transmural pressures and axial tension, which give rise to deformations in the principal directions of the cylindrical structure. Weizsacker and Pinto [72] studied the elastic properties of rat carotid arteries, simultaneously applying a wide range of internal pressures and axial forces to their tubular segments. They showed that the longitudinal force was independent of internal pressure within or in the vicinity of the averaged physiological state of deformation and that the arterial wall was isotropic for the physiological range of internal pressure and axial force. Dobrin [67] obtained a similar conclusion from the experimental results of canine carotid

arteries.

2.2.6 Heterogeneity

From histology it is clear that arteries are not materially homogeneous. Rather, they are layered structures (again see Figure 2.1), which strongly suggests that the mechanical properties vary with radius. Experiments by Burton [73] suggest that the endothelial layer does not contribute significantly to the load-carrying capability of the wall. The media and adventitia are the most important structurally. It appears that von Maltzahn et al. [74] were the first to attempt to quantify the nonlinear mechanics of the layered arterial wall. Briefly, they proposed a two-layer model based on separate strain energy functions for the media and adventitia. Their paper was based on pressure-diameter data for passive bovine carotid arteries. They concluded that "the media and the adventitia are anisotropic; that the media is stiffer, more nonlinear, and subjected to higher stresses than commonly assumed; and that both layers are stiffer in the axial direction than in the tangential". Demiray and Vito [75] also proposed separate strain energy functions for the media and adventitia. Their results were based on uniaxial and biaxial tests on isolated media and adventitia layers from a canine aorta. They suggested that the media was orthotropic but assumed that the adventitia was isotropic. They also reported values of the material parameters for each layer. These findings imply that the properties of the media and adventitia are different, but the experiments were not without shortcomings. Unknown effects of the requisite mechanical separation of the media and adventitia on the observed mechanical behaviour must be addressed further. Consequently, others have sought tests wherein the layers do not have to be separated.

Kang and Humphrey [76] proposed that finite inflation and extension experiments on inverted arteries may yield additional information on wall heterogeneity without requiring mechanical separation of the layers. Briefly, the idea is that by turning a vessel inside-out, the spatial locations of the media and adventitia are reversed. Because the inner portion of the wall carries much of the load during an inflation test, the inversion will provide additional information.

In order to determine the stress-strain relationship of the inner (intima and media) and outer (adventitia) layers of blood vessel in the neighbourhood of the zero-stress state, bending experiments were performed by Xie and Fung [77] on aortic strips of rats. In the experiments, one end of a strip was clamped, and a force was applied on the other end. The deflection curves of the strip were measured by regarding the aortic strip as a curved beam, then classical beam theory was employed to analyse the strain distribution from the experimental data. Values of the circumferential Young's modulus were 248kPa and 69kPa in the media and adventitia respectively, for rat thoracic aortas. Values were higher in the ascending aorta wherein the media was also stiffer, which is consistent with the report by von Maltzahn et al. [78] for finite strains. They also suggest that heterogeneity should be accounted for even in the elastic aorta.

Most proposed constitution relations for arteries are based on the assumption of homogeneity of the entire wall, which is sometimes rationalised because of the thinness of the adventitia in elastic arteries. Furthermore, for many practical applications such as the study of pressure-radius relationships, or the propagation of pressure waves, only the properties of the vessel wall (averaged for the wall) are relevant and the possible radial variation of the properties does not significantly affect the problem. It is practical to lump the response of the wall layers and consider the wall as statistically homogeneous.

2.2.7 Dynamic behaviour of arterial walls

The arterial wall is subjected to unsteady loads due to the pulsatile nature of the flow in the cardiovascular system. Arteries are non-linear [79], as they do not meet the definition of an elastic body, which requires that there must be a single-valued relationship between stress-strain. Arteries show hysteresis when they are subjected to cyclic loading and unloading (that is, they have different stress-strain relationships in loading and unloading). When held at a constant strain, they show stress relaxation (that is, decreasing stress). When held at a constant stress, they show creep (that is, increasing strain). When subjected to a sinusoidally varying stress, they exhibit a phase lag in the strain response.

Hysteresis, relaxation, and creep are features of viscoelasticity. There are basically three mechanical models frequently used to describe the linear viscoelastic behaviour of materials [80, 81]. They are the Maxwell, the Voigt, and the Kelvin models, all of which are composed of combinations of linear springs with spring constant μ and dashpots with coefficients of viscosity η. Most authors discuss their experimental results in the framework of the linear theory of viscoelasticity relating stress and strain, generally on the basis of the three above models. More general models may be built by adding increasing number of elements to the Kelvin model. It may happen that none of the models can fit all the experimental data. The conclusion could be reached from such data that the linearised viscoelasticity theory does not apply. A nonlinear theory of the Kelvin type was proposed by Viidik [81] on the basis of a sequence of springs of different natural length, with the number of participating springs increasing with increasing strain.

Numerous studies have been made of the dynamic behaviour of arterial wall by investigating relaxation function and strain effect [82, 83, 84, 85]. For example, Fung [82] investigated the relaxation function of the aorta. As is the case with other tissues, the relaxation of the aorta depends on the stress level. The value of relaxation function at a given value of time is smaller for smaller arteries. This means that the smaller arteries relax faster and more fully.

The strain rate effect also affects the performance of arterial walls. In a study relevant to the safety against automobile crash problem, Collins and Hu [83] used explosive methods to impose a high strain rate ($\dot{\epsilon}$) onto human aortic tissue to express the stress σ. They obtained the result

$$\sigma = (0.28 + 0.18\dot{\epsilon})(e^{12\epsilon} - 1) \qquad for \quad \dot{\epsilon} < 3.5s^{-1} \tag{2.1}$$

Mohan and Melvin [84] performed uniaxial tension tests of human thoracic aortas at quasi-static strain rates in the range $0.01 - 0.07s^{-1}$ and dynamic rates in the range $80 - 100s^{-1}$ to determine the effects of strain rate and direction of loading on the failure properties of the tissue. The results obtained showed that in dynamic tests ultimate circumferential stresses were significantly greater than axial stresses by a mean factor of 1.54, although

there were no significant differences at low strain rates. In addition, they showed ultimate stresses at the dynamic strain were about twice as large as those at the quasi-static strain rates for uniaxial tests in both directions. Following these experiments, they performed biaxial inflation tests on the same tissue at quasi-static and dynamic strain rates [85]. The tissue consistently failed in a direction perpendicular to the long axis of the aorta, and pressure values at failure were greater by a factor of two in the dynamic tests than those in the quasi-static tests.

There are situations in which the departures from elastic behaviour are not of prime interest, in which case elastic theory is adequate. On the other hand, in problems like those involving study of pulse waves travelling along the arterial tree, viscous aspects of the vascular rheology are often quite pertinent. It is therefore important to characterise the vascular tissue not only as an elastic but also a viscoelastic material.

2.3 Constitutive Laws

2.3.1 Measurement of arterial elasticity

Although uniaxial and biaxial tests on flat specimens are often performed to determine the mechanical properties of arterial walls, pressure-diameter data obtained from tubular segments are more informative and realistic. A variety of techniques have been used to measure wall diameters during pressure-diameter testing. These include still or movie camera [86], video dimension analyser [87, 88], photocell combined with light emitting diode or scanning laser [69], sono-micrometer [68], differential transformer [89, 67], wire strain gauge-pasted cantilever or caliper [90], electrolytic transducer [91], several of them being applied to *in vivo* animal experiments. The first three methods are advantageous because they are noncontacting systems. For clinical cases, as well as for *in vivo* animal experiments, ultrasonic echo tracking system [92], ultrasound imaging technique [93, 94], multigate pulsed Doppler system [95], and cineangiography [96] have been used. There is an increased possibility of the use of magnetic resonance imaging method for this purpose [97]. These methods, except for cineangiography, are fully noninvasive.

In the cases of in vitro and *in vivo* animal experiments, arterial blood pressure is measured with pressure transducer positioned as close as possible to the locations where the wall diameter is measured, while sphygmomanometers for the measurement of brachial blood pressure are commonly used in clinical cases. Besides these methods, Liu et al. [98] proposed an improved method of estimating aortic compliance from pressure waveform based on a two-elements Windkessel model of the arterial system, assuming exponential, logarithmic and parabolic pressure-volume relations.

2.3.2 Measures of stress and strain in finite deformation

It is well known that the vascular tissue is capable of undergoing large deformations and that its mechanical response in terms of the usual definitions of stresses and strains is nonlinear. The classical linear theories of elasticity and viscoelasticity are therefore unsatisfactory in describing the mechanical properties of the vascular tissue [99]. Inasmuch as the tissue can be considered to be a one-phase continuum, its nonlinear mechanics can be described by characterisation of the overall force-deformation response using the theories of nonlinear continuum mechanics. Considerable work has been done in vascular mechanics over the past decade and a half wherein this approach has been successfully used to characterise the elastic, viscoelastic and thermoviscoelastic properties of the tissue. Another approach to characterise the nonlinear behaviour of the tissue is through characterisation of its mechanical response in the neighbourhood of various states of deformation of interest. This is the so-called incremental approach. A variety of possible options of stress and strain definitions exist in characterising the properties of soft biological tissue including the vascular tissue, and each definition has advantages and disadvantages. In this review a detailed presentation of different definitions for stress and strain used in overall nonlinear formulations and incremental formulations is given.

With reference to Figure 2.2, consider the unstressed configuration A of a body in the form of a cuboid of dimensions l, b, and h within a rectangular Cartesian coordinate system (x_1, x_2, x_3). Let B be another cuboidal configuration of the body with dimensions λ_1l, λ_2b, and λ_3h where λ_1, λ_2, λ_3 are the stretches or extension ratios describing the deformation

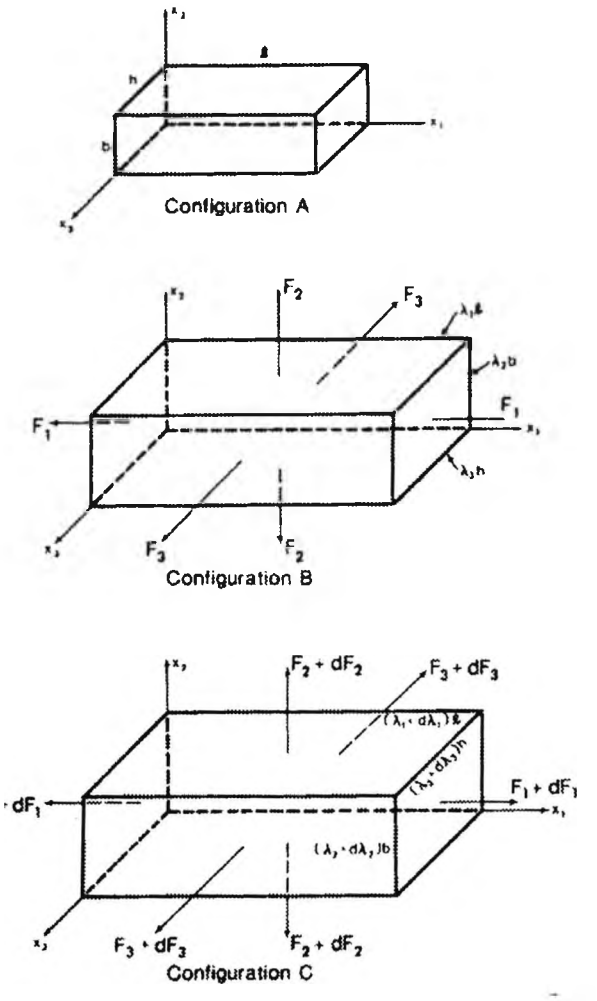

Figure 2.2: Three configurations of a rectangular cuboid of tissue.

of B relative to A. Let us assume that the cuboid is composed of an orthotropic elastic material and that the coordinate axes are also the axes of material symmetry (which is correct in the case of the arterial wall). Then, to effect the assumed deformation, a force system composed solely of three pairs of uniformly distributed equal and opposite forces, F_1, F_2 and F_3 will be required. In an arbitrary material these forces would be time dependent and there would be additional time-dependent shear forces on the faces of the cuboid. Consider, finally, a third cuboidal configuration C of the body, with dimensions $(\lambda_1 + d\lambda_1)$l, $(\lambda_2 + d\lambda_2)$b, and $(\lambda_3 + d\lambda_3)$h, held in equilibrium by three pairs of uniformly distributed, equal and opposite forces $F_1 + dF_1$, $F_2 + dF_2$, and $F_3 + dF_3$. If $\lambda_1, \lambda_2, \lambda_3$ differ only slightly from unity, the deformation from A to B is said to be *infinitesimal.* The classical theory of elasticity considers only such deformations. For soft biological tissues and other rubberlike materials, this is too restrictive and "finite " deformation of B relative to A have to be considered. The relations describing F_1, F_2, and F_3 in terms $\lambda_1, \lambda_2, \lambda_3$, when l=b=h=1, are in general nonlinear. Often the configuration A is not available for observation. Configuration B can then be used as an initially stressed reference configuration. The deformations in configuration C relative to B are said to be *incremental.*

Initial Strains (strains in configuration B)

A large number of measures of strain or deformation of configuration B relative to A have been used in the past. The stretches λ_1, λ_2, and λ_3 can themselves be used as a measure of deformation. Their excess over unity can be used as a definition of strain. Thus we have

$$\epsilon_1 = \lambda_1 - 1; \quad \epsilon_2 = \lambda_2 - 1; \quad \epsilon_3 = \lambda_3 - 1 \tag{2.2}$$

which are the conventional or engineering strains and are the quantities used as strains in the classical infinitesimal theory of elasticity. When deformations are finite, other measures of strains are often used. One such set is given by

$$\gamma_1 = \frac{1}{2}(\lambda_1^2 - 1); \quad \gamma_2 = \frac{1}{2}(\lambda_2^2 - 1); \quad \gamma_3 = \frac{1}{2}(\lambda_3^2 - 1) \tag{2.3}$$

These are called Green-St Venant strains. Tensors whose eigenvalues involve squared stretches arise more naturally in the analysis of finite strain; this is why measures such as

γ_1, γ_2, and γ_3 are often used in large strain theories.

Another set of strains known as Almansi-Hamel strains are given by

$$\mu_1 = \frac{1}{2}(1 - \lambda_1^{-2}); \quad \mu_2 = \frac{1}{2}(1 - \lambda_2^{-2}); \quad \mu_3 = \frac{1}{2}(1 - \lambda_3^{-2}) \tag{2.4}$$

Finally, the so-called "natural" or Hencky strains are defined as

$$\nu_1 = ln(\lambda_1); \quad \nu_2 = ln(\lambda_2); \quad \nu_3 = ln(\lambda_3) \tag{2.5}$$

Initial Stresses (stresses in configuration B)

Denote by f_1, f_2, and f_3, the first Piola-Kirchhoff, conventional or engineering stresses obtained by dividing the forces F_1, F_2, and F_3 in configuration B by the areas in configuration A of the faces on which they act. Thus,

$$f_1 = \frac{F_1}{bh}; \quad f_2 = \frac{F_2}{lh}; \quad f_3 = \frac{F_3}{lb} \tag{2.6}$$

The second Piola-Kirchhoff stresses, denoted by S_1, S_2, and S_3, are defined by introducing "fictitious" forces (i.e., the actual forces modified by a deformation gradient tensor). They are:

$$S_1 = \frac{F_1}{bh\lambda_1}; \quad S_2 = \frac{F_2}{lh\lambda_2}; \quad S_3 = \frac{F_3}{lb\lambda_3} \tag{2.7}$$

Thus, they are not measurable in the laboratory and do not have physical interpretation. However, the second Piola-Kirchhoff stress tensor is conjugate to the Green's strain tensor, and therefore very natural in constitutive formulations–by conjugate it means that the stress can be determined directly from an energy function by differentiating with respect to the conjugate measure of deformation (see section 2.3.4.1).

Similarly denote by t_1, t_2, and t_3, Cauchy or "true" stresses, which are the ratios of the forces F_1, F_2, and F_3 in configuration B and the areas in that configuration on which they act. Thus,

$$t_1 = \frac{F_1}{\lambda_2\lambda_3 bh} = \frac{f_1}{\lambda_2\lambda_3}; \quad t_2 = \frac{F_2}{\lambda_1\lambda_3 lh} = \frac{f_2}{\lambda_1\lambda 3}; \quad t_3 = \frac{F_3}{\lambda_1\lambda 2lb} = \frac{f_3}{\lambda_1\lambda_2} \tag{2.8}$$

Because the initial areas are easy to measure, the engineering literature generally uses Kirchhoff stresses. Occasionally, when large area changes are involved, Cauchy or"true" stresses are often computed. The advantage of the latter definition of stress is that it is probably most closely related to what materials actually "feel". It is convenient for solving the spatial momentum (e.g., equilibrium) equation.

Incremental Strains

Differentials of the four types of strains yield the following alternate definitions of incremental strains

$$d\epsilon_1 = d\lambda_1; \quad d\epsilon_2 = d\lambda_2; \quad d\epsilon_3 = d\lambda_3 \tag{2.9}$$

$$d\gamma_1 = \lambda_1 d\lambda_1; \quad d\gamma_2 = \lambda_2 d\lambda_2; \quad d\gamma_3 = \lambda_3 d\lambda_3 \tag{2.10}$$

$$d\mu_1 = \frac{1}{\lambda_1^3} d\lambda_1; \quad d\mu_2 = \frac{1}{\lambda_2^3} d\lambda_2; \quad d\mu_3 = \frac{1}{\lambda_3^3} d\lambda_3 \tag{2.11}$$

$$d\nu_1 = \frac{d\lambda_1}{\lambda_1}; \quad d\nu_2 = \frac{d\lambda_2}{\lambda_2}; \quad d\nu_3 = \frac{d\lambda_3}{\lambda_3} \tag{2.12}$$

Incremental Stresses

Incremental stresses can be defined as (df_1, df_2, df_3), (dt_1, dt_2, dt_3) or as $(d\tau_1, d\tau_2, d\tau_3)$, where

$$df_1 = \frac{dF_1}{bh}; \quad df_2 = \frac{dF_2}{lh}; \quad df_3 = \frac{dF_3}{lb} \tag{2.13}$$

$$dt_1 = \frac{df_1}{\lambda_2\lambda_3} + f_1 d(\frac{1}{\lambda_2\lambda_3}); \quad dt_2 = \frac{df_2}{\lambda_1\lambda_3} + f_2 d(\frac{1}{\lambda_1\lambda_3}); \quad dt_3 = \frac{df_3}{\lambda_1\lambda_2} + f_3 d(\frac{1}{\lambda_1\lambda_2}) \tag{2.14}$$

$$d\tau_1 = \frac{df_1}{\lambda_2\lambda_3}; \quad d\tau_2 = \frac{df_2}{\lambda_1\lambda_3}; \quad d\tau_3 = \frac{df_3}{\lambda_1\lambda_2} \tag{2.15}$$

In the infinitesimal theory of initially unstressed bodies, all three definitions become identical. The stresses of (df_1, df_2, df_3) and $(d\tau_1, d\tau_2, d\tau_3)$ are directly related to force increments and therefore give a better feel of increase in resistance of the specimen in going from configuration B to configuration C. These would also be easier to use in cases where a strain energy density function is assumed to exist. On the other hand, the incremental stresses of (dt_1, dt_2, dt_3) represent actual changes in forces per unit area in going from configuration B to configuration C. Thus in tissue failure considerations, for example, these would appear to be more pertinent.

Because of different definitions of stress and strain, the same material will exhibit different stress-strain curves depending on the choice of definitions [100].

2.3.3 Uniaxial constitutive laws

From the point of view of biomechanics, the mechanical behaviour of a tissue can be described if its constitutive equation is known. Without constitutive equations boundary-value problems cannot be formulated and detailed analysis cannot be made. Careful study of the existing literature on continuum mechanics does not yield a good understanding, because the best known materials like metals seem to have *few counterparts* in living tissues as far as the mechanical properties are concerned. The constitutive equation of a material can only be determined by experiments.

A uniaxial loading test of a sliced ring of an arterial wall or a strip of tissue is simple but, nevertheless, provides basic and useful information on the material properties. Many authors proposed a large variety of mathematical expressions to describe the stress-strain relationship in uniaxial tests [99, 100, 101].

2.3.4 Multiaxial constitutive laws

The uniaxial loading experiments cannot provide the full relationship between all stress and strain components. To obtain the *tensorial* relationship, it is necessary to perform biaxial and triaxial loading tests.

Multiaxial constitutive equations that have so far been proposed for the arterial wall are divided into three types:
(1) viscoelastic [63],
(2) elastic [78],
and (3) hyperelastic [102, 103].

Although it is well known that the arterial wall is viscoelastic, constitutive equations which describe nonlinearity and viscoelasticity might be of very complex form and contain many coefficients. For the formulation of elastic properties of arterial walls, several assumptions have been incorporated: for example, ideal cylindrical geometry, material homogeneity, incompressibility, cylindrical orthotropism and hyperelasticity. Mechanical properties of the arterial wall have been often analysed on the basis of strain energy density function, that is, on the assumption of hyperelasticity.

2.3.4.1 Strain energy density function

Most experimental data on the elastic properties of highly deformable biological soft tissues are generally analysed with the help of strain energy density functions. If there is a one-to-one relationship between strain and stress, then the theory of elasticity shows that there exists a strain energy density function (SEDF) from which stresses can be computed from the strains by differentiation [82]. That is

$$S_{ij} = \frac{\partial W}{\partial E_{ij}} \qquad (i, j = 1, 2, 3) \tag{2.16}$$

where W is the strain energy per unit volume of the tissue in the initial state. S_{ij} and E_{ij} are the second Piola-Kirchhoff stresses and Green's strains respectively. Although arterial tissues exhibit hysteresis in cyclic loading, the stress and strain are *uniquely* related in each branch of a specific process if the artery is well preconditioned by cyclic loading and unloading manoeuvres at a constant strain rate. The material can be treated as two different elastic materials under loading and unloading [79]. Thus, the concept of SEDF can be used on arterial tissues.

For the description of stress-strain relationships of arterial tissue in biaxial and triaxial tests, there are essentially three forms of SEDF:

(1) polynomials [102, 104],

(2) exponential functions [103, 105, 106],

and (3) logarithmic expressions [107].

For example, Vaishnav et al. [102] proposed three multiaxial polynomial forms of $W(E_{\Theta\Theta}, E_{ZZ})$ which contained different numbers (3,7,or 12) of material parameters. Overall a 7-parameter relation was deemed best. It may be expressed as

$$W = C_1 E_{\Theta\Theta}^2 + C_2 E_{\Theta\Theta} E_{ZZ} + C_3 E_{ZZ}^2 + C_4 E_{\Theta\Theta}^3 + C_5 E_{\Theta\Theta}^2 E_{ZZ} + C_6 E_{\Theta\Theta} E_{ZZ}^2 + C_7 E_{ZZ}^3 \tag{2.17}$$

where W represents the strain energy density function, $E_{\Theta\Theta}$ and E_{ZZ} are Green's strains in the circumferential and axial directions respectively, and C_i are material parameters. Vaishnav et al. determined "best fit " values of the parameters from mean stress-strain data and then determined the values for global equilibrium which accounted for transmural variations in stress and strain. Differences in the two sets of parameter values prompted the deduction that the "thick-walled" approach was preferable, a conclusion that is held today.

Chuong and Fung [108] proposed an exponential W for rabbit carotid arteries of the form

$$W = \frac{1}{2} C e^Q \tag{2.18}$$

where C is a material parameter, and Q was given as

$Q = b_1 E_{\Theta\Theta}^2 + b_2 E_{ZZ}^2 + b_3 E_{RR}^2 + 2b_4 E_{\Theta\Theta} E_{ZZ} + 2b_5 E_{ZZ} E_{RR} + 2b_6 E_{RR} E_{\Theta\Theta} + b_7 E_{\Theta Z}^2 +$
$b_8 E_{ZR}^2 + b_9 E_{R\Theta}^2$

Actually, Chuong and Fung suggested only the first six (that is, extensional) terms. In fact, the $E_{Z\Theta}$ term was later included by Deng et al. [106], although their relation was 2-D.

Takamizawa and Hayashi [107] used a logarithmic form of the function described by

$$W = -C \ln(1 - C_1 E_{\Theta\Theta}^2/2 - C_2 E_{ZZ}^2/2 - C_3 E_{\Theta\Theta} E_{ZZ}) \tag{2.19}$$

where C, C_i characterise the mechanical properties of the material. They also evaluated the three functions using experimental data obtained from the canine common carotid artery. The diversity of numerical values for the coefficients was somewhat less in the logarithmic form of function than in the exponential, although the fit to the experimental data was similar for both functions. The polynomial form of strain energy function did not fit as well as the other two forms which used the results from rabbit arteries. On the whole, the exponential form is more suited than the polynomial form if the purpose is to determine the material constants of a vessel in order to study any systematic changes in the vessel due to some other factors, such as the age, the location in the arterial tree, the effects of drugs, and the effect of hypertension. In addition to the above functions, other functional forms also exist. Kas'yanov and Rachev [109] proposed a combined polynomial-exponential form of W, namely

$$W = C_1|e^Q - 1| + |C_7 E_{\Theta\Theta} e^{c_8 E_{\Theta\Theta}} + C_9 E_{ZZ} + C_{10}|E^2_{\Theta Z} \tag{2.20}$$

where $Q = C_2 E^2_{ZZ} + C_3 E_{ZZ} E_{\Theta\Theta} + C_4 E^2_{\Theta\Theta} + C_5 E^2_{ZZ} E_{\Theta\Theta} + C_6 E_{ZZ} E^2_{\Theta\Theta}$.
The values of material parameters are usually determined from experimental data. Because of the inherent "noise" in most data, parameter estimation is usually best accomplished via regression methods combined with a finite element method. Hayashi [110] presented a review of the constitutive laws proposed for the description of stress-strain relationships of arterial walls.

In addition to the above functions, other functional forms also exist. Kas'yanov and Rachev [109] proposed a combined polynomial-exponential form of W. Hayashi [110] presented a review of the constitutive laws proposed for the description of stress-strain relationships of arterial walls.

Besides these formulations, there are some empirical models, where arbitrary functions are assumed and fitted to particular experimental data [111, 112, 113]. For example, Elad et al. [112] presented a 2-D orthotropic quasi-linear stress-strain relation through the nonlinear definitions of generalised strain and stress which ensures the existence of a

strain energy density function. In Elad's paper, the generalised strain measure is given by

$$\epsilon_\alpha = \frac{1}{n}[(\lambda_\alpha)^n - 1] \qquad (\alpha = 1, 2, 3) \tag{2.21}$$

where ϵ_α are the generalised strain components in the principal directions, λ_α are the principal stretch ratios, and n is a nonlinearity material parameter. The inverse of the stress-strain relations, that is the strain as a function of the stresses, can be obtained through an iterative procedure. The motivation for his work was primarily to provide a simple relation for wall response for use in studies of haemodynamic inflation waves rather than for a detailed description of the wall mechanics.

As mentioned before, the arterial wall is incompressible, which requires that

$$(1 + 2E_{\Theta\Theta})(1 + 2E_{ZZ})(1 + 2E_{RR}) = 1 \tag{2.22}$$

There are two basic ways to account for *incompressibility*:
First, the components of strain can be treated as if they are independent (as in compressible behaviour) but incompressibility is enforced through an independent function H called a Lagrangian multiplier. In particular let:

$$W^* = W(C) - \frac{H}{2}(detC - 1) \tag{2.23}$$

For example, in Fung's exponential function

$$\rho W^* = \rho W + \frac{H}{2}[(1 + 2E_{\Theta\Theta})(1 + 2E_{ZZ})(1 + 2E_{RR}) - 1)] \tag{2.24}$$

Second, the constraint could be enforced directly, which requires that

$$W(E_{\Theta\Theta}, E_{RR}, E_{ZZ}) = W(E_{\Theta\Theta}, \frac{1}{(1 + 2E_{\Theta\Theta})(1 + 2E_{ZZ})}, E_{ZZ}) \rightarrow W(E_{\Theta\Theta}, E_{ZZ}) \tag{2.25}$$

This effectively says that W depends on two, not three, independent principal components of strain. Although the latter expression looks like a 2-D formulation, it yields 3-D information. Incompressibility is commonly described as a "mathematically convenient assumption". Indeed, this is true from an analytical or experimental standpoint, but it is not true in a numerical (for example, finite element) context.

2.3.4.2 Parametric expression of pressure-diameter relations

From practical aspects of characterisation and measurements of the elastic properties of arterial walls, it is more convenient to use a *single* parameter which expresses the arterial elasticity in the living condition rather than to use a thorough, but complicated constitutive expression. In particular, for non-invasive diagnosis in practical medicine, material characterisation should be simple, yet quantitative. To this end, several parameters have been proposed and frequently utilised including "pressure-strain elastic modulus, E_p" [114] and "vascular compliance, C_v" [115]. Pulse wave velocity, c, is also utilised because it is a function of the elastic modulus of the vascular wall. These parameters are described by

$$E_p = D_0(\triangle P/\triangle D_0) \qquad (a)$$

$$C_v = \triangle V/(V\triangle P) \qquad (b)$$

$$c^2 = (A/\rho)(\triangle P/\triangle A) \qquad (c) \qquad (2.26)$$

where D_0, V, and A are the outer diameter, volume, and luminal area of a blood vessel at pressure P, respectively, and $\triangle D_0, \triangle V$, and $\triangle A$ are their increments as a result of the pressure increment, $\triangle P$, ρ is the density of the blood. As may be understood from these expressions, there is no need to measure the thickness of the wall to calculate the parameters; the only necessity is pressure-diameter data at a specific pressure level. However, it should be remembered that while these parameters express the structural stiffness or distensibility of a blood vessel, they do not rigorously represent the inherent elastic properties of the wall material; in this sense, they are different from the elastic modulus [116]. In addition, the parameters are defined at specific pressures, and give different values at different pressure levels because pressure-diameter relations of blood vessels are highly non-linear.

Hayashi et al. [116] proposed the following equation to describe pressure-diameter relations of arterial walls in the physiological pressure range

$$\ln(P/P_s) = \beta(D_0/D_s - 1) \qquad (2.27)$$

where P_s is the standard pressure and D_s the wall diameter at pressure P_s. The coefficient, β, called the stiffness parameter, represents the structural stiffness of a vascular wall. At the standard pressure, P_s, the parameters described by equation(2.26) can be converted into the stiffness parameter β, as follows:

$$\beta = E_p/P_s = 2/(C_v P_s) = 2\rho c^2/P_s \tag{2.28}$$

Tozeren [117] proposed an exponential pressure-area relation using a fibre-fluid continuum analysis

$$P = K_3(1 + (K_1/K_2)(exp(K_2(A-1)) - 1)) \tag{2.29}$$

where K_1, K_2 and K_3 are constants, and A is a measure of cross-sectional area.

Other forms of the pressure-luminal volume or pressure-luminal area [89] relationships of the artery have also been proposed.

Furthermore, in some simple cases, once the strain energy density function of the arterial material is obtained, the pressure-diameter relationship of the same material under the same loading conditions can be deduced from the strain energy density function [118, 119].

Demiray [118] proposed a strain energy function

$$W = \frac{\beta}{2\alpha}\{exp[\alpha(I_1 - 3)] - 1\} \tag{2.30}$$

where α and β are two material constants to be determined from experiments, and I_1 is the first invariant of the deformation tensor. It was assumed that a cylindrical artery is subjected to an inner pressure P_i, an outer pressure zero, and an axial force N, under constant stretch ratio in the axial direction. Using equilibrium equations, boundary conditions, and the incompressibility condition, an incremental pressure-radius relationship is obtained, which is

$$\triangle P_i = [\frac{r_0^2}{r_i^2}(\lambda + \eta_i^2)F(\eta_i) - (\lambda + \eta_0^2)F(\eta_0)]\frac{\triangle r_0}{r_0} \tag{2.31}$$

where $\triangle P_i$ is incremental pressure, $\triangle r_0$ is the increment in outer radius, r_0, r_i are the inner and outer radii in the deformed configuration, $F(\eta) = \frac{\beta}{\lambda^2} exp[\alpha(\frac{\eta^2}{\lambda^2} + \frac{1}{\eta^2} + \lambda^2 - 3)]$, and $\eta \equiv \frac{R}{r}$. In the latter R and r are the radii of a material point of the artery before and after deformation. Utilising the definition of pressure-strain elastic modulus, one has

$$E_p = [\frac{r_0^2}{r_i^2}(\lambda + \eta_i^2)F(\eta_i) - (\lambda + \eta_0^2)F(\eta_0)]; \quad \triangle P = E_p \frac{\triangle r_0}{r_0} \tag{2.32}$$

Demiray [119] also employed a strain energy density function which consisted of both polynomial and exponential parts, and obtained an explicit expression of the variation of pressure-strain elastic modulus with intramural pressure. Although the present formulation is applied to isotropic elastic materials because of the form of the strain energy function, it gives an indication that there exists some interrelationship between a model describing the material with a strain energy density function and with one employing a pressure-diameter relationship.

2.3.4.3 Incremental stress-strain relationship

It is well known that the vascular tissue is capable of undergoing large deformations and that its mechanical response is nonlinear. One way of expressing the nonlinear behaviour of the tissue is through characterisation of its mechanical response in the neighbourhood of various states of deformation of interest. This is the so-called incremental approach which was applied to the arteries in the 1950s. The concept is well founded in that in the living animal the vascular bed, particularly the arterial bed, is in a state of mean distension corresponding to the mean pressure of blood on which are superimposed relatively small pulsatile deformations corresponding to the pulsations of the beating heart. The incremental stress-strain relationships are expressed by the theory of linear elasticity [99, 120]. The elastic parameters are functions of the particular state of deformation [66].

One of the physiologically important states of stress in a vascular segment of an orthotropic tissue is that caused by simultaneous action of an intravascular pressure and an extra longitudinal force which is called 'physiological loading'. The incremental constitutive behaviour of an orthotropic tissue under such loading can be expressed as

$$dS_{11} = K_{11}d\lambda_1 + K_{12}d\lambda_2 + K_{13}d\lambda_3$$

$$dS_{22} = K_{21}d\lambda_1 + K_{22}d\lambda_2 + K_{23}d\lambda_3$$

$$dS_{33} = K_{31}d\lambda_1 + K_{32}d\lambda_2 + K_{33}d\lambda_3 \tag{2.33}$$

The coefficients K_{ij} may be called incremental moduli. For incompressible materials there exists the relation:

$$\frac{d\lambda_1}{\lambda_1} + \frac{d\lambda_2}{\lambda_2} + \frac{d\lambda_3}{\lambda_3} = 0 \tag{2.34}$$

Thus, only two incremental strains are independent. Moreover, only two incremental stress differences can be determined from the two independent strains. If the material were considered to be viscoelastic, the foregoing treatment could be simply extended by considering the incremental coefficients to be complex quantities (For further discussion see Patel and Vaishnav [121]). Patel et al. [61] carried out *in vivo* experiments to evaluate dynamic incremental viscoelastic coefficients for the middle descending thoracic aorta of dogs which showed that the viscous effect is small compared to the elastic effect.

The incremental approach has been used extensively in vascular mechanics. This contrasts with the difficulties associated with the overall nonlinear formulation. These difficulties are generally acknowledged and appropriately respected.

Both the incremental and finite elasticity approaches toward material characterisation have considerable merits, but each has its own limitations. The incremental approach is linear and invertible, but it requires tabulation of the elastic parameters for each state of deformation. Under real multiaxial loading, many deformation states are possible and extensive. Experimental data must be obtained and tabulated. The finite elasticity approach is free from this problem, since the whole range of elastic response is expressed by a single set of parameters. Its advantage is that the stress is given as a nonlinear function of strains. In practical applications, the inverse strain-stress relationship is often required. Fung [122] showed that this inverse relationship can readily be obtained only if the SEDF is of quadratic form, but that SEDF's that are polynomials of strain of degree three and higher may not be invertible.

2.3.5 Changes of mechanical properties with age and disease

2.3.5.1 Aging

Numerous studies show age-associated changes in wall structure, including a tendency for endothelial cells to become irregular in shape, the intima to thicken and become more fibrotic, and the media to thicken from either a hyperplasia or hypertrophy that is accompanied by an increased decomposition of collagen but some degradation of elastin. Yet changes in mechanical properties have not been rigorously quantified, and the available data often appear to conflict. These inconsistencies may be due, in large part, to differences between species, the artery studied, and methods of data collection and reduction. Most of the data obtained from blood vessels in animals indicated that the incremental elastic modulus or the slope of stress-strain curve also increased with age [123, 124, 125], whereas Fronek and Fung [87] reported different data. There are, however, no detailed multiaxial quantifications of age-associated changes in the biomechanical properties of arteries.

2.3.5.2 Atherosclerosis

Atherosclerosis is the most commonly acquired disease of the arterial wall. There are numerous reports of uniaxial tension on strips of diseased arteries and nondiseased controls. The overall qualitative finding is: atherosclerosis increases overall stiffness [126, 127]. Similarly, numerous investigators have compared pressure-diameter data from diseased and nondiseased vessels. Interpretation of these data can be reduced in terms of either a structural or a material stiffness; the former includes wall thickness, which increases with progression of disease. Consistent with uniaxial results, pressure-diameter data suggest that the diseased arterial wall is "stiffer" than the normal wall.

In connection with this subject, the mechanical properties of atherosclerotic lesions, plaques, and intima have been studied by means of microindentation techniques and micro tensile testers. In addition, local mechanical properties and stresses at aortic and arterial branches have been experimentally and analytically studied.

2.3.5.3 Hypertension

Hypertension is a risk factor of many cardiovascular disorders. Elevated blood pressure is believed to exert some influence on the synthetic activity in vascular smooth muscle cells, causing alternations of artery wall thickness, passive mechanical properties of vessel walls and active vascular muscle contractibility. Many studies of large arteries from hypertensive subjects show that these vessels have an increased slope of the stress-strain curve in the circumferential direction under passive conditions [128, 129]. However, Vaishnav et al. [130] reported that the stress-extension ratio relationship of the canine thoracic aorta is similar in the hypertensive and normotensive animals in the circumferential direction; although the hypertensive aorta has a higher slope than its normotensive counterpart in the longitudinal direction. Matsumoto and Hayashi [131] reported that the mean circumferential wall stress in the rat aorta remained nearly constant during developing hypertension (owing to competing changes in pressure, wall thickness, and lumen radius). In conjunction with this phenomenon, Michelini and Krieger [91] studied short term changes of aortic wall distensibility and wall dimensions during the development of hypertension in the rat.

2.4 Spatial Distribution of Strain and Stress Components in the Straight Artery Segment

Direct measurement of arterial wall stress is difficult, whether invasively or noninvasively; therefore, mathematical analysis of stress and strains is useful in predicting stress and strain distribution throughout the arterial wall.

2.4.1 Thin-walled uniform distribution

Intravascular pressure and longitudinal tethering force are the primary sources of stress in the blood vessel wall. In vascular mechanics, it is often convenient to make an additional assumption, namely, that the vascular wall is thin in comparison to its mid-wall radius. From the point of view of structural mechanics, assuming a blood vessel to be thin implies that the stress distribution is uniform through the thickness of the blood vessel wall and that the radial stresses are negligible compared with the circumferential and longitudinal

stresses. Using these approximations, it is possible to estimate stresses in the blood vessel using simple equilibrium considerations.

For a blood vessel, it is not possible to designate a threshold value of this ratio beyond which the vessel may be called thin-walled. The threshold value for usual engineering materials lies between 20:1 and 10:1. However, because of nonlinearity of tissue response, a large error results in the case of vascular tissue than, say, in steel, when the stress analysis is based on the assumption of thinness.

2.4.2 Spatial distribution of stress and strain-energy density function

Experimental work by Arndt et al. [132] has shown that during the cardiac cycle the resulting *in vivo* deformation may be greater than 10% in terms of tangential strain. In addition, very large deformations ($60 - 100\%$ tangential strain) occur for pressures from 0-200mmHg. A finite deformation analysis of the arterial cross section with a thick-walled model allowing possible stress gradients in the arterial wall has shown that significant gradients in tangential stress may be present in arteries which have previously been assumed to be "thin-walled" cylinders. Hence, available elastic arterial constitutive relations should be reevaluated on the basis of a thick-walled model including finite deformations, since the necessary analytical and numerical procedures have now become available.

The distribution of stresses and of strain-energy density through the wall thickness of a blood vessel under physiological conditions influences the mechanical behaviour of the vascular system. Knowledge of the mechanical state of stress in the arterial wall is essential for understanding many aspects of vascular physiology, pathophysiology, and clinical therapy. For example, an understanding of tissue failure requires information about the magnitude of the maximum values of stresses and strain energy. Additionally, the strain-energy function could be a useful indicator in atherogenesis. Fry [133] has postulated that atherosclerosis may occur at locations in the arterial tree where the strain energy is abnormally increased. For instance, lesions commonly occur near arterial bifurcations and the distribution of strain energy density may influence the flux of lipoprotein macromolecules into the wall. An understanding of the latter phenomenon appears to be central to the

unravelling of the pathogenesis of atherosclerosis.

The complexities of stress analysis in the arterial wall are numerous. In spite of these difficulties, attempts have been made to examine the three-dimensional distributions of the stresses and strains in straight segments of the artery. Simon et al. [134, 135] assumed that the blood vessel is transversely isotropic and incompressible. They determined the material constants for each fixed longitudinal stretch by using average stress and strain to start a trial-and-error scheme until the computed pressure-radius curve agreed with experimental measurements. They concluded that thin-walled tube stress approximations resulted in inaccurate values for arterial stresses and incremental mechanical properties.

Vaishnav et al. [102] assumed the material to be incompressible, curvilinearly orthotropic, and characterised by a strain energy function of the polynomial type. In their paper, a method was presented to determine the distribution of circumferential (σ_Θ), longitudinal (σ_z), and radial (σ_r) stress and of strain energy density (W) in canine aortic segments under physiological loading. Aortic segments from 13 dogs were studied in vitro. The $3, 7, or 12$ constants were then used to calculate the distribution of stresses and of W. The results indicated that (1) $\sigma_\Theta, \sigma_z, \sigma_r$ and W were largest in magnitude at the endothelial surface and decreased toward the adventitial surface, (2) the decrease was most marked in the inner third of the vessel wall, and (3) at a given longitudinal stretch an increase in intraluminal pressure increased $\sigma_\Theta, \sigma_z, |\sigma_r|$, and W, with the effect being most marked on σ_Θ.

It has been usually assumed in the literature that the arterial wall is stress-free when all external loads are removed. This is a good strategy for a linear system, because in such a system one can compute the stresses induced by external loads and then superpose them on the initial stresses, if any. However, for a nonlinear system the principle of superposition does not apply, and the effect of such an assumption would be far reaching and difficult to evaluate. Evidence of the existence of residual stresses in the arterial wall at the unloaded state is given in Fung [136]. With a longitudinal cut along the vessel wall the unloaded specimen springs open and its cross section becomes a sector. This phenomenon

means that there exists compressive circumferential residual stress in the inner wall and tensile residual stress in the outer side before the vessels are cut. Presence of the residual stress at the unloaded state will certainly affect the evaluation of the stress distribution in the arterial wall due to actual loadings in the physiological range [108, 137]. These results indicate that the zero initial stress hypothesis is not suitable for the arterial wall.

It is important to identify the stress-free state. When pseudoelasticity [79] is used to characterise the arterial wall, a stress-free definition is needed as the reference state for strain measurements. Chuong et al. [108] presented a method to describe the geometry of the opened-up stress-free state of the artery, which is taken to be the reference state. An algorithm similar to Chuong [103] was used for the identification of the stress-strain relationship of the arterial wall. Residual stresses and strains in the unloaded state were evaluated. With the consideration of residual stresses the stress distribution due to the loadings in the physiological range were also evaluated. In their previous work using the hypothesis that the unloaded artery was stress-free, the circumferential stress at the inner wall was found to be 6.5 times larger than the average value across the vessel wall. The removal of the hypothesis has the effect of reducing the stress concentration factor from 6.5 to 1.42. It was concluded that the residual stress in the unloaded state, although small in magnitude, is significant in reducing the high stress concentration. A similar conclusion was also obtained in the study of residual stresses in oscillating thoracic arteries made by Chaudhry et al. [137].

As an alternative assumption to the zero initial stress hypothesis, Takamizawa et al. [107] proposed a uniform strain hypothesis in which the wall circumferential strain was assumed to be constant over the wall cross-section under the physiological loading condition. It should be noted that the uniform strain is not rigorously equivalent to the uniform stress if the wall material is assumed to be incompressible. The uniform strain hypothesis is quite similar to the "principle of optimal operation" proposed by Fung [136] for the left ventricular wall. The stress distributions through the wall were analysed on this assumption and compared to those calculated on the basis of the zero initial stress hypothesis. To describe the mechanical properties of the arterial wall, the authors used a logarithmic

type of strain energy density function. The material constants were determined by a least squares method. Under the uniform strain hypothesis the results showed that the high stress concentration observed in the vicinity of the wall lumen in the case of the zero initial stress hypothesis did not appear. The circumferential and axial stresses were very slightly higher at the outer side of the vessel wall than at the inner wall. In contrast with the zero initial stress hypothesis, residual stresses and strains appear in the case of the uniform strain hypothesis when the intraluminal pressure and axial force are removed. These results imply that the thin walled theory is a good approximation and simplifies the analysis of stress in the arterial wall.

All problems involving bending of the wall must consider the shell as a three-dimensional body. Problems in which the external load is nonaxisymmetric, localised, or concentrated are three-dimensional. Studies concerning curved or branching arteries or vessels with stenosis or aneurysm belong to this category.

2.5 Structural Analysis of Arterial Walls

2.5.1 Arterial wall models

Biomechanical structural analysis should be able to provide predictions of deformation and stresses in normal, diseased, and prosthetic arteries. In addition, biomechanicians are attempting to understand the interrelationship between arterial wall mechanics and transport and how this might relate to atherogenesis. Because of the complex geometry and properties of the arterial wall, the *finite element method* (FEM) is likely to be the only computational tool suitable for the study of arterial mechanics.

The FEM has proven to be one of the most popular methods for structural analysis of soft arterial tissues. Depending on the application, arteries can be treated as either a solid-fluid mixture or a homogenised solid (most common); the former is particularly important in calculations of mass transport within the wall, as in the studies of atherogenesis, whereas the latter is employed in most experimental, theoretical, and numerical studies of the constitutive behaviour of, and stress distribution in, the wall.

Over the last 20 years, elastic (or viscoelastic) material laws have been primarily structural models. The artery is modelled as a one-phase solid such as a thin-walled tube and shell structure. During the early 1970s, several FEM models were developed, including transversely isotropic [138] and isotropic [139] hyperelastic material models. The stresses and deformations in diseased and normal arterial cross sections were considered by Vito et al. [140] using FEM. Their results included the distribution of strain in the cross section of the canine thoracic aorta, which was used in a nonlinear finite element model to determine material properties.

Thubrikar et al. [26] calculated stress concentration levels in bovine arterial branches. In the study, the arterial branch is modelled as two intersecting thin cylindrical shells incorporating local variations in the branch geometry, thickness, and material properties. The intramural stress and stress concentration in the arterial branch area were determined by finite element analysis. Orthotropic material properties and incremental pressure loads were introduced. Maximum stresses were found to be localised at the proximal and distal regions of the ostium and were not significantly affected by the elastic properties.

More recently, arterial FEM models have been extended to include mobile tissue fluid motion (based on poroelastic constitutive laws) and to simulate wall transport phenomena (based on diffusion and convective laws) for the study of species flux in the wall. An artery can be considered to be a "porohyperelastic" material, that is, a fluid-saturated porous medium (continuum) composed of an incompressible fluid (fluid phase) that flows through the pores in a highly deformable incompressible, hyperelastic porous solid skeleton (solid phase). Early efforts to model arterial tissue as poroelastic materials were reported by Kenyon [141] and later by Jain and Jayaraman [142] using analytical models. The first poroelastic FEM for the arterial cross section was described by Simon and Gaballa [143]. Yuan et al. [144] presented a general FEM for soft arterial tissues and identified constraints on porohyperelastic material properties for porous media composed of incompressible solids and fluids. A detailed development of the field equations and FEM formulation was given. An artery was simulated as a porohyperelastic neo-Hookean

Table 2.1: Model matrix.

Order of models	1	2	3
No. of layers[a]	Homogeneous	2-layer	Multi-layer
Anisotropy[b]	Isotropic	Orthotropic	Anisotropic
Geometry[c]	Circular tube	Thin shell	3-D
Displacement[d]	Small displacement	Large displacement	
Material law[e]	One-phase elasticity	Viscoelasticity	Poroelasticity
Elasticity[f]	Linear elastic	Incremental linear-elastic	Hyperelastic

material and deformations, stresses, pore fluid pressure, and relative fluid motion were calculated in order to demonstrate both transient and steady-state FEM procedures. Simon [145] reviewed the applications of poroelastic and mixture-based theories and the associated FEMs for the study of the biomechanics of soft tissues.

There have been numerous papers which consider transport in the arterial wall with application to atherogenesis (for example, see review by Fry and Vaishnav [146]. There is a potential future use for FEM that allows detailed simulation of these transport process. A review of elastic, poroelastic, and transport FEM models for arteries has been made by Simon et al. [147].

Table 2.1 summarizes the model matrix available in structural analysis of arterial walls[1].

[1] ABAQUS can accommodate any models in this matrix

2.5.2 Stress analysis of a human abdominal bifurcation based on MRI data

Atherosclerotic lesions generally develop at *arterial branching sites.* Repeated occurrences of the disease at these sites have stimulated a great deal of research in various aspects of haemodynamics. Disturbed flow pattern, however, is not the only factor contributing to the formation of lesions. Studies in other areas have shown that intramural stresses are also related to the disease [140]. Only very few numerical studies of intramural stress calculations are available in the literature. The section presents results of a stress analysis study performed by the author.

An anatomically realistic model is necessary for a clinically relevant study of wall stress distribution in the vessels. Using MR angiograms of a human abdominal aorta and iliac arteries, the three-dimensional structure of the aortic bifurcation was reconstructed, which provided a realistic geometric model for the study. A finite element package ABAQUS was employed to carry out the stress analysis (Referred to Table 2.1, this analysis is classified as $a_1 b_1 c_2 d_2 e_1 f_2$). The selected element type is S4R5, which in finite element terminology is a four node doubly curved, shear flexible element with reduced integration and hourglass control using five degrees of freedom. This is especially suitable for large displacements. Figure 2.3 shows the basic mesh developed for this model.

The nonlinear behaviour of the artery wall has been approximated, and it was assumed that this behaviour was incrementally linearly elastic over the pressure range from the diastolic level to systolic phase [148]. Local change in wall properties was not considered. The model was loaded with a pressure of 40mmHg which corresponds to the increase in pressure from a diastolic of 80mmHg to a systolic of 120mmHg. To prevent rigid body motion, the ends of the model were constrained against longitudinal motion. The inclusion of geometric nonlinearity in the calculations is required due to the relatively large displacements occurring in the bifurcation considered here.

Figure 2.4 shows the maximum principal stress distribution on the inner surface of the bifurcation predicted with ABAQUS. Since in a living system an artery never experiences

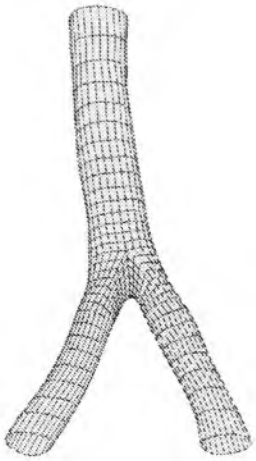

Figure 2.3: Geometric model of a human abdominal bifurcation.

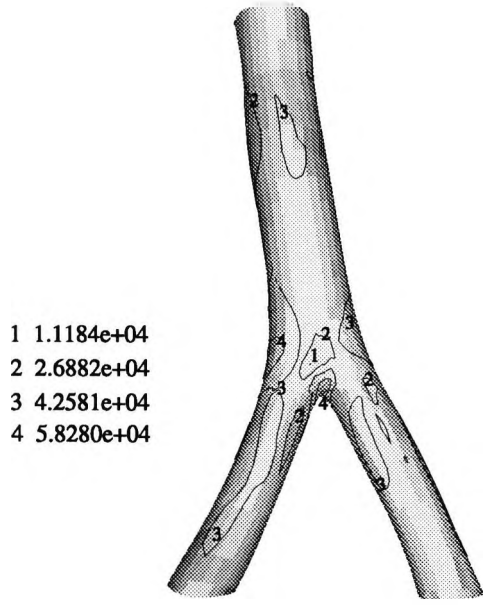

Figure 2.4: Maximum principal stress distribution (Pa) on the inner surface of the model(The wall thickness and Young's modulus were taken to be 0.6mm and $5X10^5$ Pa respectively).

a state of zero stress, which customarily in engineering is helpful in quantitatively defining the level of stress. The results were obtained in terms of incremental stresses and strains above the diastolic pressure level because it was suggested that increased stress may play a role in atherogenesis. It was found that, in the branch area, the stresses were not uniformly distributed, but localised. There was a stress concentration at the arterial branch, the intramural stress being increased by a factor of 2.65 in the apex region. The patterns of deformation and principal stress were in agreement with published data [26]. This study was only an initial but essential step of the project in which a coupled fluid-solid suite of computational codes using data from MRI and ultrasound is developed for clinical applications.

2.6 Wave Propagation in Arteries

2.6.1 The propagation of pressure waves

Blood is ejected from the left ventricle into the circulatory system by a periodic action of the heart. This added blood creates a change in pressure and results in a flow of blood along the aorta and throughout the circulatory system. At any given point the pressure and velocity will change periodically, and hence the flow is pulsatile and associated with the propagation of a pressure wave. The pressure wave changes both its shape and peak value as it travels down the arterial system. By the time the pressure reaches the capillaries, the pulsations are almost completely damped out. This damping is due to the viscosity of the blood and the viscous component of the viscoelastic arterial wall. Viscosity has the effect both of reducing the speed of propagation of the pressure wave and of attenuating it. Waves in any real system are attenuated, because the inevitable presence of friction or viscosity causes their mechanical energy to be dissipated into heat. In fact, visco-elastic dissipation in the vessel wall proves to be more important than viscous dissipation in the blood [149]. Structural changes in the arterial wall greatly influence the speed of propagation. Pathological changes such as hypertension as well as muscle contraction in the arterial wall (that result in decreased distensibility of the walls) result in an increase in speed of propagation, which is closer to a rigid tube behaviour.

In vivo the time-course of the pressure pulse is not similar or synchronous everywhere, the time-course of the volume flow-rate is not the same in the vena cava as in the aorta, and at neither location is it proportional to the applied pressure difference. The reason for these lies in the elasticity of blood vessels. The simplest model of the vascular system is the Windkessel model [149]. In this model the peripheral blood vessels are replaced by a rigid tube of constant resistance so that

$$P = R_e Q \tag{2.35}$$

where P is the aortic pressure, Q is the flow rate into the peripheral vessels from the aorta and R_e is the constant peripheral resistance. The aorta and large arteries are represented as an elastic chamber with a linear pressure-volume relation, which is described as:

$$\dot{V}_e = C_v \dot{P} \tag{2.36}$$

where $\dot{V}_e$ denotes the time derivative of aortic volume V_e and C_v is the arterial compliance(ml/mmHg). The differential equation governing the time variation of aortic pressure in the Windkessel model can be obtained by considering the conservation of mass of the blood flowing through the aorta:

$$-\dot{V} = (P/R_e) + C_v \dot{P} \tag{2.37}$$

where $(-\dot{V})$ is the flow rate into the aorta from the left ventricle. The three equations can be combined to form a single equation giving P, V_e, or Q, and this can be solved to relate the pressure in the arteries to the flow-rate into them from the heart at any time. Actually, a linear pressure-volume relation is only a simplification. Tozeren [117] proposed an exponential pressure-volume relation of aorta and large arteries to modify the linear pressure-volume relation of the Windkessel model. The principal shortcoming of the model lies in the assumption that all arteries are distended simultaneously. Actually, the pressure peak occurs later in peripheral arteries than in the aorta, and the pulse is propagated along the blood vessels in the form of a wave.

2.6.2 Pulse velocity in arteries

Arterial walls are flexible and their effect on pressure wave propagation has been studied extensively. Several experimental and theoretical studies have been conducted in the past to determine the pulse wave in distensible elastic tubes containing a viscous or inviscid fluid. If the method of characteristics is used in the analysis of an inviscid fluid contained in a distensible tube, the results reveal that the phase velocity c may be expressed as [150]

$$c^2 = \frac{1}{\rho_f}\frac{\triangle P}{\triangle A}A \tag{2.38}$$

where A is the cross-sectional area of the vessel lumen, $\triangle A$, $\triangle P$ are incremental cross-section area and pressure respectively, and ρ_f is the mass density of the fluid medium. This result is the same as the Newton-Young equation for pulse wave velocity.

Bergel [151] proposed the wave speed in an elastic tube under constant axial stretch containing an inviscid fluid to be

$$c^2 = \frac{E}{\rho_f}(\frac{R_0^2 - R_i^2}{3R_0^2}) \tag{2.39}$$

where E is the incremental Young's modulus, and R_0, R_i are outer and inner radii respectively. Furthermore, if the arterial wall is very thin, then equation(2.39) becomes

$$c^2 = \frac{4}{3}c_{MK}^2; \quad c_{MK}^2 = \frac{Eh}{2\rho_f R} \tag{2.40}$$

where R is the mean radius, h is the thickness of the arterial wall and c_{MK} is the wave speed proposed by Moens-Korteweg, which is a highly simplified form of Bergel's result. If no additional longitudinal stresses are applied (so that the tube will shorten when it is stretched), then

$$c^2 = \frac{Eh}{2\rho_f R} \tag{2.41}$$

In the case of pulsatile blood flow, the arteries are subjected to large initial deformations [152, 79]. These deformations might affect the explicit expression of the wave speed namely, the transmission coefficients. Demiray [153] obtained such an expression of the

wave speed in an elastic tube containing an inviscid fluid as a function of material and geometrical characteristics as well as the large initial deformations of the artery utilising the strain energy density function that he proposed previously [154]. The effects of lumen pressure and the axial stretch on the wave speed are discussed. The artery was treated as a thick-walled cylindrical shell element undergoing large deformations. The results of numerical evaluation for a particular type of artery revealed that the phase velocity of the wave increased with the intramural pressure whereas it decreased with axial stretch ratio. However, for engineering materials this is not the case, that is, the speed decreases with intramural pressure [155]. This result indicates that large deformation theories give larger values of phase velocity than those given by classical linear elasticity theory.

The study of propagation of pressure waves in a viscous fluid contained in an elastic tube has a long history going back at least as far as the work of Witzig [156]. He derived an approximate solution of the equations of viscous fluid motion, neglecting the non-linear terms and deduced a "frequency equation" from which he derived an approximate formula for the wave velocity in terms of the thickness and radius of the tube, its elastic constants, the viscosity of the liquid, and the frequency. Morgan gave two approximate formulae for the wave velocity, characterised by them as solutions for large and small viscosity. These are more precisely described as solutions for large and small values of the important non-dimensional Womersley parameter α. They also extended their approximate formulae to take account of internal damping in the wall of the tube by replacing its elastic constants by complex quantities whose imaginary parts were proportional to the frequency.

2.7 Fluid-Wall Coupled Problems

2.7.1 Introduction

Traditional interest in elastic vessels has focused on the problem of propagation of pressure and flow pulses in the cardiovascular system [157]. Less attention has been paid to the influence of wall elasticity on the local flow field at a particular position in an artery. This is because radial wall motion of the blood vessels is small compared to the flow of the

fluid. It is thus often assumed that changes in geometry and wall velocities should not significantly affect the major features of the flow field. However, since the interaction of the artery wall with the local haemodynamic environment takes place in the immediate neighbourhood of the vessel surface, it is appropriate to consider the effects of wall motion resulting from compliance upon the velocity field and wall shear stress in this region.

Oscillatory flow of a Newtonian fluid in an elastic tube, which is a model of blood flow in arteries, has been widely analysed. Theoretically, the pioneering work was carried out by Womersley [38] based on a linearization of the basic equations. In his study, the effects of wall elasticity, fluid viscosity and the coupling between fluid and wall motion have been taken into account and the oscillatory velocity profile across the vessel due to an imposed sinusoidal pressure gradient are predicted as a function of the Womersley number. Womersley's analysis has provided a basis for understanding many aspects of unsteady flow in elastic tubes. However, these are *linearised* solutions for flow in elastic tubes. To evaluate the importance of nonlinear effects resulting from the convective acceleration, a perturbation solution by Wang and Tarbell [158] has also been developed. The nonlinear effects on the amplitude of the wall shear rate, on the amplitude of the pressure gradient, and on the mean velocity profile have been considered. Nonlinear effects on the oscillatory components depend on the Womersley's parameter, the ratio between the mean and amplitude of the flow rate, the diameter variation, and the phase difference between the diameter variation and the flow rate. Dutta et al. [159] achieved a numerical analysis of flow in an elastic model under Ling and Atabek's assumption allowing for the axial convective acceleration term, which involves the axial velocity gradient, to be expressed in terms of the local axial velocity. With this assumption, the problem can be solved locally without axial boundary conditions. So far, the arterial wall has been characterised by linear stress-strain or pressure-diameter relationships in both analytical and numerical studies.

Numerous experimental studies have been made to investigate the flow field in compliant models of arterial bifurcations, where atherosclerotic lesions have been frequently encountered [160, 161, 162, 163, 164]. On the basis of Caro's low shear theory [1], shear stress has been investigated thoroughly. In addition to experimental studies, several recent numeri-

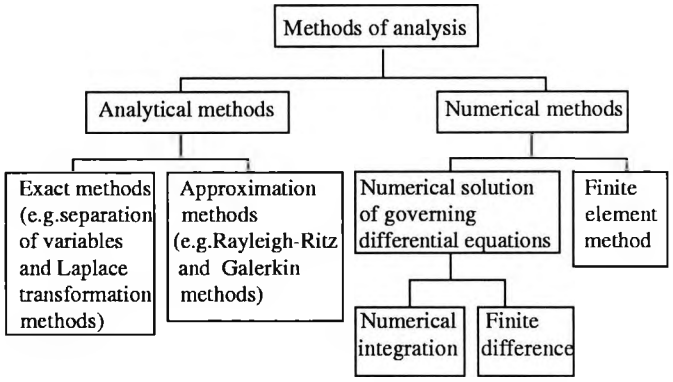

Figure 2.5: Classification of general field analysis methods.

cal studies have been modelled in simplified 2-D or 3-D distensible geometries [40, 41, 42]. This is in contrast to most numerical studies of flow in distensible systems, which are concerned with 1-D modelling of waveform behaviour, e.g.,Horsten et al. [165]. The comparison of the results for rigid and distensible wall models demonstrated the quantitative influence of the vessel wall motion.

2.7.2 Numerical methods in coupled problems

Mathematical analysis of arterial flow including wall motion is only possible for the simplest of cases due to the requirement that the equations of motion for the flow and the wall have to be solved simultaneously. Alternative approaches which can solve the coupled system of equations governing the flow and wall motion in complex geometries are needed. Common analysis methods available for the solution of a general problem (such as elastic deformation, fluid flow and heat transfer) is shown in Figure 2.5 [166].

While the finite element method remains the most commonly used discretization approach

in structural analysis, computational fluid dynamics can be approached using any of the three main types of discretization techniques: finite difference, finite volume, and finite element. Details of these numerical methods are outlined below, and their applications in practical problems are discussed later.

2.7.2.1 Finite difference /Finite volume method

The finite difference method is widely employed in CFD, with most common difference representatives of derivatives in equations based on Taylor's series expansions. Thus the unknowns of the resulting algebraic equations contain only the values of the variables at discrete points. One of the most attractive features of the finite difference approach is that it is easy to understand. However, the significant drawback of finite difference methods is that they are less amenable to irregular-shaped geometries. This problem has been partially overcome by the introduction of body-fitted curvilinear coordinates. The multi-block grid made it possible to deal with complex geometries.

In the finite volume method, the computational domain is split into a number of non-overlapping control volumes, and the differential equations are integrated over each volume. The resulting discrete equations forms a system of nonlinear algebraic equations containing the values of variables at grid points (provided the method is cell-vertex based).

CFX, which is a general purpose code for the numerical solution of laminar and turbulent flows with heat transfer, developed at the Harwell Laboratory UK, uses the finite volume method to solve the governing equations on general, three-dimensional, non-orthogonal grids. It allows both grid and solution domain boundaries to move in some prescribed manner. One of the key features of CFX is its poly-algorithmic structure, whereby options are available for users to specify different solution algorithms and different linear algebraic solvers.

2.7.2.2 Finite element method

The finite element method as known today was presented in 1956 by Turner et al. [167]. This paper presented the application of simple finite elements for the analysis of aircraft

structure and is considered one of the key contributions in the development of the finite element method. Although the method has been used extensively in the field of structural mechanics, the general nature of its theory makes it applicable to a wide variety of boundary problems, so it has been successfully applied to solve several other types of engineering problems like heat conduction, fluid dynamics, seepage flow and electric and magnetic fields.

The finite element method subdivides the computational domain into a set of elements, and it has the great advantage in offering geometrical flexibility, so that complex geometries can be modelled with relative ease. The solution of a general continuum problem by the finite element method follows an orderly step-by-step process. Among these steps, the derivation of the discretized equations usually involves any of the following approaches: (i) Direct approach, (ii) Variational approach, or (iii) Weighted residual approach. In the weighted residual approach, there are four different methods based on a weighted residual criterion. They are (1) Collocation method, (2) Subdomain collocation method, (3) Galerkin method, and (4) Least squares method. The FEAT code, which was developed at Berkeley Nuclear Laboratories, UK, has been designed as a general computational tool for simulating incompressible turbulent flow and heat transfer based on Galerkin weighted residuals finite element methodology. It therefore offers several key advantages over conventional finite difference based models, such as complex boundary geometries, arbitrary local refinement, and non-structured meshes. Many of the early arterial FEMs were not developed with commercial codes. Subsequently, commercial codes such as ANSYS and ABAQUS become available that allow analysis of arteries as nonlinear hyperelastic material. Detailed discussions of commercial packages will be presented in chapter 3.

2.7.3 Outline of the problem

The solution of the Navier-Stokes equations is a boundary value problem. That means, from the engineering point of view, that the geometric boundaries and Dirichlet and/or Neumann conditions have to be specified. In general, strictly speaking, there is always an interaction between the fluid motion and the surrounding body which cannot be neglected

in such mechanisms as blood flow through a vessel. The interactions between the flowing blood and arterial wall are complex. On one hand, there is the direct effect of the flow on the wall. The total load imposed on the arterial wall by the flow of blood is manifested through both a normal component, essentially equal to the fluid pressure, and a tangential component, which is the wall shear stress. The macroscopic effect of these two haemodynamic forces is to distend and distort the wall to produce stresses and strains within the wall itself. In this aspect it is the pressure, which is much the larger of the two forces, that plays the principal role. The other side of the blood/arterial wall interactions is that changes in shape and size of the arterial wall will change the geometry which bounds the flow, resulting in altered velocity and stress distributions in the artery.

2.7.4 The governing equations of fluid and wall motion

The equations governing the conservation of mass and momentum for an incompressible fluid are the 3-D time-dependent Navier-Stokes equations:

$$\frac{\partial u_i}{\partial x_i} = 0 \qquad (i = 1, 2, 3) \tag{2.42}$$

$$\rho_f(\frac{\partial u_i}{\partial t} + u_j\frac{\partial u_i}{\partial x_j}) = \frac{\partial \sigma_{ij}}{\partial x_j} + \rho_f f_i \qquad (i = 1, 2, 3) \tag{2.43}$$

where u_i and σ_{ij} are the components of the velocity vector and the components of the stress tensor, respectively; ρ_f is the fluid density and f_i are the components of body force.

The basic equations for the motion of an elastic solid (wall):

$$\rho_s\frac{\partial^2 d_i}{\partial t^2} = \frac{\partial \sigma_{ij}}{\partial x_j} + \rho_s F_i \qquad (i = 1, 2, 3) \tag{2.44}$$

where d_i and σ_{ij} are the components of the displacement vector and the components of the stress tensor in the solid, ρ_s is the density of the solid and F_i are the components of

body force acting on the solid. The equations of the equilibrium are derived in the actual configuration of the structure at any instant. This frame of reference is known as the Eulerian frame and refers to quantities which actually exist, e.g. true stress (Cauchy stress). For finite strains, equations associated with the other measures of stress are different.

The equations of motion for the flow and the wall have to be solved simultaneously so as to predict the full, time-dependent displacement and stress fields within the wall, as well as the details of the flow field. The arterial walls are complex both in their structures and their stress-strain relationships [82]. The wall consists of different layers being organised in such a manner that it becomes stiffer when stretched. The arteries are subjected to a large initial deformation. The complexity renders the formulation of a complete model a difficult task. For this reason, certain appropriate simplifications are necessary.

Three basic artery models that have been proposed based on the material laws are: elasticity, viscoelasticity, and poroelasticity. Each of these basic models can be further divided into linear, incrementally linear and nonlinear models. In Table 2.1, these aspects were systematised into a model matrix.

In coupled problems of arterial flows, an alternative simplified formation of wall motion is the "tube law" described as

$$R = R(P) \tag{2.45}$$

where R is the radius of the artery and P is the transmural pressure. In this case, the mechanical properties of arteries can be defined in terms of a distensibility or compliance. Most theoretical and numerical models of the complex interaction between fluid and solid mechanics have used this relatively simple "tube law". For example, in Steinman's 2-D distensible end-to-side anastomosis model [168] the artery was assumed to be a thin-walled, linearly elastic channel under axial constraint. Neglecting longitudinal displacements the transverse arterial wall displacement ξ is related to the transmural pressure, P, via:

$$\xi = D(P - \overline{P}) \tag{2.46}$$

where D is the distensibility of the wall and $\overline{P}$ is a reference transmural pressure. Dutta et al. [159] used a constant of $\partial R/\partial P$ to characterize the elastic response of the artery for the ascending aorta of man in their numerical analysis of flow in an elastic artery model. Up to now, only one publication is known in which a viscoelastic wall model has been used in the coupled problem treating the simplified formulation of wall motion. In the study presented by Lou and Yang [41] the Voigt model (a linear viscoelastic model) was used to describe the wall viscoelasticity. In the case of an artery, it took the form of

$$P = K(A - A_0) + C\frac{dA}{dt} \tag{2.47}$$

where P is the dynamic pressure; A, the cross section area of the artery; A_0, the reference area when P=0; K, the wall stiffness; and C, the wall damping constant.

The motion of the wall can take the form of *stress equations* if the magnitude and variation of the stresses at the endothelium/blood interface and the stresses within the wall are of interest because of their role in atherogenesis. Alternatively it can be expressed in terms of the *pressure-diameter relation* if research interest is only in the effect of wall distensibility on the flow field. In either case, the equations governing the fluid remain the 3-D time-dependent Navier-Stokes equations.

2.7.5 Coupled methods

2.7.5.1 Three essential coupled methods

There are essentially three numerical methods which can couple the motion of the wall and the motion of the fluid. They are simultaneous [49, 10, 169],iterative [42, 9, 170, 148] and hybrid [168]. Details of these methods are given below.

Simultaneous Approach

For a comprehensive treatment of flow-wall models the equations of flow and wall must be solved together, followed by simultaneous solution of the equations. In Xu and Collins [49], the momentum equations for both the fluid and the wall were discretised using the Galerkin finite element method with the continuity equations of the fluid being incorporated by a penalty augmented Lagrangian-multiplier method. The fluid flow was solved with a transformation of fluid region at any time back to the initial one, and the elastic stress equations governing the motion of the solid were discretised in terms of time derivatives (velocities) of the displacements rather than the displacements themselves. This is only applicable to linear elastic, small deformation problems, because under nonlinearity of material or finite deformation, either there is no direct relationship between stress and strain or a rather complex strain-displacement relationship. The elastic stress equations and the transformed N-S equations were solved always on the initial mesh, the traction between the solid and the fluid being cancelled out in the integration stage of the finite element method process. As a result, the solid/fluid interaction problem was solved *fully coupled.* An implicit predictor/corrector method was used to solve the fully-coupled time-dependent equations. The coupled solution procedure was implemented into a special version of the FE-based computational fluid dynamics code FEAT. However, it should be noted that the wall model is limited to linear elastic and small strains which is an approximation of the arterial wall behaviour.

Rast [169] studied the fluid flow through a significantly compressed elastic tube. This paper describes a finite element technique which solved the incompressible Navier-Stokes equations simultaneously with the elastic membrane equations on the flexible boundary. Both the grid and the spine positions were adjusted in response to membrane deformation, and the coupled fluid and elastic equations were solved by a Newton-Raphson scheme which displays quadratic convergence down to low membrane tensions and extreme states of collapse.

Iterative Approach

An alternative solution technique is to decouple the solid and fluid mechanics, solving

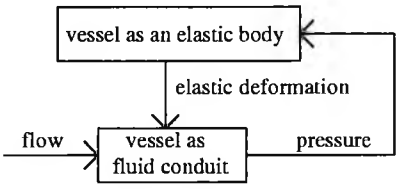

Figure 2.6: A haemoelastic feedback system.

for each separately and converging iteratively on a solution which satisfies both. More specifically, it is to analyse a haemoelastic situation as a feedback system of two functional units: an elastic body and a fluid mechanism (Figure 2.6). First, the vessel is regarded as a rigid segment with a specific wall shape. For a given flow the distribution of pressure is computed. This pressure is then applied as a loading on the elastic body (wall) and the deformation of the elastic body is calculated in the usual manner of the theory of elasticity. The result of the calculation is then used to determine the boundary shape of the haemodynamic problem. When a consistent solution is obtained the pressure distribution corresponding to a given flow is determined. In short, the elastic and fluid problems are coupled through a) wall position and b) the traction exerted by the fluid on the wall. Perktold et al. [42] employed this iteratively coupled approach in the study of local blood flow in a compliant carotid artery bifurcation model. The numerical procedure for the non-Newtonian inelastic Navier-Stokes equations was based on a pressure correction method and used the Galerkin finite element method with streamline upwinding, implicit time discretization and Picard iteration for the non-linear terms present. The wall displacement and stress analysis used non-linear shell theory with incremental linearly elastic wall behaviour, an improvement on a simple elastic behaviour model. The wall deformation and intramural stresses were obtained using the finite element program package ABAQUS. The total inner wall pressure resulting from the Navier-Stokes calculation, together with outflow pressure boundary condition and the wall inertial force, constituted the total load. However, its CFD code was purpose-built which would involve a large

team work and based on finite element method which was computationally expensive for problems of fluid dynamics. In Henry and Collins's paper [9], the equations governing the fluid together with the equations governing the motion of a linearly elastic, incompressible tube undergoing infinitesimal strains are discretised using a finite volume method. The coupled procedure was similar to the one used by Perktold, but limited to axisymmetric flows and infinitesimal solid strains.

Hybrid Approach

In the study presented by Steinman and Ethier [168], the artery was assumed to be a thin-walled, linear elastic channel. The transmural arterial wall displacement was described by equation(2.46). The no-slip boundary condition allows the transverse fluid velocity at the wall, v_w, to be expressed simply as

$$v_w = \frac{\partial \xi}{\partial t} \tag{2.48}$$

Equations(2.46 and 2.48) represent constraints which must be satisfied in addition to the Navier-Stokes and continuity equations. These latter equations, with the constraints, were treated using a finite element computer code developed by Steinman. This can be achieved in either an explicit manner (that is, by solving for the flow field and then updating the wall variables ξ and v_w in an iterative fashion) or in an alternative implicit manner, where the fluid and wall variables are solved simultaneously. The first (iterative) solution technique is potentially unstable, while the second technique is extremely computationally intensive within the context of a finite element approach. Thus, a hybrid approach was developed in which the wall velocity was expressed in terms of the transmural pressure and the resulting discrete equation forms a Dirichlet boundary condition, which was used to constrain the fluid velocities at the channel walls in the finite element solver. The wall velocities are solved simultaneously with the fluid and pressure fields, while the wall displacements are treated via an iterative update.

2.7.5.2 Use of commercial CFD and structural mechanics codes

In simultaneous and hybrid approaches, the equations governing the flow and the wall are solved totally or partly simultaneously, which limits the employment of available commercial packages and the extension to more complex wall behaviour. Up to now only specially developed codes are available having the capability of addressing fluid-solid interaction. Most authors have used either self-developed packages or improved commercial packages. So far these two approaches have mostly been applied to simplified models of wall behaviour such as linear elasticity and small strains.

However, in the iterative approach, the fluid and solid computational analysis is coupled externally in an iterative way. The essential task is to find a way to couple them. A wide range of commercial packages are available, forming investigative tools, which can treat comprehensively the complex material and deformation behaviour of the wall. For example, in Perktold's paper, both material nonlinearity and geometry nonlinearity are incorporated. The main problem lies in the lack of connection between the packages for the fluid and those for the wall because there is no universality regarding the data formats of interfaces which do not initially exist. Müller and Jacob [171] studied the feasibility of overcoming this problem by making the steady state and transient calculations of flow in a tube with a stricture. In this paper, they used (i) FIDAP as a fluid code, (ii) finite element code PERMAS as well as (iii) a boundary element code BEASY as the structural mechanics code. The common interface was performed by (iv) PATRAN, which proved to be useful due to its PCL(PATRAN-Command-Language). As a common shell for the calculations they used PATRAN with several specific subroutines written in PCL. In PATRAN, they not only generated the meshes and set up the boundary conditions, but also the specific routines to write the data from output to input files and vice versa, and even the calls for running the different codes were initiated by PATRAN files.

2.7.6 Uncoupled methods

In addition to the three coupled approaches, there are also some other methods to solve solid/fluid interaction problems. For example, Reuderink [172] proposed a numerical ap-

proach for an uncoupled solution of the equations of wall motion and the equations of fluid flow. The feature of this approach is the assumption that the wall motion can be calculated on the basis of the pressures due to wave phenomena. The first step in the approach is the calculation of the time-dependent pressure distribution due to wave phenomena. Next, the wall motion due to this time-dependent pressure is evaluated. Finally, this wall motion is prescribed as a boundary condition for equations for the fluid flow which was solved using Galerkin's finite element method.

2.7.7 Coupled problems in conventional engineering

The review is concluded by pointing out that development of a reliable fluid-solid algorithm for medical engineering has substantial implications for conventional engineering also. Since the arterial wall requires a high-level solid mechanics model to treat it comprehensively, once a coupled fluid-solid overall code can be quantitatively validated for arterial flows, it should be applicable for what are usually simpler engineering materials.

Now while in engineering, continuum mechanics is customarily subdivided into solid mechanics and fluid mechanics, there is a wide range of problems that require a simultaneous solution of fluid flow and solid body deformations. For examples, we have
(a) casting of metal components, which involves a continuous transformation from flowing liquid to a deforming solid as one of the key features of the process,
(b) welding, where a region of flow liquid "travels through" the deforming solid, and generalising fluid-structure interaction (FSI) systems.

Of great interest is the general flow-structure interaction system. For example, large engineering structures in nuclear power plants are often separated by narrow fluid-filled cavities and represent a typical FSI system. The fluid moving with the structure has an important effect on the dynamics of the vibrating structure, particularly its natural frequencies. Substantial progress has been achieved since the mid-1970s in developing and validating computing methods (including finite element and finite difference methods, the method of characteristics and combined procedures) for the treatment of such coupled fluid-structure effects. Other applications arise in the analysis of many complex structures, such as off-

shore platforms, ships, reservoir-dam systems, water towers, aerospace vehicles, turbines, piping systems, and widely in other nuclear reactor components [173].

FSI-studies may involve weakly or strongly coupled fluid-structure systems. Weak coupling implies that the structure can be considered stationary while the fluid field is solved. The fluid-structure coupling forces for the structural response in such a case can be expressed to a first order of approximation in terms of added mass and stiffness matrices. In a strongly coupled fluid-structure system, however, the fluid and structural equations of motion are coupled because the structural motion becomes large enough to change the fluid field; some of the fluid forces amplify, rather than inhibit, the structural motion that produced them.

Whereas in all recent numerical modelling of arterial flows the full Navier-Stokes equations have been used, in conventional engineering, the coupled strategy to date has involved equations of a different form for the fluid. This is assumed to be inviscid, irrotational, compressible, and adiabatic. The flow is assumed laminar and the fluid undergoes only small deformations. The equilibrium and constitutive equations of the fluid are the Helmholtz equations as follows:

$$\frac{1}{c^2}\ddot{P} = \nabla\nabla P; \qquad \frac{1}{c^2}\ddot{u}_{(x,y,x)} = \nabla\nabla u_{(x,y,z)} \tag{2.49}$$

The equations governing the motion of the structure remain the same (equation(2.44)). Most FSI analyses are based on one of the two following approaches. In the Lagrangian-displacement approach the displacements are considered unknown in both the fluid and the solid. The Eulerian-pressure formulation assumes nodal displacements as the basic unknowns for the solid, and nodal pressures as the variables in the fluid. General purpose FE codes for structural analysis (such as ANSYS and ADINA) have already implemented displacement-based fluid elements because the mass and stiffness matrices of the coupled problem are symmetric, banded, and positive definite so that minimum modifications are necessary and existing equation solution methods perform efficiently. In this pseudo-elastic approach the fluid is normally treated as a degenerated solid continuum with a proper choice of the element material properties (elastic modulus and Poisson's ratio). The mass matrix is a simple diagonal matrix and the interaction of these fluid

elements with structural elements is achieved by selective node coupling. For example, Engel et al. [173] analysed a model of core support barrel using the FE package ANSYS. For this interaction between a fluid and an elastic shell structure the fluid was modelled by the displacement-based fluid element (STIF80) and the cylindrical shell by the 4-noded quadrilateral shell element (STIF63).

The great effort and progress made over the past few years in solving FSI problems by the FE method give rise to the assumption that such complex problems can be treated in an efficient and general manner by commercially-oriented standard FE packages in the years ahead.

2.8 Conclusion

The arterial wall behaviour and applications in arterial mechanics research have been reviewed. Biomechanical models play an important role in the study of diseased vessels. From the perspective of mechanics, the arterial wall exhibits a complex behaviour. The exact determination of arterial mechanical properties remains a challenge. The rapid advance of computational techniques and the advent of supercomputers can treat complex wall behaviour as well as 3D pulsatile flow. Nevertheless, there is a need for a coupled solid/fluid model to simulate the dynamic interactions between blood and the vessel wall.

Fluid/solid interaction in general is a very challenging area of application for computer simulation. The term fluid/solid interaction describes phenomena in which both fluid and structural responses are dynamically coupled. Recent progress in the development of numerical modelling approaches for the coupled fluid/solid interaction problems in both biomedical engineering and conventional engineering has been reviewed with special emphasis on the former. A novel coupled algorithm will be presented in chapter 3.

Chapter 3

Numerical Techniques for Fluid/Solid Coupling

In this chapter, a novel numerical method combining two commercial codes for coupled solid/fluid problems is presented. Detailed discussions concerning the numerical techniques are dedicated to CFX and ABAQUS on which the coupled model is based. Automatic grid generation from clinical data for complex geometry models is included. Also covered are the numerical convergence problem arising from the coupled model. Whenever there is iteration, there is always convergence problem. Because in an iterative coupled model, in addition to convergence considerations within each code, convergence between the two codes must also be dealt with. A relaxation technique is introduced to improve the convergence performance. A number of numerical experiments have been performed to test the convergence of the iterative procedure implemented and have demonstrated the effectiveness of the relaxation scheme.

3.1 Fluid/Solid Coupling Procedure

3.1.1 Introduction

Coupled fluid-solid interaction problems arise frequently in engineering applications [173, 174, 175]. The coupled system and formulations are those applicable to multiple domains and dependent variables which describe different physical phenomena and in which (a)

neither domain can be solved while separated from the other; and (b) neither set of dependent variables can be eliminated at the differential equation level. It is also usual to divide coupled systems into two categories:

(1) problems in which coupling occurs on domain interfaces via the boundary conditions imposed there.

(2) problems in which the coupling comes from different physical phenomena which occur (totally or partially) on overlapping domains.

Fluid-wall interaction problems exist in the cardiovascular system where blood interacts dynamically with its surroundings. Doubtless, this represents one of the best-known coupled problems. In this case, the coupling occurs at the interface between two different domains, one occupied by the solid and the other by the fluid. Neither the structure nor the fluid can be solved independently of the other, since the motion of the structure depends on the pressures of the fluid at the interface, and the fluid pressures depend in turn on the deformation of the solid wall. An overall coupled solution of the blood-wall interaction problem is difficult to obtain due to the very strong non-linear nature of the equations arising from the discretization of the governing equations.

As described in chapter 2, there are essentially three types of numerical schemes for the coupled solution of flow and wall motion: hybrid, simultaneous and iterative methods. In simultaneous and hybrid methods, the equations governing the flow and the wall are solved totally or partly simultaneously, limiting the employment of available commercial packages and the extension to complex wall behaviour. Up to now only a few special purpose codes have been reported to be able to treat the fluid-solid interaction problems and the applicability of the codes has been confined to simple wall mechanical models such as linear elasticity and infinitesimal strain.

Nevertheless, the iterative approach allows the fluid and solid equations to be solved separately and then coupled externally in an iterative manner. It offers a distinctive advantage

in that the most efficient codes for fluid flow and structural analysis can be used to ensure most reliable results. Therefore, in the present study, a numerical approach combining two commercial codes for coupled solid/fluid problems of periodic nature is established. The finite volume based CFX was used as the fluid dynamics code, and a finite element code ABAQUS as the structural mechanics code. The characteristic of this approach is to ensure proper interaction between the two codes during each pulse cycle because of the periodic nature of the flow. The equations for the fluid motion and solid deformation are solved separately and then coupled externally in an iterative manner at a cycle level. Employing the modified user subroutines in both codes, the updated pressure and deformation distribution at each time step during the cycle can be transferred between CFX and ABAQUS on an interface mesh. Calculations of specific test problems led to a converged solution after only several iterative cycles between the two codes. The validity of the presented method will be demonstrated in chapter 4 through the solution of flow in a tube with the tube material being (a) elastic and (b) hyperelastic. Furthermore, the application of the coupling algorithm will be extended to more complex arterial structures like human carotid artery bifurcations in a clinical context (chapter 5).

3.1.2 The coupling algorithm

The fluid and solid computational analysis is coupled externally in an iterative way. Since most unsteady flows have periodic nature with the interested period of time being the cycle period, the coupled system is solved in an iterative procedure at a cycle level.

A discrete iteration cycle consists of the following steps:

Step 1 The 3-D time-dependent Navier-Stokes equations (2.42, 2.43) governing the conservation of momentum and mass for an incompressible fluid are solved for several complete cycles using CFX, and the predicted pressures at the fluid/solid interface at each time step of the last cycle are stored for later use.

Here, discrete versions of equations were solved using CFX, which uses the finite volume

method to solve the governing equations on general, three-dimensional, non-orthogonal grids. The moving grid capability in CFX was used to account for the effect of changes in the flow domain configuration during arterial wall movement in the present study. The code solves the discrete equations using the velocity-pressure coupling schemes known as SIMPLEC. The Rhie-Chow algorithm is incorporated into the solution procedure to allow the use of non-staggered grids [176], that is, velocity components and scalar variables are defined on the same nodal points.

Multi-block structured grid was used for complex geometry such as bifurcation structures. Programs were developed to generate computational grids within the flow domain by the use of model surface information. This was done by (1) specifying a grid distribution along the vessel axial direction, (2) defining grid planes and calculating boundary points, which form grid planes, on the model surface, (3) interpolating grid points within the boundary points on each grid plane. Details of grid generation will be discussed in section 3.3.

Step 2 The dynamic nonlinear analysis of the solid is carried out by using the finite element package ABAQUS, solving the basic equations for the motion of an elastic solid (2.44), under the pressure at each time step predicted from the flow calculation of step 1. From ABAQUS calculation, the displacement and stress of the solid are obtained, with the displacement at each time interval being used for the next cycle.

ABAQUS has extensive material, element, and procedure libraries. All elements use numerical integration to allow complete generality in material behaviour including a wide range of nonlinear material behaviour. All elements in ABAQUS are formulated to provide accurate modelling for arbitrary magnitudes of displacements, rotations, and strains. ABAQUS uses complete, consistent kinematics for finite-strain calculations. Lagrangian and updated Lagrangian formulations are used for finite-strain elastic and elastic-plastic problems respectively. In each increment ABAQUS iterates for equilibrium, using the full Newton method in most cases. For fully nonlinear, dynamic stress/displacement analysis problems ABAQUS includes direct, implicit time integration, using the Hilber-Hughes operator (the Newmark method with controllable numerical damping). For the straight

tube case in chapter 4, the selected element type will be axisymmetric solid element, while shell element will be used for bifurcation structures like the carotid artery bifurcation. Non-uniformly distributed pressure loads as predicted using CFX are applied on the inner surface of the model.

The displacement was extracted from a comprehensive ABAQUS result file which involves a variety of information ranging from nodes to elements, locations to variables. In ABAQUS, the values of output variables can be printed out throughout the analysis. The result file is written as a sequential file. Each record has the following format:

Location	Length	Description
1	1	Record length(NW)
2	1	Record type key
3,4...	(NW-2)	Attributes

All words on the result file are of the same length, whether they contain integer, floating point number, or character string data. The attributes in a given record depend on the element type being considered. The result file is written using internal data management routines to minimise I/O cost. Therefore, to access the result file a postprocessing program was developed which used the same ABAQUS data management routines to read the result file and to extract the displacements required later by CFX to update the configuration. The following utility subroutines, which are part of the shared library in ABAQUS, are called to obtain data from the ABAQUS result file by the user-written postprocessing program: INITPF(initialise a file), DBRNU(set a unit number for a file), DBFILE(read from a file), POSFIL(determine position of a file), DBFILW(write to a file).

Step 3 The convergence criterion is checked, which is based on the difference between displacements at two successive iterative cycles at each time step

$$DD = MAX\left(\frac{\mid d_i^{n+1,m} - d_i^{n,m} \mid}{\mid d_i^{n,m} \mid}\right) \leq D_{crt} \tag{3.1}$$

where d_i, i=1,2,3 are the components of the displacement vector $\mathbf{D}$ at a displacement

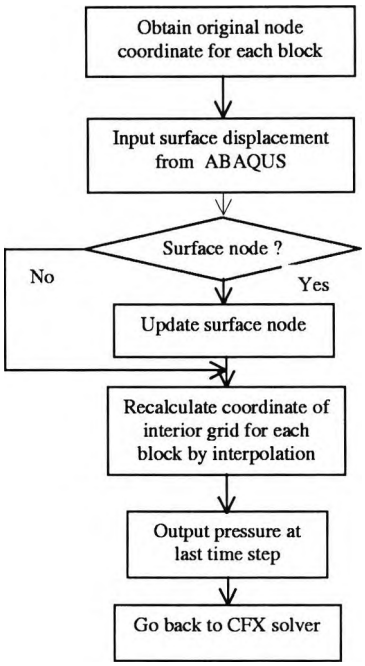

Figure 3.1: Flow chart for user subroutine USRGRD.

node of the finite element mesh on the inner surface of the solid at time step m during two successive cycles n+1 and n. D_{crt} is the convergence criterion which is case dependent and chosen as a compromise between high computational demands and appropriate numerical accuracy.

Step 4 If equation(3.1) is not satisfied, the geometry bounding the fluid will be updated using the displacements predicted from ABAQUS. With the updated surface, the computational grids within the flow domain are regenerated following the same procedure as described in step 1, with the same grid densities in order to maintain a uniform grid change within the fluid as a result of the movement of the wall. This was achieved through specifically designed grid generation subroutines which were called dynamically during the run time when the new inner wall points are established. Flow chart for the user subroutine USRGRD is illustrated in Figure 3.1.

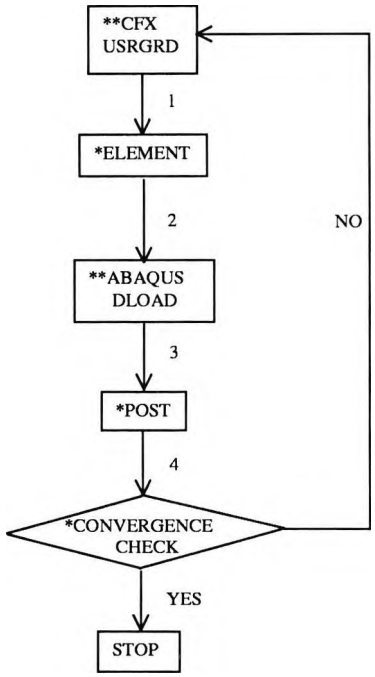

Figure 3.2: Flow chart for CFX-ABAQUS coupling, where * represents purpose-developed program and ** modified user subroutines in CFX and ABAQUS.

Step 5 Steps 1, 2, 3 and 4 are repeated until the convergence criterion is satisfied.

A flow chart is shown in Figure 3.2 where reconstructed geometries from either MRI or ultrasound are used for computational models.

In the chart, 1-4 are the output from its corresponding upper levels. They are:

1. Pressure output from CFX

2. Pressure data to be accepted by ABAQUS

3. ABAQUS result file

4. Displacement to be accepted by CFX

The concept of the coupled model is straightforward, however, its implementation is tedious and may cause numerical difficulties which will be discussed in section 3.4.

3.2 Numerical Details Related to the Coupled Modelling

3.2.1 Computational fluid mechanics

CFD is playing a strong role as a design and research tool. Historically, the early development of CFD was driven by the needs of the aerospace community. However, modern CFD cuts across all disciplines where the flow of a fluid is important. Of particular interest, CFD is a useful tool for solving haemodynamics problems.

Many powerful CFD packages are available based on FV/FD and FE methods with varying degrees of modelling capabilities. Among these, commercially available codes based on FDM are, for example, CFDS-CFX, FLUENT, PHOENICS, STAR-CD; while codes based on FEM are, for example, FIDAP, FEAT. In addition to these, most general purpose FE packages such as MSC/NASTRAN, ADINA, ANSYS, ABAQUS, include CFD modules. They are often powerful for structural analysis, which will be discussed in the next section. Pre- and Post-processings are often included. In this section, special attention is attributed to a CFD code–CFX [44], which will be used throughout the following numerical predictions.

CFX is a package for the prediction of laminar and turbulent flow, and heat transfer, together with additional models such as multi-phase flows, combustion and particle transport. The suite of CFX consists of a number of modules: (1) Geometry and Grid Generators, (2) Frontend Module, (3) Solution Module, and (4) Graphics Module. Among those, a detail discussion about Solution Module will be given including discretisation method, the treatment of convective and diffusive transport, and of moving wall.

3.2.1.1 Discretisation methods

Numerical methods used to discretise the Navier-Stokes equations are referred to as discretisation methods and fall into three main categories: Spectral method, Finite-element method, and Finite volume/finite difference method. The difference between the three methods results from the ways of choosing the profiles and deriving the discretisation equations. The discretisation of the space and of the dependent variables allows the governing equations to be replaced with simple non-linear algebraic equations, consisting of four equations, threes for the velocities and one for the pressure for each control unit.

In CFX the variables calculated are the velocity components in fixed coordinates directions and pressure, together with any scalar quantities such as enthalpy, density, turbulent kinetic energy and turbulent energy dissipation. With the choice of variables, it is relatively straightforward to express the equations as conservation equations for mass, momentum and energy etc. These equations are expressed in the form

$$Convection - Diffusion = Sources - Sinks, \tag{3.2}$$

and integrated over each control volume to give discrete equations which themselves also conserve mass, momentum and energy within the control volume. The numerical treatment therefore has to represent the convective and diffusive fluxes across the surfaces of each control volume, and to calculate the effect of the sources and sinks. Full details of this treatment are as follows.

3.2.1.2 Discretisation of equations

In this section, some details are given of the discretisation of equations, both temporal and spatial, used in CFX. The basis of the code is a conservative finite-difference, or finite-volume method with all variables defined at the centre of control volumes which fill the physical domain being considered. Each equation is integrated over each control volume to obtain a discrete equation which connects the variable at the centre of the control volume

with its neighbours.

All of the equations to be solved, apart from the continuity equation, have the same general form:

$$\frac{\partial \rho\phi}{\partial t} + \nabla \cdot (\rho U \phi) - \nabla \cdot (\Gamma \nabla \phi) = S \tag{3.3}$$

where Γ is the relevant effective diffusivity for the variable ϕ. Integrating over the control volume gives:

$$\int \frac{\partial \rho\phi}{\partial t} dV + \int \rho\phi U \cdot \mathbf{n} dA - \int \Gamma \nabla \phi \cdot \mathbf{n} dA = \int S dV \tag{3.4}$$

All terms in all the equations are discretised in space using second-order centred differencing apart from the advection terms, described below, and the convection coefficients obtained using the Rhie-Chow interpolation formula. In order to give a simple explanation of the discretisation methods, that which follows uses the framework of a rectangular grid. The extension to a body-fitted grid is straightforward.

Diffusion terms

To illustrate the diffusion and advection terms, consider the control volume shown in Figure 3.3.

The diffusion term at the west face of the control volume is discretised as:

$$\int \Gamma \nabla \phi \cdot \mathbf{n} dA = \frac{\Gamma A_w}{h_w}(\phi_P - \phi_W) = D_W(\phi_P - \phi_W) \tag{3.5}$$

Here A_w is the area of the west face, h_w is the distance between the west and the central nodes and D_W is the west diffusion coefficient.

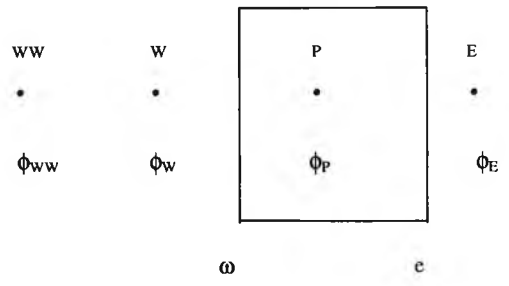

Figure 3.3: Control volume notation.

Advection terms

A significant amount of research effort has been directed toward discretisation of the combined convection and diffusion fluxes. Inaccurate modelling of these terms can seriously degrade overall accuracy and stability of the solution, In many cases, it is almost impossible to refine the grid sufficiently so that the numerical errors will reduce to acceptable levels. Thus, it is essential to have a convection-diffusion formulation that leads to a stable and accurate solution with grids of modest fineness. Whereas many methods have been formulated, there exists no clear consensus about a preferred method. The more accurate schemes tend to be less robust and slower. The treatment of the advection terms determines the accuracy of the solutions of the model equations. Because of these, there is a choice of discretisation methods available in the CFX code. These range from diffusive, simple upwind scheme (UDS), hybrid differencing (HDS), central differencing (CDS), higher order upwind differencing (HUW) through to quadratic upwind scheme (QUICK).

For example, in the upwind scheme, the advected value of the variable ϕ at the west face of the control volume (ϕ_w) is taken to be ϕ_W, so that, at the west face,

$$\int \rho\phi\mathbf{U}\cdot\mathbf{n}dA = \rho\mathbf{U}_w A_w \phi_W = C_W\phi_W \tag{3.6}$$

Here C_W is the convection coefficient at the west face. This gives a matrix coefficient for

the west point of:

$$A_W = MAX(C_W, 0) + D_W \tag{3.7}$$

This scheme is first order accurate.

Time stepping procedures

By default, a fully implicit backward difference time stepping procedure has been implemented. That is, if the equations are written in the form :

$$\frac{\partial \phi}{\partial t} = F(\phi) \tag{3.8}$$

the discretised form is:

$$\frac{\phi^n - \phi^{n-1}}{\Delta t} = F(\phi^n) \tag{3.9}$$

The terms on the left hand sides can be absorbed into the sources and sinks for each equation and the resulting equations at the n^{th} time step look like the discrete steady state equations. These can then be solved using the standard steady state techniques.

An alternative to the above is to use a second order accurate backward difference treatment. In this case the discretised equation becomes:

$$\frac{2\Delta t + \Delta t_0}{\Delta t(\Delta t + \Delta t_0)}\phi^n - \frac{\Delta t + \Delta t_0}{\Delta t \Delta t_0}\phi^{n-1} + \frac{\Delta t}{\Delta t_0(\Delta t + \Delta t_0)}\phi^{n-2} = F(\phi^n) \tag{3.10}$$

where Δt_0 is the time difference on the previous time step. Again the terms on the left hand side can be incorporated into the source terms. However, more memory is needed

as variables at two previous times are required.

Another alternative is to use a time centred treatment. Note that this is, in effect, a two-step procedure, the first being to use a backward difference procedure over the first half step, and then an extrapolation to give the solution at the end of the time step.

Source terms

For each equation, the source term is written in the following way:

$$\int SdV = SU + SP\phi_P \tag{3.11}$$

where SP is non-positive. The SP term then enhances the diagonal of the matrix giving more diagonal dominance and thus better solution behaviours. In particular, for physical variables such as the turbulent kinetic energy k and the energy dissipation ϵ, putting the source terms into SU and the sink terms into SP ensures that the variable remains positive throughout the iteration procedure when using line relaxation.

3.2.1.3 Treatment of the moving wall in CFX

Moving boundary procedures have been developed by a number of research groups and are included in most advanced commercially available CFD codes. Moving boundaries exist throughout cardiovascular system where the ventricles and arteries expand and contract cyclically due to the pumping action of the heart.

The governing equations for the fluid are the equations for the conservation of mass and momentum. In order to allow the boundaries and the grid to move in the prescribed manner, the momentum and mass equations have to be transformed to equivalent equations on rectangular computational grid with uniform spacing. If the physical grid is moving the time derivatives have to be modified so that in computational space the grid is fixed.

Following the work in Thompson et al. [177],

$$\left(\frac{\partial \phi}{\partial t}\right)_x = \left(\frac{\partial \phi}{\partial t}\right)_\xi - \frac{\partial x_j}{\partial t}\frac{\partial \phi}{\partial x_j} \tag{3.12}$$

where the time derivative on the left of equation(3.12) is at a fixed point in physical space, and the time derivative on the right is at a fixed point in computational space.

This has the effect that the convective term

$$\frac{\partial \phi}{\partial t} + \frac{\partial (\phi u_j)}{\partial x_j} \tag{3.13}$$

becomes

$$\frac{1}{\sqrt{g}}\frac{\partial (\sqrt{g}\phi)}{\partial t} + \frac{\partial}{\partial x_j}\phi\left(u_j - \frac{\partial x_j}{\partial t}\right) \tag{3.14}$$

where g is the determinant of the metric tensor which represents the square of the volume in physical space and corresponding to unit volume in computational space.

Full Navier-Stokes equations can be transformed using equations(3.13) and (3.14) to give:

$$\frac{1}{\sqrt{g}}\frac{\partial (\sqrt{g}\rho)}{\partial t} + \frac{\partial}{\partial x_j}\rho\left(u_j - \frac{\partial x_j}{\partial t}\right) = 0 \tag{3.15}$$

$$\frac{1}{\sqrt{g}}\frac{\partial (\sqrt{g}\rho u_i)}{\partial t} + \frac{\partial}{\partial x_j}\rho u_i\left(u_j - \frac{\partial x_j}{\partial t}\right) = \frac{\partial \sigma_{ij}}{\partial x_j} + \rho F_i \quad i = 1,2,3 \tag{3.16}$$

In addition, an equation for the conservation of space

$$\frac{1}{\sqrt{g}}\frac{\partial \sqrt{g}}{\partial t} - \frac{\partial}{\partial x_j}\left(\frac{\partial x_j}{\partial t}\right) = 0 \tag{3.17}$$

which expresses the relationship between the rate of change of volume and the velocity of the volume boundary, and has to be solved simultaneously with mass, momentum and energy equations, as it was pointed out by Demirdzic and Peric [178]. Full details have been given in Hawkins and Wilkes [179].

The time derivative of a typical variable ϕ is discretised as:

$$\sqrt{g^{n+1}}\frac{(\phi^{n+1}-\phi^{n})}{\Delta t}+\phi^{n}\frac{(\sqrt{g^{n+1}}-\sqrt{g^{n}})}{\Delta t} \tag{3.18}$$

where the superscript n denotes the time step.

The change in volume term is calculated from grid velocities and the cell face areas. This makes it consistent with the modification to the convection coefficients and ensures that no spurious source terms are introduced. This is carried out for all variables. For computational convenience the grid velocities are stored at cell faces and are multiplied by the time averaged cell area.

In the pressure correction algorithm the current solution u_j, P, ρ is updated using corrections u_j^c, P^c, ρ^c to give a solution field $u_j^* = u_j + u_j^c, P^* = P + P^c, \rho^* = \rho + \rho^c$ which satisfies the continuity equation exactly and the momentum equation approximately.

For an incompressible flow and a fixed grid, continuity equation yields:

$$\frac{\partial(\rho u_j^*)}{\partial x_j} = 0 \tag{3.19}$$

Substituting the exact solution into the linearized momentum, gives the following approximate relationship between the pressure correction and the velocity correction.

$$\rho u_j^c = -\frac{1}{A_p}\frac{\partial P^c}{\partial x_j} \tag{3.20}$$

The definition of A_p is the key part of the approximation, in SIMPLEC it is taken to be the diagonal coefficient of the locally discretised momentum equation. This gives the following equation which in its discretised form can be solved for P^c

$$\frac{\partial}{\partial x_j}\left(\frac{1}{A_p}\frac{\partial P^c}{\partial x_j}\right) = \frac{\partial}{\partial x_j}\rho u_j \tag{3.21}$$

The solution algorithm for the calculation of unsteady flows with moving boundaries has been provided by Demirdzic and Peric [180] and is summarised as follows:

1. Provide the initial grid and the solution for the initial time t_0.

2. Determine the location of the boundary grid points for the time $t_0 + \delta t$ and move the new grid to fit the new boundaries at the new prescribed position.

3. Calculate iteratively the new solution employing the currently available pressure and mass fluxes until the sum of the absolute residuals in the momentum and continuity equations are satisfactorily reduced.

4. Advance the time by another increment δt and return to step 2.

Details of the application of the moving boundary procedures to the Navier-Stokes equations are given by Demirdzic and Peric [181], and Hawkins and Wilkes [179]. The routine USRGRD in CFX can be used to define a grid that varies with time. The validation of the moving boundary capabilities in CFX will be presented in chapter 4.

3.2.2 Structural mechanics

The most popular FE systems for structural analysis are: MSC/NASTRAN, ABAQUS, ANSYS, ADINA. ABAQUS is a general purpose finite element analysis program with special emphasis on advanced linear and nonlinear structural engineering and heat transfer applications [182]. In this section detailed discussion about ABAQUS is given. Basic

equations for virtual work statement, nonlinear numerical solution methods and element library are described.

3.2.2.1 Basic finite element equations

The virtual work equation in the classical form is:

$$\int_{V^0} \boldsymbol{\tau}^c : \delta\boldsymbol{\varepsilon} dV^0 = \int_S \mathbf{t}^T \cdot \delta\mathbf{v} dS + \int_V \mathbf{f}^T \cdot \delta\mathbf{v} dV \tag{3.22}$$

where $\boldsymbol{\tau}^c$ and $\boldsymbol{\varepsilon}$ are any conjugate pairing of material stress and strain measures, $\delta\mathbf{v}$ an arbitrary virtual velocity field, $\mathbf{t}$ the surface traction, and $\mathbf{f}$ the body force. The particular choice of $\boldsymbol{\varepsilon}$ depends on the individual element.

The finite element interpolator can be written in general as

$$\mathbf{u} = \mathbf{N}_N u^N \tag{3.23}$$

where $\mathbf{N}_N$ are the interpolation functions that depend on some material coordinate system, u^N are nodal variables, and the summation convention is adopted for the uppercase subscripts and superscripts that indicate nodal variables.

Introducing the above interpolation to displacements, the virtual fields $\delta\mathbf{v}$ and $\delta\boldsymbol{\varepsilon}$ take the form:

$$\delta\mathbf{v} = \mathbf{N}_N \delta v^N \tag{3.24}$$

$$\delta\boldsymbol{\varepsilon} = \boldsymbol{\beta}_N \delta v^N \tag{3.25}$$

where $\boldsymbol{\beta}_N$ is a matrix that depends, in general, on the current position, $\mathbf{x}$, of the material point being considered. The matrix $\boldsymbol{\beta}_N$ that defines the strain variation from the variations of the kinematic variables is derivable immediately from the interpolation functions once the particular strain measure to be used is defined. Since the δv^N are independent variables, system of nonlinear equilibrium equations can be obtained:

$$\int_{V^0} \boldsymbol{\beta}_N : \boldsymbol{\tau}^c dV^0 = \int_S \mathbf{N}_N^T \cdot \mathbf{t} dS + \int_V \mathbf{N}_N^T \cdot \mathbf{f} dV \tag{3.26}$$

This system of equations forms the basis for the standard displacement finite element analysis procedure, and is of the form:

$$F^N(u^M) = 0 \tag{3.27}$$

The above equations are valid for static and dynamic analysis. In dynamic analysis, however, the inertia contribution is more commonly considered separately, leading to the equations:

$$M^{NM}\ddot{u}^M + F^N(u^M) = 0 \tag{3.28}$$

3.2.2.2 Nonlinear numerical solution methods

The finite element models generated are usually nonlinear and can involve from a few to many thousand variables. In terms of these variables, the equilibrium equations obtained by discretizing the virtual work equation can be written symbolically as:

$$F^N(u^M) = 0 \tag{3.29}$$

where F^N is the force component conjugate to the N^{th} variable in the problem and u^M is the value of the M^{th} variable. The basic problem is to solve equation(3.29) for the u^M

throughout the history of interest.

Many of the problems are history-dependent, so the solution must be developed by a series of small increments. Generally Newton's method is used for numerical solution of the nonlinear equilibrium equations. The basic formalism of Newton's method is as follows. Assume that, after an iteration i, an approximation u_i^M, to the solution has been obtained. Let c_{i+1}^M be the difference between this solution and the exact solution to the discrete equilibrium equation(3.29). This means that

$$F^N(u_i^M + c_{i+1}^M) = 0 \tag{3.30}$$

Expanding the left hand side of this equation in a Taylor series about the approximate solution u_i^M then gives

$$F^N(u_i^M) + \frac{\partial F^N}{\partial u^P}(u_i^M)c_{i+1}^P + \frac{\partial^2 F^N}{\partial u^P \partial u^Q}(u_i^M)c_{i+1}^P c_{i+1}^Q + ... = 0 \tag{3.31}$$

If u_i^M is a close approximation to the solution, the magnitude of each c_{i+1}^M will be small, and so all but the first two terms above can be neglected giving a linear system of equations:

$$K_i^{NP} c_{i+1}^P = -F_i^N \tag{3.32}$$

where

$$K_i^{NP} = \frac{\partial F^N}{\partial u^P}(u_i^M) \tag{3.33}$$

is the Jacobian matrix and

$$F_i^N = F^N(u_i^M) \tag{3.34}$$

The next approximation to the solution is then

$$u_{i+1}^M = u_i^M + c_{i+1}^M \tag{3.35}$$

and the iteration continues.

The principal advantage of Newton's method is its quadratic convergence rate when the approximation at iteration i is within the radius of convergence–that is, when the gradients defined by K_i^{NM} provide an improvement to the solution. However, Newton's method is usually avoided in large finite element codes, apparently for two reasons. First, the complete Jacobian matrix is sometimes difficult to formulate; and for some problems it can be impossible to obtain this matrix in closed form, so it must be calculated numerically–an expensive process. Secondly, the method is expensive per iteration, because the Jacobian must be formed and solved at each iteration. The most commonly used alternative to Newton is the modified Newton method, in which the Jacobian in equation(3.32) is only recalculated occasionally. This method is attractive for mildly nonlinear problems, but is not suitable for more severely nonlinear cases.

Another alternate is the BFGS (Broyden, Fletcher, Goldfarb, Shanno) quasi-Newton method, in which equation(3.32) is symbolically rewritten

$$c_{i+1}^P = -[K_i^{NP}]^{-1} F_i^N \tag{3.36}$$

and the inverse Jacobian is obtained by an iteration process. Matthies and Strang [183] have shown that, for systems of equations with a symmetric Jacobian matrix, the BFGS method can be written in a simple form that is especially effective on the computer and is successful in such applications. The basis of quasi-Newton methods is to obtain a series of

improved approximations to the Jacobian matrix, $\tilde{K}_i^{NM}$, that satisfy the secant condition:

$$F^N(u_i^M) - F^N(u_{i-1}^M) = \tilde{K}_i^{NM}(u_i^M - u_{i-1}^M) \tag{3.37}$$

so that $\tilde{K}_i^{NM}$ approaches K_i^{NM} as the iterations proceed. Equation(3.37) is the basic quasi-Newton equation.

For convenience the change in the residual from one iteration to the next is defined as:

$$\gamma_i^N = F_i^N - F_{i-1}^N \tag{3.38}$$

so that equation(3.37) can be written:

$$\gamma_i^N = \tilde{K}_i^{NM} c_i^M \tag{3.39}$$

where c_i^M is the correction to the solution from the previous iteration.

Matthies and Strang's implementation of the BFGS method is a computationally inexpensive method of creating a series of approximation to $\left[\tilde{K}_i^{NM}\right]$ that satisfy equation(3.37) and retain the symmetry and positive definiteness of $\tilde{K}_i^{NM}$. They accomplish this by updating $\left[\tilde{K}_{i-1}^{NM}\right]^{-1}$ to $\left[\tilde{K}_i^{NM}\right]^{-1}$ using a product plus increment form:

$$\left[\tilde{K}_i^{MN}\right]^{-1} = \left[I^{NL} - \rho_i c_i^N \gamma_i^L\right] \left[\tilde{K}_{i-1}^{PL}\right]^{-1} \left[I^{PM} - \rho_i \gamma_i^P c_i^M\right] + \rho_i c_i^N c_i^M \tag{3.40}$$

where

$$\rho_i = \left(c_i^M \gamma_i^M\right)^{-1} \tag{3.41}$$

In the actual implementation of the BFGS method, each $\left[\tilde{K}_i^{MN}\right]^{-1}$ is not stored: rather, a kernel matrix, $\left[\tilde{K}_I^{MN}\right]^{-1}$, is used, and the update is accomplished by premultication of the kernel matrix by the terms:

$$\left[I^{NL} - \rho_j c_j^N \gamma_j^L\right] \tag{3.42}$$

and postmultication of the kernel matrix by the terms:

$$\left[I^{PM} - \rho_j \gamma_j^P c_j^M\right] \tag{3.43}$$

for j=I+1, I+2, ...i. Because of the form of these terms, the premultication and postmultication operations result in inner products of vectors and the scaling of vectors by constants: it is this organization that makes the method computationally attractive. However, too many such products are not attractive, so that usually a new kernel matrix is formed and stored after some iterations.

In general, the rate of convergence of the quasi-Newton method is slower than the quadratic rate of convergence of Newton's method, though faster than the linear rate of convergence of the modified Newton method.

When any iterative algorithm is applied to a history-dependent problem, the intermediate, nonconverged solutions obtained during the iteration process are usually not on the actual solution path; thus, the integration of history-dependent variables must be performed completely over the increment at each iteration and not obtained as the sum of intergations associated with each iteration, c_i. In ABAQUS this is done by assuming that the basic nodal variables, u, vary linearly over the increment, so that

$$u(\tau) = (1 - \frac{\tau}{\Delta t})u(t) + \frac{\tau}{\Delta t}u(t + \Delta t) \tag{3.44}$$

where $0 \leq \tau \leq \Delta t$ represents time during the increment. Then, for any history-dependent variable, g(t),

$$g(t + \Delta t) = g(t) + \int_t^{t+\delta t} \frac{dg}{d\tau}(\tau) d\tau \tag{3.45}$$

is calculated at each iteration.

The issue of choosing suitable time steps is a difficult problem to resolve. First of all, the considerations are quite different in static, dynamic or diffusion cases. It is always necessary to model the response as a function of time to some acceptable level of accuracy. In the case of dynamics or diffusion problems, time is a physical dimension for the problem, and the time stepping scheme must provide suitable steps to allow accurate modelling in this dimension. In contrast, most static problems have no imposed time scales, and the only criterion involved in time step choice is accuracy in modeling nonlinear effects.

3.2.2.3 Element library in ABAQUS

The ABAQUS element library provides a complete geometric modeling capability. For this reason any combination of elements can be used to make up the model. Shell and beam element properties can be defined as general section behaviours, or each cross-section of the element can be integrated numerically, so that nonlinear response can be tracked accurately when needed. A composite layered section can be specified, with different materials at different heights through the section. Some special elements (such as line springs) use an approximate analytical solution to model nonlinear behaviour.

All of the elements are formulated in global Cartesian coordinate system except the axisymmetric elements which are formulated in terms of r-z coordinates. In almost all elements, primary vector quantities (such as displacements $\mathbf{u}$ and rotations $\boldsymbol{\phi}$) are defined in terms of nodal values with scalar interpolation functions. For example, in elements with a two-dimensional topology the interpolation can be written as:

$$\mathbf{u}(g,h) = N^N(g,h)\mathbf{u}^N \tag{3.46}$$

where the interpolation functions $N^N(g,h)$ are written in terms of parametric coordinated g and h. In most element types the same parametric interpolation is also used for coordinate vector $\mathbf{x}$:

$$\mathbf{x}(g,h) = N^N(g,h)\mathbf{x}^N \tag{3.47}$$

Such isoparametric elements are guaranteeded to be able to represent all rigid body modes and homogeneous deformation modes exactly, a necessary condition for convergence to the exact solution as the mesh is refined.

All elements are integratedly numerically. Hence, the virtual work integral as described in equation(3.22) will be replaced by a summation:

$$\int_V \boldsymbol{\sigma} : \delta\mathbf{D} dV \qquad \rightarrow \sum_{i=1}^{n} \boldsymbol{\sigma}_i : \delta\mathbf{D}_i V_i \tag{3.48}$$

where n is the number of integration points in the element and V_i is the volume associated with integration point i. ABAQUS uses either full or reduced integration. For full integration the number of integration points is sufficient to integrate the virtual work expression exactly, at least for linear material behaviour. All triangular and tetrahedral elements use full integration. Reduced integration can be used for quadrilateral and hexahedral elements; in this procedure the number of integration points is sufficient to integrate exactly the contributions of the strain field that are one order less than the order of interpolation. The higher-order contributions to the strain field present in these elements will not be integrated.

The advantage of the reduced integration elements is that the strains and stresses are calculated at the locations that provide optimal accuracy, the so-called Barlow points [184].

A second advantage is that the reduced number of integration points decreases CPU time and storage requirements. The disadvantage is that the reduced integration procedure can admit deformation modes that cause no straining at the integration points. These zero-energy modes make the element rank-deficient and cause a phenomenon called hourglass, where the zero energy modes starts propagating through the mesh, leading to inaccurate solutions. This problem is particularly severe in first-order quadrilaterals and hexahedra. To prevent these excessive deformations, an additional artificial stiffness is added to the element. In this hourglass control procedure, a small artificial stiffness is associated with the zero-energy deformation modes. This procedure is used in many of the solid and shell elements in ABAQUS.

Most fully integrated solid elements are unsuitable for the analysis of (approximately) incompressible material behaviour. The reason for this is that the material behaviour forces the material to deform (approximately) without volume change. Fully integrated solid element meshes, and in particular lower-order element meshes, do not allow such deformations. For that reason ABAQUS uses selectively reduced integration in these elements: reduced integration is used for the volume strain and full integration for the deviatoric strains. As a consequence, the lower-order elements give an acceptable performance for approximately incompressible behaviour. For fully incompressible material behaviour, another complication occurs: the bulk modulus and, hence, the stiffness matrix becomes infinitely large. For this case a mixed (hybrid) formulation is required, where the displacement field is augmented with a hydrostatic pressure field. In this formulation only the inverse of the bulk modulus appears, and consequently the contribution to the operator matrix vanishes. The hydrostatic pressure field plays the role of a Lagrange multiplier field enforcing the incompressibility constraints.

ABAQUS also provides elements for multifield problems. Examples are the pore pressure elements used for the analysis of porous solids with fluid diffusion, thermally coupled elements that couple heat transfer with stress analysis, and piezoelectric elements that couple electrical conduction with stress analysis. In these multifield elements the scalar variable (such as temperature) is usually interpolated with different scalar functions as

the displacement field, that is:

$$T(g,h) = M^N(g,h)T^N \tag{3.49}$$

where $M^N(g,h)$ may differ from $N^N(g,h)$. The coupling of the field will generally occur at the integration points; for instance, in thermally coupled elements the coupling is due to temperature-dependent mechanical properties and heat generation is due to inelastic work. Finally, ABAQUS offers a complete set of diffusion elements to analyse conductive and convective heat transfer. In these elements only temperatures appear as nodal degrees of freedom. The temperatures are interpolated with essentially the same interpolation function, $M^N(g,h)$, as used in the thermally coupled elements.

Due to space limitation, only a couple of related element types, which were chosen for use in the study, are discussed here.

Axisymmetric elements

ABAQUS includes two libraries of solid elements, CAX and CGAX, whose geometry is axisymmetric and can be subjected to axially symmetric loading conditions. In addition, CGAX elements support torsion loading. As a result, CGAX elements are referred as generalised axisymmetric elements, and CAX elements as torsionless axisymmetric elements. If the loading consists of radial and axial components that are independent of θ and the material is either isotropic or orthotropic, with θ being a principal material direction, the displacement at any point will only have radial (u_r) and axial (u_z) components. Consequently, the geometric model is described by discretising the reference cross-section at $\theta = 0$.

Shear flexible small-strain shell elements

ABAQUS provides small-strain shear flexible thin shell elements such as quadrilateral S4R5, S8R5. The essential idea of these elements is that the position of a point in the

shell reference surface and the components of a vector –which is approximately normal to the reference surface – are interpolated independently. The thin shell elements may provide enhanced performance for large problems where reducing the number of degrees of freedom through the use of five degree of freedom shells is desirable. The Discrete Kirchhoff constraint is imposed in all thin shell elements.

Finite-strain shell elements

General purpose shell elements such as S3, S4, S4R provide robust and accurate solutions in all loading conditions for thin and thick shell problems. All of these elements consider finite membrane strains and are true doubly curved shells. The kinematic formulation of these shell elements is an approximate theory intended for application to problems involving finite membrane strains and large rotations. It is derived from the approximations discussed by Rodal and Witmer [185].

3.3 Automatic Mesh Generation from Clinically Obtained Data

Computational gridding is an essential part in performing the coupled simulation. Model reconstruction and grid generation for simple problem such as a straight tube is very straightforward. However, perfectly circular straight tubes do not exist in the human arterial system. Real arteries are much more complicated and model reconstruction and grid generation will be very complex because there is not only the difficulty of building a physical model but also the difficulty of the geometrical description of this model for a numerical simulation. So far two techniques have been widely employed to acquire vessel geometry. They are: ultrasound angiography (USA) and magnetic resonance imaging (MRI). Each has advantages and disadvantages when used to define vascular geometry (Table 3.1). The resultant 3D geometry data are organized in a format that allows for grid generation to be performed, which is essential for subsequent coupled modelling. This section describes details of grid generation.

Table 3.1: Comparison of MRI and USA for application to numerical modelling.

	MRI	USA
Non invasive angiogram	Yes	Yes
3D Velocity measurement	Easy	Difficult
Spatial resolution	Low(axial),high(plane)	High(axial), low(plane)
Temporal resolution	Low	High
On line imaging	No	Yes
Wall movement tracking	Difficult	Easy
Signal/noise	High	Low
Signal loss	Complex flow regions	Each cross-section image
Imaging region	No limit	Limited by scan window
3D reconstruction	Good	Errors in 3D registration, additional devices needed
Cost	High	Low
Patient acceptability	Difficult	Easy

3.3.1 Structures of computational grid for complex geometry domains

There are three basic types of computational grid in use:

(1) Single-block, fully structured grids,

(2) Multi-block structured grids,

(3) Unstructured grids.

Single-block, fully structured grids are traditionally used in FD/FV. They transform the physical space into a rectangular (or hexahedronal in 3-D) computational space. In complex geometry domains, to have accurate solutions, special techniques are required for gridding, such as multi-block structured grid and unstructured grids.

The multi-block approach is a very popular method of applying structured grids to complex geometrical regions. The physical domain is segmented into sub-regions, which constitute contiguous blocks. Each block has to be transformed into a hexahedron, so that several

local curvilinear systems are constructed and connected together. However, the global distortion of the grid is relatively less accentuated. Grid points at block interfaces have to be treated so that points at the common edge of any two adjacent blocks are continuous and so that slope continuity may be enforced. Multi-block grids are very powerful in that they allow the use of a wide range of mesh topology for a given configuration and different coordinate systems are allowed in each block. Although the concept of multi-block mesh is very attractive from a mesh generation point of view, additional complexities are introduced in the solution procedures, that involve a slow-down of the calculation time.

Unstructured meshes, traditionally used in FEM, are generally composed of triangles and/or arbitrary quadrilaterals in 2-D, and tetrahedra and/or hexahedra in 3-D. Therefore, the number of cells surrounding a typical node of the mesh is not the same. Techniques for the generation of unstructured meshes have been discussed by Peraire et al. [186].

The unstructured nature of the mesh requires a local coordinate system for each element. The resultant mesh, therefore, is poorly ordered and less amenable to the use of vectorization algorithms. Also larger computer time and storage are required in comparison with structured grids. However, unstructured meshes are more efficient in complex geometry domains, and offer the possibility of incorporating adaptivity. In order to minimise computer time requirements, renumbering strategies for unstructured grids have been proposed.

3.3.2 Geometry reconstruction and computational grid generation

Using MRI data

In our group, a set of purpose-built software has been developed to process MRI images, generate anatomically realistic 3D arterial models and computational grids [187, 35]. The existing program has been modified to allow the incorporation of the movement of the model surface and regeneration of the grid to ensure a uniform grid change within the whole fluid domain for use in the coupled model.

The key issue here is to define locations of points on the vessel surface. This is done via a sequence of 2-D cross-sectional images. Details are as follows:

- Images are processed to give smooth 2D cross-sectional contours, using the active contour or snake model. The MR imaging system guarantees these images are parallel, and related to one coordinate system.
- The 3-D vessel geometry is found by:
  - assembling all the 2-D images, in a 3D space using known distances between them.
  - smoothing the 3D surface of the resultant 3D image.
  - final surface rendering by using least-square cubic splines.
- Computational grids are generated based on the smooth 3-D surface obtained.

Using ultrasound data

Because only 2-D longitudinal images were available for the present study, assumption has to be made on circular symmetry for three vessels (common, internal and external carotid), with elliptic merging at bifurcation. The 2D US images are processed manually. Essentially, the software described above for processing MR images has been modified to deal with ultrasound images as well. Computer programs were developed for automatic generation of 3-D surfaces once the basic geometric parameters were entered. A schematic diagram for the input parameters is shown in Figure 3.4. Once the 3-D surface is defined, further specifications of axial direction and cross-plane grid densities are needed to establish interface with the program already developed for MR images. The procedure requires only basic geometrical data, such as vessel diameters at a number of locations in the axial direction, lengths and bifurcation angles. The generated grids are suitable for use with the computer simulation.

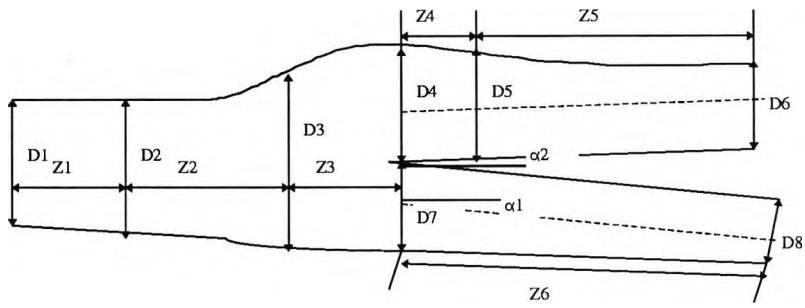

Figure 3.4: A schematic diagram for the input parameters obtained by USA.

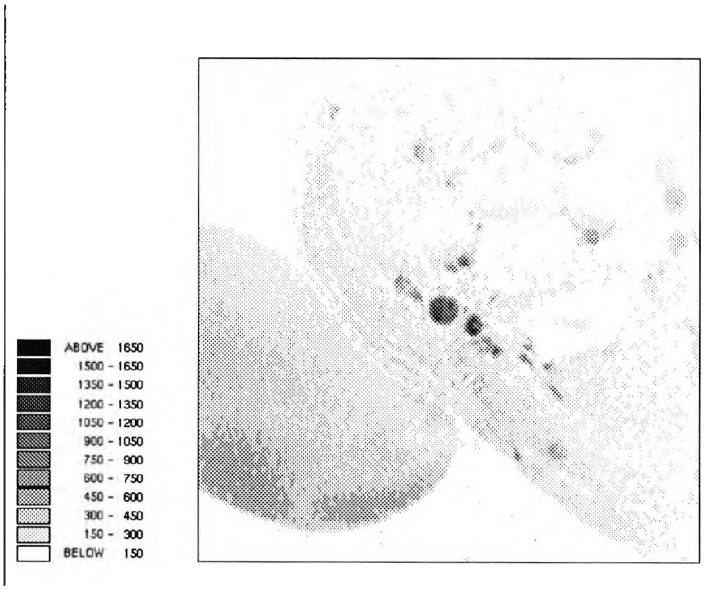

Figure 3.5: Typical original image from MR acquired in the carotid bifurcation of a human subject, where the dark circles are vessel cross-sections.

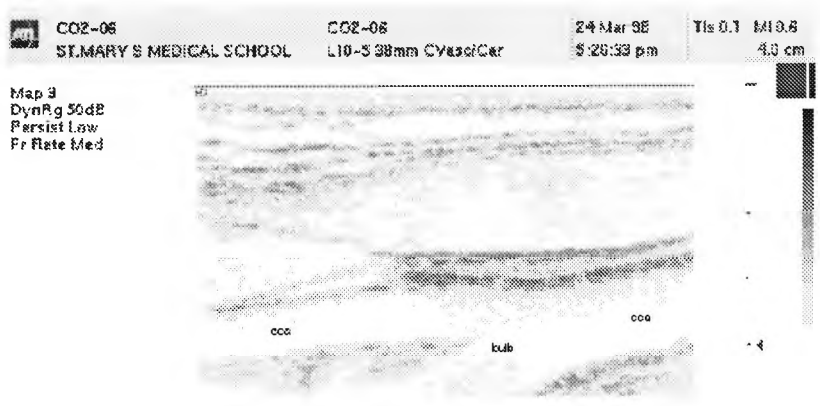

Figure 3.6: Typical original image from USA, where CCA, bulb, and ECA emphasize the region of interest and correspond to longitudinal locations in the vessel.

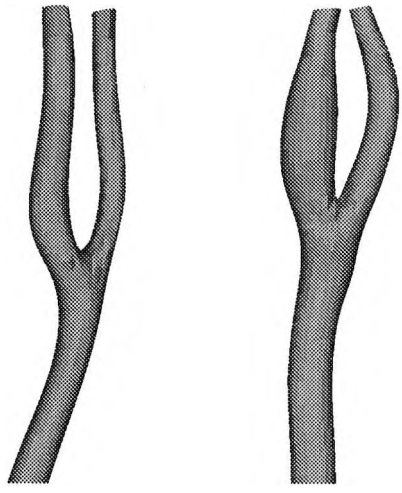

(a) (b)

Figure 3.7: Two human carotid bifurcations reconstructed from MRI.

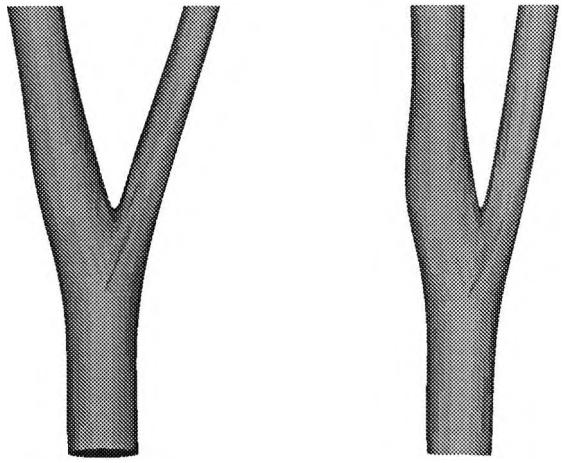

(a) (b)

Figure 3.8: Two human carotid bifurcations reconstructed from USA.

All the software referred to above was purpose-written, permitting mesh generation directly from clinical data. It thus forms a 'seamless' interface between *in vivo* measurements and the computer model (also velocity boundary condition data are needed).

Figures 3.5 and 3.6 show typical original images from MRI and USA respectively. The geometric models reconstructed from MR and USA for two subjects are shown in Figures 3.7 and 3.8.

So far, due to limitations of the current US technique and facility, only 2-D USA has been used. It is apparent that model geometries (from USA) tend to be simpler than their real arterial counter-parts (MRI). To reflect the real situation in the human body, 3-D ultrasound is being developed with a position sensor mounted on the scan header. For this purpose an extra stage of 'image registration' is required in three dimensions, to substitute for MRI digital control.

Computational grids for the wall mechanics calculations are simply the outer surface mapping of the flow domain. Logical locations at each node on the surface have to be stored to establish the link among surface nodes. The existing program has been modified in such a

way as to generate computational grids for both fluid and wall calculations simultaneously.

3.4 Convergence Technique

Having presented a computational, comprehensive coupled fluid-wall interaction dynamics model for the simulation of blood flow in arterial structures, this section discusses numerical convergence related to the coupled model.

3.4.1 Introduction

According to the interactive coupled approach presented in section 3.1, the time-dependent Navier-Stokes equations of the fluid are not explicitly assembled with the dynamics equilibrium equations of the wall, but instead an iterative procedure is used to obtain the solution. Combining two established commercial codes, CFX for fluid flow and ABAQUS for wall motion, this iterative algorithm preserves the nature of software modularity and offers a distinct advantage in that the most efficient codes for fluid flow and structural analysis can be used to deal with complex problems.

A convergence criterion has to be introduced to control the iterative procedure. This is based on the difference between displacements at two successive iterative cycles at each time step (DD), as defined in equation(3.1). Under this criterion, the convergence is achieved when there is little or no change in the position of interface surface at each time step. A similar convergence criterion has been adopted by Müller and Jacob [171], while Hofer et al. [148] employed a different criterion based on the difference in successive velocities.

3.4.2 Numerical simulations

Numerical predictions were carried out for pulsatile flows in three compliant models of human carotid artery bifurcations (Figure 3.9) to demonstrate the validity and the convergence characteristics of the proposed coupled scheme. The first two bifurcation geometries

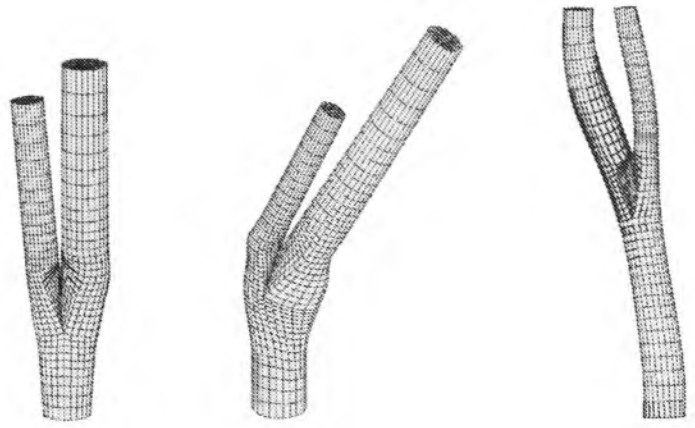

(a) Model 1 (b) Model 2 (c) Model 3

Figure 3.9: Geometries of the three carotid bifurcation models.

were based on ultrasound images. The software described in the preceding section was used to generate 3-D surfaces automatically using the key geometric parameters. Based on the 3-D surface data together with further specification of grid densities in the axial direction, and cross-planes, the program automatically generated the computational mesh. The third numerical model was generated from MRA images, again with the use of the grid generation software.

The configurations were defined as the diastolic reference geometry. The essential geometric parameters are as follows: Model 1: common carotid diameter is 6.25mm, maximum sinus diameter is 6.0mm, internal carotid diameter is 6.0mm, external diameter is 4.3mm, angle between internal and external axes is 5^0; Model 2: common carotid diameter is 6.0mm, maximum sinus diameter is 6.2mm, internal carotid diameter is 4.3mm, external diameter is 3.3mm, angle between the common and internal axes is 30^0 and angle between the common and external axes is 25^0; Model 3: common carotid diameter is 5.9mm, internal carotid diameter is 4.6mm, external diameter is 3.2mm. As the last model is reconstructed from *in vivo* MR angiogram, there is no symmetric plane as in the first two cases.

The nonlinear behaviour of the artery wall has been approximated, by assuming it to be incrementally linearly elastic over the pressure range from the diastolic level to systolic phase [42]. The incremental elastic modulus of the arterial wall is $5x10^5$ Pa, which was chosen according to the range suggested by Fung [82] for the human carotid artery. The thickness (h) of the carotid artery walls is 8-10% of the vessel diameters [188] which are 0.5mm, 0.5mm, and 0.45mm respectively for the three models. To prevent rigid body motion, the ends of the model were constrained against motion. The flow domain discretizations result in 12,960, 12,960, and 20,480 eight-noded brick elements and the wall discretizations yield 1,798, 1,798, and 2,560 four-noded shell elements respectively for the three models. Flow waveforms obtained from Perktold and Rappitsch [42] were applied as the time-dependent boundary conditions. The flow pulse waveform at the common carotid inlet and the external carotid outlet as well as the pressure pulse waveform at the internal carotid outflow boundary are shown in Figure 3.10. As the boundary conditions used do not correspond to the individual models studied here, these calculations were meant to demonstrate the coupled method and convergence technique rather than to simulate the real cases.

3.4.3 Convergence technique

The coupling for a fluid/solid problem is not a trivial task and several difficult issues related to both theory and implementation aspects may arise. The problem of convergence within the calculations of each single code lies in the scope of the code itself. However, the convergence behaviour between the codes has to be monitored and controlled for a coupled solution. Preliminary calculations for the first two models reached converged states after six to seven iterations between the codes without the aid of any special techniques. However, convergence difficulty has been encountered for the third model. A summary of the convergence behaviour for the three coupled models is given in Table 3.2.

The calculations show that it is necessary to introduce a relaxation factor because during

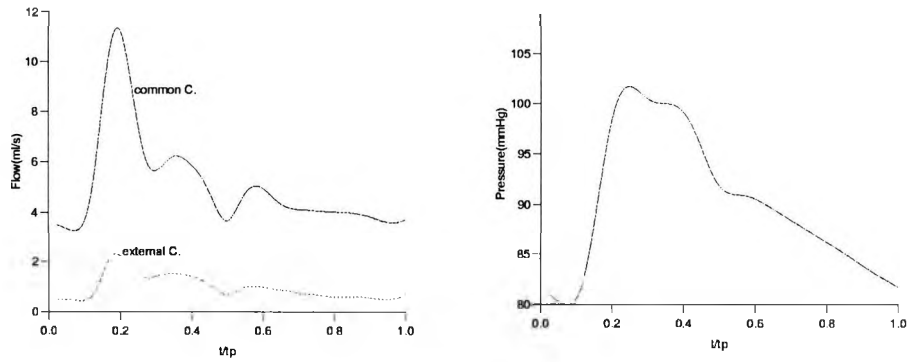

(a) (b)

Figure 3.10: Boundary conditions for the calculations. (a) Flow pulse waveforms in the common and external carotid artery (b) Pressure pulse waveform in the internal carotid artery, tp being the cycle period.

Table 3.2: Summary of the convergence behaviour for the three coupled models.

Iteration	1-2	2-3	3-4	4-5	5-6	6-7
MODEL 1 DD(%)	91.0	13.7	3.5	1.8	1.1	
MODEL 2 DD(%)	187.89	172.79	46.96	12.88	4.64	2.33
MODEL 3 DD(%)	317.22	221.38	174.57	152.44	124.31	103.04

Table 3.3: Convergence behaviour of the coupled model 3 under a relaxation factor of 0.5.

Iteration	1-2	2-3	3-4	4-5	5-6	6-7	7-8
DD(%)	159.63	48.14	27.19	12.38	6.63	4.44	2.61

Table 3.4: Convergence behaviour of the coupled model 1 after mesh refinement.

Iteration	1-2	2-3	3-4	4-5	5-6
DD(%)	68.32	14.99	4.21	1.92	1.03

the calculations the fluid domain geometry tends to converge very slowly if the total geometric deformation as a result of the structural analysis is fed in as the new geometry. Under-relaxation has several interlinked purposes in the solution process. The relaxation factor is introduced to reduce the calculated deformations to a certain amount. In this way, difficulties caused by instability are overcome. Thus the stable state is reached under a relaxation factor (Table 3.3) which is set to 0.5. It can be seen that with a relaxation factor, convergence is obtained after 6 iterations between the two codes.

Furthermore, to test both temporal and spatial resolutions, mesh and time-step refinement experiments are carried out on the first model. Firstly, the mesh number was nearly doubled (total computational cells in the fluid domain was 12,960 and 25,200 before and after the refinement, total node number in the arterial wall was 1,798 and 3,430 respectively.) Before the mesh refinement, the calculated maximum displacement is 0.547mm. After the refinement, the maximum displacement is predicted to be 0.562mm, a difference of 2.7%. The convergence process is given in Table 3.4.

Secondly, regarding to the temporal resolution, the number of time steps was increased from 40 to 80 per cardiac cycle. However, for the time step refinement, convergence difficulty was again encountered. Tables 3.5 & 3.6 give the convergence process before and after relaxation. For a total of 40 time steps, the calculated maximum displacement is 0.547mm. For 80 time steps, the maximum displacement is 0.5427mm, showing a differ-

Table 3.5: Convergence behaviour of the coupled model 1 after time step refinement without relaxation.

Iteration	1-2	2-3	3-4	4-5	5-6	6-7
DD(%)	102.07	128.00	189.70	399.38	894.47	1415.67

Table 3.6: Convergence behaviour of the coupled model 1 after time step refinement with a relaxation factor of 0.5.

Iteration	1-2	2-3	3-4	4-5	5-6	6-7	7-8
DD(%)	79.36	32.53	20.49	12.07	6.83	4.22	1.94

ence of 0.73% only.

The convergence history of the maximum displacement point without and with relaxation are plotted in Figures 3.11 & 3.12 respectively. To verify the relaxation scheme, time-dependent displacement at the maximum displacement point is compared before and after the time step refinement with a relaxation factor as shown in Figure 3.13. Comparison

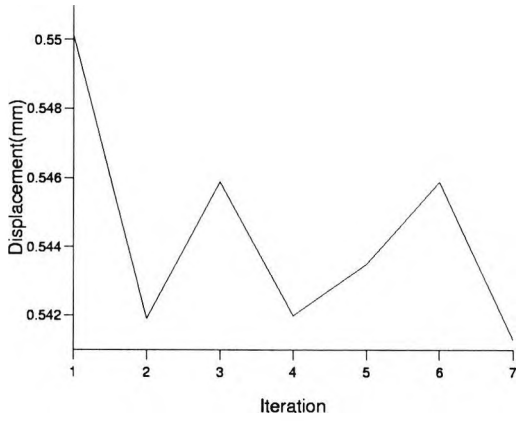

Figure 3.11: Oscillating geometry at the maximum displacement point of model 1 without relaxation.

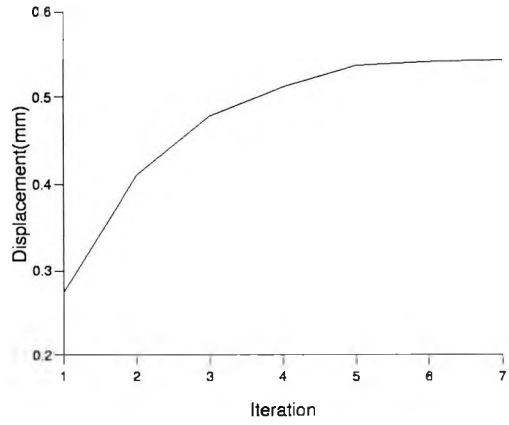

Figure 3.12: Converging geometry at the maximum displacement point of model 1 with a relaxation of factor 0.5.

Table 3.7: Wall shear stress comparison between coupled model and its corresponding rigid model (N m^{-2})–Model 1.

	Rigid model	Coupled model
Max W.S.S.	18.52	16.06
Max time-averaged W.S.S.	6.78	6.47
Min time-averaged W.S.S.	0.18	0.17

is also given of a time-dependent displacement component at node 174, which is near the apex of the bifurcation and was chosen randomly to check the accuracy of the results, for a total number of time steps of 40 and 80 (Figure 3.14). During the second half of the cycle minor oscillation can be noticed. This is due to the computational accuracy as the displacement is very small at this site. In fact, the total displacement of this point does not show any oscillation at all (Figure 3.15). Very good agreement has been achieved between predictions obtained with and without under-relaxation for both the maximum displacement point (Figure 3.13) and the small displacement point (Figure 3.15).

Comparisons of time-dependent wall shear stress were also made at four selected points

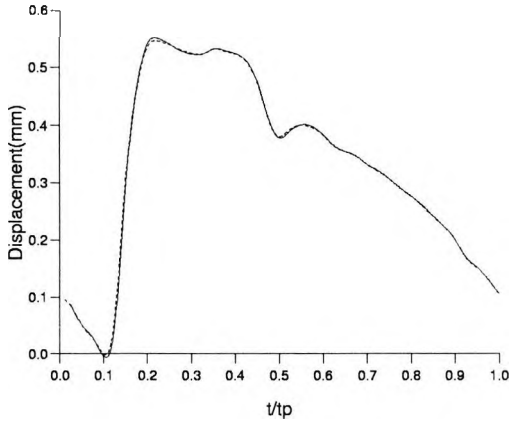

Figure 3.13: Comparison of displacement at the maximum displacement point of model 1 before time step refinement without relaxation factor (solid line) and after time step refinement with a relaxation factor of 0.5 (dashed line).

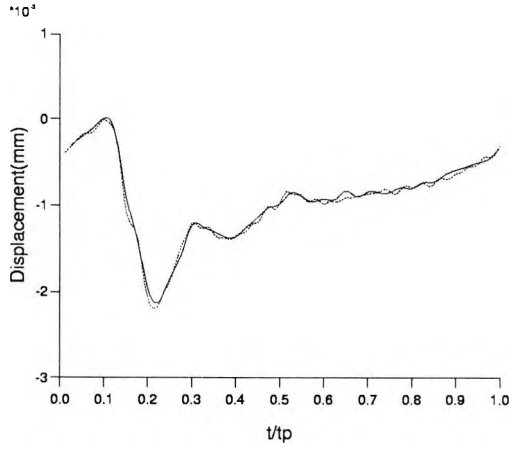

Figure 3.14: Comparison of one of the displacement components at a point near the apex of bifurcation model 1 before time step refinement without relaxation factor (solid line) and after time step refinement with a relaxation factor of 0.5 (dashed line).

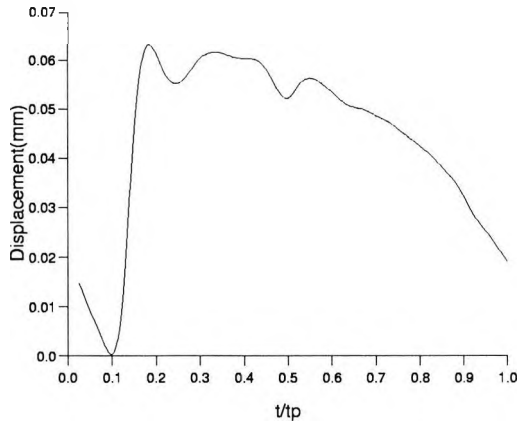

Figure 3.15: The total displacement of the same point as in Figure 3.14.

Table 3.8: Wall shear stress comparison between coupled model and its corresponding rigid model (N m^{-2})–Model 2.

	Rigid model	Coupled model
Max W.S.S.	22.35	16.86
Max time-averaged W.S.S.	8.00	7.09
Min time-averaged W.S.S.	0.18	0.15

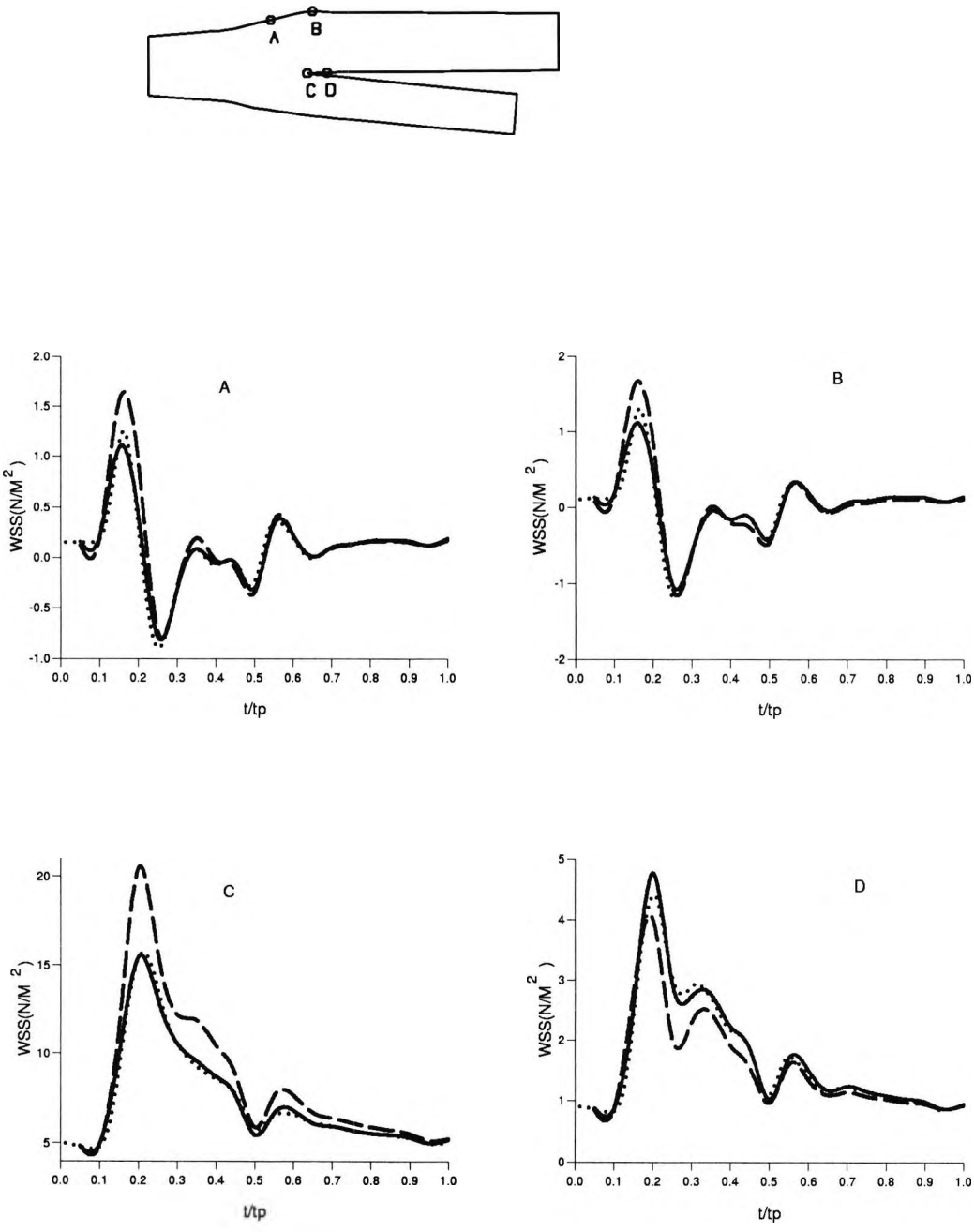

Figure 3.16: Wall shear stress comparisons at four selected points of model 1 before time step refinement without relaxation factor (solid line), after time step refinement with a relaxation factor of 0.5 (dotted line) and in the rigid model (dashed line).

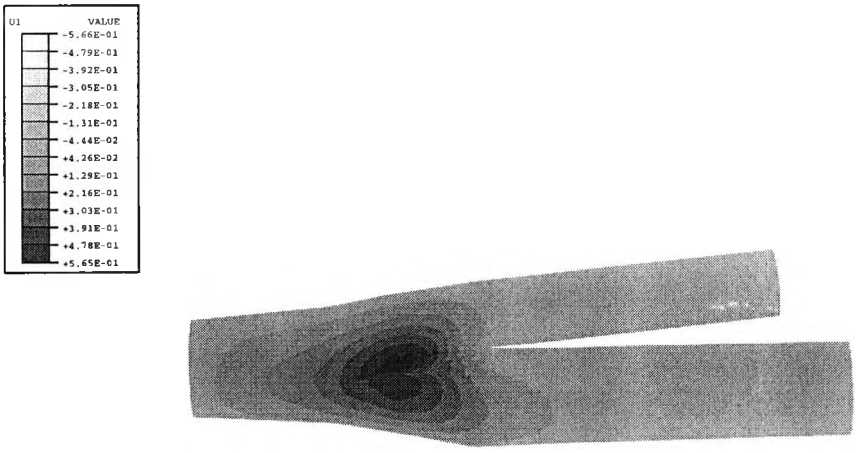

Figure 3.17: Displacement distribution (mm) at the pulse phase of maximum pressure load–Model 1.

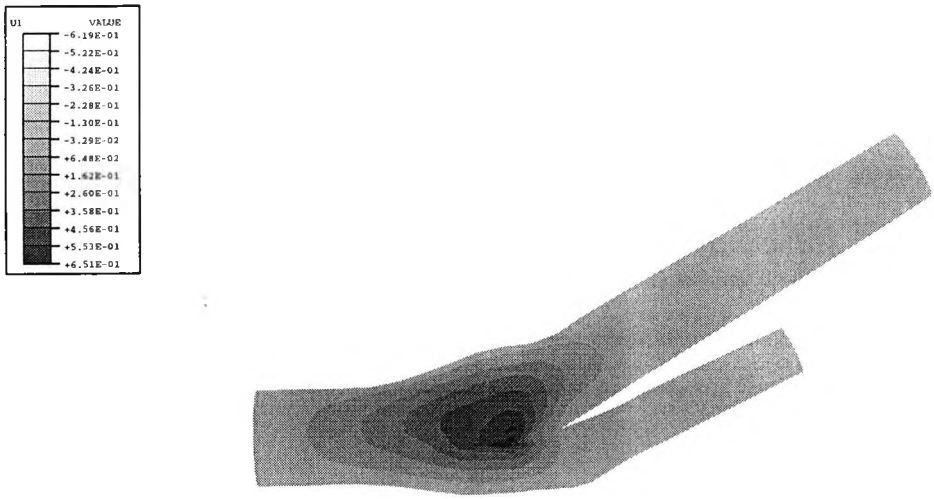

Figure 3.18: Displacement distribution (mm)at the pulse phase of maximum pressure load–Model 2.

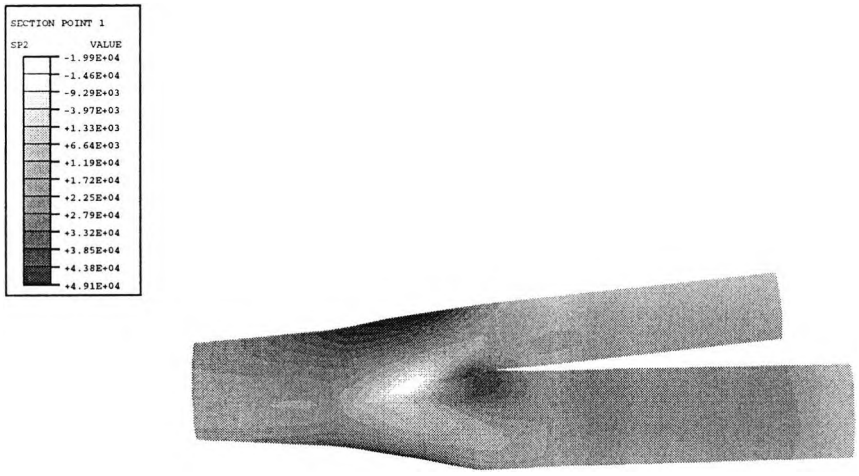

Figure 3.19: Maximum principal stress distribution (Pa) at the inner surface at the pulse phase of maximum pressure load–Model 1.

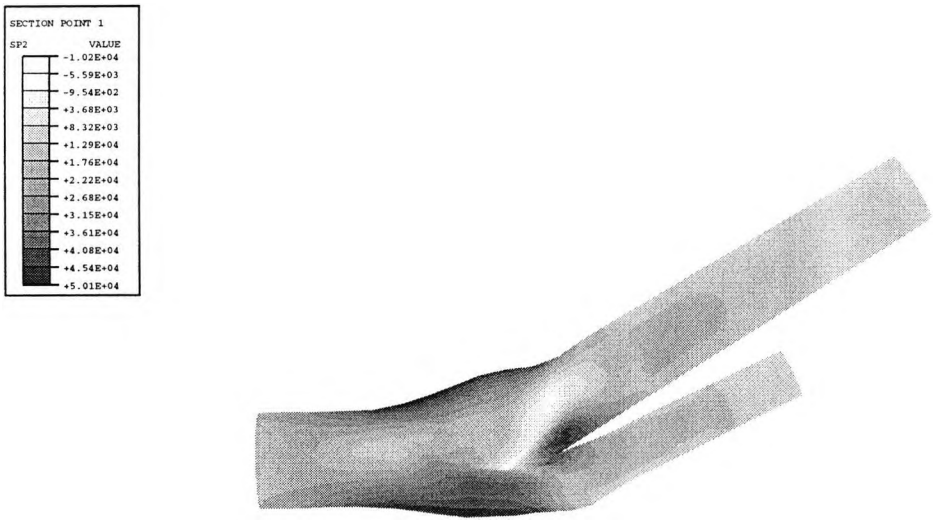

Figure 3.20: Maximum principal stress distribution (Pa) at the inner surface at the pulse phase of maximum pressure load–Model 2.

(A, B,C, and D) (Figure 3.16). Generally the results indicate very low wall shear stresses which changed direction and magnitude during the cycle at the outer wall of the sinus, and relatively large and unidirectional wall shear stresses at the apex and the inner wall of the sinus. As can be seen, the results before and after the time step refinement are quite close, while significant differences exist between the coupled model and its corresponding rigid model. The quantitative influences of the wall distensibility on wall shear stress for the first two models are given in Tables 3.7 & 3.8. The effect of wall compliance on flow patterns and wall shear stress in realistic carotid bifurcation models will be discussed in detail in chapter 5.

Since this section focuses on problems associated with convergence of coupled computations, neither detailed flow data nor arterial transmural stresses are given. However, the predictions provide all these information. Because the predicted flow patterns exhibit features which are consistent with previous simplified symmetric carotid model studies [164, 42], it is not intended to show them here. Figures 3.17 and 3.18 show the displacement distributions at the pulse phase of maximum pressure. In both models the maximum displacements are observed at the intersections between the two branches. The maximum principal stress distributions at the inner wall at maximum pressure load are presented in Figures 3.19 and 3.20. At the side wall of the bifurcation region a zone of low stresses is found in both cases. It is interesting to note that in this zone the maximum deformation occurs. The patterns of deformation and principal stress are in agreement with published data on simplified models [42, 148] in some essential features such as "stretchless membrane deformation".

3.4.4 Summary

The convergence problem, an important issue arising from coupled fluid/solid computations, has been discussed in detail. A number of numerical experiments have been performed to test the convergence of the iterative procedure implemented. In some cases it is necessary to introduce a relaxation factor in order to avoid oscillatory or even divergent solutions. It is found that by updating the deformations incrementally, the dynamic loads

resulting from the flowing fluid would not change drastically. This relaxation method assimilates a fraction of the geometric deformation that are relaxed from their full values at each update interval, so that a stable state could be reached. The proposed iterative coupling scheme can also be used for solving a wide range of engineering problems involving fluid/solid interactions. Numerical examples have been presented to demonstrate the validity of the coupled scheme and relaxation technique. Unfortunately, a general theory does not exist to establish the overall convergence of a coupled model. The convergence behaviour is very much case-dependent.

Chapter 4

Benchmark Tests

In order to be able to rely on the numerically predicted results, computer codes have to be validated carefully. Analytical solutions of simple problems may be used to test the numerical predictions. As mentioned in chapter 3, the coupled model involves the use of a computational fluid dynamics code CFX and structural analysis code ABAQUS. A comprehensive set of code validation exercises to related problems will be discussed in detail in this chapter.

For code validation purpose, a simple structure–circular tube is adopted in most of the exercises, because analytical solution is usually available for such a simple geometry. Firstly a decoupled treatment (a)unsteady flows in a semi-infinite contracting or expanding tube, and (b) an incompressible elastic tube under uniform internal pressure, was considered. Then the Womersley problem of oscillating flow in an elastic tube was studied to test the fluid/solid coupling algorithm.

4.1 Decoupled Moving Wall Test (CFX)–unsteady flows in a semi-infinite contracting/expanding tube

It is necessary to test the capability of moving boundary algorithm in CFX because this feature will be used throughout the coupled model. For this purpose unsteady flows of an incompressible viscous fluid through a semi-infinite contracting/expanding pipe were

considered as an analytical solution to this problem has been developed by Uchida and Aoki [189]. Their solution was based on the full Navier-Stokes equations for unsteady flow in a semi-infinite tube with a contracting or expanding wall at low Reynolds numbers. Although the model is restricted to a type of wall motion that does not represent well in the vascular system, it offers some definitely useful features. For example, it is not restricted to small wall displacements. Within CFX the three-dimensional momentum and mass conservation equations have been modified to allow both the grid and solution domain boundaries to move in some prescribed manner by a user-defined subroutine, which allows the user to define a grid or to specify movement of the grid with time.

4.1.1 Analytical solution

In this problem, the flow is driven by a single expansion or contraction of the wall with initial radius of a_0, moving at the temporal function of the radius a(t) :

$$a/a_0 = \sqrt{1 + 2\alpha(\nu t/a_0^2)} \tag{4.1}$$

A full solution of the Navier-Stokes equations similar both in space and time has been derived. By introducing a non-dimensional diameter $\alpha(t) = \dot{a}a/\nu$, $\dot{a}$ is the velocity of the wall ($\dot{a} = da/dt$), ν is the kinematic viscosity and further assuming that α is constant representing the dynamic scale of the wall motion, a similar solution for axial and radial velocity distributions can be expressed as follows:

Axial velocity

$$\frac{u}{u_m} = -(2\alpha)^{-1}(F'/\eta) \tag{4.2}$$

Radial velocity

$$\frac{v}{v_w} = \frac{v}{\dot{a}} = -\alpha^{-1}(F/\eta) \tag{4.3}$$

Wall shearing stress along the wall is given by:

$$\frac{\tau_w}{\rho\nu^2/a_0^2} = (F'')_{\eta=1}\frac{x}{a_0}\left(\frac{a}{a_0}\right)^{-3} \tag{4.4}$$

Where the non-dimensional radius $\eta = r/a$ with r denoting the radial distance, mean flow velocity u_m and the expansion rate of the wall radius $\dot{a}$ are given by

$$\frac{u_m}{\nu/a_0} = \frac{-2\alpha}{1+2\alpha(\nu t/a_0^2)}\frac{x}{a_0} \tag{4.5}$$

$$\dot{a} = \frac{\alpha\nu}{a_0}[1+2\alpha(\nu t/{a_0}^2)]^{-\frac{1}{2}} \tag{4.6}$$

with x being the axial distance from the closed end. $F(\eta)$ is calculated by numerical integration of the following equation:

$$(\frac{F'}{\eta})'' + (\frac{1}{\eta}+\frac{F}{\eta}+\alpha\eta)(\frac{F'}{\eta})' - (\frac{F'}{\eta}-2\alpha)\frac{F'}{\eta} = K \tag{4.7}$$

Since equation(4.7) is singular at the origin, for the region $0 \leq \eta \leq 0.01$, $F(\eta)$ can be calculated from the power series:

$$F(\eta) = b_2\eta^2 + b_4\eta^4 + b_6\eta^6 + b_8\eta^8 + ... \tag{4.8}$$

where

$$b_4 = \frac{1}{16}[K+4(b_2-\alpha)b_2] \quad b_6 = \frac{1}{12}(b_2-2\alpha)b_4 \quad b_8 = -\frac{1}{72}(9\alpha b_6 - 2b_4^2) \tag{4.9}$$

and for n≥2

$$b_{2n+4} = -\{[(2n-4)b_2 + (2n+2)\alpha](2n+2)b_{2n+2} + \sum_{1}^{n-1}(2n-2-4m)(2n+2-2m)b_{2m+2}b_{2n+2-2m}\}/(2n+2)^2(2n+4) \quad (4.10)$$

Values of b_2 and K are determined to satisfy the boundary conditions at $\eta = 1$, i.e., the radial velocity of fluid at the wall is equal to the wall velocity expressed in the transformed form:

$$F/\eta = 0, (F_\eta/\eta)_\eta = 0 \quad at \quad \eta = 0 \quad (4.11)$$

$$F/\eta = -\alpha, F_\eta/\eta = 0, \quad at \quad \eta = 1 \quad (4.12)$$

Assuming values of b_2 and K, the function F is calculated from this power series from η=0 to η=0.01, where the calculation is continued by numerical intergration by the Runge-Kutta-Gill method up to η=1.

4.1.2 Numerical predictions

In the analytical solution, the semi-infinite tube is closed at one end by an idealized elastic membrane which prevents only axial motion of the fluid, while leaving radial motion completely free. In the numerical modelling, this membrane was prescribed as a plane of symmetry. The initial tube diameter was set to be 10mm, and its length 15 times the initial diameter. The wall moved in a manner defined in equation(4.1). The kinematic viscosity ν of $4X10^3m^2/s$ was used. The tube outlet was set to be a surface of constant pressure. While this was an obvious approximation, it was found not to affect the final velocity profiles away from the tube. The predicted results have been plotted at mid-length of the tube. In the study both contraction and expansion have been modelled at different Reynolds numbers. The parameter α, defined as $\dot{a}a/\nu$, is the Reynolds number which represents the dynamical scale of the wall motion and is different from the conventional

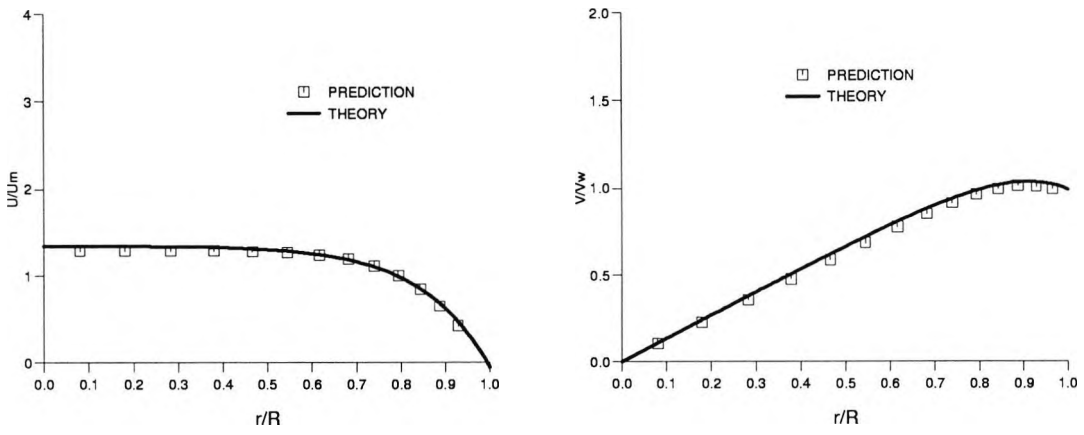

(a) (b)

Figure 4.1: Comparisons of the distributions of (a) axial, and (b) radial velocity in an contracting tube with Re=-10.0, and simulation time of 0.1s.

definition in tube flow. Thus, contracting and expanding pipes have $\alpha < 0$ and $\alpha > 0$ respectively.

Contraction with Re=-10.0

The selected time increment is 3.125ms. For this case, the agreement is very satisfactory as shown in Figure 4.1 with a simulation time of 0.1s. An extreme case has also been considered with a simulation time of 0.3s which represents a state where the contraction is down to nearly complete collapse of the tube to zero diameter. As shown in Figure 4.2, the distribution of the axial velocity is monotonic and the effect of viscosity is limited to a thin layer attached to the wall, implying that CFX performs very well even in extreme cases. Comparison for wall shear stress between the predicted and analytical results along the wall is shown in Figure 4.3. Again good agreement has been achieved.

Expansion with Re=1.0

The selected time step is 20ms. A simulation time of 1.0s has been chosen mainly to see whether a similar solution could be achieved over the time scale of the cardiac cycle period.

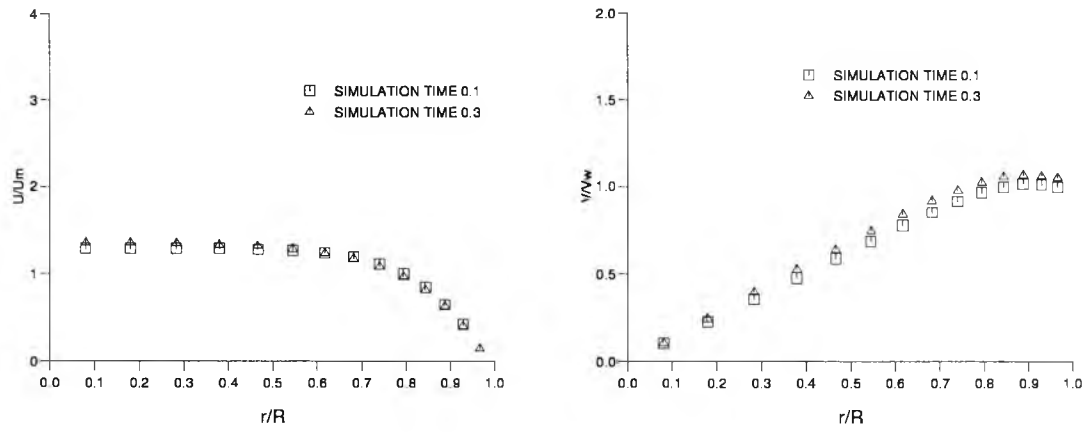

(a) (b)

Figure 4.2: Comparisons of the distributions of (a) axial, and (b) radial velocity in an contracting tube with Re=-10.0, between simulation time of 0.1s and simulation time of 0.3s.

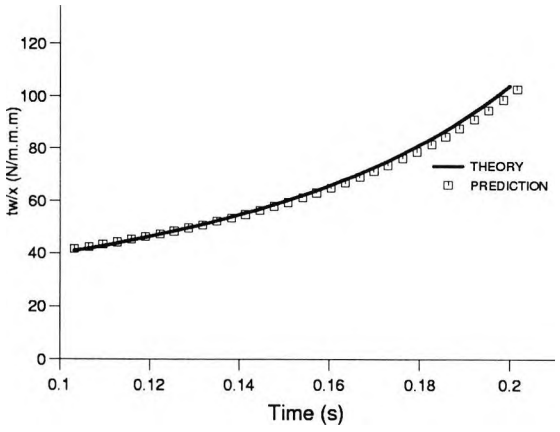

Figure 4.3: Comparisons of wall stress stress along the wall in an contracting tube with Re=-10.0.

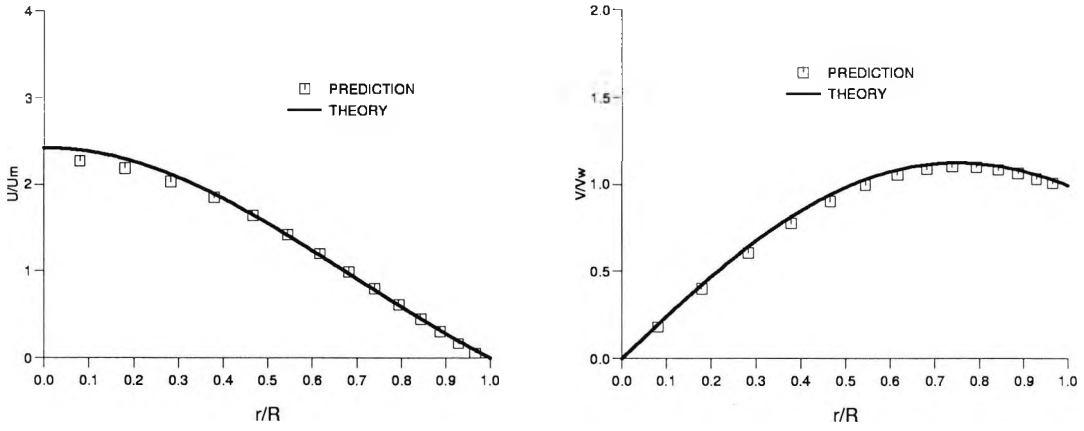

(a) (b)

Figure 4.4: Comparisons of the distributions of (a) axial, and (b) radial velocity in an expanding tube with Re=1.0, and time step of 20ms.

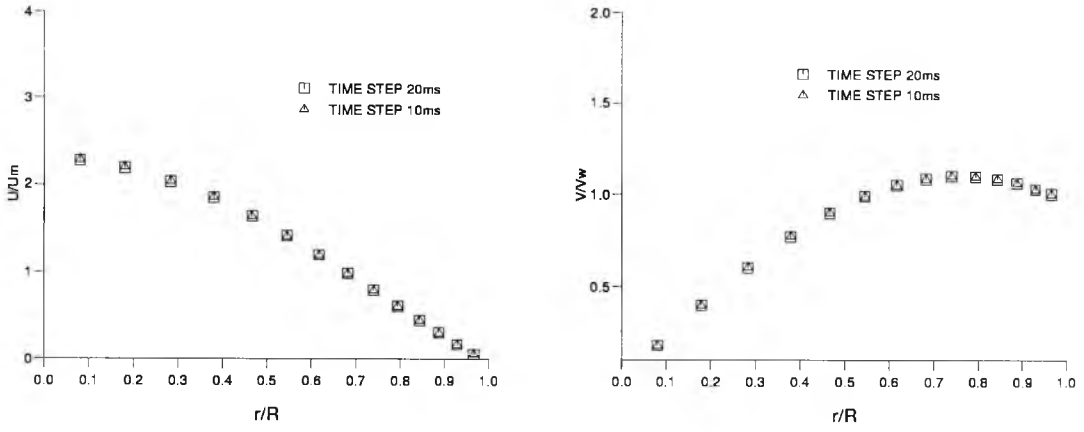

(a) (b)

Figure 4.5: Comparisons of the distributions of (a) axial, and (b) radial velocity in an expanding tube with Re=1.0, between time step of 10ms and time step of 20ms.

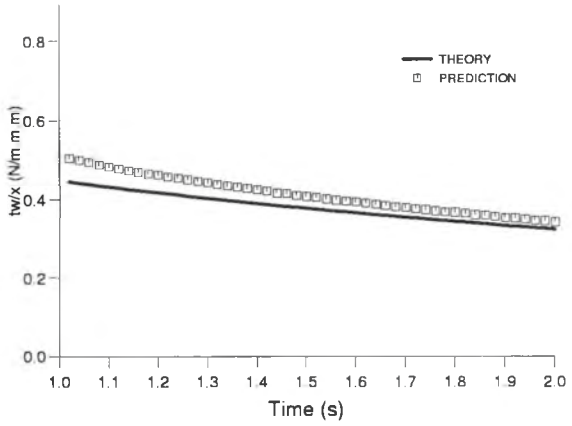

Figure 4.6: Comparisons of wall stress stress along the wall in an expanding tube with Re=1.0.

Also very good agreement between the predicted and analytical results has been achieved (Figure 4.4). It can be noticed that the axial velocity distribution approaches a parabolic distribution while the radial distribution falls to zero at the centre of the tube. A refined time step of 10ms has also been chosen to see if the predicted results are time-step dependent. From Figure 4.5, it can be seen that the predicted results for both cases are almost identical. Comparison of wall shear stress along the wall is also given (Figure 4.6). It can be noted that as time proceeds, that is when the initial guess influence in the numerical calculation becomes less, the predicted wall shear stress converges to that of the theory.

In this section, a validation exercise of the moving wall capability of CFX has been presented. Predicted velocity profiles and wall shear stress in an expanding/contracting semi-infinite tube have been compared with the analytical solutions. Very good agreement between the predictions and theoretical solutions has been achieved.

4.2 Decoupled Solid Wall Movement Test (ABAQUS)— deformation of an incompressible elastic tube

Another indispensable part of the couple model involves the prediction of wall movement under internal pressure. In this section, the case where the middle surface is a surface of revolution, including technically important problems relating to cylindrical shells will be dealt with. To test ABAQUS's capability of predicting the wall motion, the problems of an incompressible elastic tube under uniform internal pressure of (a) infinite length with free ends and (b) finite length with fixed ends are considered. Again this is because analytical solutions of displacement and stress field for both problems are available and can be used for the validation purpose.

4.2.1 Long elastic tube with free ends

First, consider the case of a tube with infinite length and free ends. In general, structural analysis consists of finding the stresses, and the displacements in an elastic body subjected to surface forces, surface displacements and body forces. There are six components of the state of stress at each point, and the three equations of equilibrium are not sufficient to obtain the solution of the problem. Additional equations are therefore introduced, these include six stress-strain relations together with six strain-displacement relations, making a total of 15 equations with 15 unknowns (σ_{ij}, e_{ij}, d_i). To ensure a unique value of the displacement components at each point, the strains must satisfy the compatibility relations. The original 15 equations can be reduced to three equations in terms of the components of the displacement. By introducing Lame strain potential ϕ, a variety of solutions satisfying practical boundary conditions can be generated from this parameter, such as the case of infinite length tube considered here. As a plane stress state, no axial boundary conditions are needed. Consider the strain function :

$$\phi = C \ln \frac{r}{K} \tag{4.13}$$

where r is the radial distance, C and K are constants to be determined by boundary con-

ditions.

The boundary conditions for the problem are :

$$\sigma_{rr} = -P \quad at \quad internal \quad radius; \qquad \sigma_{rr} = 0 \quad at \quad external \quad radius \qquad \sigma_{zz} = 0 \tag{4.14}$$

Together with the axial strain e_{zz}= constant which is required by symmetry yields the following displacement and stress fields [190]:

Radial displacement:

$$d_r = \frac{a^2 P}{E(b^2 - a^2)}[\frac{(1+\mu)b^2}{r} + (1-\mu)r] \tag{4.15}$$

Circumferential displacement:

$$d_\theta = 0 \tag{4.16}$$

Axial displacement:

$$d_z = \frac{2\mu}{E}\frac{Pa^2}{a^2 - b^2}z \tag{4.17}$$

Radial stress:

$$\sigma_{rr} = \frac{a^2 P}{b^2 - a^2}\left(1 - \frac{b^2}{r^2}\right) \tag{4.18}$$

Circumferential stress

$$\sigma_{\theta\theta} = \frac{a^2 P}{b^2 - a^2}\left(1 + \frac{b^2}{r^2}\right) \tag{4.19}$$

Axial stress:

$$\sigma_{zz} = 0 \tag{4.20}$$

with a, b being internal and external radii, and E, μ the Young's modulus and Poisson's ratio of the tube material. P is the applied internal pressure. r and z are radial and axial positions on the tube.

The problem considered is that of a tube with internal diameter of 10mm, and a wall thickness of 1.0mm. Young's modulus and density of the wall are taken to be $5X10^5$ Pa and $1.0X10^3 kg/m^3$ respectively. A Poisson's ratio of 0.49 is used to model the incompressibility of the wall material. The internal pressure is set to 2668Pa, which is within the range of physiological pressure variations.

Because of simplicity of the geometry, an axisymmetric solid element CAX4H is used. In the numerical calculation, the tube is divided into 20 elements in the axial direction and 9 elements in the radial direction. One end of the tube is constrained in the axial direction to prevent any rigid body movement, while the other end remains absolutely free.

Figure 4.7 and 4.8 show the comparisons of radial and axial displacement calculated using the analytical solution of equations(4.15) and (4.17) and predictions using ABAQUS. Predicted and analytical distributions of radial and circumferential stresses are given in Figure 4.9. In each case the agreement between the prediction and analytical solution is very good.

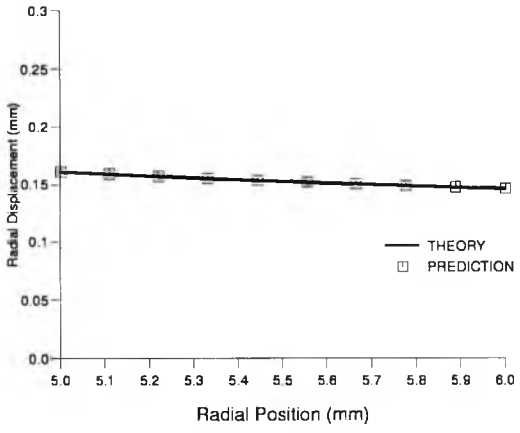

Figure 4.7: Comparisons of the analytical and predicted radial displacement in a tube under uniform pressure with free ends.

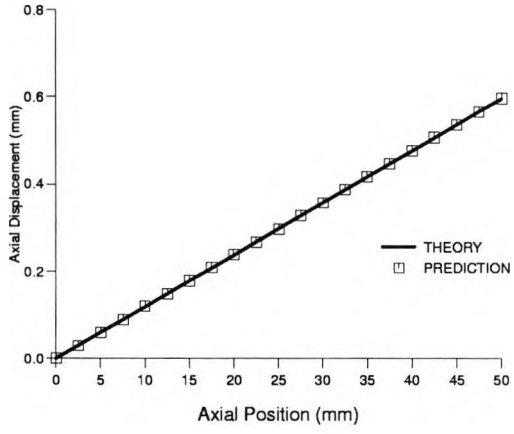

Figure 4.8: Comparisons of the analytical and predicted axial displacement in a tube under uniform pressure with free ends.

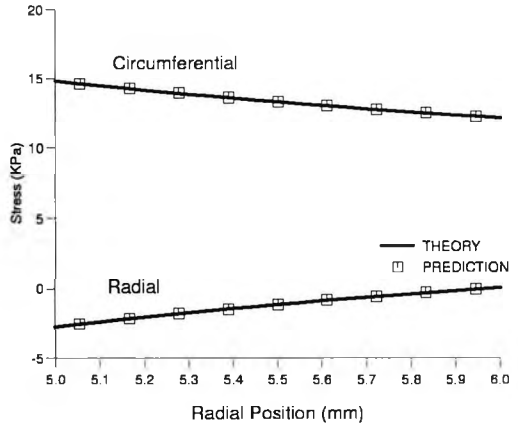

Figure 4.9: Comparisons of the analytical and predicted stresses in a tube under uniform pressure with free ends.

4.2.2 Finite-length elastic tube with fixed ends

Then, the tube is assumed to be of finite length with fixed ends. The internal actions between the parts of a shell are best expressed in terms of stress-resultants and stress-couples reckoned across the whole thickness. The equations of equilibrium, subjected to external forces, are a set of six equations connecting the six stress-resultants and the four stress-couples with the displacements. It is clear that, when the boundary conditions are suitable, solutions can be obtained which are sufficiently accurate for practical purposes, by omitting those values of small orders. When all the conditions are symmetrical about the axis, and torsion is not dealt with, a specific extensional solution can be expressed as:

$$W = a\nu\frac{dU}{dz} + a^2\frac{1-\nu^2}{Eh}R' \tag{4.21}$$

$$U = a_2 + \frac{a_1 z}{1-\nu^2} - \frac{1}{Eh}\int_0^z\int_0^z Z'dzdz - \frac{\nu a}{Eh}\int_0^z R'dz \tag{4.22}$$

where a_1 and a_2 are arbitrary constants. Z' and R' are the components parallel to the axes of axial z and radial r of the force of the externally applied forces estimated per unit

of area of the middle surface. ν is Poisson's ratio, and W, U are radial and axial displacements. It appears that by means of the extensional solution the external forces can be eliminated, but in general the boundary conditions at the edges can not be satisfied. For example, the problem of a tube strained by external pressure and plugged at ends cannot be solved. In such problems the stress-resultants do not vanish.

Consider another specific solution expressed as:

$$W = e^{qz/a}(A_1 \cos qz/a + B_1 \sin qz/a) + e^{-qz/a}(A_2 \cos qz/a + B_2 \sin qz/a) \tag{4.23}$$

$$\begin{aligned} U &= \frac{\nu}{2q}\{e^{qz/a}\{(A_1 - B_1)\cos qz/a + (A_1 + B_1)\sin qz/a\} \\ &- e^{-qz/a}\{(A_2 + B_2)\cos qz/a - (A_2 - B_2)\sin qz/a\}\} \end{aligned} \tag{4.24}$$

where A_1, B_1, A_2, B_2 are arbitrary constants, and

$$q = (a/h)^{\frac{1}{2}}\{3(1-\nu^2)\}^{\frac{1}{4}} \tag{4.25}$$

The results here obtained indicate a state of stress existing in the parts of the shell that are near the edges and such that the stress-resultants and stress-couples diminish to very small values at a distance from the edges, which is comparable to a mean proportional between the thickness and the diameter which is called "edge-effect" state.

The "edge-effect" is of quite different character from those which have been encountered in the extensional state, where the extensional strains are in general small compared with the flexural strains, but rise in importance near to free edges so as to secure the satisfaction of the boundary conditions. Here the flexural strains are in general small compared with the extensional strains but rise in importance in the neighbourhood of fixed edges so as to secure the satisfaction of conditions of fixity.

It was found that combining the above two specific solutions together with proper boundary conditions would yield solution for the particular problem of a finite-length tube with fixed ends [191].

Considering a tube of length l and measuring z from one end, the boundary conditions are:

$$U = 0, W = 0, \frac{dW}{dz} = 0 \quad at \quad z = 0 \quad and \quad at \quad z = l \tag{4.26}$$

In this problem $Z^{'} = 0$ and $R^{'}$=p which is the internal pressure. The complete expressions for U and W are:

Axial displacement:

$$\begin{aligned} U &= a_2 + a_1 \frac{z}{1-\nu^2} - \frac{\nu a z}{Eh} p + \frac{\nu}{2q} \{ e^{qz/a} \{ (A_1 - B_1) \cos qz/a + (A_1 + B_1) \sin qz/a \} \\ &- e^{-qz/a} \{ (A_2 + B_2) \cos qz/a - (A_2 - B_2) \sin qz/a \} \} \end{aligned} \tag{4.27}$$

Radial displacement

$$\begin{aligned} W &= a_1 \frac{\nu a}{1-\nu^2} - \frac{\nu^2 a^2}{Eh} p + \frac{1-\nu^2}{Eh} a^2 p + e^{qz/a} (A_1 \cos qz/a + B_1 \sin qz/a) \\ &+ e^{-qz/a} (A_2 \cos qz/a + B_2 \sin qz/a) \end{aligned} \tag{4.28}$$

The boundary conditions at the end $z = 0$ give:

$$a_2 + \frac{\nu}{2q}(A_1 - B_1) - (A_2 + B_2) = 0 \tag{4.29}$$

$$a_1 \frac{\nu a}{1-\nu^2} + \frac{1-2\nu^2}{Eh} a^2 p + A_1 + A_2 = 0 \tag{4.30}$$

$$A_1 + B_1 - A_2 + B_2 = 0 \tag{4.31}$$

The boundary conditions at the end $z = l$ give, on writing z_0 for ql/a:

$$\begin{aligned}(B_1 - B2)(\sinh z_0 \cos z_0 + \cosh z_0 \sin z_0) \quad + \quad & (A_1 + A_2)(\sinh z_0 \cos z_0 - \cosh z_0 sinz_0) \\ & +2(B_1 + B_2)\sinh z_0 \sin z_0 = 0 \end{aligned} \tag{4.32}$$

$$\begin{aligned}-(A_1 + A_2) + (A_1 + A_2)\cosh z_0 \cos z_0 \quad + \quad & (B_1 + B_2)(\cosh z_0 \sin z_0 - \sinh z_0 \cos z_0) \\ + \quad & (B_1 - B_2)\sinh z_0 \sin z_0 = 0 \end{aligned} \tag{4.33}$$

$$\frac{\nu}{q}(B_1 + B_2) + a_2 + a_1 \frac{l}{1 - \nu^2} - \frac{\nu a l}{Eh} p = 0 \tag{4.34}$$

The displacement field is known once the constants are determined.

In the numerical calculations, the tube length is taken to be 20 mm, while all other remaining geometry dimensions and material property parameters remain the same as those described in the free-end case. It is well known that shell treatment is an approximation of the real three-dimensional solid problems. To test whether the shell approximation is appropriate, two totally different types of element were selected: (a) the axisymmetric solid element (CAX4H), and (b) three-dimensional shell elements (see Figure 4.10(a) and (b)). Furthermore, in shell elements, four-node thin shell element (S4R5), four-node general purpose shell element (S4), and 3-node general purpose shell element (S3) were all tested to see if there might be any differences among different shell element selections. The Discrete Kirchhoff (DK) constraint, which refers to the satisfaction of the Kirchhoff constraint at discrete points on the shell surface, is imposed in all thin shell elements. In thin shell element type S4R5 the discrete Kirchhoff constraint is imposed numerically where the transverse shear stiffness acts as a penalty that enforces the constraint. The

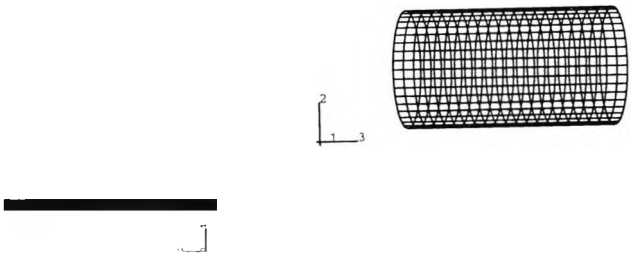

(a) (b)

Figure 4.10: Two different types of element configuration (a) axisymmetric solid element (b) three-dimensional shell element.

general purpose elements allow transverse shear deformation, and change in thickness as a function of in-plane deformation. These elements use thick shell theory as the shell thickness increases and become discrete Kirchhoff thin shell elements as the thickness decreases; the transverse shear deformation becomes very small as the shell thickness decreases.

Figure 4.11 (a) and (b) shows the comparisons of the predicted radial and axial displacements using axisymmetric solid element and the four-node thin shell element with the analytical solutions. It is obvious that the agreement is quite good. And therefore it can be deduced that the shell treatment is a fair approximation to three-dimensional problems where one dimension (thickness) is small (10%) compared with the overall dimensions of the bounding surfaces. Figure 4.12 (a) and (b) is the comparisons of predicted displacements using four-node thin and four-node general purpose shell elements. Figure 4.13 is the predicted displacements using general purpose three-node and four-node shell elements. In general, there is very good agreement between predicted results using a selection of shell elements and analytical solution, justifying our choice of shell element used in this study.

In this section, numerical calculations of an incompressible tube, subjected to uniform internal pressure, were presented. Results predicted using a finite element code ABAQUS have been compared with well-established theoretical solutions and good agreement is

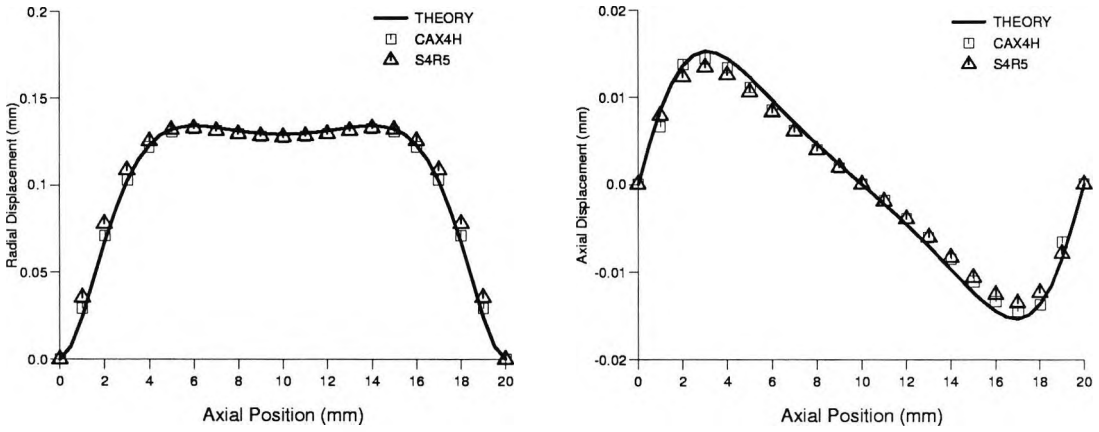

(a) (b)

Figure 4.11: Comparisons of the predicted (a) radial, and (b) axial displacements using axisymmetric solid element and the four-node thin shell element with the analytical solutions.

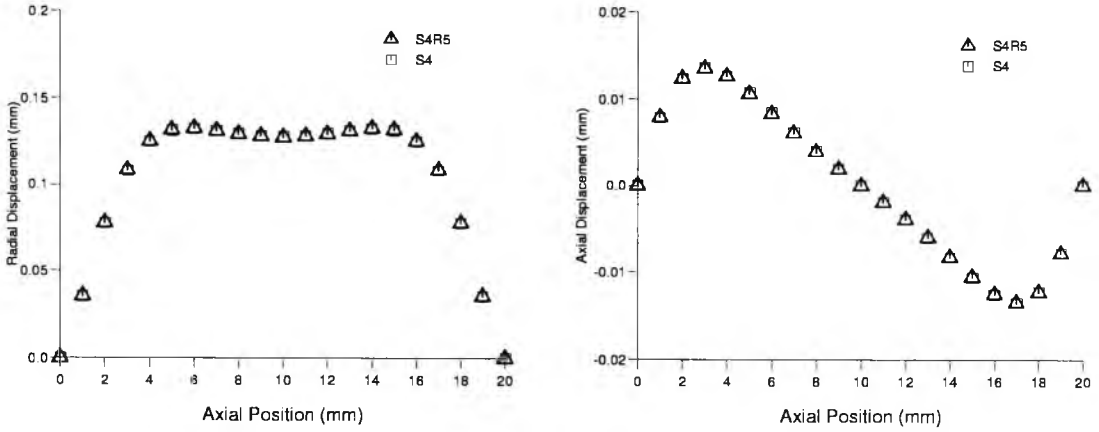

(a) (b)

Figure 4.12: Comparisons of the predicted (a) radial, and (b) axial displacements using four-node thin shell element with four-node general purpose shell element.

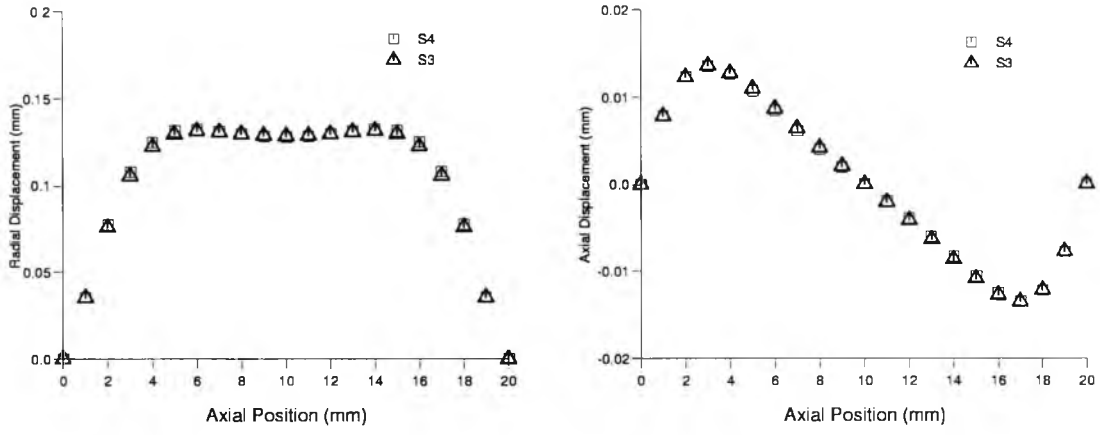

(a) (b)

Figure 4.13: Comparisons of the predicted (a) radial, and (b) axial displacements using general purpose three-node and four-node shell elements.

achieved. The capability and reliability of predicting wall movement using ABAQUS is well demonstrated.

4.3 Coupled Fluid/Solid Motion Test–Womersley solution

4.3.1 Analytical solution

Consider a case of pulsatile flow with negligible inertia in an elastic tube. The fluid must follow the motion of the wall, which is a pulsatile expansion. This necessitates the existence of radial flow component that is much smaller than longitudinal one, so that the main flow is in the longitudinal direction. This assumption is linked to another assumption that the tube radius is much smaller than the wave-length. The governing equations for the system are:

Fluid dynamics equations:

$$\frac{\partial u_r}{\partial r} + \frac{u_r}{r} + \frac{\partial u_z}{\partial z} = 0 \tag{4.35}$$

$$\frac{\partial u_r}{\partial t} + u_r\frac{\partial u_r}{\partial r} + u_z\frac{\partial u_r}{\partial z} = -\frac{1}{\rho}\frac{\partial P}{\partial r} + \nu(\frac{\partial^2 u_r}{\partial r^2} + \frac{1}{r}\frac{\partial u_r}{\partial r} + \frac{\partial^2 u_r}{\partial z^2} - \frac{u_r}{r^2}) \tag{4.36}$$

$$\frac{\partial u_z}{\partial t} + u_r\frac{\partial u_z}{\partial r} + u_z\frac{\partial u_z}{\partial z} = -\frac{1}{\rho}\frac{\partial P}{\partial z} + \nu(\frac{\partial^2 u_z}{\partial r^2} + \frac{1}{r}\frac{\partial u_z}{\partial r} + \frac{\partial^2 u_z}{\partial z^2}) \tag{4.37}$$

elasticity equations:

$$\frac{\partial^2 \xi}{\partial t^2} = \frac{E}{\rho_w(1-\sigma^2)}\left(\frac{\partial^2 \xi}{\partial z^2} + \frac{\sigma}{R}\frac{\zeta}{\partial z}\right) + \frac{\mu}{\rho_w h}\left(\frac{\partial u_z}{\partial z} + \frac{\partial u_r}{\partial r}\right)_{r=R} \tag{4.38}$$

$$\frac{\partial^2 \zeta}{\partial t^2} = \frac{P}{h\rho_w} - \frac{E}{\rho_w(1-\sigma^2)}\left(\frac{\sigma}{R}\frac{\partial \xi}{\partial z} + \frac{\zeta}{R^2}\right) \tag{4.39}$$

and boundary conditions:

$$u_r = \frac{\partial \zeta}{\partial t} \quad u_z = \frac{\partial \xi}{\partial t} \quad at \quad r = R \tag{4.40}$$

where u_r, u_z are the radial and axial components of velocity in fluid, ξ, ζ are the axial and radial displacements of the wall's midline, and ρ, ρ_w are densities for the fluid and wall respectively.

The haemodynamic equations for the fluid must match the elasticity equations for the motion of the wall by matching velocity at the interface. As the phenomenon is that of a wave propagation, it is appropriate to assume that the variables have the same nature, namely:

$$P = P_1 e^{in(t-\frac{z}{c})} \tag{4.41}$$

$$u_r = u_{r1} e^{in(t-\frac{z}{c})} \tag{4.42}$$

$$u_z = u_{z1} e^{in(t-\frac{z}{c})} \tag{4.43}$$

Looking at the fluid dynamics equations, it is obvious that the homogeneous solution is Bessel function. Then approximate solutions can be obtained :

$$u_z = \frac{A_1}{\rho c}\left(1 + \eta \frac{J_0(\alpha y i^{3/2})}{J_0(\alpha i^{3/2})}\right) e^{int} \tag{4.44}$$

$$u_r = \frac{inRA_1}{2\rho c^2}\left(\eta \frac{2J_1(\alpha i^{3/2} y)}{\alpha i^{3/2} J_0(\alpha i^{3/2})} + y\right) e^{int} \tag{4.45}$$

whereJ_0, J_1 are Bessel functions of order 0 and 1, α is the Womersley number, and η is given by:

$$\eta = \frac{2}{x(F_{10} - 2\sigma)} - \frac{(1-2\sigma)}{F_{10} - 2\sigma} \tag{4.46}$$

$$x = \frac{h}{R}\frac{1}{\rho c^2}\frac{E}{(1-\sigma^2)} \doteq \frac{2}{1-\sigma^2)} \tag{4.47}$$

$$F_{10} = \frac{2J_1(\alpha i^{3/2})}{\alpha i^{3/2} J_0(\alpha i^{3/2})} \tag{4.48}$$

Where c is the Mones-Korteweg wave speed.

As the solution is a Bessel function, it is therefore simpler to assume that the pressure is also given by a Bessel function:

$$P = A_1 J_0(ky) e^{in(t-\frac{z}{c})} \tag{4.49}$$

where y=r/R is the normalized radius.

Then,

$$\frac{\partial P}{\partial z} = -\frac{in}{c} A_1 J_0(ky) e^{in(t-\frac{z}{c})} \tag{4.50}$$

The value of k in the physiological system is very small (smaller than 0.1). It is therefore appropriate to assume that the Bessel function :

$$J_0(ky) \doteq 1 \tag{4.51}$$

If the oscillating pressure gradient is expressed as:

$$-\frac{\partial P}{\partial z} = Ae^{int} \tag{4.52}$$

Then, comparing with equation(4.50), we have:

$$A = \frac{inA_1}{c} \tag{4.53}$$

Substituting equation(4.53) into equations(4.44) and (4.45):

$$u_z = \frac{A}{in\rho}\left(1 + \eta\frac{J_0(\alpha y i^{3/2})}{J_0(\alpha i^{3/2})}\right) e^{int} \tag{4.54}$$

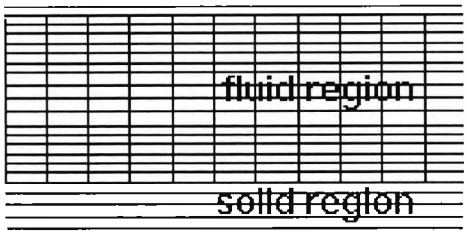

Figure 4.14: A schematic diagram for the computational grid.

$$u_r = \frac{RA}{2\rho c}\left(\eta\frac{2J_1(\alpha y i^{3/2})}{\alpha i^{3/2}J_0(\alpha i^{3/2})} + y\right)e^{int} \tag{4.55}$$

The wall shear stress is given by:

$$\tau_w = \frac{A\eta\alpha^2\mu}{2n\rho R}F_{10}(\alpha)e^{int} \tag{4.56}$$

A table for $1 - F_{10}(\alpha)$ is given is Womersley's report [38].

4.3.2 Numerical calculations

The coupled algorithm described in chapter 3 was first applied to unsteady flow in a circular tube, with the tube material being (a) elastic and, (b) hyper-elastic. The hyper-elastic case was chosen just to test the application of the coupled algorithm to arterial-related flow. In this case, it was assumed that the nonlinear material behaviour of the tube was known and the tube was loaded from zero-state. Geometrically non-linear theory was used in the displacement and stress analysis for the hyper-elastic case. The Navier-Stokes equations in their axis-symmetric form were solved.

In the calculation the tube is 50 mm long, 1 mm thick and has a 10 mm internal diameter. Figure 4.14 shows the computational grid for both the fluid and solid regions (because of symmetry, only axisymmetric plane is given).

It was assumed that the flow was axisymmetric and the solid material to be incompressible. The adopted element type CAX4H is defined as a 4-node bilinear, hybrid, constant pressure axisymmetric solid element. This hybrid element is primarily intended for use with incompressible and nearly incompressible material behaviour. When the material response is incompressible, the solution to a problem cannot be obtained in terms of the displacement history alone, since a purely hydrostatic pressure may be added without changing the displacements. This problem is resolved by treating the pressure stress as an independently interpolated basic solution variable, coupled with the displacement solution through the constitutive theory and the compatibility condition, with this coupling being implemented by a Lagrange multiplier. To prevent the movement of rigid body, both ends of the tube were constrained against axial motion in the finite element model.

(a) *Linear elastic material*

The tube was assumed to be linear elastic and the flow was driven by an oscillatory pressure gradient. This problem was considered first because, away from the fixed ends, the solution could be compared with the analytical solution for oscillatory flow in a freely-moving elastic tube. If the flow is driven by an oscillatory pressure gradient expressed as $-\partial P/\partial x = A * exp(int)$, assuming the fluid velocity is small compared to the wave speed, the approximate solution for axial and radial velocities can be obtained from equations(4.54, 4.55).

At the tube inlet, a sinusoidally varying pressure was applied. The pressure variation was given as

$$P = \begin{cases} P_{max}\cos(\omega t) & \text{inlet} \\ 0 & \text{outlet} \end{cases}$$

where $P_{max} = 100Pa$, $\omega = 2\pi$ /tp, tp is the cycle period which was set to 0.75s. Each cycle consists of 40 equally spaced time steps. The tube is incompressible, linearly elastic with a Young's modulus of $5.0X10^5$ Pa and Poisson's ratio of 0.48. Velocity profiles at the mid-section along the length of the tube at four different times in the cycle are given in Figure 4.15. Comparison of time-dependent wall shear stress along the wall is shown in

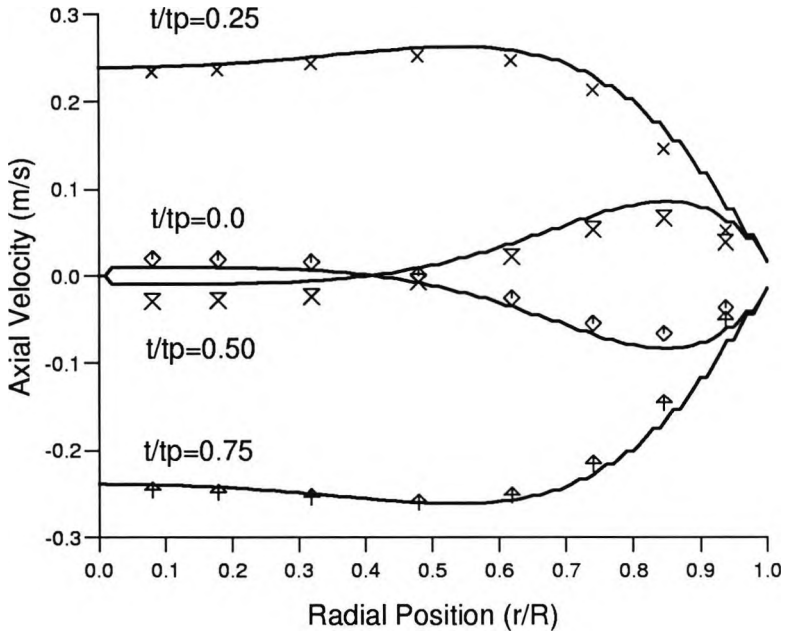

Figure 4.15: Predicted (symbols) and analytical (lines) axial velocity profiles for oscillatory flow in an elastic tube.

Figure 4.16. The analytical curves were generated from Womersley's solution [38]. Predicted distributions of radial displacement and stress at four times in the cycle are given in Figure 4.17 and Figure 4.18 respectively for which no analytical solutions are available. Good agreement with the analytical solution can be found from the velocity profiles. Only three iterations were required to meet the convergence criterion. Results of a similar calculations using the FV method can be found in Henry & Collins [9]. However, the fully coupled FV code is currently restricted to axisymmetric flows and infinitesimal strains.

(b) *Hyperelastic material*

The coupled method is also capable of dealing with large deformation and nonlinear material behaviour. In order to demonstrate its applicability to complex material problems, unsteady flow in a hyperelastic tube was considered. The inflow boundary was defined by a sinusoidally varying mass flow condition with its minimum and maximum values being

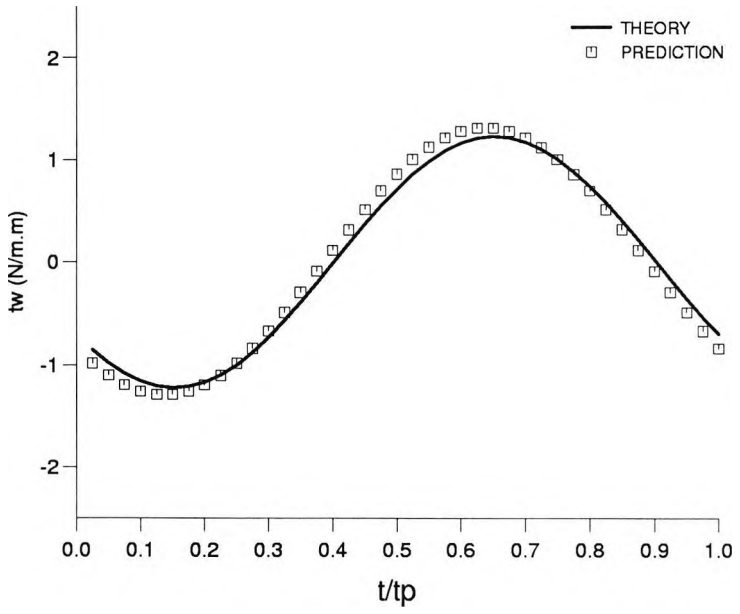

Figure 4.16: Predicted (symbols) and analytical (lines) wall shear stress for oscillatory flow in an elastic tube.

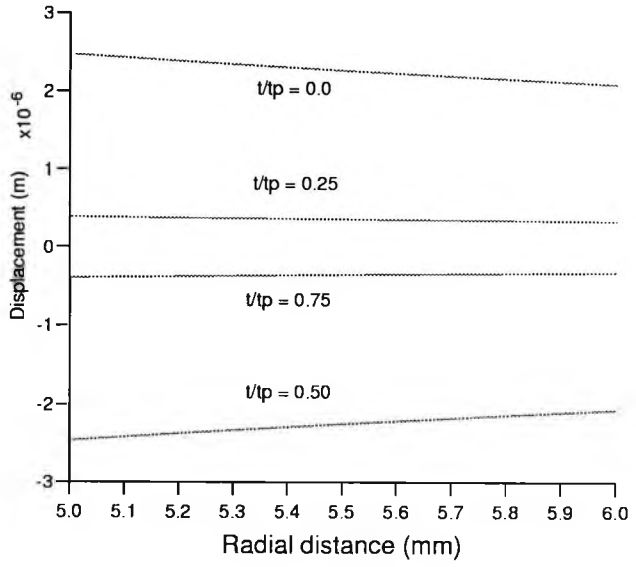

Figure 4.17: Predicted distribution of radial displacements across the wall (elastic model).

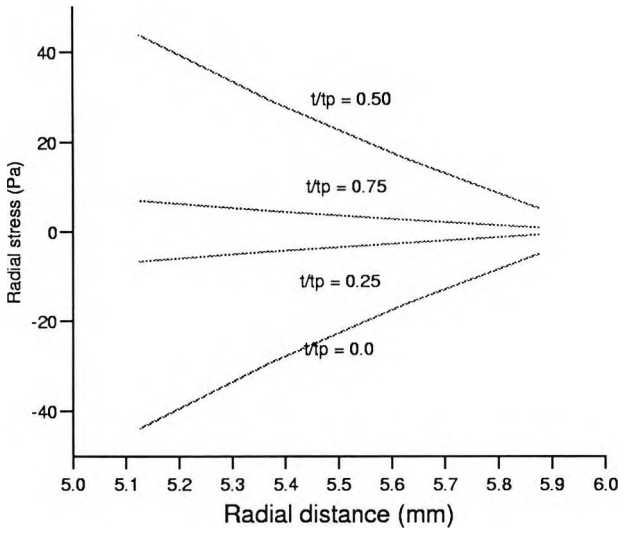

Figure 4.18: Predicted distribution of radial stresses across the wall (elastic model).

20ml/s and 31ml/s respectively and the outflow was controlled by a sinusoidally varying pressure with the minimum and maximum values being 80mmHg and 120mmHg. The cycle period was 1.0s. This set of boundary conditions was chosen to represent the physiological conditions in large arteries with a mean Re=300.

The hyperelastic material is described in terms of a strain energy potential, which defines the strain energy stored in the material per unit volume in the initial configuration as a function of strain. Using the energy function proposed by Demiray [153]

$$W = \frac{\beta}{2\alpha}\{exp\{\alpha[I_1 - 3]\} - 1\} \tag{4.57}$$

where I_1 is the first invariant of the Finger deformation tensor. α and β are two material constants and are found to be α=1.948 and β=9900 Pa for the abdominal aorta of dogs. The incompressibility is included in the model, which is a reasonable description of most biological tissues.

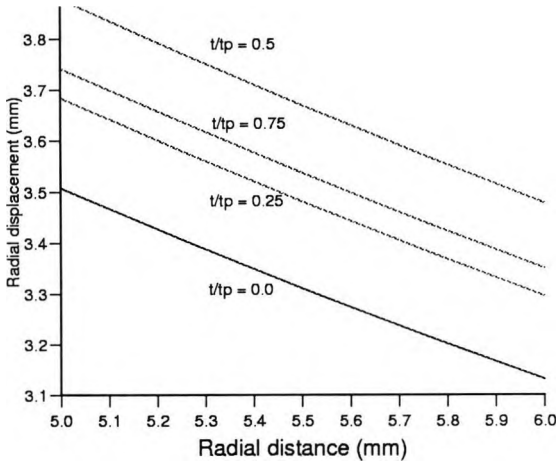

Figure 4.19: Predicted distribution of radial displacements across the wall (hyperelastic model).

As shown in Figure 4.19, the internal radius of the tube increased sharply from its original value of 5 mm (unloaded state) to 8.51 mm, exhibiting large deformation (60%) due to the hyperelastic behaviour. During the cycle the displacement oscillated at an average value of 4.5% (Radius increased from 8.51mm to 8.89mm.). Velocity profiles at the mid-section along the length of the tube at four different times in the cycle and their corresponding predicted values for a rigid tube are given in Figure 4.20. Velocities are always lower compared with the rigid model because of the large deformation. Predicted distributions of radial stress at four times in the cycle are given in Figure 4.21.

It is of interest to compare the predicted results for the elastic and hyperelastic cases. There are differences in the deformation and stress distribution between the two cases. The gradient of the displacement across the tube wall is much steeper in the hyperelastic tube and the gradient of stress distribution across the wall is not uniform but becomes slightly smaller towards the outer surface of the wall. Unfortunately, no analytical solutions are known in order to verify these predictions. Similar to the linearly elastic case, three iterations were required to satisfy the prescribed convergence criterion due to the simple geometry.

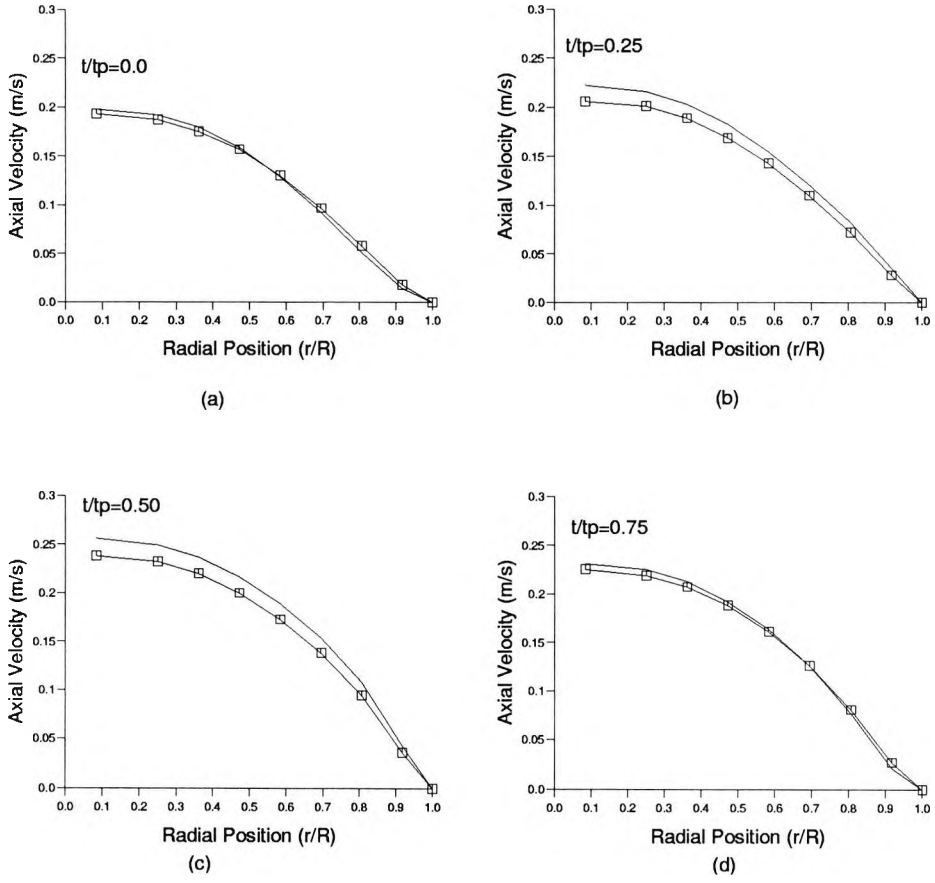

Figure 4.20: Predicted axial velocity profiles for pulsatile flow in the hyperelastic model (with symbols) and its corresponding rigid model (without symbols).

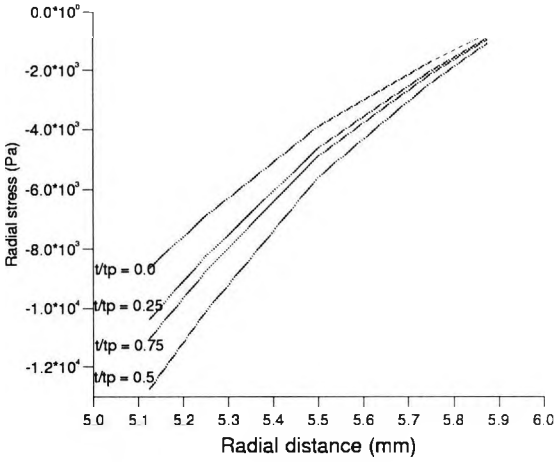

Figure 4.21: Predicted distribution of radial stresses across the wall (hyperelastic model).

The validity of the numerical results for the hyperelastic case can be assessed from the view point of structural analysis. The distribution of displacement is linear across the wall, suggesting that the radial strain difference is constant and the magnitude of the radial strain decreases towards the outer surface. However, from the results shown in Figure 4.21, it can be observed that the radial stress difference through the wall thickness is not uniform but varies with larger value at the inner surface of the wall. All these phenomena are consistent with the characteristics of this specific hyperelastic material, which exhibits smaller strain difference with increased stress level, the typical effect of the collagen.

An numerical method for coupled fluid/solid interaction problems has been presented in chapter 3, which was designed to be able to treat a wide range of material behaviour, such as, elastic and hyperelastic, small and large deformations. Results of the benchmark tests in this section have demonstrated good agreement with available analytical solutions for oscillatory flow in a linearly elastic tube. Its applicability to large deformation problem is also tested, although there is no established analytical solution to compare with. The coupled method is not confined to simple geometries and can be performed in complex geometries as to be shown in chapter 5.

Chapter 5

Modelling of Blood Flow and Vessel Mechanics in the Human Carotid Arterial Bifurcations

This chapter describes the advanced application of the coupled model. The pulsatile flows in anatomically realistic compliant human carotid bifurcations were simulated numerically. *In vivo* pressure and mass flow waveforms in the carotid arteries were obtained from individual subjects using non-invasive techniques. The geometry of the computational models was reconstructed from magnetic resonance angiograms. The results of the study revealed complex natures of both flow field and wall mechanical behaviour in the carotid bifurcations. Maps of wall shear stress, contours of velocity in the flow field as well as wall movement and tensile stress on the arterial wall are presented for two healthy human subjects. This non-invasive approach enables the evaluation of local geometries, haemodynamic and vessel mechanical parameters in individual subjects.

Comparison of the results with those under the rigid wall assumption demonstrated the quantitative influence of the vessel wall motion. Generally there was a reduction in the magnitude of wall shear stress, and an enlargement of flow separation zone in the compliant model, but the global characteristics of the flow and stress patterns remained unchanged.

Comparisons of predicted and measured wall movement and blood velocity at selected locations demonstrated good agreement.

5.1 Introduction

The precise role played by haemodynamics in the development and progression of vascular disease is incompletely understood. The inability to conclusively identify the haemodynamic factors that influence atherosclerosis may relate to the indirect nature of the correlations made between haemodynamics and vascular disease. Conventional averaged or simplified bifurcation models mask interesting features observed in real arteries [194, 37]. More direct studies, in which the presence or absence of disease can be compared with haemodynamic parameters acquired from individual subjects, are required, since subtle changes in geometry can affect the flow field significantly [192]). More conclusive evidence regarding the decisive factors in vascular diseases may be derived from such individual studies.

Experimental studies in vascular replicas, in which true vessel geometry was retained, yielded new insights into arterial fluid mechanics that had not been revealed by experiments in idealised models. It is reasonable to expect a similar benefit from Computational Fluid Dynamics in more realistic conditions, however, at present only limited numerical work has been performed where the computational region was based on real vascular anatomy [193, 194, 195], but all these studies involved the rigid wall assumption.

This chapter therefore deals with the simulation of flow and stress in the real human carotid bifurcations using the coupling algorithm presented in chapter 3. The coupled model is able to simulate physiologically and clinically relevant blood flow in compliant bifurcations. Magnetic resonance imaging can produce high resolution images of the carotid arteries relatively noninvasively and in scan times suitable for patient studies. In this study, modern MR imaging techniques were used to obtain the carotid bifurcation anatomy. Pressure in the common carotid artery and mass flow rates in the internal and external carotid were obtained with applanation tonometry and pulsed Doppler ultrasound respectively from the

same subject, while wall thickness was measured by B-mode ultrasound. This combined MRI/Ultrasound/CFD/Solid Mechanics approach provides a useful tool for non-invasive, *in vivo* human studies of haemodynamics and vascular mechanics.

5.2 Assumptions and Models

5.2.1 Models for blood flow and arterial structure

In this study, blood is assumed to be incompressible, homogeneous, and Newtonian. The Newtonian approximation is acceptable in large arteries where relatively high shear rates occur. A previous study of the influence of the shear thinning behaviour of blood on flow in a model carotid artery bifurcation by Perktold et al. [34] showed an average difference between Newtonian and non-Newtonian wall shear stress of under 10%. The mathematical analysis of flow phenomena in segments of large arteries requires the solution of the full time-dependent Navier-Stokes equations with appropriate prescription of boundary conditions.

The thicknesses of the carotid artery walls are about 8 to 10% of the vessel diameters according to Pedley [188]. Thus, for the description of the mechanics of an artery segment, a shell model was applied. The behaviour of a shell structure is governed by the behaviour of the middle surface as reference surface. In shell theories the membrane and the bending strains are coupled in the energy expression. The coupled deformations consisting of stretching and change of curvature of the middle surface are required in predicting the strains and subsequently the stresses in the shell. Relatively large deformations were expected in the calculation, therefore geometric non-linear analysis was performed. The material of the vessel wall was assumed to be incrementally linear elastic. A similar treatment has been used in most previous numerical studies of idealised models [42, 5, 26, 148].

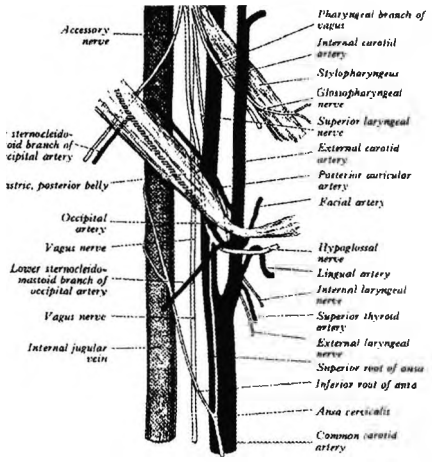

Figure 5.1: The structures crossing the internal jugular vein and carotid arteries and those intervening between the external and internal arteries from Ref. [196].

5.2.2 The influence of the superior thyroid artery

The common carotid artery is a large bilateral vessel supplying the head and neck; it ascends to just above the level of the thyroid cartilage's upper border, where it divides into an external carotid and an internal carotid. Figure 5.1 shows the carotid arteries and related structures. The external carotid artery is one of the terminal branches of the common carotid artery. The superior thyroid artery arises from the front of the external carotid artery near its origin. It runs superficial and parallel to the external laryngeal nerve to reach the upper pole of the thyroid gland. It gives off (1) a branch to the sternocleidomastoid muscle, and (2) the superior laryngeal artery.

In addition to the assumptions for models of blood flow and arterial structure, the superior thyroid artery was always ignored in previous fluid dynamics studies of carotid bifurcations, mainly to avoid the complexity caused by introducing this small artery [197, 198, 199]. From anatomical point of view, the presence of this small artery is a very common phenomenon (73% of males, 55% of females) [200]. However, it is not clear to what extent the flow patterns within the carotid might be influenced by the presence of this outflow tract in reality. Therefore, a CFD study was performed to quantify the effects of the superior thyroid artery upon the flow patterns and wall shear stress in the carotid bifurcation. The study, taking into account the fact that 3D reconstruction and mesh generation for

a carotid bifurcation with the superior thyroid artery would be much more complicated than for a bifurcation without this artery, was intended to answer the following questions: (i) Is it necessary to include this small artery in the simulation, and (ii) Is there an alternative way to account for the presence of this artery without having to model it explicitly?

Due to the wide variability in the location of this small artery, three different models based on the geometry of a typical adult human carotid bifurcation including the sinus and superior thyroid artery obtained by Bharadvaj et al. [201] were constructed to represent carotid bifurcations expected in normal human subjects with the distance from the bifurcation apex to the superior thyroid artery being 5mm, 10mm, and 20mm respectively. A model without the small superior thyroid artery was used for comparison. Figure 5.2 illustrates the geometry of the bifurcation models. Since the primary concern was the effect of the superior thyroid artery on haemodynamics in general, an average bifurcation geometry was employed.

Numerical calculations have been performed for three cases:

(1) a simplified case–Flow division ratio between internal and external arteries was set to be 70:30 for the model without the small superior thyroid artery (model 1). This is the common procedure followed by previous carotid model studies.

(2) a realistic case–Flow division ratio among the internal, external and superior thyroid arteries was set to be 65:28:7 for models with the small artery (models 2, 3, and 4). This division ratio was chosen under the assumption that the ratio between flows exiting the internal and external carotid remains 70:30, while flow through the superior thyroid artery is 20% of the total flow into the external artery, a maximum value from our clinical experience. To understand how this ratio may influence the flow patterns, values of 10% and 5% were also tested.

(3) a compensation case–Flow division ratio between the internal and external arteries was set to be 65:35 for the model without the small artery (model 1). This is for the

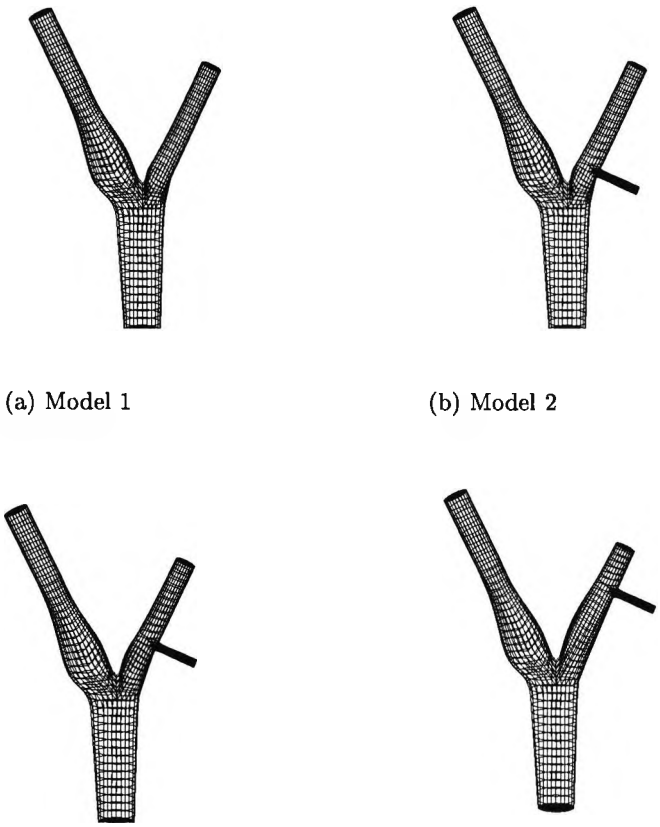

(a) Model 1

(b) Model 2

(c) Model 3

(d) Model 4

Figure 5.2: Carotid bifurcation models without and with the superior thyroid artery at different locations.

simplification of the calculations, yet to compensate the neglecting of the small artery by adding the flow through it to the external artery so as to keep the total flow through the external artery plus the small artery unchanged.

Comparisons of the maximum reversed flow velocities, flow patterns and wall shear stress were made between models with and without the superior thyroid artery. The major findings of this study can be summarised as follows:

(1) The presence of the small artery is found to have marginal effect on both the flow and wall shear stress in the common-external side branch, and very little effect on the flow field and wall shear stress distribution in the common-internal side branch. This finding suggests that in practice the existence of the superior thyroid artery in geometry reconstruction can be ignored if the common and internal carotid is only of interest.

(2) The smaller the flow division ratio between the superior thyroid artery and the external plus superior thyroid arteries, the less effect on the maximum reversed flow velocity and the wall shear stress within the carotid.

(3) If the same amount of flow as it goes through the superior thyroid artery is compensated to the external carotid, results within the carotid sinus would be more or less the same regardless of the presence or absence of this small artery.

(4) The above conclusions hold no matter where the superior thyroid artery is located.

Details of this investigation were reported in a paper, which has just been published in *Medical Engineering & Physics* [202]. Based on the above findings, any small arterial branches in the ECA were ignored during image segmentation and geometry reconstruction process in the present study, as primary focus was the flow behaviour in the CCA and ICA, especially in the sinus region of the latter.

5.3 Model Geometry

The human carotid bifurcation is unusual among the systemic arteries because of the presence of the carotid sinus in most subjects and because of the low distal resistance of the vascular bed supplied by the internal carotid branch, resulting in a continuously forward flow even during diastole and a time-varying flow division during the cardiac cycle. The carotid bifurcation is important clinically because of its predilection to the development of atherosclerotic plaques which can lead to transient ischemic attacks and strokes due to plaque ulceration and embolic events.

It is known that individual variations in the anatomy of arterial bifurcations both in human and in other mammalian species are rather astonishing which can be clearly demonstrated by the reconstructed models in chapter 3.

In this study, two healthy male volunteers aged 40 and 30 respectively with no previous history of vascular disease underwent MR imaging of the right carotid artery bifurcation with 45 degree turning angle. The scan protocol was approved by the local institutional review board and the regional research ethnics committee, and both subjects gave informed consent. The imaging was performed with a 1.5T scanner (Signa, GE medical system), using 2-D TOF gradient echo sequence (TR 45ms, TE 8.7ms, Flip Angle 60, NEX=1) and a continuous 1.5mm slices with an in-plane resolution of 0.47mm (FOV=12cm). A 5-inch coil was used to obtain high ratio of signal to noise. To minimize the influence of signal loss especially in the bulb region, the contrast-agent Gd-DTPA was used in the scan. The scan covered 50mm proximal and 46mm distal to the carotid bifurcations. An original MR cross-sectional image has already been shown in chapter 3 (Figure 3.5).

The geometry and computational grid of the carotid models were then generated from the MRI angiograms for the two subjects (Figure 5.3 and 5.4). The orientation in the figures posterior to anterior (P/A) and left to right (L/R) will be used in the following result discussions. Viewing from different angles, it can be seen that there is no symmetric plane at all for the realistic bifurcations. A mild curvature of common carotid artery (CCA) is evident for subject No.1. In the subjects examined, the internal carotid arteries are

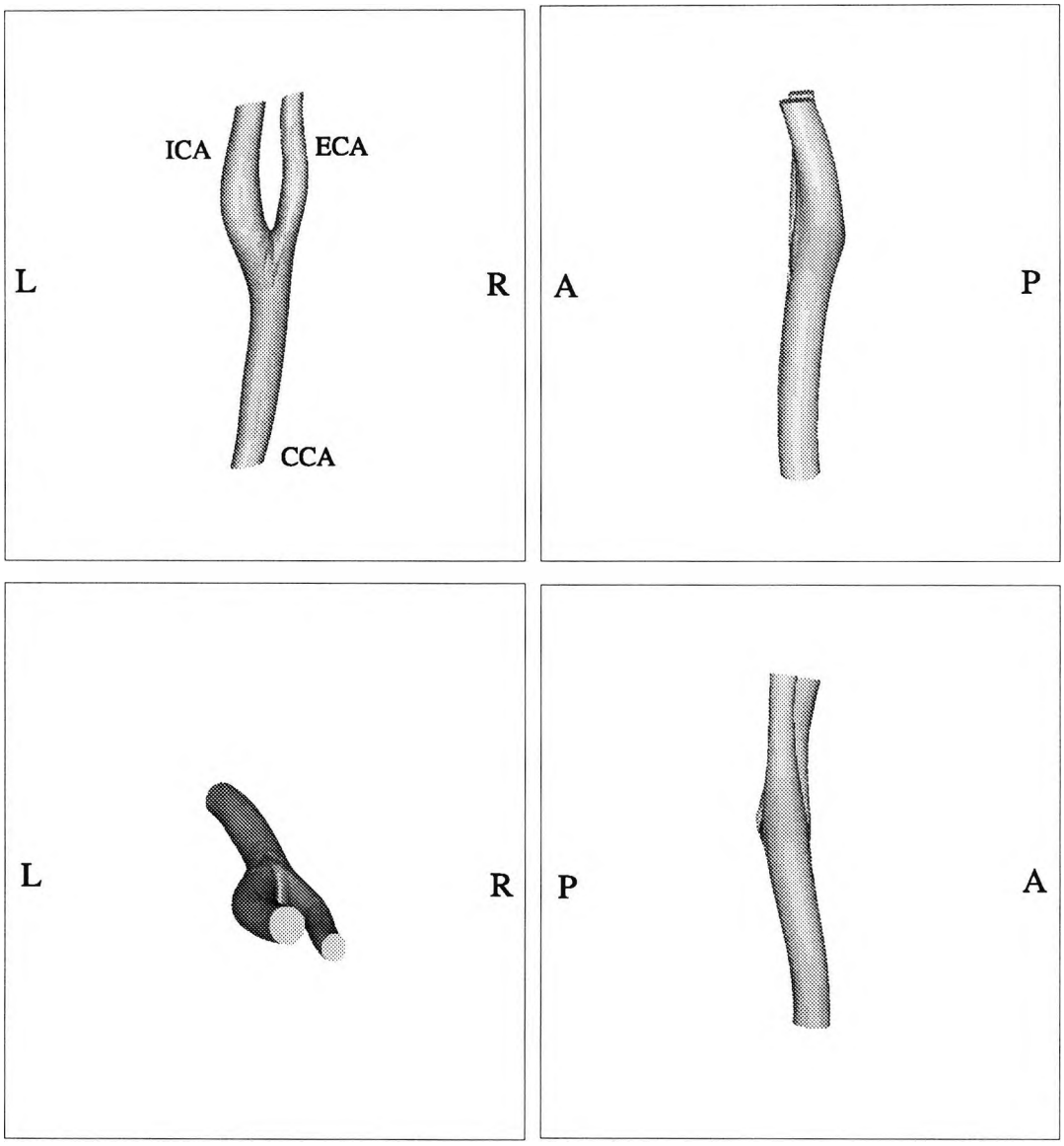

Figure 5.3: Computer reconstructed model of the right human carotid bifurcation–subject No.1.

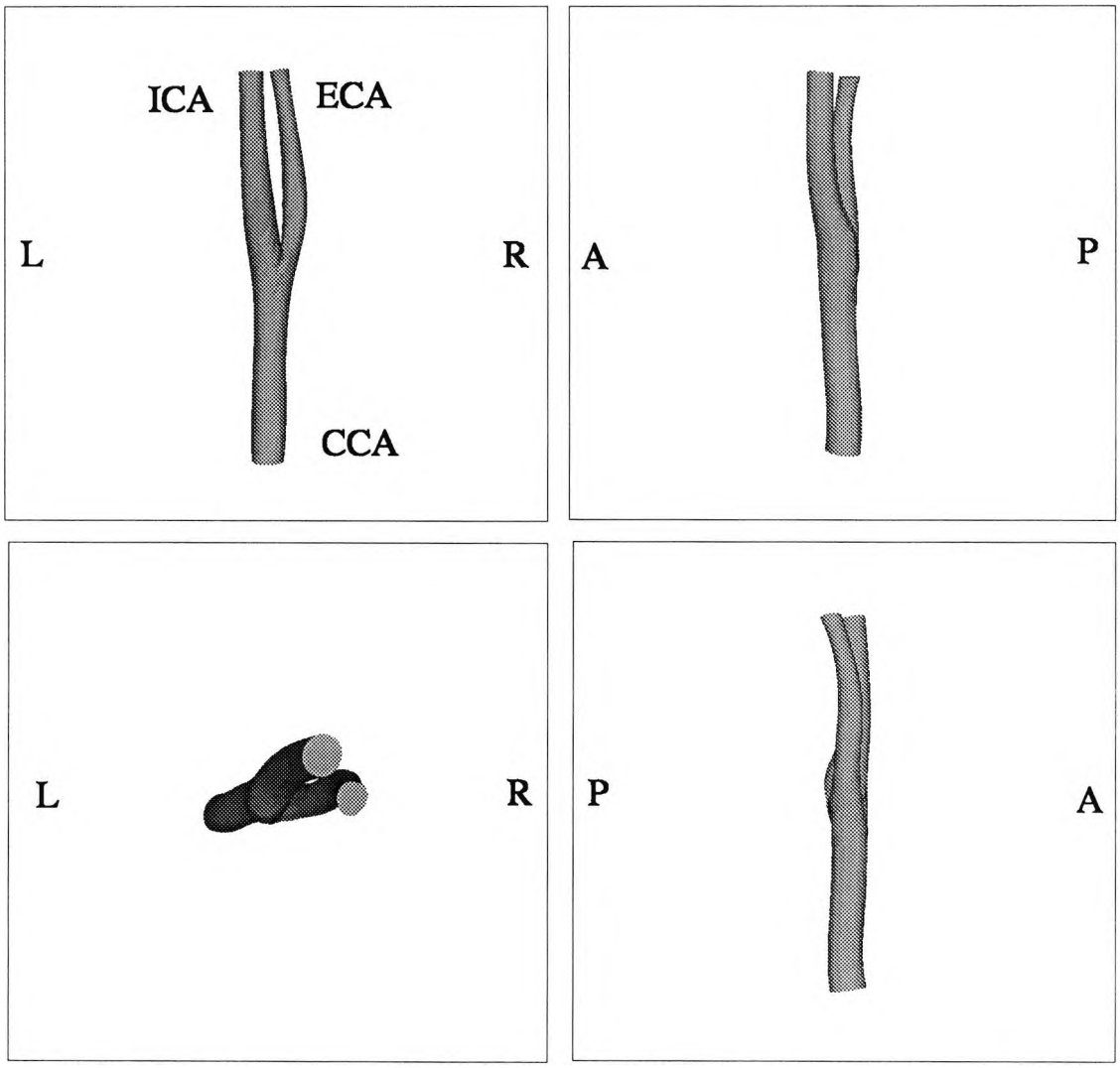

Figure 5.4: Computer reconstructed model of the right human carotid bifurcation–subject No.2.

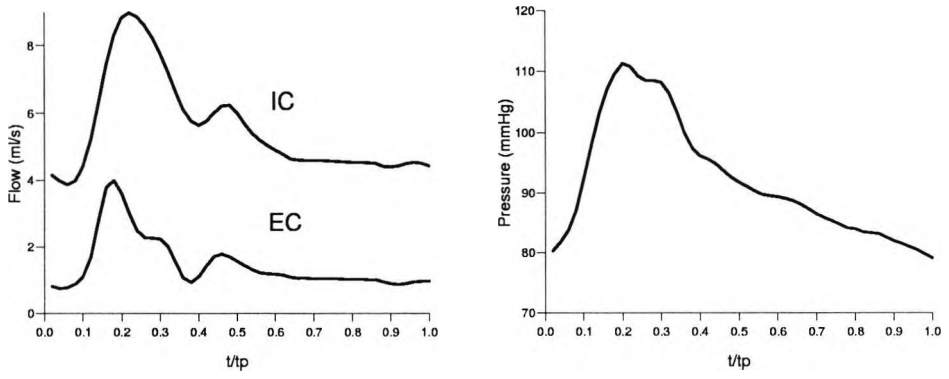

(a) (b)

Figure 5.5: (a)Flow waveforms of the internal and external carotid arteries, and (b) pressure waveform of the common carotid used as boundary conditions–subject No.1.

tortuously curved with both in- and out-of-plane curvatures. The CCA of subject No.2 is relatively straight compared to that for subject No.1. The cross-sectional area expands at the end of CCA which eventually forms the internal carotid bulb. Furthermore, subject No.2 has a smaller bifurcation angle (the angle between ICA and ECA) than subject No.1. All those complex bendings and curvatures may have a non-planar effect on the flow. The numerical study was aimed to provide the detailed fluid flow and wall behaviour within these geometrically complex models.

5.4 Boundary Conditions

In order to incorporate subject specific flow conditions into the simulation, flow waveforms obtained by pulsed Doppler ultrasound and pressure waveforms by applanation tonometry were applied as the time-dependent boundary conditions. Flow was measured using an HDI 3000 ultrasound system (Advanced Technology Laboratories, Bothel, Washington) with a 5-10 Mhz broadband linear array scanhead. Blood flow velocity waveforms of central vessel of exits at internal and external carotid (which were selected as far as possible

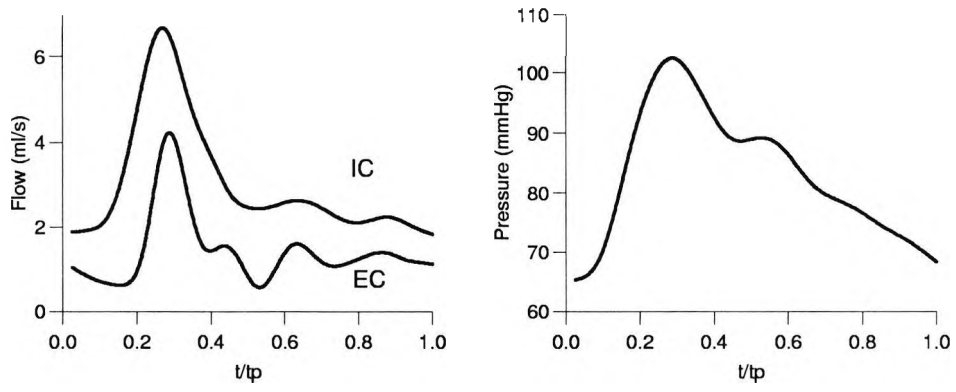

(a) (b)

Figure 5.6: (a)Flow waveforms of the internal and external carotid arteries, and (b) pressure waveform of the common carotid used as boundary conditions–subject No.2.

from the bifurcation region) were measured using pulsed Doppler. Flow rates were then derived by the assumption of fully developed flow.

Continuous carotid pulse pressure was measured non-invasively using a high-fidelity external pressure transducer (model SPT-301; Millar Instruments, Inc., Texas, USA) applied to the skin overlying the pulse of the common carotid artery. This non-invasive method of pressure wave measurement is based on the principle of applanation tonometry. Actual carotid blood pressure values were achieved from the recorded changes in applied pressure, by external calibration using brachial artery pressure measured with an automated sphygmomanometer (Sentron, Bard Biomedical, Illinois, USA).

The flow pulse waveforms used at the internal and external carotid (IC, EC) outlets as well as the pressure pulse waveform at the common carotid inlet are shown in Figure 5.5 and 5.6 for the two subjects respectively. Averaged over the cardiac cycle, the IC:EC flow splits in the models were approximately 75:25 and 60:40 respectively. Pressure and flow exhibited characteristic patterns. Both showed an initial sharp rise to the peak value, after which pressure dropped off more gradually than flow. The choice of this set of boundary conditions was made on the basis of making the most of available data. The reason for

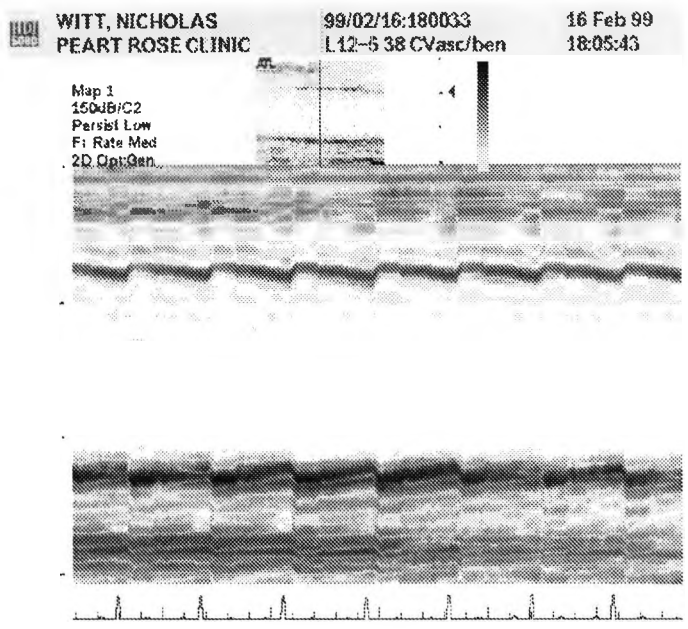

Figure 5.7: A typical original image from M-mode ultrasound.

choosing this boundary setting is twofold. Firstly, due to technical limitations, it is much more difficult to measure pressure in the IC and EC than in the CCA. Secondly it is more appropriate to derive flow rates in the ICA and ECA using the fully developed assumption, because of their smaller vessel diameters compared to the CCA.

The wall thickness of the common carotid, proximal to the bifurcation, internal carotid, and external carotid were estimated to be 0.60mm, 0.66mm, 0.55mm, and 0.40mm respectively, using B-mode ultrasound for subject No.1, and being 0.60mm, 0.69mm, 0.53mm, and 0.46mm for subject No.2. For modelling purpose a smooth transition in between was assumed.

The incremental elasticity parameter describing the wall loaded with the incremental pressure from the diastolic pressure to the peak systolic pressure level was determined with a finite element method using the data from M-mode ultrasound measurements (as shown in Figure 5.7). Knowing the internal diameter, thickness of the arterial wall, diameter increment, and pressure increment, it is not difficult to obtain the material property by FEA. This can be done by adjusting the modulus on the criterion that the right pres-

sure increment results in the right amount of diameter change. In this study the derived material properties by the finite element method were E=2.6X10^5 Pa and 2.7X10^5 Pa for subjects No.1 and No.2 respectively, which were within the range suggested by Fung [82].

5.5 Results

The grid contained 24 blocks and the flow domain was divided into 25,600 computational elements and the wall discretisation yielded 5120 shell elements. Considering the arbitrary *in vivo* geometry, a 3-noded shell element was used. A fine mesh was used at the near wall region in the flow domain with the distance of the nearest grid point from the wall being less than 2.6% of the lumen diameter. The coupled calculations provided a complete set of haemodynamic data including velocity, wall shear stress distributions in the flow domain and mechanical data including displacement and intramural stress distributions on the arterial wall during the whole cardiac cycle. Due to the time-dependent nature of the results, they can only be presented at a number of selected time points.

5.5.1 Flow field

Figures 5.8 and 5.9 show the velocity magnitude contours and slow moving zones (as shown in dark color) at the flow acceleration and deceleration phases for subjects 1 and 2 respectively. For subject No.1 flow in the CCA follows the curvature of the vessel and is slightly skewed towards the outer bend of the curvature, while a concentric velocity distribution is observed for subject No.2. Downstream of the bifurcation, a strong skewing towards the flow divider walls occurs in both IC and EC as a result of branching for both subjects. One noticeable feature is that the skewing in ICA rotates from the R aspect to the R-P aspect due to the nonplanarity of IC in subject No.1. This feature does not exist in subject No.2. There are two slow moving zones in subject No.1, one is located in the internal carotid bulb and another is at the entrance to ECA. The first one exists for the whole cycle and the second for flow deceleration only. In subject No.2, only one slow moving zone is found which is located in the carotid bulb and appears only at flow deceleration. Here the slow moving zone was the region with stagnant and reverse flow

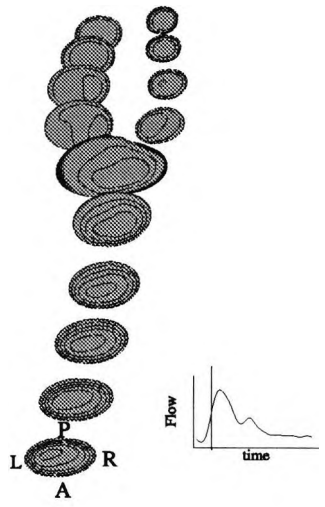

(a)

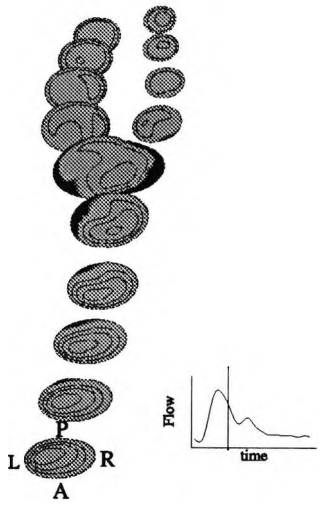

(b)

Figure 5.8: Velocity magnitude contours midway through (a)flow acceleration phase, and (b) flow deceleration phase–subject No.1.

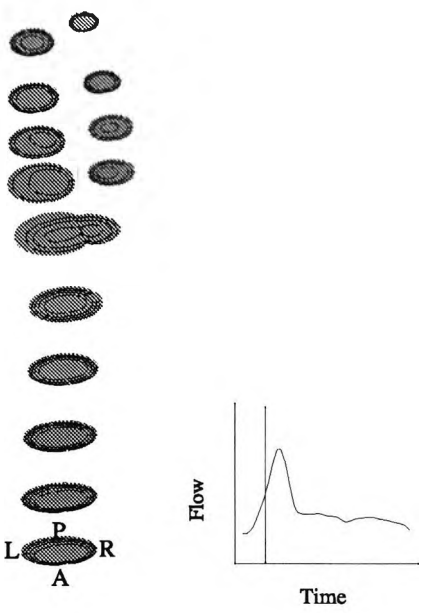

(a)

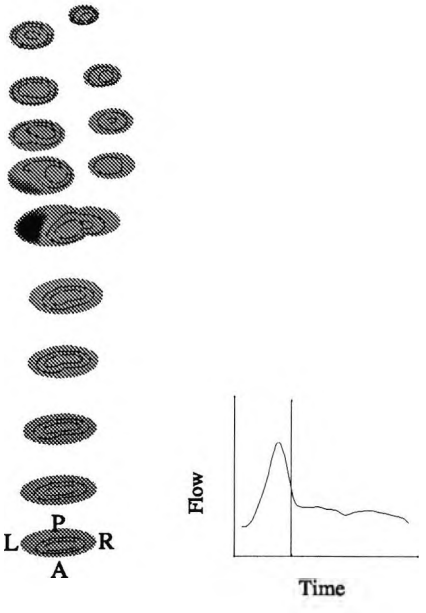

(b)

Figure 5.9: Velocity magnitude contours midway through (a)flow acceleration phase, and (b) flow deceleration phase–subject No.2.

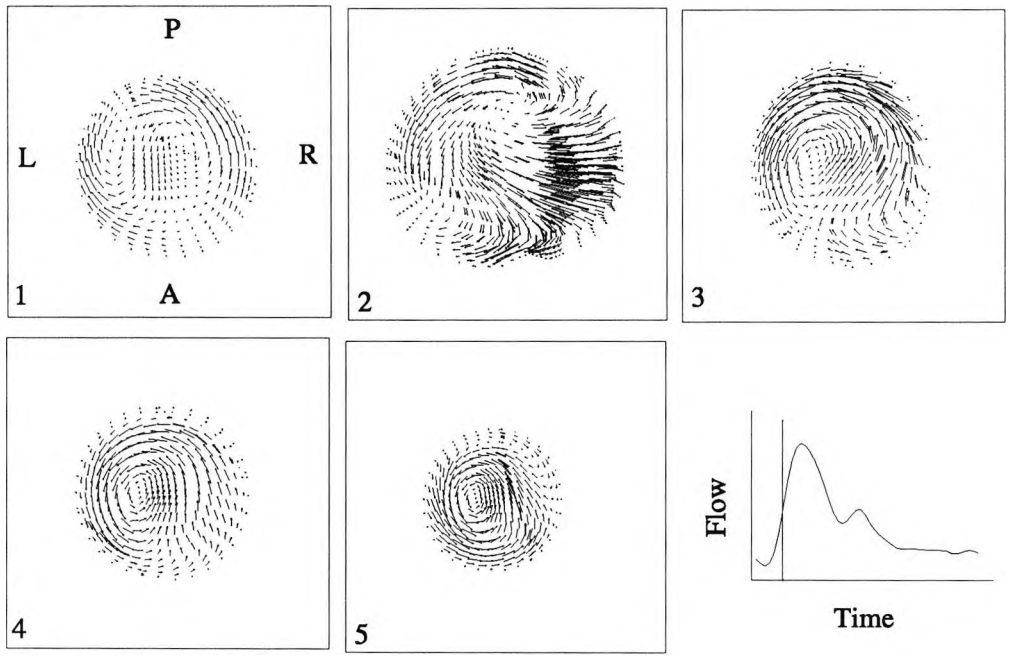

(a)

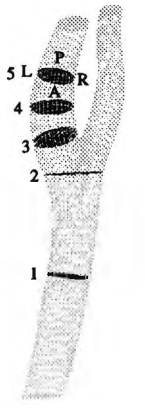

(b)

Figure 5.10: Secondary flow patterns midway through flow acceleration phase in selected planes–subject No.1.

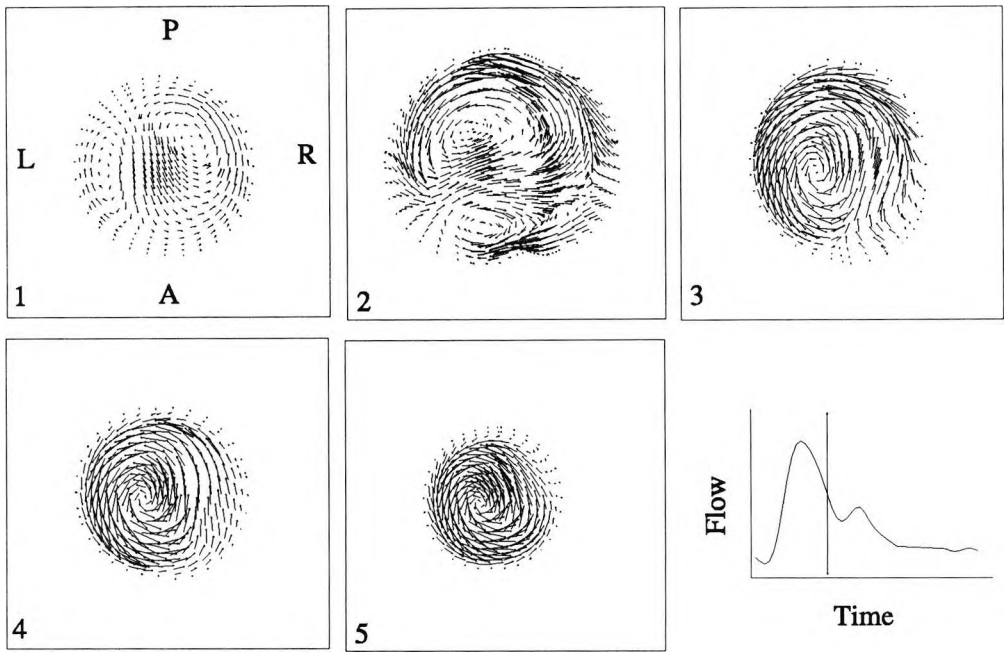

Figure 5.11: Secondary flow patterns midway through flow deceleration phase in selected planes, as shown in Figure 5.10b–subject No.1.

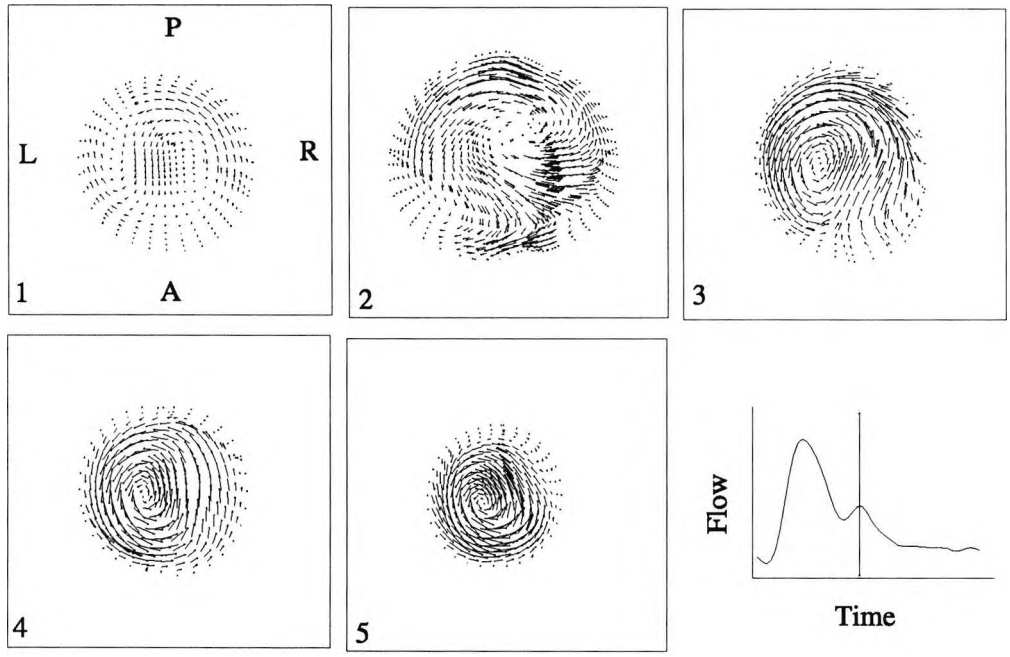

Figure 5.12: Secondary flow patterns at second peak flow phase in selected planes, as shown in Figure 5.10b–subject No.1.

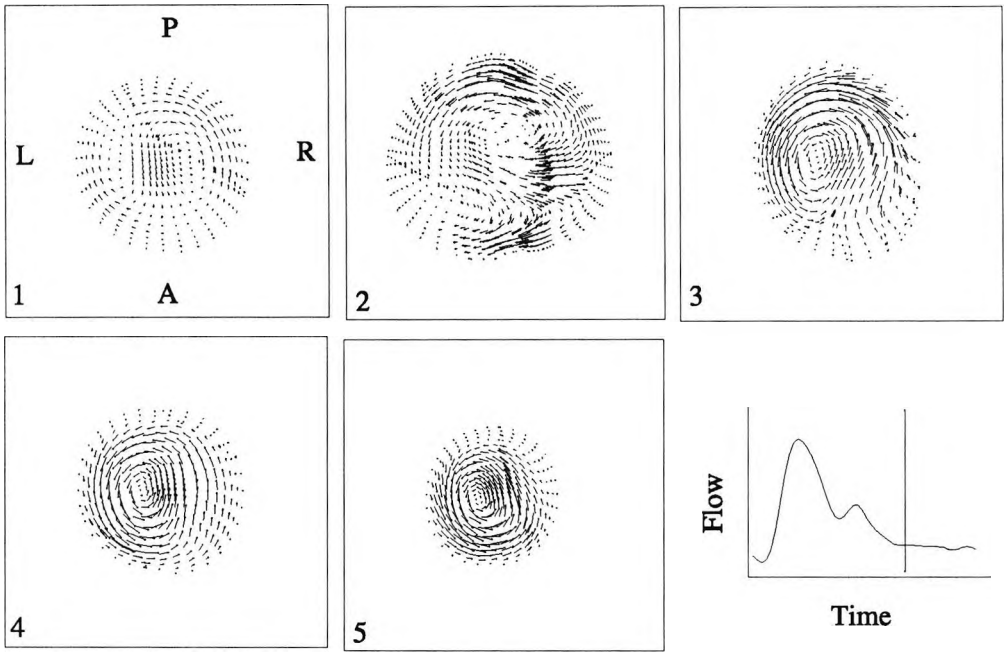

Figure 5.13: Secondary flow patterns at minimum flow phase in selected planes, as shown in Figure 5.10b–subject No.1.

(defined as axial velocity component less than 0.001m/s).

Figures 5.10 to 5.13 and Figures 5.14 to 5.17 display the secondary flow patterns especially in the bulb region at selected time points for subjects No.1 and No.2 respectively. In the common carotid near the bifurcation (plane 2), double vortices are evident during most part of the cycle in subject No.1. Treble vortices can be seen during flow deceleration in subject No.2. Consistent with previous findings, very strong secondary flow can be found in the bulb area in both subjects. However, in contrast to previous studies of planar bifurcations, secondary flow in the ICA is asymmetric with a singe dominant vortex. This is presumably a combined result of bifurcating and non-planarity. The flow during the deceleration phase was more disturbed and the region of reversed or slow flow zone was larger than during the acceleration phase, even though the instantaneous flow rates at these two time points were equivalent. Very intensive secondary flows were observed in flow deceleration phase (Figures 5.11 and 5.15), while less intensity at flow acceleration and the diastolic phase. It can also be seen that both the strength and centre of the vortex

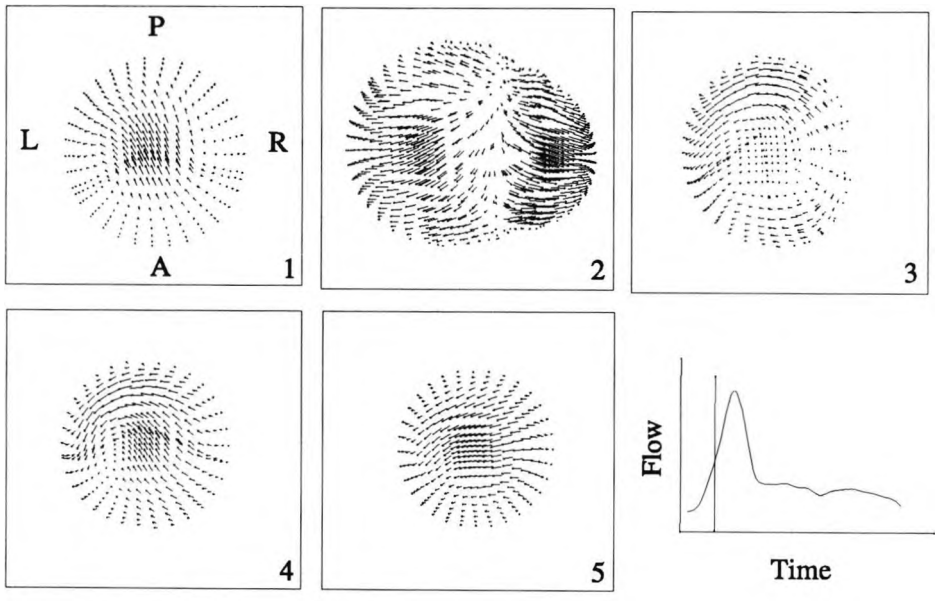

(a)

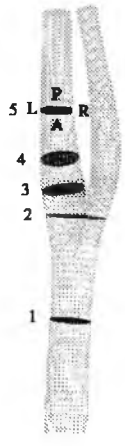

(b)

Figure 5.14: Secondary flow patterns midway through flow acceleration phase in selected planes–subject No.2.

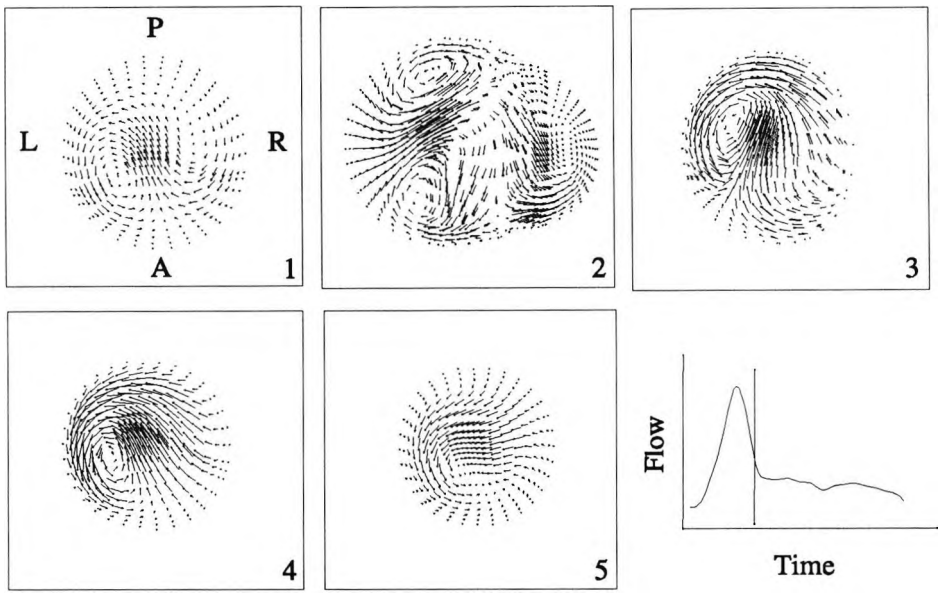

Figure 5.15: Secondary flow patterns midway through flow deceleration phase in selected planes, as shown in Figure 5.14b–subject No.2.

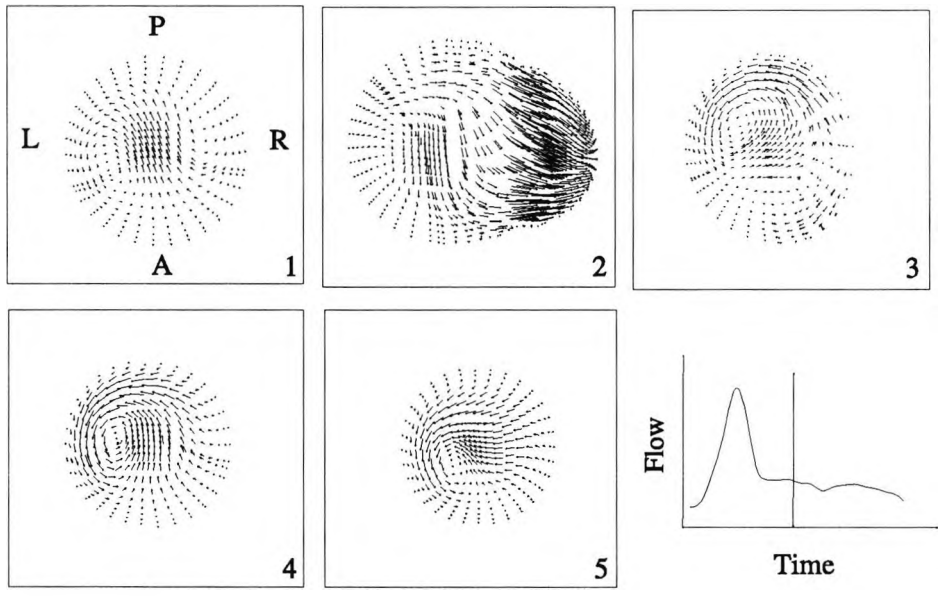

Figure 5.16: Secondary flow patterns at mid-diastole phase in selected planes, as shown in Figure 5.14b–subject No.2.

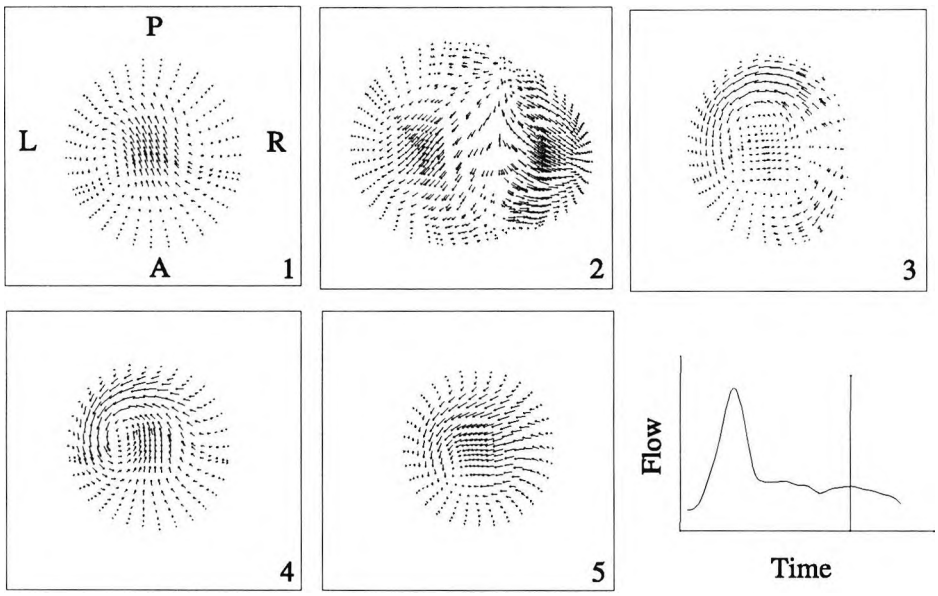

Figure 5.17: Secondary flow patterns at the end of diastole phase in selected planes, as shown in Figure 5.14b–subject No.2.

change with time, as the flow moves downstream.

In summary, inconsistent with previous findings from planar geometry models, flow in the carotid sinus is dominated by strong helical flows accompanied by a single secondary vortex motion. This type of flow is induced primarily by the asymmetry and curvature of the *in vivo* geometry.

5.5.2 Wall shear stress

Wall shear stress (WSS) is another very important feature of haemodynamics and still cannot be measured *in vivo* directly by current techniques. Numerical modelling is able to provide 4D quantitative distributions of WSS. Wall shear stress is a measure of the tangential shear forces acting on the wall by the fluid. It is determined by the wall shear rate (gradient of velocity at the wall) multiplied by the molecular viscosity of the fluid. In the present study, quadratic near wall velocity profiles were assumed so that wall shear

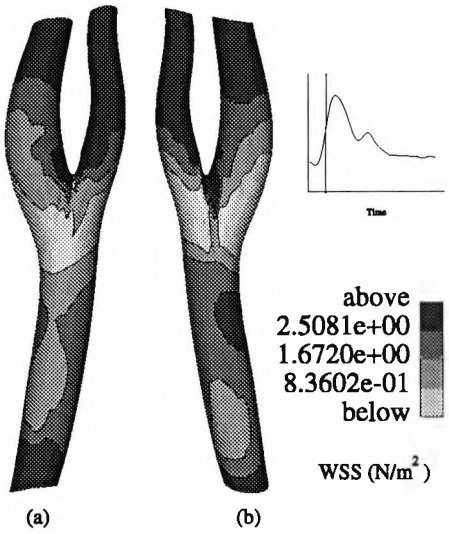

Figure 5.18: Wall shear stress magnitude distributions at flow acceleration phase seen from (a) posterior and (b) anterior aspects–subject No.1.

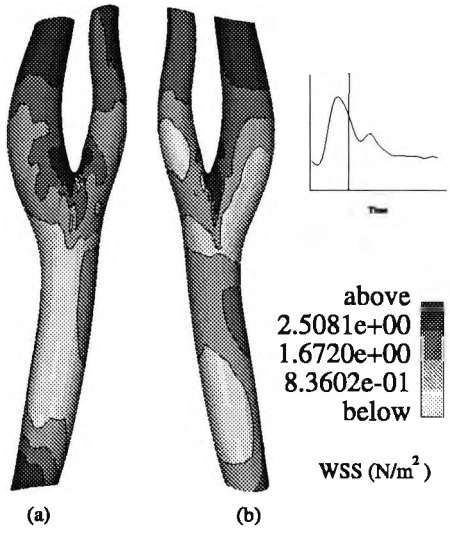

Figure 5.19: Wall shear stress magnitude distributions at flow deceleration phase seen from (a) posterior and (b) anterior aspects–subject No.1.

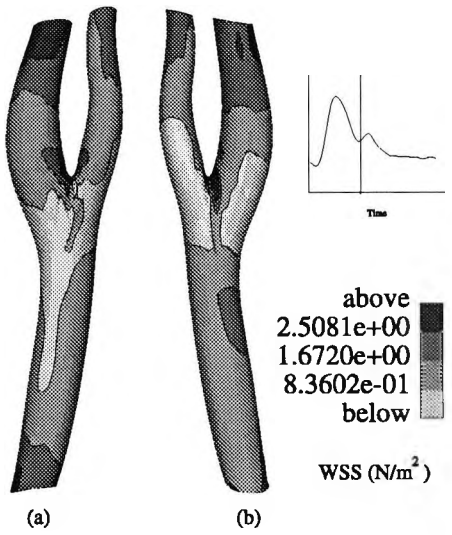

Figure 5.20: Wall shear stress magnitude distributions at end of first deceleration seen from (a) posterior and (b) anterior aspects–subject No.1.

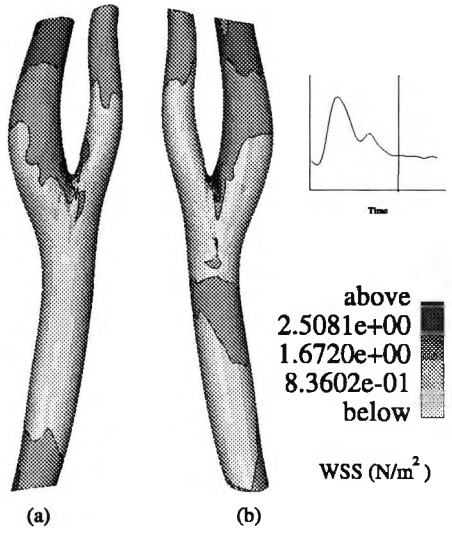

Figure 5.21: Wall shear stress magnitude distributions at minimum flow phase seen from (a) posterior and (b) anterior aspects–subject No.1.

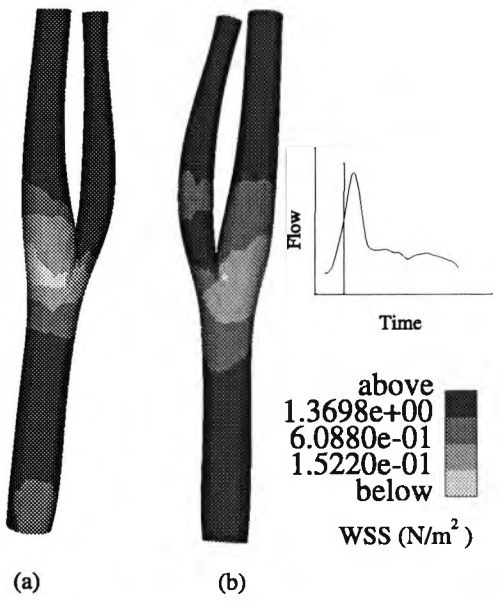

Figure 5.22: Wall shear stress magnitude distributions at flow acceleration phase seen from (a) posterior and (b) anterior aspects–subject No.2.

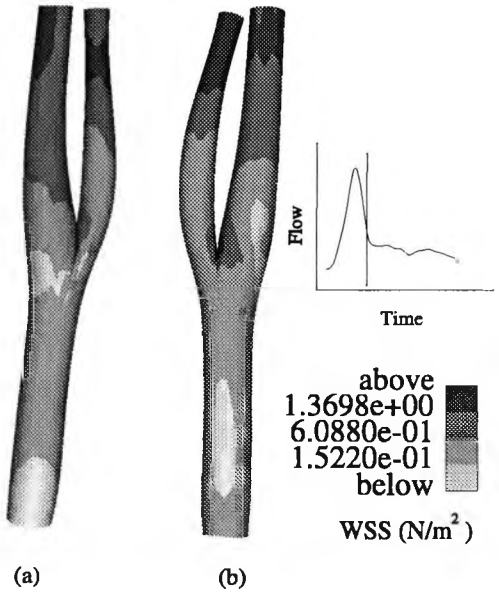

Figure 5.23: Wall shear stress magnitude distributions at flow deceleration phase seen from (a) posterior and (b) anterior aspects–subject No.2.

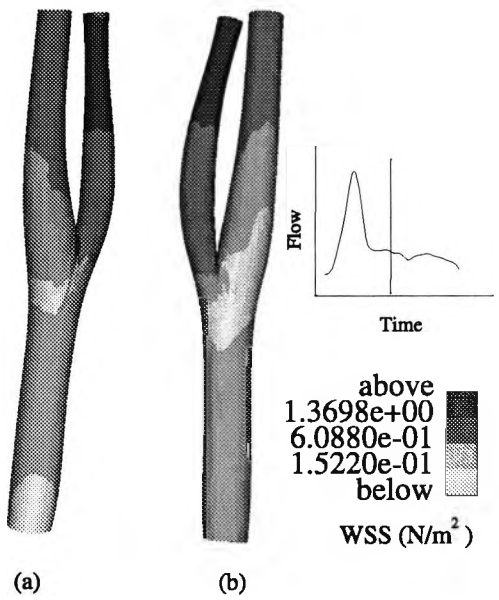

Figure 5.24: Wall shear stress magnitude distributions at mid-diastole phase seen from (a) posterior and (b) anterior aspects–subject No.2.

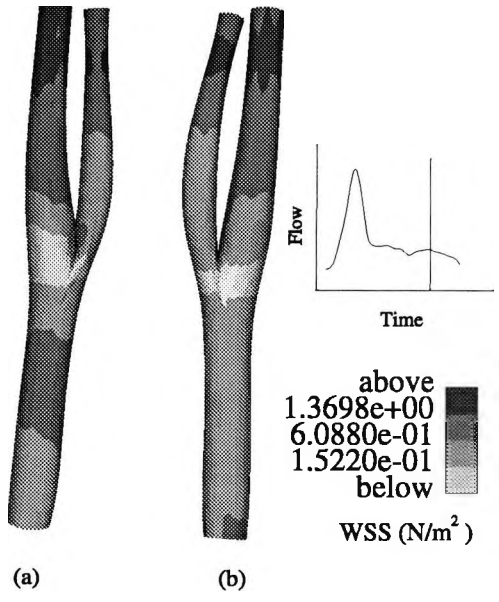

Figure 5.25: Wall shear stress magnitude distributions at the end of diastole phase seen from (a) posterior and (b) anterior aspects–subject No.2.

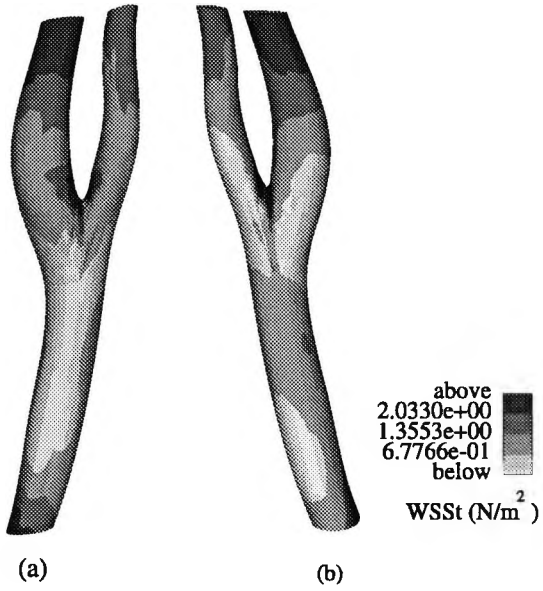

Figure 5.26: Time-averaged wall shear stress magnitude distribution seen from (a) posterior and (b) anterior aspects–subject No.1.

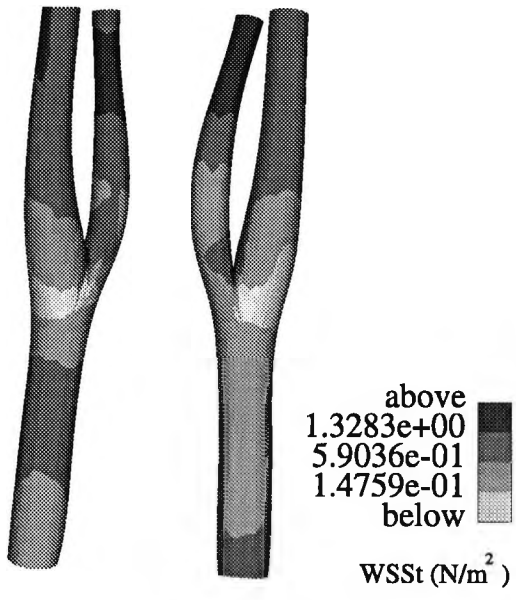

Figure 5.27: Time-averaged wall shear stress magnitude distribution seen from (a) posterior and (b) anterior aspects–subject No.2.

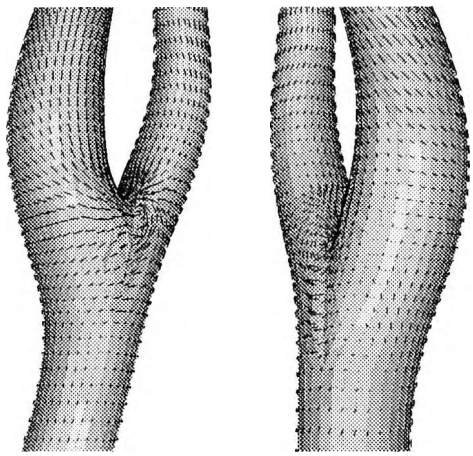

Figure 5.28: Zoom-in view of wall shear stress vector distributions at flow deceleration seen from (a) posterior and (b) anterior aspects–subject No.1.

rates were calculated by using velocities at three near wall points.

Maps of instantaneous wall shear stress magnitude at selected time points are presented in Figures 5.18 – 5.21 and Figures 5.22 – 5.25 for subjects No.1 and No.2 respectively. During flow acceleration, low wall shear is found in both proximal IC and EC in subject No.1. However, during flow deceleration, low shear still occurs in proximal IC but only at anterior aspect, while at posterior aspect low shear zone moves to most part of the CC, due to the skewing towards the anterior aspect of CC. At the end of the first deceleration phase, the region of low shear in CC becomes smaller. As flow reaches its minimum phase, low shear occurs nearly everywhere, because at this time flow velocity is overally low. In subject No.2, low shear occurs at the outer wall of proximal IC at flow acceleration with the lowest at the posterior aspect. The region becomes larger at flow deceleration and diastolic phase, but only confined to the internal-common side.

The time-averaged wall shear stress magnitude revealed high values at the bifurcation apex and moderately elevated values spiralling around the IC from the inner wall along

the superior direction for both subjects (Figure 5.26 and 5.27). In subject No.1, it can be seen that WSS is higher on the posterior wall (outer bend of the curvature) than on the anterior wall in both IC and EC. The lowest average shear was seen primarily at the proximal IC and EC. Average wall shear in the CC is higher on the anterior than on the posterior aspect due to the mild curvature of CC. In subject No.2, low wall shear mainly happens on the outer wall of ICA at both anterior and posterior aspects. Averaged wall shear in CC is slightly higher on the posterior aspect than on the anterior aspect.

Directional change of wall shear stress is very complicated in such *in vivo* carotid models. A vector-representation of wall shear stress distribution is presented in Figure 5.28 at the time of flow deceleration for subject No.1. It can be seen that the WSS vectors are unidirectional and is along the vessel axis in most part of the bifurcation. But at the carotid sinus, they are directed from the outer wall towards the inner wall, perpendicular to the vessel axis as a result of very strong helical flow in the region. Furthermore, the magnitudes of these cross WSS are almost comparable to those along the axial direction.

5.5.3 Wall movement and mechanical stress

The vessel wall mechanical behaviour was analysed in terms of of displacements and principal stresses. In a general shell structure, stresses in global system do not give a clear picture of shell surface stresses. It is convenient to compute the principal stresses which are defined as the stress state associated with the principal planes that are subjected to only normal stresses. Figures 5.29 to 5.32 and 5.33 to 5.36 show the displacement magnitude distribution at selected time points for both subjects. In subject No.1, the maximum wall movement occurs at the proximal end of EC. Further examination of the displacement variations at different cross-sectional levels (Figures 5.37 to 5.40) show that wall movement in the CCA and ICA is mainly due to cross sectional dilation, while in the ECA it involves dilation as well as lateral movement. In these figures, horizontal lines represent the original locations of corresponding diameters at the end of diastolic phase, so together with the deformed lumen outlines they demonstrate how much and in which direction the vessels have moved. In subject No.2, the maximum displacement occurs at

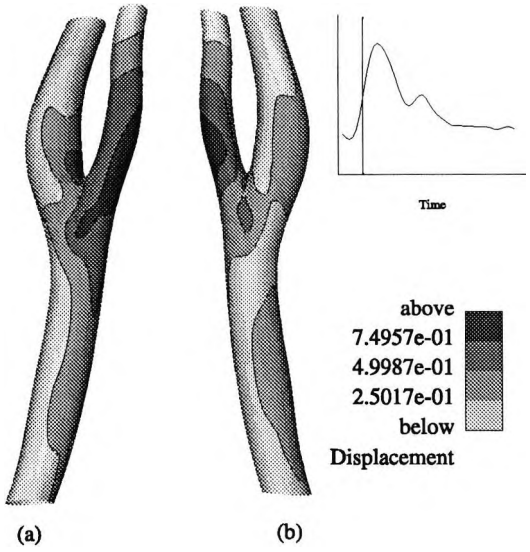

Figure 5.29: Wall movement distribution (mm) at flow acceleration seen from (a) posterior and (b) anterior aspects–subject No.1.

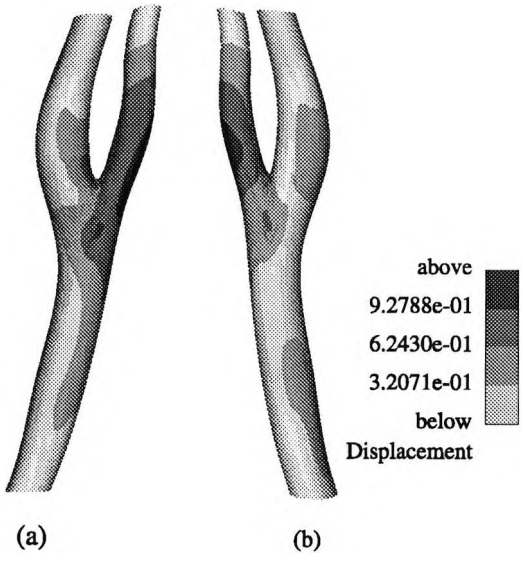

Figure 5.30: Wall movement distribution (mm) at peak systole seen from (a) posterior and (b) anterior aspects–subject No.1.

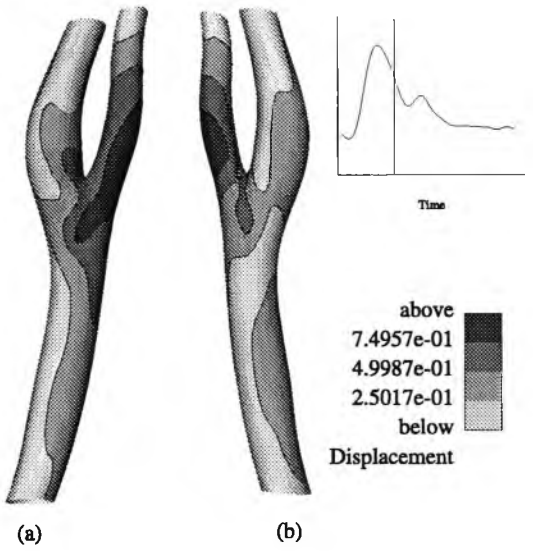

Figure 5.31: Wall movement distribution (mm) at flow deceleration seen from (a) posterior and (b) anterior aspects–subject No.1.

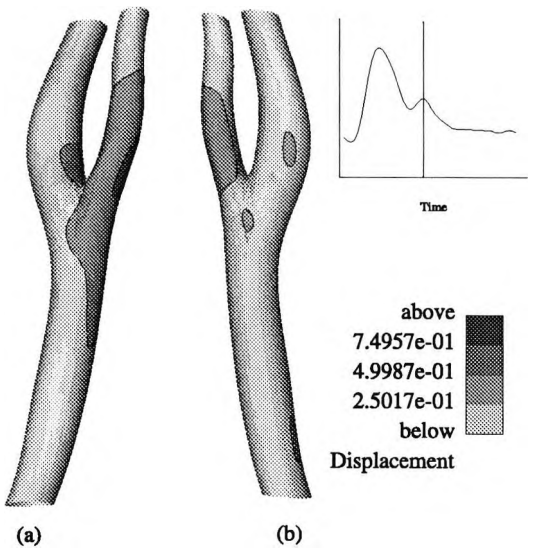

Figure 5.32: Wall movement distribution (mm) at second peak flow phase seen from (a) posterior and (b) anterior aspects–subject No.1.

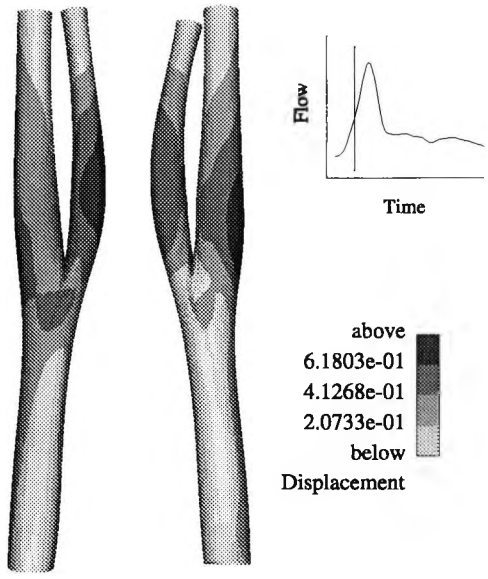

Figure 5.33: Wall movement distribution (mm) at flow acceleration seen from (a) posterior and (b) anterior aspects–subject No.2.

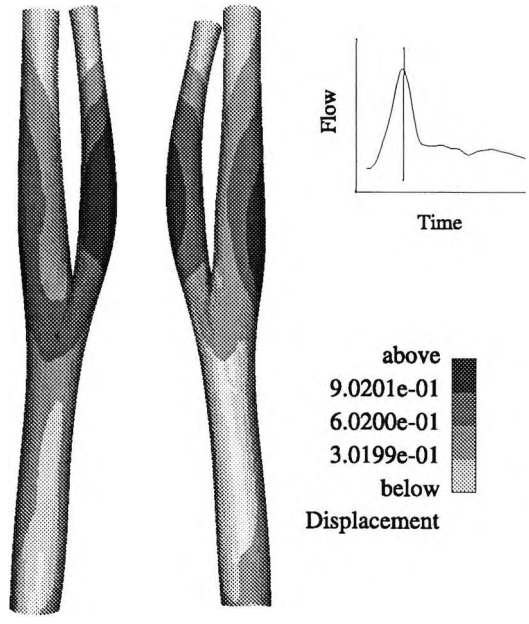

Figure 5.34: Wall movement distribution (mm) at peak systole seen from (a) posterior and (b) anterior aspects–subject No.2.

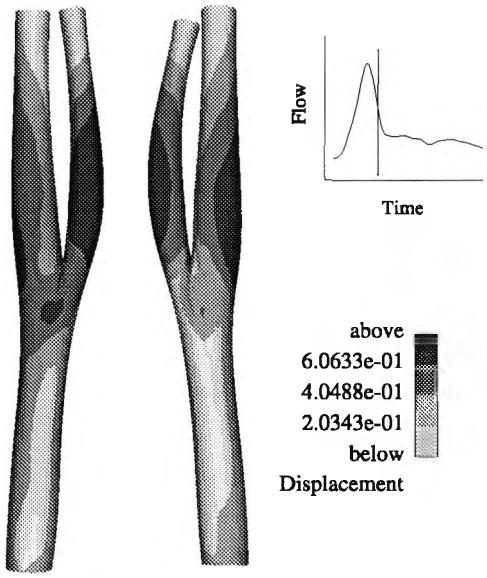

Figure 5.35: Wall movement distribution (mm) at flow deceleration seen from (a) posterior and (b) anterior aspects–subject No.2.

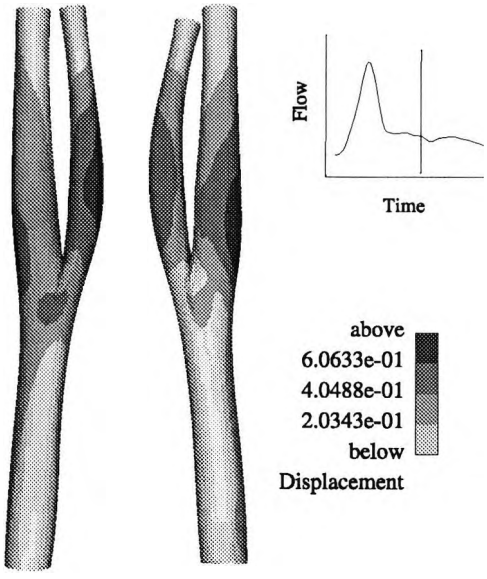

Figure 5.36: Wall movement distribution (mm) at mid-diastole phase seen from (a) posterior and (b) anterior aspects–subject No.2.

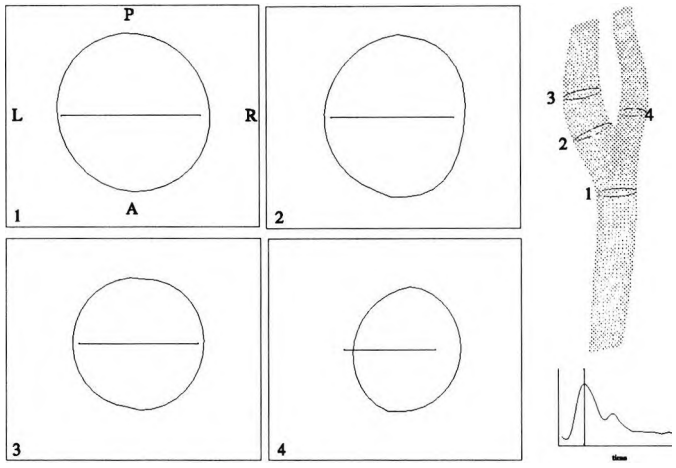

Figure 5.37: Cross sectional variations at peak systole in different locations. The horizontal lines represent the original positions of corresponding diameters in diastole–subject No.1.

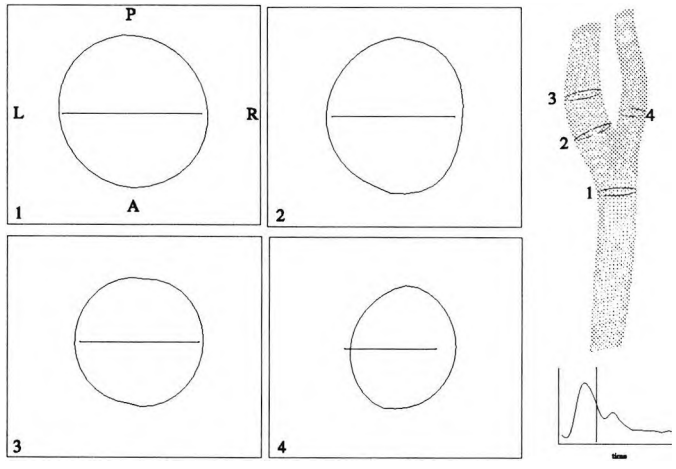

Figure 5.38: Cross sectional variations at flow deceleration in different locations. The horizontal lines represent the original positions of corresponding diameters in diastole–subject No.1.

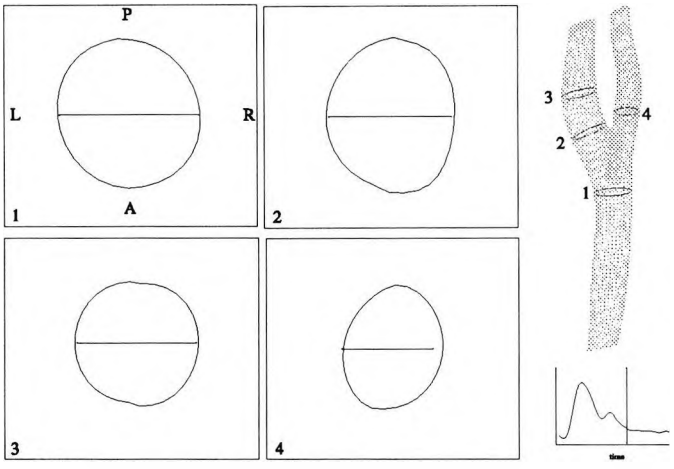

Figure 5.39: Cross sectional variations at mid-diastole in different locations. The horizontal lines represent the original positions of corresponding diameters in diastole–subject No.1.

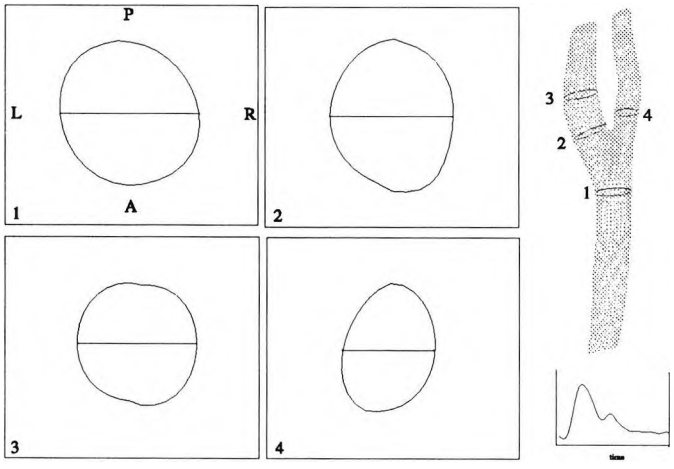

Figure 5.40: Cross sectional variations at the end of diastole in different locations. The horizontal lines represent the original positions of corresponding diameters in diastole–subject No.1.

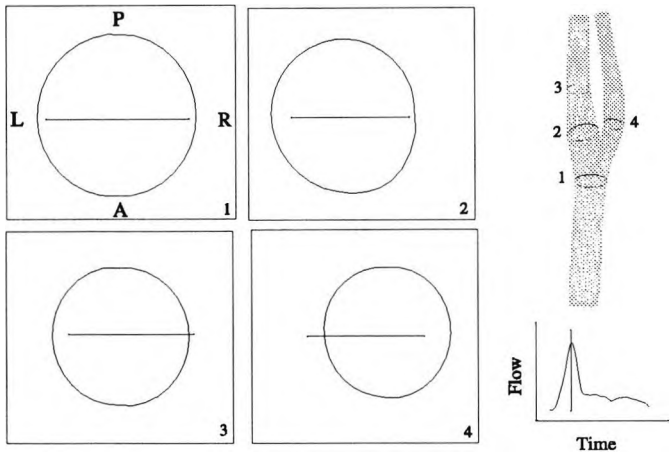

Figure 5.41: Cross sectional variations at peak systole in different locations. The horizontal lines represent the original positions of corresponding diameters in diastole–subject No.2.

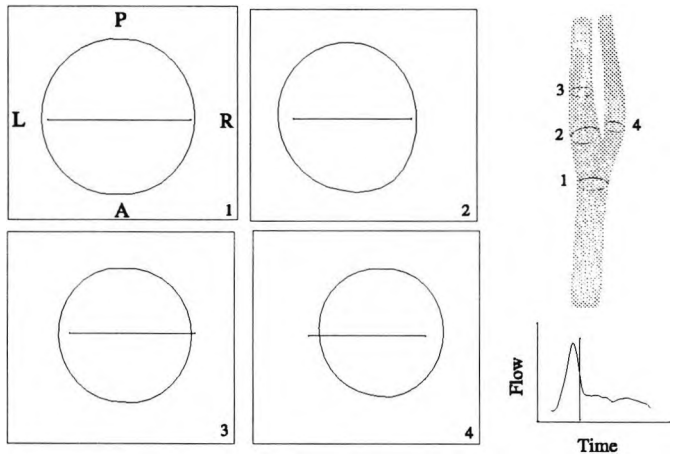

Figure 5.42: Cross sectional variations at flow deceleration in different locations. The horizontal lines represent the original positions of corresponding diameters in diastole–subject No.2.

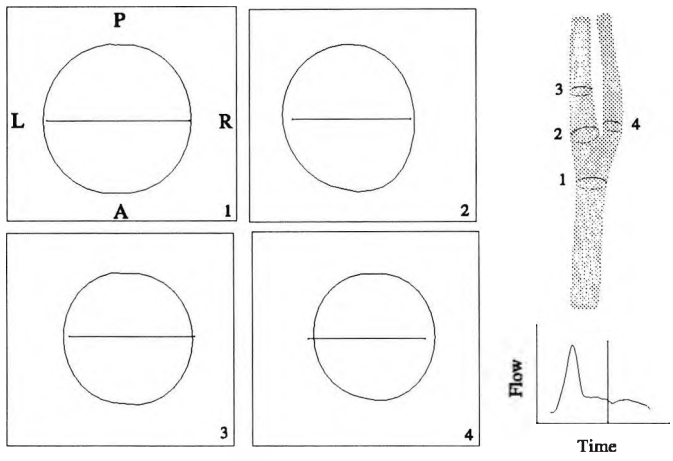

Figure 5.43: Cross sectional variations at mid-diastole in different locations. The horizontal lines represent the original positions of corresponding diameters in diastole–subject No.2.

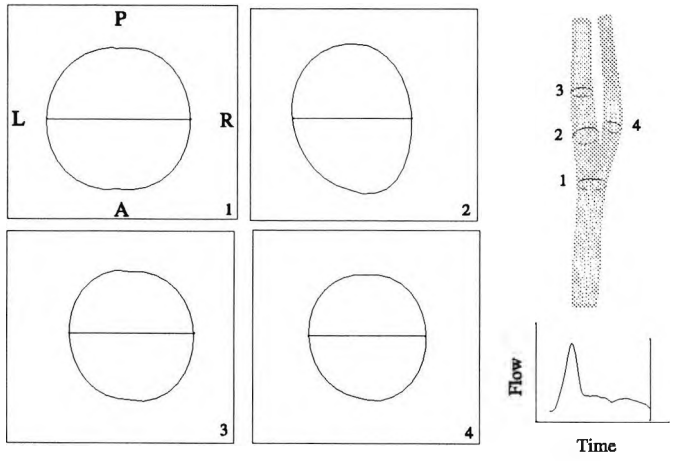

Figure 5.44: Cross sectional variations at the end of diastole in different locations. The horizontal lines represent the original positions of corresponding diameters in diastole–subject No.2.

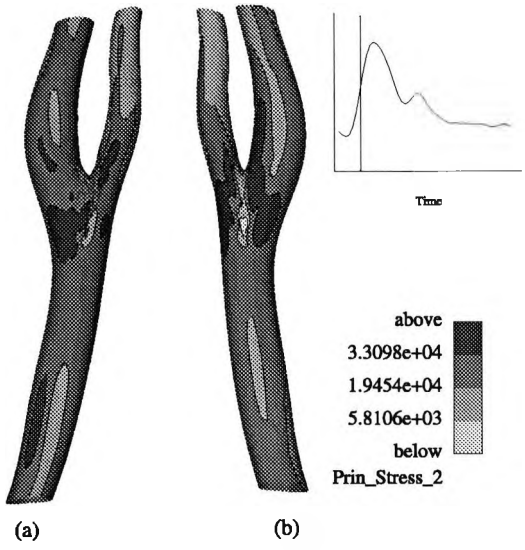

Figure 5.45: Maximum principal stress distribution (Pa) on the inner surface at flow acceleration seen from (a) posterior and (b) anterior aspects–subject No.1.

proximal ends of ICA and ECA. By further analysing cross-sectional variations (Figures 5.41 to 5.44), it can be found that the movement of IC and EC involves dilation and lateral movement which is in the direction away from the flow divider.

Figures 5.45 to 5.48 and Figures 5.49 to 5.52 are plots of the maximum principal stress distribution at the inner surface of the wall at selected time points. Generally the bifurcations exhibit similar patterns during the cardiac cycle, but differ in magnitude at different time during the cycle. For subject No.1, the stress concentration factor, defined as the ratio of the local stress to the nominal circumferential stress (which is Pr/t, where P is the pressure, r the radius, and t the thickness of the common carotid), is 3.10 and is in the bulb region. The analysis showed a small high stress region at the anterior aspect of the proximal EC. It can be noticed that the maximum principal stress is stretched along the anterior aspect of the bulb, which covers much greater area than those in the EC. In subject No.2, it is observed that high stress happens only at the proximal IC, with a stress concentration factor of 2.8. By comparing with Figures 5.26 and 5.27, it can be noticed that these high stress regions overlap to a great degree with the areas of low wall shear stress in both subjects. It may be this fact that allows the lesions in the sinus bulb to

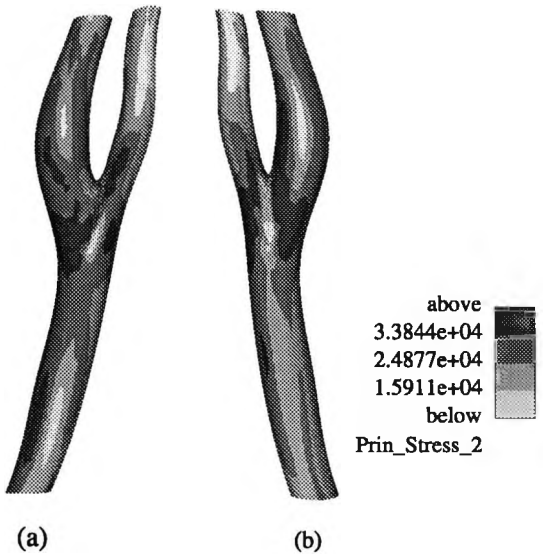

Figure 5.46: Maximum principal stress distribution (Pa) on the inner surface at peak systole seen from (a) posterior and (b) anterior aspects–subject No.1.

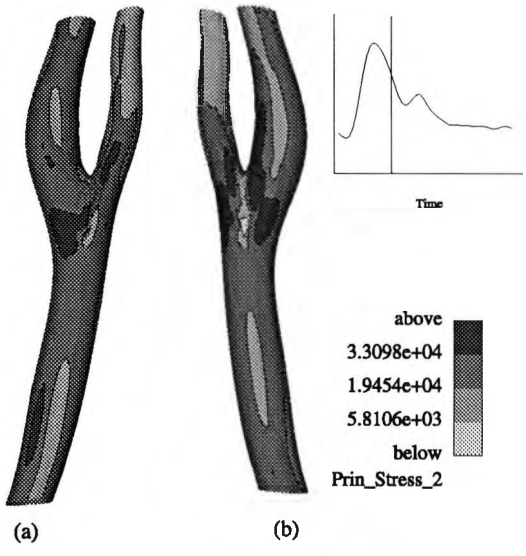

Figure 5.47: Maximum principal stress distribution (Pa) on the inner surface at flow deceleration seen from (a) posterior and (b) anterior aspects–subject No.1.

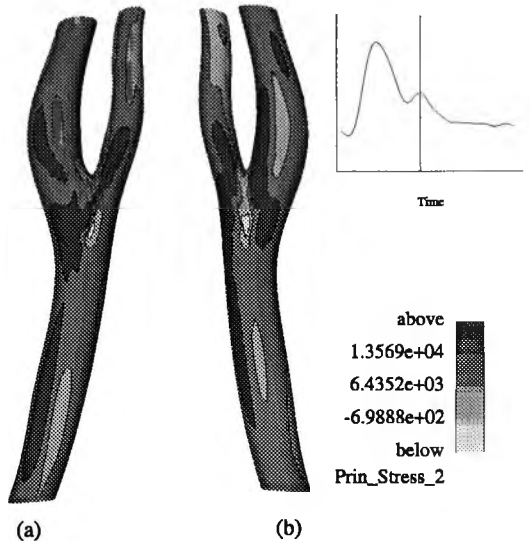

Figure 5.48: Maximum principal stress distribution (Pa) on the inner surface at mid-diastole seen from (a) posterior and (b) anterior aspects–subject No.1.

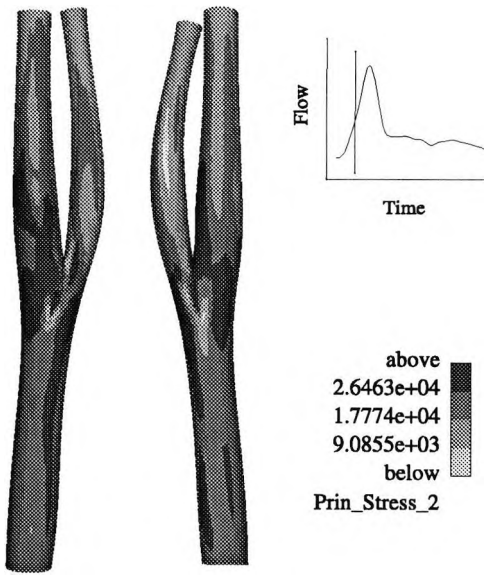

Figure 5.49: Maximum principal stress distribution (Pa) on the inner surface at flow acceleration seen from (a) posterior and (b) anterior aspects–subject No.2.

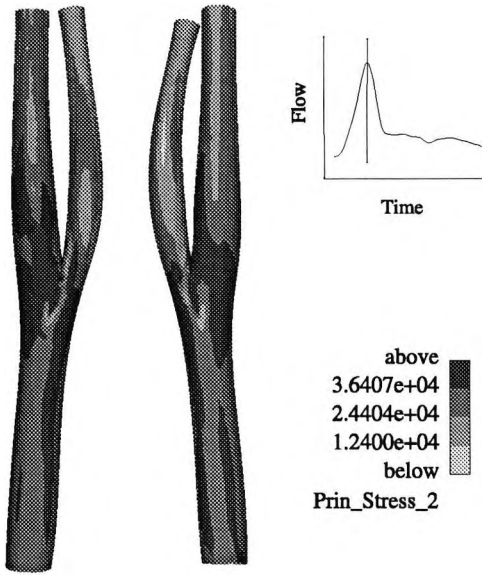

Figure 5.50: Maximum principal stress distribution (Pa) on the inner surface at peak systole seen from (a) posterior and (b) anterior aspects–subject No.2.

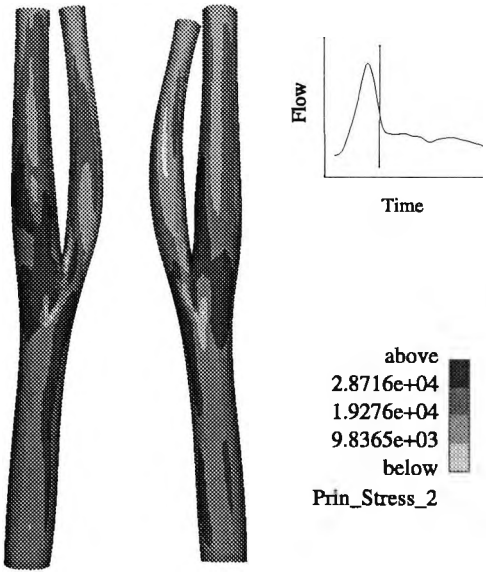

Figure 5.51: Maximum principal stress distribution (Pa) on the inner surface at flow deceleration seen from (a) posterior and (b) anterior aspects–subject No.2.

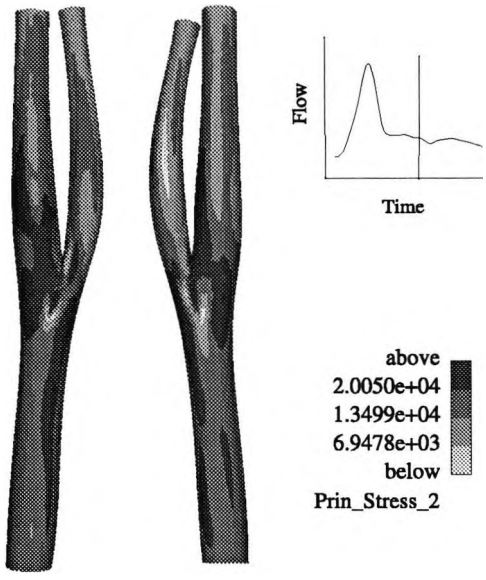

Figure 5.52: Maximum principal stress distribution (Pa) on the inner surface at mid-diastole seen from (a) posterior and (b) anterior aspects–subject No.2.

develop.

Generally, the analysis of mechanical stresses on the vessel surface shows a complicated stress field. High stress distribution occurs at both the anterior and posterior aspects of the proximal internal bulb. These are also regions of low wall shear stress.

5.5.4 Effect of wall distensibility

To examine the influence of wall compliance, numerical predictions for subject No.1 under the rigid wall assumption have been performed for the purpose of comparison. The influence of wall distensibility on slow moving zone is shown in Figure 5.53 and 5.54 at peak systole and the end of diastole respectively. By examining similar figures to the above two at different time points during the cardiac cycle (not shown here due to space limit), it can be found that the influence of wall movement on the slow moving zone varies during the cardiac cycle with maximum at peak systole and minimum at the end of diastole. In the compliant model the slow moving zones extend further upstream at peak systole

and are much greater than those in the rigid model during most of the cycle, while the slowing moving zone is slightly smaller at the end of diastole. Secondary flow is not found to differ significantly between the rigid and compliant models. The quantitative influence of wall distensibility on wall shear stress is demonstrated in Figure 5.55, by comparing the magnitude of wall shear stress with the results under the rigid wall assumption. Two cross sections in the carotid sinus were selected for the comparison, with one at the immediate entrance and another at one diameter downstream. The wall shear stress (WSS) magnitude variations are plotted versus time. Information regarding direction was not included in this plot because directional changes are very complicated in such an *in vivo* bifurcation model (again see Figure 5.28). The largest difference occurs at peak systole with less influence of wall distensibility at diastole. This may be attributed partly to the wall motion which transiently enlarged the cross-sectional area, causing the instantaneous velocities everywhere in the cross section to decrease by comparison with rigid model, in accordance with the conservation of mass. The peak systolic phase exhibits significant wall motion and can be considered as an extreme case of shear stress deviation between the compliant and rigid models.

Comparisons of the results for both compliant and rigid cases have demonstrated the quantitative influence of the vessel wall motion. Generally in a compliant model there is a reduction in the magnitude of wall shear stress, with its degree depending on location and phase of the cardiac cycle. It can be reduced as much as 60% at some locations in the case examined. The region of slow or reversed flow is greater, in both spatial and temporal terms during most part of the cycle in the compliant model, but the global characteristics of the flow and stress patterns remain unchanged.

It is widely accepted that the magnitude and distribution of wall shear stress exerted by the flowing blood on an artery wall have an important influence on biological changes in the wall [203, 204]. This study indicates that assumption of a rigid wall model underestimates the temporal and spatial magnitude of the slow moving zone and overestimates wall shear stress magnitude. It is widely believed that this haemodynamic condition (like wall shear stress, slow moving zone) is an important determinant of atherogenesis, conse-

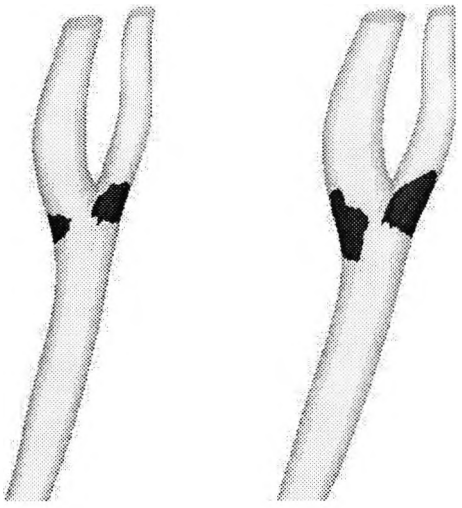

(a) (b)

Figure 5.53: Comparison of slow moving zone of (a) rigid model, and (b) compliant model at peak systolic phase.

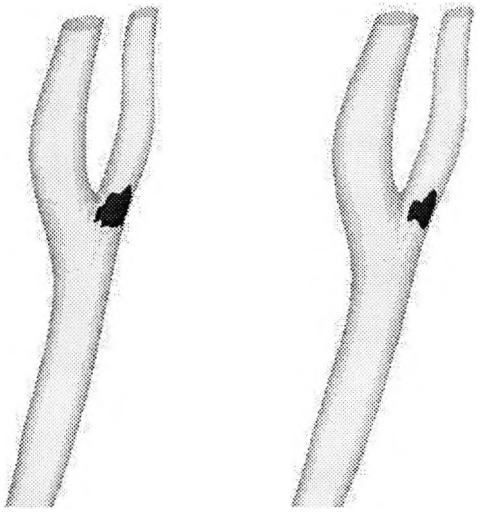

(a) (b)

Figure 5.54: Comparison of slow moving zone of (a) rigid model, and (b) compliant model at the end of diastole.

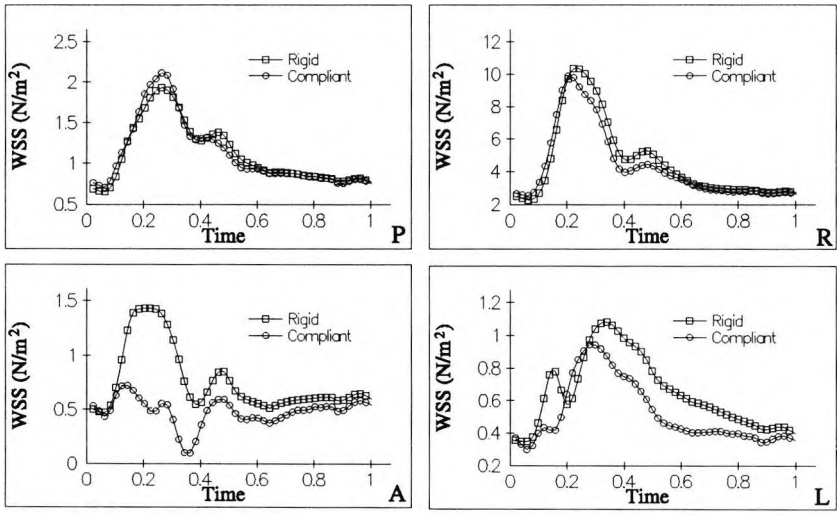
WSS (N/m²)
Time
Rigid
Compliant
P
R
A
L

(a)

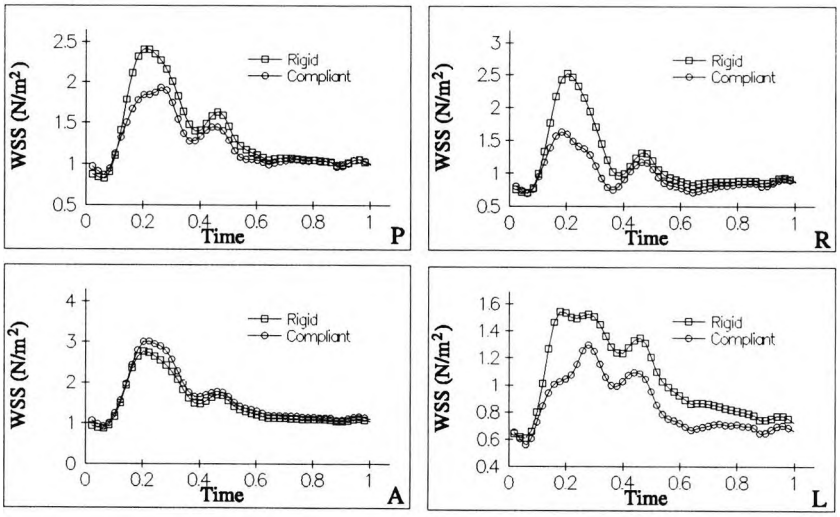
WSS (N/m²)
Time
Rigid
Compliant
P
R
A
L

(b)

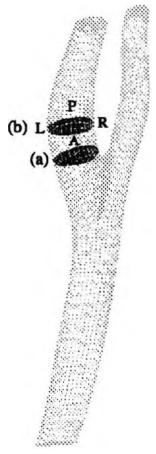

(c)

Figure 5.55: Comparisons of wall shear stress magnitude at two selected locations in the internal carotid artery (Posterior, Right, Anterior, and Left points) of the coupled model and its corresponding rigid model ((a) carotid sinus, and (b) one-diameter downstream of (a), as shown in (c)).

quently inclusion of compliant wall would appear to be important for the understanding of the pathogenesis of this condition.

The influence of wall distensibility has also been reported by others. Duncan et al. [163] have studied experimentally a compliant model of an aortic bifurcation and found that compliance reduced the shear rate at the outer walls and increased the shear rate at the inner walls. Liepsch et al. [160] investigated the flow fields in rigid and silicon rubber models of renal leg and coronary arteries. They reported that shear stresses were reduced in compliant models. Anayiotos et al. [164] compared wall shear stress distribution in rigid and compliant models of a carotid bifurcation using laser Doppler velocimetry. Their compliant model displayed a diameter variation of 4 to 7 percent. Their results indicated that vessel compliance reduced the mean wall shear rate level by about 30% at most locations. The effect of compliance was more significant for both positive and negative shear stresses, which were reduced by as much as 100% in the compliant model in some locations. Similarly in computer simulations, Perktold and Rappitsch [42] reported a 25% decrease of WSS in a compliant rather a rigid, model of the carotid bifurcation; and Hofer et al.

[148] reported that the WSS was in general lower for a distensible end-to-side anastomosis model when compared to a rigid one.

5.6 Validations

The sources of errors which may arise in the numerical predictions may be attributed to : (1)the mathematical model, (2) the discretisation method, and (3) the numerical algorithm. The validity of the mathematical model for arterial flows has been discussed extensively [170, 42, 98]. Since the flow is laminar for which the mathematical equations involve no empiricism, the accuracy of the predictions is expected to be in a good order. The magnitude of the discretisation error is dependent upon both the discretisation method and the mesh density. This error can be reduced by either using a higher-order discretisation formula designed to reduce the truncation error, or refining the grid. The latter is problem dependent. The errors associated with the numerical algorithm are dominated by the convergence criteria.

No numerical codes could give guaranteed reasonable and accurate results to all types of problems, even within the code's capability. Their successful use often requires experienced staff, and even then, the degree to which codes can be routinely used as black boxes may be quite limited. In general, validation exercises involve one or all of the following comparisons:

Internal validations

- refining the density of the mesh,
- refining the time step, if the problem is time-dependent.

External validations

- comparison with analytical solutions if one exists,
- comparison with *in vivo* or *in vitro* measurements,

- code to code comparisons.

Although accurate results (grid-independent and/or time step-independent) are the first requirement for reliable numerical predictions, the use of cells and time steps infinitely small is prohibitive and impracticable due to the large amount of CPU time, memory, and storage space required. Moreover, a huge dump file will cause difficulties or even crash down the computer during post-processing.

Due to the large amount of data involved, validations were only made for subject No.1. In this study, validations were carried out in two aspects. Firstly, computational uncertainties were assessed by the internal validation. The internal validation has been achieved by testing the predicted results of the numerical model at different grid density and time steps to guarantee results are grid and time-step independent. Secondly, comparison was made between the predicted results and *in vivo* measured data.

5.6.1 Internal temporal and spatial resolution tests

The idea was to use smaller time steps and refined grid density to examine whether the same results could be obtained. It is known that the flow and the resulting wall shear stress in the bulb region are very sensitive to any change and are also our particular area of interest. Because of this, selected points at two cross-sectional areas in this region were chosen for the comparison. First, the number of time steps used in one cardiac cycle was increased from 50 to 100. The wall shear stress variations at the two cross-sections (as indicated in Figure 5.55c) in the IC are shown in Figure 5.56. It can be seen that the curves are almost identical. Further tests were made on grid density. The computational grid was refined from 25,600 to 30,400 cells, with proportional changes in the radial, circumferential and longitudinal directions respectively. The comparisons of wall shear stress variations at the same selected two planes as in the temporal test are shown in Figure 5.57. As can be seen, no significant change in the resulting wall shear stress can be found between the two cases. Results of these calculations indicated that the first set of parameters were sufficient for the present purpose and could give reasonably accurate predictions.

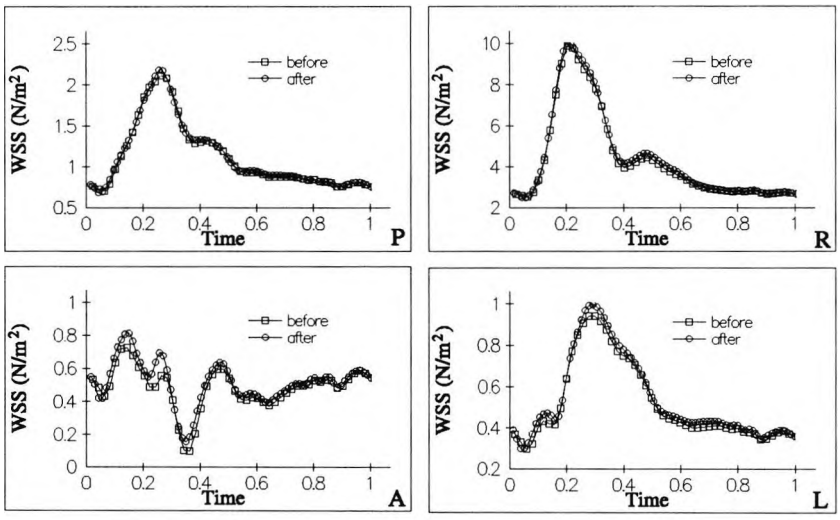

(a)

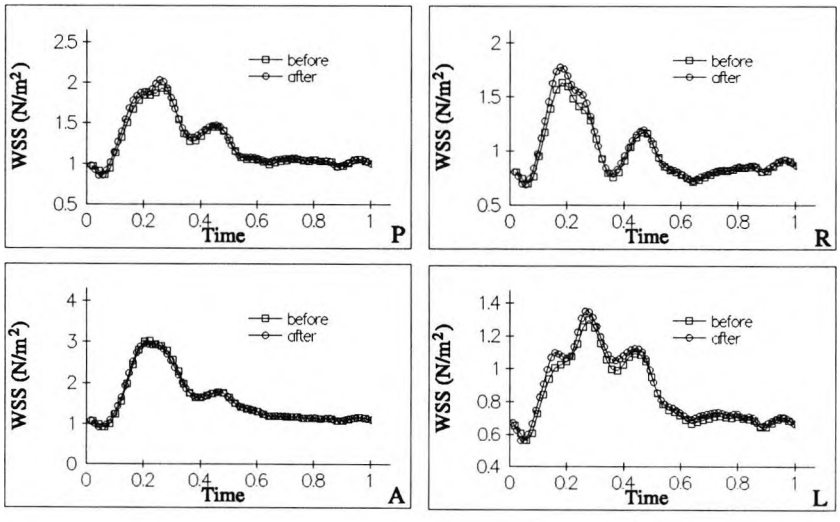

(b)

Figure 5.56: Comparisons of wall shear stress magnitude at two selected locations in the internal carotid artery (Posterior, Right, Anterior, and Left points) of the coupled model before and after time step refinement ((a) carotid sinus, and (b) one-diameter downstream of (a), as shown in Figure 5.55(c)).

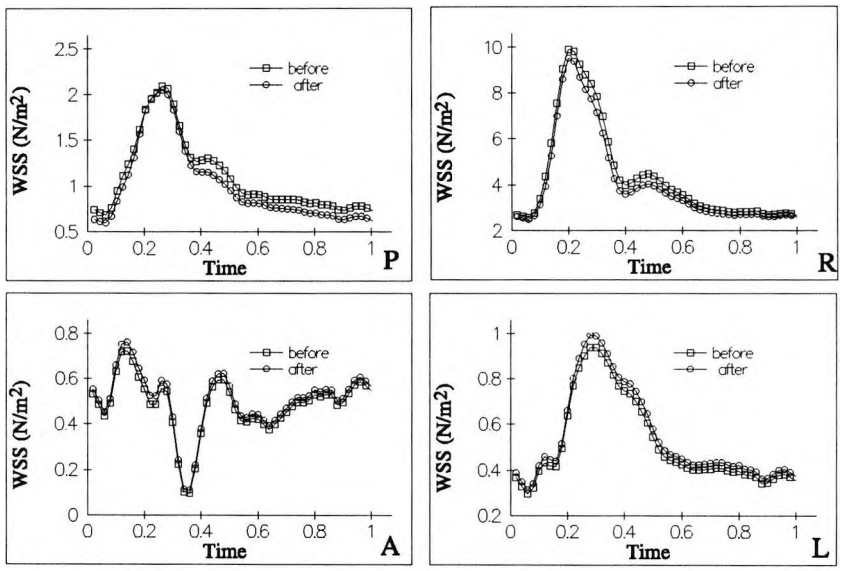

(a)

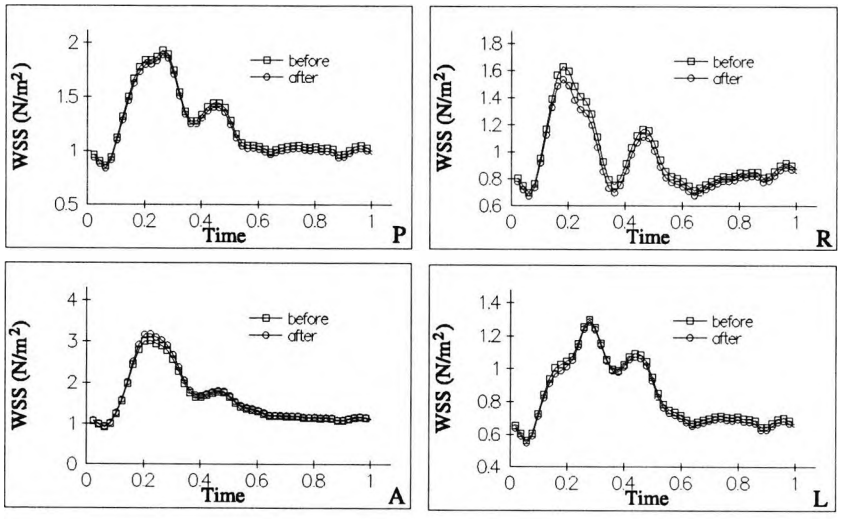

(b)

Figure 5.57: Comparisons of wall shear stress magnitude at two selected locations in the internal carotid artery (Posterior, Right, Anterior, and Left points) of the coupled model before and after grid refinement ((a) carotid sinus, and (b) one-diameter downstream of (a), as shown in Figure 5.55(c)).

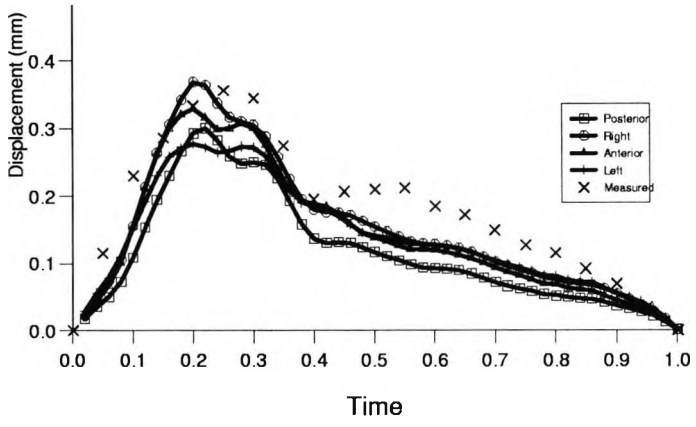

Figure 5.58: Validated wall movement variation in the common carotid at two diameters upstream from the bifurcation against measured data.

5.6.2 Overall validation against experimental measurements

To verify the computational results, quantitative comparisons between calculations and the *in vivo* measurements were made. Figure 5.58 shows the computed and experimentally measured wall movement at a cross-section two diameters inferior to the bifurcation apex during a cardiac cycle. The experimental data was obtained by analysing the ultrasound M-mode image acquired at this site, and showed that the wall motion could be divided into three phases: rapid dilation, rapid partial contraction, and slow contraction. The numerical predictions also demonstrate these phases. The quality of the agreement between the physical and numerical experiments is more likely to be limited by the accuracy of the former (see Figure 5.7), where the spatial resolution requirements are rigorous. From Figure 5.58 it can also be seen that the wall movement curve follows that of the pressure waveform (Figure 5.5(b)). This demonstrates that the pressure waveform plays the main part in driving the wall movement while the pressure gradient resulting from the flow only has a secondary influence.

For the flow field, the predicted velocities were compared with those obtained by experiment. In this study, MR measured velocities at a plane in the common carotid were used for comparison. The scan parameters were: TR: 36ms, TE: auto, Flip angle: 25°, FOV: 12x12cm, Slice thickness: 5mm, Matrix 256x256, NEX: 2. Comparisons were presented by plotting velocity profiles along the L-R and A-P axes. Figure 5.59 shows the

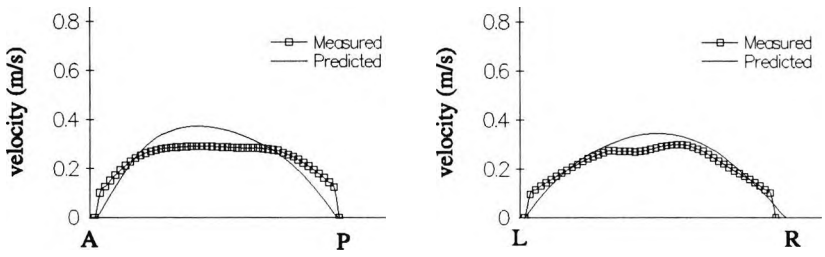

(flow acceleration)

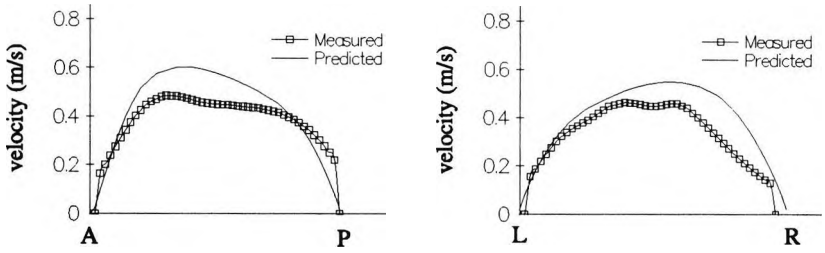

(flow acceleration)

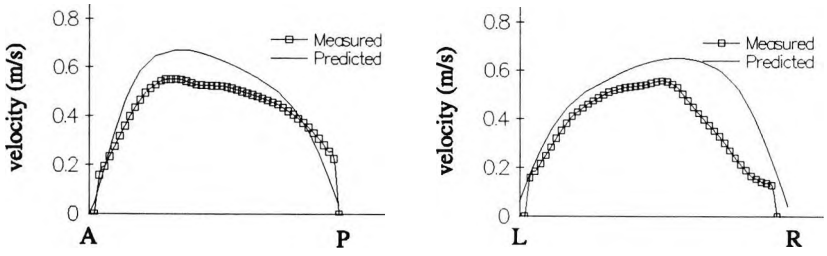

(peak flow)

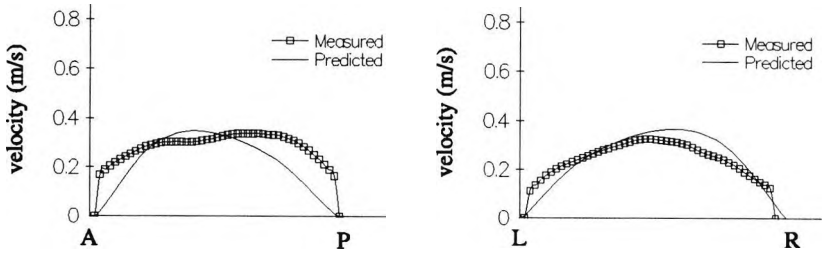

(flow deceleration)

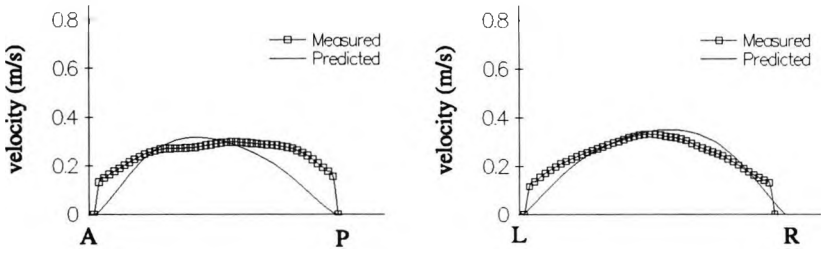

(flow deceleration)

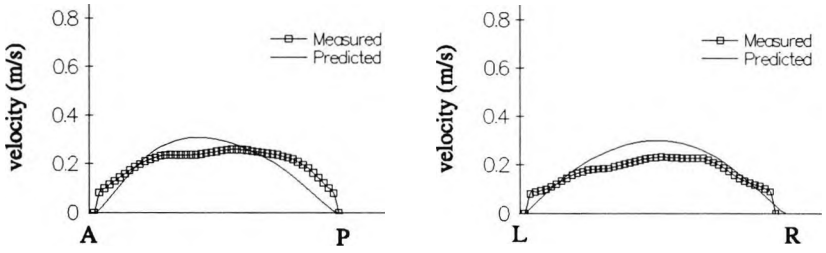

(flow deceleration)

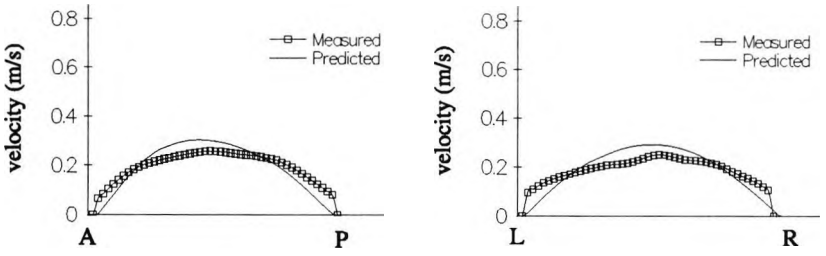

(end of diastole)

Figure 5.59: Comparisons of predicted and measured velocity profiles at a cross-sectional plane in the common carotid.

predicted velocity profiles and those of the *in vivo* measurements at the selected plane during the cardiac cycle. The plot is organised according to the progression of time. Comparisons demonstrate good agreement between the calculations and measurements in both directions except at peak systole, where predicted results are somewhat higher than measurements. But the curve tendency follows those of the measurements very well. In both measured and predicted results, profiles are generally skewed towards the anterior and right walls.

Although, generally a good agreement has been obtained, local discrepancies at some part during the cardiac cycle exist. These discrepancies may be attributed to several factors. Firstly, the velocity was measured by a typical MR Cine 2D PC scan which involved uncertainties about the velocity close to the wall and the position of the moving wall itself due to the partial volume effects which account for the sharp jump in Figure 5.59 at near wall points A, P, L, and R. In this case, most of the spins have near zero velocities so that an accurate velocity image segmentation becomes very difficult. Errors can also come from velocity image processing and registration. Secondly, the accuracy of the simulation is sensitive to boundary conditions. Therefore, some uncertainties may be introduced by boundary condition settings in the numerical model, such as the fully developed flow assumption. Thirdly, factors such as complex flow, subject movement during scanning may introduce additional errors in MR velocity imaging, which is likely to give misleading results. Therefore, comparison at this stage can only be done with caution.

5.7 Summary

Numerical simulations of blood flow and vessel mechanics in real human carotid arterial bifurcations have been carried out under physiological pulsatile flow conditions. The current work employs realistic geometry models derived from *in vivo* MRI scans of the human carotid bifurcations and a comprehensive, coupled fluid-wall approach to deal with the blood/wall interactions. This minimises the assumptions adopted in previous numerical models in two ways: (1) it adopts *in vivo* bifurcation geometry rather than averaged or idealised models; (2) use of a coupled blood/wall simulation rather than rigid wall as-

sumption. To prove the stability and reliability of the approach, the validation has been designed to include both numerical accuracy and overall validations. In the latter, the calculated wall movement and velocities were validated against experimental data.

The numerical simulation displays a pattern of high tensile stress and low wall shear stress distribution in those areas most prone to atherosclerosis. Perhaps the combination of low wall shear stress and high stress concentration might be correlated to the vascular disease. High tensile stresses are associated with vessel wall thickening and alternations in composition [27]. Currently, the detailed mechanisms for stress or strain-induced wall thickening are not completely understood and may involve effects on endothelial and smooth muscle function [205]. Recent studies have demonstrated that endothelial cells respond to flow by producing a range of transcription factors [206, 207]. This induces a complex pattern of change in the endothelial cells in addition to stimulating the release of a variety of chemotactic factors and mitogens which cause smooth muscle cells to migrate and proliferate [208, 11]. Shear stress has also been shown to upregulate the expression of endothelial nitric oxide synthase which controls the production of the potent vascular smooth muscle relaxing factor nitric oxide [209, 210]. Davies [204, 211] and Du et al. [212] suggested that mechanical forces may induce the transcription factors responsible for the above events via intracelluar signal transduction pathways. In this way, the large and concentrated mechanical forces which exist at bifurcations and curvatures may lead to the cellular proliferation and chemotactic factor production associated with intimal thickening and atherosclerosis.

Chapter 6

Conclusions

In this thesis a comprehensive numerical method combining two established commercial codes for solving coupled solid/fluid problems has been developed and applied to the simulation of blood flow in arterial structures. The finite volume method based CFX was used as the fluid dynamics code, and a finite element package ABAQUS as the structural mechanics code. The equations for the fluid motion and solid deformation were solved separately and then coupled externally in an iterative manner. The hybrid nature (finite volume method for the fluid and finite element for the solid) makes the present scheme a highly efficient tool for modelling fluid/solid interactions. Such a model is of considerable novelty, as it solves the time-dependent, three-dimensional flow as well as the wall motion, allowing the dynamic interactions between the fluid and wall to be investigated. Employing modified user subroutines in both codes, an interface program was completed for the data transfer between the fluid dynamics code and the solid mechanics code. Thus updated pressure and deformation distribution at each time step during the cycle could be transferred between CFX and ABAQUS on an interface mesh. One numerical difficulty encountered from the coupled model is the convergence problem. In addition to convergence considerations within each code, convergence between the two codes must also be dealt with. A relaxation technique has been introduced. In some cases the fluid domain boundary was likely to oscillate if the total geometric deformation as a result of the structural analysis was fed in as the new boundary. It was found that by updating the deformations incrementally, the dynamic loads resulting from the flowing fluid would not change drastically. A number of numerical experiments have been performed to test

the convergence of the iterative procedure implemented.

To test the reliability of both the codes and the coupled algorithm, a wide range of code validation exercises have been carried out. First, a decoupled treatment (a)unsteady flows in a semi-infinite contracting or expanding tube, and (b) an incompressible elastic tube under uniform internal pressure was considered. Then, the coupled algorithm has been applied to predictions of unsteady flow in a compliant circular tube, with the tube material being (a) elastic and, (b) hyper-elastic. Geometrically non-linear theory has been used in the displacement and stress analysis for the hyper-elastic case. Quantitative comparisons with analytical solutions (obtained by Uchida and Aoki [189] for expanding/contracting pipe, Love [191] for tube under internal pressure, and Womersley [38] for unsteady flow in a compliant tube) have demonstrated very good agreement between the numerical results and analytical solutions.

The coupled method was applied to the investigation of human carotid bifurcations. In the study, MRI and 2-D USA (System is being set up for the measurement of 4-D time-dependent carotid geometry by USA.) have been used to obtain *in vivo* 3-D carotid bifurcation anatomy. A purpose-built program based on the existing one for MRI has been developed to process images obtained by USA or MRA, to reconstruct the bifurcation models and generate automatically the computational grids which can then be used in the coupled simulation. This enables computer simulations of the complex flow and vessel wall behaviour to be carried out on an individual basis. The program has the ability of incorporating the movement of the surface of the model and regenerating the grid within the whole fluid domain.

Numerical analysis of blood flow and vessel mechanics in realistic human carotid artery bifurcations was performed and detailed information on both flow and arterial wall were obtained. Geometry plays the key role in determining the nature of haemodynamic patterns. The results confirmed the complex nature of both flow field and mechanical wall behaviour in the carotid bifurcations concerned. For example, in the *in vivo* models secondary flows were markedly different from that observed in planar geometry models. Comparison of

the results for both compliant and rigid cases demonstrated quantitative influence of the vessel compliance on local flow field such as wall shear stress and slow moving zone. The validation has been designed to include both numerical accuracy and overall validations. In the latter, the calculated wall movement and velocities were validated against *in vivo* experimental data, demonstrating satisfactory agreement. These results have indicated that the combination of modern codes like CFX and ABAQUS, together with *iv vivo* measured vessel anatomy and boundary conditions, is capable of simulating physiologically realistic flow in individual arterial structures.

The coupled method is capable of treating a wide range of material behaviour, such as, elastic and hyperelastic, linear and nonlinear, small and large deformations. Its applicability to large deformation problems has been demonstrated by a number of numerical predictions of human carotid artery bifurcations. From the results discussed in the preceding chapters, it can be concluded that both qualitative and quantitative aspects of reliability of the numerical predictions have been established by critical validations against analytical and experimental data. In order to investigate particle trackings and residence times, which are clinically relevant, a visualisation of the predicted results is intended to be performed using the most advanced computer visualisation techniques.

As a consequence of the present study, wall effects can now be included in the predictions of haemodynamics in a clinical context. The combination of SM and CFD with *in vivo* vascular geometry may further elucidate the roles of haemodynamics and vessel wall mechanics in atherosclerosis. Together with the study of disease patterns, the application of the coupled model to a large number of clinical cases may establish the link among low wall shear stress, high wall tensile stress to atherosclerosis. In future this is likely to lead to better use of currently available anti-atherosclerosis strategies. It may also facilitate discovery, evaluation and development of novel treatments. The resultant generic code, combining two major disciplines of fluid dynamics and structural mechanics, will have wide applicability within conventional engineering. It has the potential for in depth insight into the behaviour of various fluid-structure interactions.

Compared to MRI, ultrasound is well tolerated, widely available and relatively cheap. Therefore, in future studies, 4D ultrasound will be used to obtain time-dependent geometry and integrated with the coupled model for the purpose of both calculations and validations. In the present study, local change of wall properties was not considered due to lack of clinical data. Advanced techniques need to be developed to be able to obtain *in vivo* local changes in wall properties, then to be incorporated in the numerical modelling.

Appendix A

Publication list during the project

S.Z.Zhao et al.(1999) Blood Flow and Vessel Mechanics in a Physiologically Realistic Model of a Human Carotid Arterial Bifurcation. *Journal of Biomechanics* (in press)

S.Z.Zhao et al.(1999) Flow in Carotid Bifurcations: Effect of the superior thyroid artery. *Medical Engineering & Physics*, **21**, 207-214

S.Z.Zhao et al.(1999) The Application of Computational Fluid Dynamics and Solid Mechanics to Haemodynamics in Arterial Organs and to Related Problems. *In: Sajjadi S et al. (ed.), Cardiovascular flow modelling and measurement with applications to clinical medicine*, Oxford press, 83-112

S.Z.Zhao et al.(1999) The Convergence Technique in Numerical Solutions of Coupled Fluid-Wall Problems. *In: Sajjadi S et al. (ed.), Cardiovascular flow modelling and measurement with applications to clinical medicine*, Oxford press, 125-134

S.Z.Zhao et al.(1998) The Numerical Analysis of Fluid-Solid Interactions for Blood Flow in Arterial Structures Part I: A review of models for arterial wall behaviour. *Proc. Instn. Mech. Engrs. Part H: J. ENG. in Medicine*, **212**, 229-240

S.Z.Zhao et al.(1998) The Numerical Analysis of Fluid-Solid Interactions for Blood Flow in Arterial Structures Part II: Development of coupled fluid-solid algorithms. *Proc. Instn.*

Mech. Engrs. Part H: J. ENG. in Medicine, **212**, 241-252

S.Z.Zhao et al.(1998) Numerical Analysis of Blood-Wall Interactions in Human Carotid Bifurcations. *J. of Biomechanics*, **31**, Suppl. 1, 18(Abstract)

S.Z.Zhao et al.(1997) Flow Patterns in Stented Arteries. *Internal Medicine*, **5**, 29-32

S.Z.Zhao et al.(1997) A Novel Numerical Method for Analysis of Fluid and Solid Coupling. *In: Taylor C(ed.), Numerical Methods in Laminar and Turbulent Flows*, Swansea:Pineridge Press, 525-534

S.Z.Zhao et al.(1997) Stress Analysis of a Human Abdominal Bifurcation Based on MRI Data. *Proceedings of 9th International Conference on Biomedical Engineering*, 511-513

Bibliography

[1] Caro, C.G., Fitz-Gerald, J.M, and Schroter, R.C. (1971) Atheroma and Arterial Wall Shear:Observation Correlation and Proposal of a Shear Dependent Mass Transfer Mechanism for Atherogenesis. *Proc. Roy. Soc. London*, **177**, 109-159.

[2] Friedman,M.H.(1989) A biological plausible model of thickening of arterial intima under shear. *Atherosclerosis*, **9**, 511-522.

[3] Moore, J.E.. Jr and Ku, D.N. (1994) Pulsatile velocity measurements in a model of the human abdominal aorta under resting conditions. *ASME J. Biomech. Eng.*, **116**, 337-346.

[4] Caro,C.G., Doorley D.J., Tarnawski,M. et al. (1996) Nonplanar curvature and branching of arteries and non-planar-type flow. *Proceedings of the Royal Society of London,***A,452(1944)**, 185-197.

[5] Salzar, R.S., Thubrikar, M.J. And Eppink, R.T. (1995) Pressure-induced Mechanical Stress in the Carotid Artery Bifurcation: A Possible Correlation to Atherosclerosis. *J. Biomechanics*, **28**, 1333-1340.

[6] Hofer M., Rappitsch G., Perktold K., Trubel W. and Schima H. (1996) Numerical study of wall mechanics and fluid dynamics in end-to-side anastomoses and correlation to intimal hyperplasia. *J. Biomech.*, **29**, 1297-1308.

[7] Perktold, K. and Rappitsch, G.(1995) Computer simulation of local blood flow and vessel mechanics in a compliant carotid artery bifurcation model. *J. Biomech.*, **28**, 845-856.

[8] Liepsch, D. and Moravec, S.(1984) Pulsatile flow of non-Newtonian fluid in distensible models of human arteries. *Biorheol.*, **21**, 571-586.

[9] Henry, F.S. and Collins, M.W. (1993) A Novel Predictive Model with Compliance for Arterial Flows. *1993 Advances in Bioengineering, ASME BED-Vol.26*, 131-135.

[10] Lan, T.H., Xu, X.Y., Hutton A., Collins, M.W. (1995) A numerical Algorithm for Solving Coupled Solid/Fluid Interaction Problems. In: Taylor C(ed), *Numerical Methods in Laminar and Turbulent Flows*, Vol. IX, Part 2. Swansea:Pineridge Press, 1539-1550.

[11] Ross, R. (1993) The pathogenesis of atherosclerosis: a perspective for the 1990s. *Nature*, **362**, 801-809.

[12] Davies, M.J. and Thomas, A. (1984) Thrombosis and acute coronary-artery lesions in sudden cardiac ischemic death. *New England J. Med.*, **310**, 1137-1140.

[13] Lou,Z. and Yang,W.J.(1992) Biofluid dynamics at arterial bifurcations. *Critical Reviews in Biomed. Eng.*, **19**, 455-493.

[14] Heiss, G., Sharrett, R., Barnes, R.,Chambless, L.E., Szklo, M. , and Alzola, C. (1991) Carotid atherosclerosis measured by B-mode ultrasound in populations. *Am J. Epidemiol*, **134**, 250-256.

[15] Crouse, J.R., Byington, R.P., Bond, M.G. et al. (1995) Pravastatin, lipids, and atherosclerosis in the carotid arteries(PLAC-II). *AM J. Cardiol*, **75**, 455-459.

[16] Mayet, J., Stanton, A.V., Sinclair, A.M. et al. (1995) The effects of antihypertensive therapy on carotid vascular structure in man. *Cardiovasc. Res.*, **30**, 147-152.

[17] Ku,D.N. and Giddens,D.P. (1983) Pulsatile flow in a model carotid bifurcation, *Arteriosclerosis*, **3**,31-39.

[18] Ku, D.N., Giddens, D.P., Zarins, C.K. and Glagov, S. (1985) Pulsatile flow and atherosclerosis in the human carotid bifurcation-positive correlation between plaque location and low and oscillating shear stress. *Atherosclerosis*, **5**, 293-302.

[19] Reneman,R.S.,van Merode,T.,Hick,P. and Hoeks,A.P.G. (1985) Flow velocity patterns and distensibility of the carotid artery bulb in subjects of various ages, *Circulation*, **71**,500-509.

[20] Ku,D.N. and Giddens,D.P. (1987) Laser Doppler anemometer measurements of pulsatile flow in a model carotid bifurcation, *J. Biomechanics*, **20**,407-421.

[21] Zaris, C.K., Giddens, D.P., Bharadvaj, B.K., Sottiuri, V.S., Mabon, R.F., Glagov, S. (1983) Carotid bifurcation atherosclerosis: quantitative correlation of plaque localisation with flow velocity profiles and wall shear stress. *Circulation Research*, **53**, 502-514.

[22] Davies, P.F. (1972) Turbulent fluid shear stress induces vascular endothelial cell turnover in vitro. *Proc. Natl. Acad. Sci.* USA **83**, 2114-2117.

[23] Davies, P.F. (1984) Influence of haemodynamic forces on vascular endothelial function. *J. Clin. Invest.*, **73**, 1121-1129.

[24] Niim, H. (1979) Role of stress concentration in arterial walls in atherogenesis. *Biorheology*, **16**, 223-230.

[25] Harvey, J.F. (1974) Modern Pressure Vessels, p.338, Von Nostrand Reinhold, New York.

[26] Thubrikar, M.J., Roskelley, S.K., and Eppink, R.T. (1990) Study of Stress Concentration in the Walls of the Bovine Coronary Arterial Branch. *J. Biomech.*, **23**, 15-26.

[27] Glagov, S., Bassiouny, H.S., Sakaguchi, Y., Goudet C.A., and Vito, R.P. (1997) Mechanical determinants of plaque modelling, remodelling and disruption. *Atherosclerosis*, **131(suppl)**, 913-914.

[28] Glagov, S (1972) Haemodynamic risk factors: Mechanical stress, mural architecture, medical nutrition and the vulnerability of arteries to atherosclerosis. In Wissler RW, Geer JC(eds): The pathogenesis of atherosclerosis. Baltimore, Williams & Wilkins, chap 6.

[29] Bardy, N., Karillon, G.J., Merval, R., Samuel, J.L. and Tedgui, A. (1995) Differential effects of pressure and flow on DNA and proteins synthesis, and on fibronectin expression by arteries in a novel organ culture system. *Circulation Research*, **77**, 684-694.

[30] Bardy, N., Merval, R., Benessiano, J., Samuel, J.L., Tedgui, A. (1996) Pressure and angiotensin II synergistically induce aortic fibronectin expression in organ culture model of rabbit aorta - Evidence for a pressure-induced tissue renin-angiotensin system. *Circulation Research*, **79**, 70-78.

[31] Rindt,C.C.M., van Steenhoven, A.A., Janssen,J.D.,Reneman,R.S. and Segal,A. (1990) An numerical analysis of steady flow in a three-dimensional model of the carotid artery bifurcation, *J. Biomechanics*, **23**,461-473.

[32] Perktold,K.,Resch,M. and Peter,R.O. (1991) Three-dimensional numerical analysis of pulsatile flow and wall shear stress in the carotid artery bifurcation, *J. Biomechanics*, **24**, 409-420.

[33] Taylor,T.W. and Yamaguchi,T. (1994) Three dimensional simulation of blood flow in an abdominal aortic aneurysm - steady and unsteady flow cases. *ASME J. Biomech. Eng.*, **116**, 89-97.

[34] Perktold,K., Resch,M. and Florian,H. (1991) Pulsatile non-Newtonian flow characteristics in a three-dimensional human carotid bifurcation model. *ASME J. Biomech. Eng.*, **113**, 464-475.

[35] Long, Q., Xu,X.Y.,Collins, M.W. et al. (1998) The combination of magnetic resonance angiography and computational fluid dynamics: a critical review. *Critical Reviews in Biomed. Eng.*, **26**, 227-274.

[36] Long, Q., Xu, X.Y., Bourne, M., Griffith, T.M. (1999) Numerical study of blood flow in an anatomically realistic aorto-iliac bifurcation generated from MRI data. *Magnetic Resonance in Medicine* (in press).

[37] Milner, J.S., Moore, J.A., Rutt, B.K., and Steinman, D.A. (1998) Haemodynamics of human carotid artery bifurcations: Computational studies with models reconstructed from magnetic resonance imaging of normal subjects. *J. of Vascular Surgery*, **27**, 143-156.

[38] Womersley, J.R. (1957) The Mathematical Analysis of the Arterial Circulation in a State of Oscillatory Motion. *WADC-TR56-614, Wright Air Development Centre.*

[39] Wang,D.M. and Tarbell, J.M. (1992) Nonlinear analysis of flow in an elastic tube (artery). *J. Biomech.*, **21**, 477-487.

[40] Reuderink, P.J. (1991) Analysis of the Flow in a 3-D Distensible Model of the Carotid Artery Bifurcation. *PhD. Thesis, Department of Mechanical Engineering, University of Technology, Eindhoven.*

[41] Lou, Z., and Yang, W.J. (1993) A Computer Simulation of the Blood Flow at the Aortic Bifurcation with Flexible Walls. *ASME J. Biomech. Engr.*, **115**, 306-315.

[42] Perktold, K., and Rappitsch, G. (1995) Computer Simulation of Local Blood Flow and Vessel mechanics in a Compliant Carotid Artery Bifurcation Model. *J. Biomech.*, **28**, 845-856.

[43] Lonsdale,R. (1998) An algorithm for solving thermal-hydraulic equations in complex geometry. *The ASTEC code* UKAEA Report.

[44] FLOW3D Release 3.2: User Manual. (1994) *Harwell Laboratory, UK:AEA Industrial Technology.*

[45] Anonymous (1991) User guide to FEAT. Engineering Analysis Centre, Nuclear Electric Plc, UK.

[46] Patankar, S.V. and Spalding, D.B. (1972) A calculation procedure for heat, mass and momentum transfer in three-dimensional parabolic flows. *Int. J. Heat Mass Transfer*, **15**, 1787-1806.

[47] Xu,X.Y. and Collins,M.W. (1990) A Review of the numerical analysis of blood flow in arterial bifurcation. *Proc. Instn. Mech. Engrs. Part H: J.Eng. in Medicine*, **204**, 205-216.

[48] Xu,X.Y. and Collins,M.W. (1994) Studies of blood flow in arterial bifurcation using a numerical simulation method. *Proc. Instn. Mech. Engrs. Part H: J.Eng. in Medicine*, **208**, 163-175.

[49] Xu,X.Y. and Collins, M.W. (1995) Numerical modelling of blood flow in compliant arteries and arterial bifurcation. In:*Biofluid Mechanics*, Ed. by H.Power, Computational Mechanics Publications, Southampton, Boston, 55-94.

[50] Xu,X.Y., Collins,M.W. and Jones,C.J.H. (1997) A problem-oriented approach to the numerical modelling of haemodynamic problems. *Advances in Engineering Software*, **28**, 365-377.

[51] Xu,X.Y. Collins,M.W., and Jones,C.J.H. (1992) Flow studies in canine artery bifurcations using a numerical simulation method. *ASME J. Biomech. Eng.* , **114**, 504-511.

[52] Henry,F.S., Collins,M.W., Hughes,P.E. and How,T.V. (1996) Numerical investigation of steady flow in proximal and distal end-to-side anastomoses. *ASME J. Biomech. Eng.* , **118**, 302-311.

[53] Henry,F.S., Shortland,A.P., Iudicello,F., Black,R.A., Jarvis,J.C., Collins,M.W. and Salmons,S. (1997) Flow in a simple model skeletal muscle ventricle: Comparison between numerical and physical simulations. *ASME J. Biomech. Eng.* , **119**, 13-19.

[54] Cleave, J. and Roach, M.R. (1983) Comparison of longitudinal elastic properties of proximal and distal strips of aorta-branch junctions from the abdominal aorta of sheep. *Can. J. Physiol. Pharmacol*, **61**, 614-618.

[55] Macfarlane, T.W.R., Canham, P.B. and Roach, M.R. (1982) Shape changes at the apex of isolated human cerebral bifurcations with changes in transmural change. *Stroke*, **14**, 70-76.

[56] Thubrikar, M.J., Baker, J.W. and Nolan, S.P. (1988) Inhibition of atherosclerosis associated with reduction of arterial intramural stress in rabbits. *Atherosclerosis*, **37**, 410-420.

[57] Wolf, S. and Werthessen, N.T. (1979) Dynamics of arterial flow. *Advances in Experimental Medicine and Biology*, Vol. 115, Plenum Press, New York.

[58] Dinnar, U. (1981) Cardiovascular Fluid Dynamics. *CRC Press.*

[59] Humphrey, J.D.(1995) Mechanics of the Arterial Wall:Review and Directions. *Critical Review in Biomedical Engineering*, **30**, 1-138.

[60] Cox, R.H. (1978) Regional Variation of Series Elasticity in Canine Arterial Smooth Muscle. *Am. J. Physiol.*, **234**, 542-551.

[61] Patel, D.J., Janicki, J.S., (1973) Vaishnav, R.N., and Yong, J.T. Dynamic Anisotropic Viscoelastic Properties of the Aorta in Living Dogs. *Circulation Research,* 1973, **32**, 93-107.

[62] Vaishnav, R.N., Yong, J.T., Janicki, J.S., and Patel, D.J. (1972) Nonlinear Anisotropic Elastic Properties of the Canine Aorta.*Biophys. J.*, **12**, 1008-1027.

[63] Young, J.T., Vaishnav, R.N., and Patel, D.J. (1977) Nonlinear Anisotropic Viscoelastic Properties of Canine Arterial Segments. *J. Biomech.,* **10**, 549-559.

[64] Carew, T.E., Vaishnav, R.N., and Patel, D.J. (1968) Compressibility of the Arterial Wall. *Circulation Research,* **23**, 61-68.

[65] Chuong, C.J. and Fung, Y.C. (1984) Compressibility and Constitute Relation of Arterial Wall in Radial Compression Experiments. *J. Biomech.*, **17**, 35-40.

[66] Cox, R.H. (1975) Anisotropic Properties of the Canine Carotid Artery In Vitro. *J. of Biomech.*, **8**, 293-300.

[67] Dobrin, P.B. (1986) Biaxial Anisotropy of Dog Carotid Artery:Estimation of Circumferential Elastic Modulus. *J. of Biomech.*, **19**, 351-358.

[68] Gentile, B.J., Chuong, C.J., and Ordway, G.A. (1988) Regional Volume Distensibility of Canine Thoracic Aorta During Moderate Treadmill Exercise. *Circulation Research*, **63**, 1012-1019.

[69] Papageorgiou, G.L., and Jones, N.B. (1988) Circumferential and Longitudinal Viscoelasticity of Human Iliac Arterial Segments In Vitro. *Journal of Biomedical Engineering*, **10**, 82-90.

[70] Tanaka, T.J., and Fung, Y.C. (1974) Elastic and Inelastic Properties of the Canine Aorta and Their Variation Along the Aortic Tree.*J. Biomech.*, **7**, 357-370.

[71] Patel, D.J., and Fry, D.L. (1969) Elastic Symmetry of Arterial Segments in Dogs. *Circulation Research*, **24**, 1-18.

[72] Weizsacker, H.W., and Pinto, J.G. (1988) Isotropy and Anisotropy of the Arterial Wall. *J. Biomech.*, **21**, 477-487.

[73] Burton, A.C. (1954) Relation of Structure to Function of the Tissues of the Blood Vessels. *Physiol. Rev.*, **34**, 619-642.

[74] von Maltzahn, W.W., Besdo, D., and Wiemer, W, (1981) Elastic Properties of Arteries:a Nonlinear Two-Layer Cylindrical Model. *J. Biomech.*, **14**, 389-397.

[75] Demiray, H., and Vito, R.P. (1991) A Layered Cylindrical Shell Model for an Aorta. *Int. J. Engr. Sci.*, **29**, 47-54.

[76] Kang, T., and Humphrey, J.D. (1991) Finite Deformation of an Inverted Artery. in *1991 ASME Advances in Bioengineering*, Vanderby, R., ed., New York, 1991.

[77] Xie, J., and Fung, Y.C. (1995) Bending of Blood Vessel Wall:Stress-Strain Laws of the Intima-Media and Adventitial Layers. *ASME J. Biomech. Engr.*, **117**, 136-145.

[78] von Maltzahn, W.W., Warriyar, R.G., and Keitzer, W.F. (1984) Experimental Measurements of Elastic Properties of Media and Adventitia of Bovine Carotid Arteries. *J. Biomech.*, **17**, 839-847.

[79] Fung. Y.C., Fronek, K., and Patitucci, P. (1979) Pseudoelasticity of Arteries and the Choice of Its Mathematical Expression. *Am. J. Physiol.*, **237**, H620-H631.

[80] Hall, I.H. (1968) Deformation of Solids. *The Universities Press Limited, Northern Ireland.*

[81] Viidik, A. (1966) Biomechanics and Functional Adaptation of Tendons and Joint Ligaments. In *Studies on the Anatomy and Function of Bone and Joints*, F.G.Evans(ed.) Springer-Verlag, New York, 17-39.

[82] Fung, Y.C. (1981) Biomechanics-Mechanical Properties of Living Tissues. *Springer-Verlag New York Inc.*

[83] Collins, R., and Hu, W.C.L. (1972) Dynamic Deformation Experiments on Aortic Tissue. *J. Biomech.*, **5**, 333-337.

[84] Mohan, D., and Melvin, J.W. (1982) Failure Properties of Passive Human Aortic Tissue. I-Uniaxial Tension Tests. *J. Biomech.*, **15**, 887-902.

[85] Mohan, D., and Melvin, J.W. (1983) Failure Properties of Passive Human Aortic Tissue. II-Biaxial Tension Tests. *J. Biomech.*, **16** 31-44.

[86] Sato, M., Hayashi, K., Niim, H., Moritake, K., Okumura, A., and Handa, H. (1979) Axial Mechanical Properties of Arterial Walls and Their Anisotropy. *Medical&Biological Engineering&Computing*, **17**, 170-176.

[87] Fronek, K., and Fung, Y.C. (1980) Mechanical Properties of Arteries as a Function of Topography and Age. *Biorheol.*, **17**, 227-234.

[88] Carmines, D.V., McElhaney, J.H., and Stack, R. (1991) A Piece-Wise Non-linear Elastic Expression of Human and Pig Coronary Arteries Tested In Vitro. *J. Biomech.*, **24**, 899-906.

[89] Langewouters, G.L., Wesseling, K.H., and Goedhard, W.J.A. (1984) The Elastic Properties of 45 Human Thoracic and 20 Abdominal Aortas In Vitro and the Parameters of a New Model. *J. Biomech.*, **17**, 425-435.

[90] Gow, B.S., and Hadfield, C.D. (1979) The Elasticity of Canine and Human Coronary Arteries with Reference to Postmortem Changes. *Circulation Research*, **45**, 588-594.

[91] Michelini, L.C., and Krieger, E.M. (1986) Aortic Caliber Changes During Development of Hypertension in Freely Moving Rats. *Am. J. Physiol.*, **25**, H662-H671.

[92] Powalowski, T., and Pensko, B. (1988) A Noninvasive Ultrasonic Method for the Elasticity Evaluation of the Carotid Arteries and Its Application in the Diagnosis of the Cerebro-Vascular System. *Archives of Acoustics*, **13**, 109-126.

[93] Kalath, S., Tsipouras, P., and Silver, F.H. (1986) Non-Invasive Assessment of Aortic Mechanical Properties. *Annals of Biomedical Engineering*, **14**, 513-524.

[94] Buntin, C.M., and Silver, F.H. (1990) Noninvasive Assessment of Mechanical Properties of Peripheral Arteries. *Annals of Biomedical Engineering*, **18**, 549-566.

[95] Reneman, R.S., van Merode, T., Hick, P. (1986) Aged-Related Changes in Carotid Artery Wall Properties in Men. *Ultrasound in Medicine and Biology*, **12**, 465-471.

[96] Gozna, E.R., Marble, A.E., and Holland, J.G. (1974) Age-Related Changes in the Mechanics of the Aorta and Pulmonary Artery of Man. *Journal of Applied Physiology*, **36**, 407-411.

[97] Mohiaddin, R.H., Underwood, S.R., Bogren, H.G., Firmin, D.N., Klipstein, R.H., Rees, R.S.O., and Longmore, D.B. (1989) Regional Aortic Compliance Studied by Magnetic Resonance Imaging: The Effects of Age, Training, and Coronary Artery Disease. *British Heart Journal*, **62**, 90-96.

[98] Liu, Z., Brin, K.P., and Yin, F.C.P. (1986) Estimation of Total Arterial Compliance: An Improved Method and Evaluation of Current Methods. *Am. J. Physiol.*, **251**, H588-H600.

[99] Vaishnav, R.N., and Vossoughi, J. (1984) Incremental Formula**Fung, Y.C.** Biodynamics:Circulation. *Springer, New York*, 1984.
tions in Vascular Mechanics. *ASME J. Biomech. Engr.*, **106**, 105-111.

[100] Vossoughi, J., and Vaishnav, R.N. (1981) Uniaxial Mechanical Properties of Blood Vessels. *The Proceedings of the Brazilian Conference on Biomedical Engineering*, 125-130.

[101] Hayashi, K., Washizu, T., Kiraly, R.J., and Nose, Y. (1981) Mechanical Properties of Aortas and Pulmonary Arteries of Calves Implanted with Cardiac Prostheses. *J. Biomech.*, **14**, 173-182.

[102] Vaishnav, R.N., Young, J.T., and Patel, D.J. (1973) Distribution of Stress and Strain-Energy Density Through the Wall Thickness in a Canine Aortic Segment. *Circulation Research*, **32**, 577-583.

[103] Chuong, C.J., and Fung, Y.C. (1983) Three-Dimensional Stress Distribution in Arteries. *ASME J. Biomech. Engr.*, **105**, 268-274.

[104] von Maltzahn, W.W. (1983) Parameter Sensitivity Analysis and Improvement of a Two-Layer Arterial Wall Model. *ASME J. Biomech. Engr.*, **105**, 389-392.

[105] Hudetz, A.G., and Monos, E. (1981) Characterisation of Anisotropic Elastic Properties of the Arteries by Exponential and Polynomial Strain Energy Functions. *Acta Physiological Academiae Scientiarum Hungaricae*, **57**, 111-122.

[106] Deng, S.X., Tomioka, J., Dehes, J.C., and Fung, Y.C. (1994) New Experiments on Shear Modulus of Elasticity of Arteries. *Am. J. Physiol.*, **266**, H1-10.

[107] Takamizawa, K., and Hayashi, K. (1987) Strain Energy density Function and Uniform Strain Hypothesis for Arterial Mechanics. *J. Biomech.*, **20**, 7-17.

[108] Chuong, C.J., and Fung, Y.C. (1986) On Residual Stress in Arteries. *ASME J. Biomech. Engr.*, **108**, 189-192.

[109] Kas'yanov, V.A., and Rachev, A.I. (1980) Deformation of Blood Vessels Upon Stretching, Intramural Pressure and Torsion. *Mech. Comp. Matls.*, **16**, 76-80.

[110] Hayashi, K. (1993) Experimental Approaches on Measuring the Mechanical Properties and Constitute Laws of Arterial Walls. *ASME J. Biomech. Engr.*, **115**, 481-488.

[111] Manak, J.J. (1980) The Two Dimensional In-Vitro Passive Stress-Strain Elasticity Relationships for Steer Thoracic Aorta Blood Vessel Tissue. *J. Biomech.*, **13**, 637-646.

[112] Elad, D., Foux, A., and Kivity, Y. (1988) A Model for the Nonlinear Elastic Response of large Arteries. *ASME J. Biomech. Engr.*, **110**, 185-189.

[113] Humphrey, J.D., Strumpf, R.K., Yin, F.C.P. (1989) A Theoretically Based Experimental Approach for Identifying Vascular Constitute Relations. *Biorheol.*, **26**, 687-702.

[114] Peterson, L.H., Jensen, R.E., and Parnell, R. (1960) Mechanical Properties of Arteries In Vivo. *Circulation Research*, **8**, 622-639.

[115] Gow, B.S., and Taylor, M.G. (1968) Measurement of Viscoelastic Properties of Arteries in the Living Dogs. *Circulation Research*, **23**, 111-122.

[116] Hayashi, K., Handa, H., Nagasawa, S., Okumura, A., and Moritake, K. (1980) Stiffness and Elastic Behaviour of Human Intracranial and Extracranial Arteries. *J. Biomech.*, **13**,175-184.

[117] Tozeren, A. (1984) Elastic Properties of Arteries and Their Influence on the Cardiovascular System. *ASME J. Biomech. Engr.*, **106**, 182-185.

[118] Demiray, H. (1983) Incremental Elastic Modulus for Isotropic Elastic Bodies With Application to Arteries. *ASME J. Biomech. Engr.*, **105**, 308-309.

[119] Demiray, H., Weizsacker, H.W., Pascale, K., and Erbay, H.A. (1988) A Stress-Strain Relation for a Rat Abdominal Aorta. *J. Biomech.*, **21** 369-374.

[120] Anliker, M., Moritz, W.E., and Ogden, E. (1968) Transmission Characteristics of Axial Waves in Blood Vessels. *J. Biomech.*,**1**, 235-246.

[121] Patel, D.J., and Vaishnav, R.N. (1980) Basic Haemodynamics and Its Role in Disease Process. *University Park Press*, Baltimore, Md.

[122] Fung, Y.C. (1979) Inversion of a Class of Nonlinear Stress-Strain Relationship of Biological Soft Tissues. *ASME J. Biomech. Engr.*, **101**, 23-27.

[123] Cox, R.H. (1977) Effects of Age on the Mechanical Properties of Rat Carotid Artery. *Am. J. Physiol.*, **8**, 293-300.

[124] Pagani, M., Mirsky, I., Baig, H., Manders, W.T., Kerkhof, P., and Vatner, S.F., (1979) Effects of Age on Aortic Pressure-Diameter and Elastic Stiffness-Stress Relationships in Unanesthetised Sheep. *Circulation Research*, **44**, 420-429.

[125] Yin, F.C.P., Spurgeon, H.A., and Kallman, C.H. (1983) Age-Associated Alternations in Viscoelastic Properties of Canine Aortic Strips. *Circulation Research*, **53**, 464-472.

[126] Pynadath, T.I., and Mukherjee, D. P. (1977) Dynamic Mechanical Properties of Atherosclerotic Aorta. *Atheroscl.*, **26**, 311-318.

[127] Hasegawa, M., and Watanabe, Y. (1988) Rheological Properties of the Thoracic Aorta in a Normal and WHHL Rabbits. *Biorheol.*, **25**, 147-156.

[128] Sharma, M.G., and Hollis, T.M. (1976) Rheological Properties of Arteries Under N Normal and Experimental Hypertension Conditions. *J. Biomech.*, **9**, 293-300.

[129] Cox, R.H., and Bagshaw, R.J. (1988) Effects of Hypertension and Its Reversal on Canine Arterial Wall Properties. *Hypertension*, **12**, 301-309.

[130] Vaishnav, R.N., Vossoughi, J., Patel, D.J., Cothran, L.N., Coleman, B.R., and Ison-Franklin, E.L. (1990) Effect of Hypertension on Elasticity and Geometry of Aortic Tissue From Dogs. *ASME J. Biomech. Engr.*, **112**, 70-74.

[131] Matsumoto, T., and Hayashi, K. (1994) Mechanical and Dimensional Adaptation of Rat Aorta to Hypertension. *ASME J. Biomech. Engr.*, **116**, 278-283.

[132] Arndt, J.O., Stegall, H.F., and Wicker, H.J. (1971) Mechanics of the Aorta In Vivo:Radiographic Approach. *Circulation Research*, **28**, 693-704.

[133] Fry, D.L. (1969) Certain Chemorheologic Considerations Regarding the Blood Vascular Interface with Particular Reference to Coronary Artery Disease. *Circulation*, **29**(Suppli. IV):IV-38-59.

[134] Simon, B.R., Kobayashi, A.S., Strandness, D.E., and Wiederhielm, C.A. (1971) Large Deformation Analysis of the Arterial Cross Section. *Journal of Basic Engineering*, **93**, 138-146.

[135] Simon, B.R., Kobayashi, A.S., Strandness, D.E., and Wiederhielm, C.A. (1972) Reevaluation of Arterial Constitute Relations. *Circulation Research*, **30**, 491-500.

[136] Fung, Y.C. (1984) Biodynamics:Circulation. *Springer, New York.* 1984.

[137] Chaudhry, H.R., Bukiet, B., Davis, A., Ritter, A.B. and Findley, T. (1997) Residual Stresses in Oscillating Thoracic Arteries Reduce Circumferential Stresses and Stress Gradients. *J. Biomech.*, **30**, 57-62.

[138] Simon, B.R., Kobayashi, A.S., Wiederhielm, C.A., and Strandness, D.E. (1973) Deformation of the Arterial Vasa Vasorum at Normal and Hypertensive Arterial Pressures. *J. Biomech.*, **6**, 349-359.

[139] Ayorinde, O.A., Kobayashi, A.S., and Merati, J.K. (1975) Finite Elasticity Analysis of Unanesthetised and Anesthetised Aorta. *ASME J. Appl. Mech.*, **42**, 547-551.

[140] Vito, R.P., Whang, M.C., Glagov, S., and Aoki, T. (1991) Distribution of Strains and Stresses in the Arterial Cross Section. *1991 Advances in Bioengineering, ASME BED-Vol.20*, 639-642.

[141] Kenyon, D.E. (1979) A Mathematical Model of Water Flux Through Aortic Tissue. *Bull. Math. Biol.*, **41**, 79-90.

[142] Jain, R., and Jayaraman, G. (1987) Theoretical Model for Water Flux Through the Artery Wall. *ASME J. Biomech. Engr.*, **109**, 311-317.

[143] Simon, B.R., and Gaballa, M.A. (1986) Poroelastic Finite Elements Models for large Arteries. *1986 Advances in Bioengineering, ASME BED-Vol.2*, 140-141.

[144] Yuan, Y., and Simon, B.R. (1992) Constraint Relations for Orthotropic Porohyperelastic Constitute laws and Finite Element Formulations for Soft Tissues. *1992 Advances in Bioengineering, ASME BED-Vol.22*, 203-206.

[145] Simon, B.R. (1992) Multiphase Poroelastic Finite Element Models for Soft Tissue Structures. *Applied Mechanics Reviews*, **45**, 191-2218.

[146] Fry, D.L., and Vaishnav, R.N. (1980) Mass Transport in the Arterial Wall. *Basic Haemodynamics and Its Role in Disease Process*, D.J.Patel and R.N.Vaishnav, eds, Chapter 10, University Park Press, Baltimore, MD, 425-482.

[147] Simon, B.R., Kaufmann, M.V., McAfee, M.A., and Baldwin, A.L. (1993) Finite Element Models for Arterial Wall Mechanics. *ASME J. Biomech. Engr.*, **115**, 489-496.

[148] Hofer M., Rappitsch G., Perktold K., Trubel W., and Schima H. (1996) Numerical Study of Wall Mechanics and Fluid Dynamics in End-To-Side Anastomoses and Correlation to Intimal Hyperplasia. *J. Biomech.*, **29**, 1297-1308.

[149] Caro, C.G., Pedley, T.J., Schroter, R.C., and Seed, W.A. (1978) The Mechanics of the Circulation. *Oxford University Press, Oxford.*

[150] Moodie, T.B., and Haddow, J.B. (1977) Waves in Thin Walled Elastic Tubes Containing an Incompressible Inviscid Fluid. *Int. J. Non-linear Mech.*, **12**, 223-231.

[151] Bergel, D.H. (1961) The Static Elastic Properties of the Arterial Wall. *J. Physiol.*, **156**, 445-457.

[152] Mirsky, I. (1973) Ventricular and Arterial Wall Stress Based on Large Deformation Analysis. *Biophys. J.*, **13**, 1141-1159.

[153] Demiray, H. (1988) Pulse Velocities in Initially Stressed Arteries. *J. Biomech.*, **21**, 55-58.

[154] Demiray, H. (1972) A Note on the Elasticity of Soft Biological Tissues. *J. Biomech.*, **5**, 309-311.

[155] Atabek, H.B., and Lew, H.S. (1966) Wave Propagation Through a Viscous Incompressible Fluid Contained in An Initially Stressed Elastic Tube. *Biophys. J.*, **7**, 480-503.

[156] Witzig, K. (1914) Uber Erzwungene Wellenbewegungen Zaher, Incompressibler Flussigkeiten in Elastischen Rohren. *Ph.D. Dissertation*, University of Bern.

[157] O'Rourke, M.F., and Taylor, M.G. (1967) Input Impedance of the Systemic Circulation. *Circulation Research*, **20**, 365.

[158] Wang, D.M., and Tarbell, J.M. (1992) Nonlinear Analysis of Flow in an Elastic Tube(Artery):Steady Streaming Effects.*J. Fluid Mech.*, **239**, 341-358.

[159] Dutta, A., Wang, D.M., and Tarbell, J.M. (1992) Numerical Analysis of Flow in an Elastic Artery Model. *ASME J. Biomech. Engr.*, **114**, 26-33.

[160] Liepsch, D., and Moravec, S. (1984) Pulsatile Flow of Non-Newtonian Fluid in Distensible Models of Human Arteries. *Biorheol.*, **21**, 571-586.

[161] Friedman, M.H., Bargeson, C.B., Deters, O.J., Hutchins, G.M. and Mark, F.F. (1987) Correlation Between Wall Shear and Intimal Thickness at a Coronary Artery Branch. *Atherosclerosis*, **68**, 27-33.

[162] Nerem, R.M. and Cornhill J.F. (1980) The Role of Fluid Mechanics in Atherogenesis. *ASME J. Biomech. Eng.*, **102**, 181-189.

[163] Duncan, D.D., Bargeron, C.B., Borchardt, S.E., Gearhart, O.J., Mark, F.F., and Friedman, M.H. (1990) The Effect of Compliance on Wall Shear in Casts of a Human Aortic Bifurcation. *ASME J. Biomech. Engr.*, **112**, 183-188.

[164] Anayiotos, A.S., Jones, S.A., Giddens, D.P., Glagov, S., Zarins, C.K. (1994) Shear Stress at a Compliant Model of the Human Carotid Bifurcation. *ASME J. Biomech. Engr.*, **116**, 98-106.

[165] Horsten, J.B.A.M., van Steenhoven, A.A., and Dongen, M.E..H. (1989) Linear Propagation of Pulsatile Waves in Visco-Elastic Tubes. *J. Biomech.*, **22**, 477-484.

[166] Rao, S.S. (1989) The Finite Element Method in Engineering. *Pergamon Press.*

[167] Turner, M.J., Clough, R.W., Martin, H.C., and Topp, L.J. (1956) Stiffness and Deflection Analysis of Complex Structures. *Journal of Aeronautical Sciences*, **23**, 805-824.

[168] Steinman, D.A., and Ethier, C.R. (1994) The Effect of Wall Distensibility on Flow in a Two-Dimensional End-to-Side Anastomosis. *ASME J. Biomech. Engr.*, **116**, 294-301.

[169] Rast, M.P. (1994) Simultaneous Solution of Navier-Stokes and Elastic Membrane Equations by Finite Element Method. *Int. J. for Numerical Methods in Fluids*, **19**, 1115-1135.

[170] Perktold, K., and Rappitsch, G. (1993) Numerical Analysis of Arterial Wall Mechanics and Local Blood Flow Phenomena. *1993 Advances in Bioengineering, ASME BED-Vol.26*, 127-130.

[171] Müller, A., and Jacob, N. (1994) Explicit Fluid-Solid Interaction. *Int. J. of Computer Applications in Technology*, **7**, 185-192.

[172] Reuderink, P.J., Willems, P.J.B., Schreurs, P.J.G., and van Steenhoven, A.A. (1989) Fluid Flow Through Distensible Models of the Carotid Artery Bifurcation. in D.Liepsch(ed.), *Biofluid Mechanics, Blood Flow in Large Vessels, Springer, Berlin*, 329-334.

[173] Engel, R. (1994) Analysis of Fluid-Structure Interaction Problems in Nuclear Reactor Engineering. *Int. J. of Computer Applications in Technology*, **7**, 193-205.

[174] Feng, Y.T. and Owen, D.R.J. (1996) Iterative solution of coupled fe/be discretizations for plate-foundation interaction problems. *Int. J. for Numerical Methods in Engineering*, **39**, 1889-1901.

[175] Makhijani, V.B., Yang, H.Q., Dionne, P.J. and Thubrikar, M.J. (1997) Three-dimensional coupled fluid-structure simulation of pericardial bioprosthetic aortic valve function. *ASAIO Journal*, **43**, ppM389-M392.

[176] Rhie, C.M. and Chow, W.L. (1983) Numerical study of the turbulent flow past an airfoil with trailing edge separation. *AIAA J.*, **21**, 1527-1532.

[177] Thompson, J.F., Warsi, Z.U.A. and Mastin, C.W. (1985) Numerical Grid Generation Foundations and Applications. *Elsevier Science Publishing Amsterdam.*

[178] Demirdzic, I. and Peric, M. (1988) Space conservation law in finite volume calculations of fluid flow. *In. J. Numerical Methods in Fluids*, **88**, 1037-1058.

[179] Hawkins, I.R., Wilkes, N.S. (1991) Moving Grids in Harwell Flow3D. UKAEA Report AEA-In Tech-0608.

[180] Demirdzic, I. and Peric, M. (1990) Finite Volume Method Prediction of Fluid in Arbitrarily Shaped Domains with Moving Boundaries. *In. J. Numerical Methods in Fluids*, **88**, 771-790.

[181] Demirdzic I. and Peric, M (1990) Finite volume method prediction of fluid in arbitrarily shaped domains with moving boundaries. *Int. J. Numerical Methods in fluids*, **10**, 771-790.

[182] Hibbit, Karlsson & Sorensen Inc. (1996) ABAQUS(version 5.5). *1080 Main Street, Pawtucket, R.I. 02860.*

[183] Matthies, H and Strang, G (1979) The Solution of Nonlinear Finite Element Equations. *Int. J. for Numerical Methods in Engineering*, **14**, 1613-1626.

[184] Barlow, J. (1976) Optimal Stress Locations in Finite Elements Methods. *Int. J. for Numerical Methods in Engineering*, **10**, 243-251.

[185] Rodal, J.J.A. and Witmer, E.S. (1979) Finite-strain large-deflection elastic-plastic finite element transient response analysis of structures. MIT, NASA contractor report 159874.

[186] Peraire, J. Morgan, K., and Perio, J. (1990) Unstructured Mesh methods for CFD. Von Karman Institute for Fluid Dynamics. Numerical Grid Generation Lecture Notes.

[187] Long, Q., Xu,X.Y., Collins,M.W., Bourne,M. and Griffith,T.M., (1998) Magnetic resonance image processing and structured grid generation of a human abdominal bifurcation. *Computer Methods and Programs in Biomedicine*, **56**, 249-259.

[188] Pedley, T.J.(1980) The fluid mechanics of large blood vessels, Cambridge University Press, Cambridge.

[189] Uchida, S. and Aoki, H. (1977) Unsteady Flows in a Semi-infinite contracting or expanding pipe. *J. of Fluid Mech.*, **82**, 371-387.

[190] Saada,A.S. (1973) Elasticity Theory and Applications. *Pergamon Unified Engineering Series.*

[191] Love,A.F.H. (1944) A Treatise on the Mathematical Theory of Elasticity. Dover Publications, New York.

[192] Perktold,K. and Resch,M. (1990) Numerical flow studies in human carotid artery bifurcations: basic discussion of the geometric factor in atherogenesis, *J.Biomech. Eng.*, **22**,111-123.

[193] Moore, J.A., Steinman, D.A., Prakash, S., Johnston, K.W. and Ethier, C.R. (1999) A numerical study of blood flow patterns in anatomically realistic and simplified end-to-side anastomoses, *ASME J. Biomech. Eng.*, **121**, 265-272.

[194] Perktold, K., Hofer, M., Rappitsch, G., Loew, M., Kuban, B.D., and Friedman, M.H. (1998) Validated computation of physiologic flow in a realistic coronary artery branch. *J. Biomech.*, **31**, 217-228.

[195] Ethier,C.R., Moore,J.A., Steinman, D.A., Martin, A.J., and Rutt,B. (1995) Flow simulations in a physiological arterial bifurcation. In:Hochmuch,R.M., Langrana, N.A., Hefzy, M.S.., (eds.), Bioengineering Conference, BED-Vol29, ASME, New York, 471-472.

[196] Bannister, L.H. (eds) (1995) Gray's Anatomy, Churchill Livingstone.

[197] Caro,C.G. (1981) Arterial fluid mechanics and atherogenesis, *Recent Advances in Cardiovascular disease*, **2**,6-11.

[198] Lou, Z. and Yang, W.J.(1992) Biofluid dynamics at arterial bifurcations. *Critical Rev. Biomed. Engng*, **19**, 455-493.

[199] Perktold,K.,Resch,M. and Florian,H. (1991) Pulsatile non-Newtonian flow characteristics in a three-dimensional human carotid bifurcation model, *ASME J. Biomech. Eng.*, **113**,464-475.

[200] Yamasaki,M (1995) Comparative anatomical studies on the thyroid and thymic arteries.3. Guinea-pig (cavia-cobaya), *Journal of Anatomy*, **186**, No.Pt2, 383-393.

[201] Bharadvaj,B.K., Mabon,R.F. and Giddens,D.P. (1982) Steady flow in a model of the human carotid bifurcation. Part I-Flow visualization, *J. Biomechanics*, **15**,349-362.

[202] Zhao, S.Z., Xu,X.Y. and M.W.Collins et al. (1999) Flow in Carotid Bifurcations: Effect of the superior thyroid artery. *Medical Engineering & Physics* **21**, 207-214.

[203] Barbee, K.A., Davies, P.F., Ratneshwar, L. (1994) Shear stress-induced reorganisation of the surface topography of living endothelial cells imaged by atomic-force microscopy. *Circulation Research*, **74**, 163-171.

[204] Davies, P.F. (1995) Flow mediated endothelial mechanotransduction. *Physiological Reviews*, **75**, 519-560.

[205] Glagov, S. (1994) Intimal hyperplasia, vascular modeling, and the restenosis problem. *Circulation*, **89**, 2888-2891.

[206] Li, G., Mills,I., Sumpio,B.E. (1994) Cyclic strain stimulates endothelial cell proliferation: Characterization of strain requirements. *Endothelium*, **2**, 177-181.

[207] Resnick, N., Gimbrone, M.A.Jr. (1995) Haemodynamic forces are complex regulators of endothelial gene expression. *Faseb J*, **9**, 874-882.

[208] Letsou,G.V., Rosales,O., Maitz,S., Vogt, A., Sumpio, B.E. (1990) Stimulation of adenylate cyclase activity in cultured endothelial cells subjected to cyclic stretch. *Journal of Cardiovascular Surgery*, **31**, 634-639.

[209] Awolesi, M.A., Widmann, M.D., Sessa, W.C., Sumpio, B.E. (1994) Cyclic strain increases endothelial nitric oxide synthase activity. *Surgery*, **116**, 439-445.

[210] Busse, R. and Fleming, I. (1998) Pulsatile stretch and shear stress: physical stimuli determining the production of endothelium-derived relaxing factors. *Journal of Vascular Research*, **35**, 73-84.

[211] Davies, P.F. (1997) Temporal and spatial relationships in shear-mediated endothelial signalling-Overview. *Journal of Vascular Research*, **34**, 208-211.

[212] Du, W., Mills,I., Sumpio, B.E. (1995) Cyclic strain causes heterogeneous induction of transcription factors, AP-1, CRE binding protein and NF-kB, in endothelial cells: species and vascular bed diversity. *J. Biomech.*, **28**, 1485-1491.